Basaltic Plinian and violent Surtseyan eruptions from the Masaya Caldera Complex, Nicaragua

Dissertation
zur Erlangung des Doktorgrades
der Mathematisch-Naturwissenschaftlichen Fakultät
der Christian-Albrechts-Universität
zu Kiel

vorgelegt von
Wendy Pérez Fernández

Kiel, 2007

Referent:	PD Dr. Armin Freundt
Korreferent:	Prof. Dr. Volker Schenk
Tag der mündlichen Prüfung:	4. Mai 2007
Zum Druck genehmigt:	Kiel, den 4. Mai 2007
	Der Dekan

Hiermit erkläre ich, daß ich die vorliegende Doktorarbeit selbständig und ohne unerlaubte Hilfen erstellt habe. Ferner habe ich weder diese noch eine ähnliche Arbeit an einer anderen Abteilung oder Hochschule im Rahmen eines Prüfungsverfahrens vorgelegt, veröffentlicht oder zur Veröffentlichung vorgelegt.

Wendy Pérez Fernández

Abstract

The Masaya volcanic complex in central-western Nicaragua consists of an older shield volcano whose central part has subsided to form a 6x11 km, >150 m deep, oval caldera basin that hosts a cluster of intra-caldera cinder cones. Subsidence of the Masaya caldera was caused by highly explosive Plinian, Phreatoplinian and violent Surtseyan basaltic eruptions during the last 6,000 years. The first eruption at ~6 ka produced the 14 km^3 San Antonio Tephra (SAT). The second eruption at 2.1 ka generated two deposit facies distinct in internal architecture and direction of distribution: La Concepción Tephra (LCT) and Masaya Triple Layer (MTL). The combined tephra volume is 3.6 km^3. The third eruption at ~1.8 ka formed the Masaya Tuff (MT) and the directly overlying Ticuantepe Lapilli (TIL), totalling 10 km^3.

The SAT consists of a lower sequence of alternating scoria lapilli fallouts and ash layers (A1-A5), followed by the most prominent Plinian fallout of fluidally-shaped scoria lapilli (A6) and a second prominent Phreatoplinian fallout (A7) containing abundant hydrothermally altered lithic fragments. The upper part of SAT is composed of phreatomagmatic cross-bedded surge deposits, accretionary lapilli-rich tuffs and an uppermost well-sorted fallout of dense lapilli. During its first half, the SAT eruption evolved through several subplinian, eruptions interrupted by phreatomagmatic pulses, to its climactic Plinian eruption (A6). During this event, collapse of a hydrothermal system initiated stronger magma-water interaction such that the second half of the eruption became fully phreatomagmatic.

The LCT is a succession of 8 main well-sorted, scoria lapilli to coarse ash fallout layers, intercalated with phreatomagmatic fallout and surge deposits, south of the caldera. The MTL, dispersed to the NW, resembles the LCT in that it is also composed of well-sorted lapilli to ash beds, separated by tuff layers. Identical geochemical compositions show that LCT and MTL derive from a single eruption. Correlation of the distinct LCT and MTL facies using lithological and geochemical characteristics allows to divide the combined LCT-MTL succession into 10 major subunits (I-X) differing in dispersal direction and eruptive mechanisms. Changing wind directions and evidence for time breaks suggest the entire eruptive period lasted probably several weeks or months, switching between Plinian and phreatomagmatic events which dominated the second half of the eruption, although the final event was the most intense Phreatoplinian eruption.

The MT is a partly indurated, poorly-sorted, ash-rich pyroclastic surge deposit of phreatomagmatic origin that extends to a distance of at least 35 km, covering much of the ground of the present Managua area. Large antidunes characterize the radially distributed medial facies but cross-bedding can be traced to 20 km, the distance to which the surges remained highly energetic. At greater distances, wind-driven surge clouds emplaced a NW fan of fallout ash. The TIL immediately overlies the MT and has the same chemical composition. It marks the terminal phase of the MT-TIL eruption that was less influenced by magma-water interaction such that high eruption columns emplaced fallout of Phreatoplinian character.

Distinctive geochemical characteristics of the Masaya tephras facilitated the correlation with distal ash layers in Pacific sediment cores; such correlations are supported by other stratigraphic relations. Resulting tephra volumes are more realistic than estimates based on land data alone. Isopach and isopleth maps for the subunits of each tephra were used to estimate eruption column heights and mass discharge rates. Basaltic Plinian eruptions are generally considered as exotic events but are common at Masaya. Water contents of <3.4 wt% measured in melt inclusions are moderate and cannot explain this eruptive behavior which is rather discussed in terms degassing dynamics in the conduit, by access of external water.

Chemical compositional parameters indicate that the Masaya magmas derived from different mantle sources. The SAT source was most strongly modified by subduction components (high Ba/La, U/Th), while the LCT-MTL source had the least modification; the MT-TIL source had intermediate characteristics. Switching between mantle sources occurred over short time periods of 10^2 to 10^3 years. The degree of partial melting (indicated by, e.g., La/Yb) varies inverse with the degree of subduction modification of the source, being lowest for the SAT and highest for the LCT-MTL. Measured melt-inclusion water contents show no relation to either degree of melting or strength of the slab signals.

Mineral thermobarometry shows that the magmas of all tephra units were stored in the upper crust (<500 MPa), in agreement with geophysical observations, at temperatures of 1100-1200°C. Magmatic differentiation at this level by fractionation of the ol-pl-cpx-mt phenocryst phases evolved somewhat differently in each case. MT-TIL achieved the most evolved bulk-rock composition but the most evolved glass occurs mingled with less evolved glass in the SAT. A change from ol-dominated to more strongly pl-controlled fractionation occurred in the MT-TIL and LCT-MTL magmas whereas the low-pressure fractionation of the SAT magma involved ol+pl in approximately constant, subequal proportions.

Central western Nicaragua is highly vulnerable for volcanic disasters, because it has the highest population density of the country, comprising the large cities of Managua, Granada and Masaya, and the principal lifelines. A risk analysis for the main population centers around the Masaya caldera shows that, in case of a similar eruption today, the most vulnerable communities would be Ticuantepe, Nindirí and Masaya. In addition, La Concepción southwest of the caldera, and the capital Managua, more than 15 km to the northwest, could be affected. Recurrence of major eruptions such as those described is likely to occur again in the future. Masaya is continuously geophysically monitored but a major problem is that precursors and mechanisms of basaltic Plinian eruptions are poorly understood. More research on basaltic Plinian eruptions is needed and mitigation plans must consider the possibility and consequences of their occurrence.

Zusammenfassung

Der Masaya Vulkankomplex in Zentralwest Nicaragua besteht aus einem älteren Schildvulkan dessen zentraler Teil sich abgesenkt hat. Dieses 6x11 km großes und >150m tiefe Calderabecken beherbergt ein Cluster aus Intra-Caldera Schlackenkegel. Die Subsidenz der Masaya Caldera wurde durch hoch explosive, plinianische, phreatoplinianische und surtseyanische, basaltische Eruptionen während der letzten 6000 Jahre ausgelöst. Vor ca. 6000 Jahre erzeugte die Erste dieser Eruptionen die 14 km^3 große San Antonio Tephra (SAT). Die zweite, 2100 Jahre alte Eruption bildete zwei Ablagerungsfazies aus, die als La Concepción Tephra (LCT) und Masaya Triple Layer (MTL) definiert sind. Sie unterscheiden sich durch ihren internen Aufbau und die Verbreitungsrichtung. Das kombinierte eruptierte Tephravolumen dieser beiden Einheiten beträgt 3.6 km^3. Die dritte und jüngste Eruption (ca. 1.8 ka) produzierte den Masaya Tuff (MT) und die direkt überlagernde Einheit von den Ticuantepe Lapilli (TIL). Zusammen ergeben die beiden Einheiten ein Tephravolumen von 10 km^3.

SAT besteht, im unteren Teil der Einheit, aus einer Abfolge aus sich wiederholenden Scoria Lapilli Fallablagerungen und Aschelagen (A1-A5). Diese wird von der markantesten Fallablagerungseinheit überlagert die aus charakteristischen Scoria Lapilli mit Fließgefügen besteht (A6). Darauf folgt die zweitbedeutendste, phreatopliniansiche Fallablagerung (A7), welche reichlich hydrothermal alterierte Fremdgesteinsfragmente besitzt. Der obere Teil von SAT setzt sich aus phreatomagmatischen, schräggeschichteten Surge-Ablagerungen, akkretionäre lapilli-reichen Tuffen und einer abschließenden, gut sortierten, aus dichten Lapilli bestehenden Fallablagerung, zusammen. Während der ersten Hälfte der SAT Eruption entwickelte sich eine subplinianisch dominierte Eruptionstätigkeit die durch sporadisch auftretende, phreatomagmatische Impulse unterbrochen wurde und sich hin zu einer klimarelevanten plinianischen Eruption (A6) veränderte. Während dieser Eruptionsphase verursachte der Zusammenbruch eines hydrothermalen Systems verstärkt Magma-Wasser Wechselwirkungen weshalb die zweite Hälfte der SAT Eruption vollständig phreatomagmatisch dominiert wurde.

LCT ist eine südlich der Caldera aufgeschlossene Abfolge von hauptsächlich acht, gut sortierten Fallablagerungen, die Korngrößen von Lapilli bis Grobasche aufweisen können. Dazwischengeschaltet sind phreatomagmatische Fallablagerungen und Surge-Ablagerungen. MTL verbreitete sich nach Nordwesten und ähnelt LCT dahingehend, dass sie aus gut sortierten Lapilli- bis Aschelagen aufgebaut ist, die durch phreatomagmatische Tuff-Lagen voneinander getrennt werden können. Eine identische chemische Zusammensetzung zeigt, das die Einheiten LCT und MTL einer Eruption entstammen. Die Korrelation beider unterschiedlichen Fazies durch lithologische und chemische Merkmale erlaubt es die kombinierte LCT-MTL Abfolge in zehn größere Untereinheiten zu unterteilen (I-X). Diese unterscheiden sich hinsichtlich der Verbreitungsrichtung und den Eruptionsmechanismen. Sich verändernde Windrichtungen und Hinweise auf Unterbrechungen innerhalb der Eruptionstätigkeit lassen vermuten, dass die gesamte Eruptionsdauer vielleicht mehrere Wochen oder Monate andauerte, wobei sich plinianische und phreatomagmatische Ereignisse abwechselten. Letztere dominieren dabei die zweite Hälfte der Gesamteruption, wenngleich das abschließende Eruptionsereignis durch die stärkste plinianische Eruption repräsentiert wurde.

Die MT ist durch eine teilweise zementierte, schlecht sortierte und Asche-reiche Ablagerung einer pyroklastischen Surge charakterisiert, welche sich bis zu 35 km von der Caldera weg ausdehnte und den größten Teil des heutigen Managua Gebiets bedeckt. Die radial verbreitete mediale Fazies wird durch große Antidünen charakterisiert, wobei Schrägschichtung bis zu einer Distanz von 20 km Entfernung von der Caldera nachgewiesen werden können und ein hochenergetisches Fließverhalten dokumentieren. In größeren Entfernungen haben windgesteuerte Surgewolken ein nordwestlich gerichteten Fächer von Aschefallablagerungen generiert. Die nachfolgenden TIL überlagern direkt die MT Ablagerungen und zeigen die identischen chemischen Zusammensetzungen. Diese finale Ablagerung repräsentiert die abschließende Eruptionsphase der gesamten MT-TIL Eruption und war weniger stark durch Magma-Wasser Wechselwirkungen geprägt, weshalb sich hohe Eruptionssäulen etablieren konnten welche phreatoplinianische Fallablagerungen erzeugten.

Unterschiedliche geochemische Merkmale der drei Masaya Tephras ermöglichten die Korrelation mit distalen Aschelagen in pazifischen Sedimentkernen, wobei diese Korrelationen zusätzlich durch andere stratigraphische Beziehungen unterstützt wurden. Die resultierenden erupierten Tephravoluminas sind realistischer als diejenigen, welche alleinig auf Landdaten basieren. Die Isopachen und Isoplethen Karten der einzelnen Untereinheiten jeder Tephraeinheit wurden außerdem dazu benutzt um Eruptionssäulenhöhen und Masseneruptionsraten abzuschätzen.
Die generell als exotisch eingestuften basaltische plinianische Eruption kommen sehr häufig in der Geschichte des Masaya Vulkankomplexes vor. Wassergehalte von Schmelzeinschlüssen <3,4 wt% sind mäßig hoch und können nicht als Erklärung für diesen Eruptionsmechanismus herangezogen werden. Bisher wurden eher diese magmatischen Wassergehalte als Ursache diskutiert als Entgasungsdynamiken die durch Zufuhr von externem Wasser innerhalb des Vulkanschlots gesteuert werden.
Chemische Parameter der Einzelnen Masaya Magmenzusammensetzungen deuten auf unterschiedliche Mantelquellen hin. Die Quelle von SAT wurde am stärksten durch Subduktionseinflüsse verändert (hohes Ba/La, U/Th), wogegen die Quelle von LCT-MTL die wenigsten, eher moderaten Einflüsse einer Subduktionskomponente aufweist. Dieser Wechsel zwischen den Mantelquellen fand innerhalb kurzer Zeiträume von 10^2 bis 10^3 Jahren statt. Der Aufschmelzgrad (gekennzeichnet durch bsp. LA/Yb) variiert gegenläufig zum stärker oder schwächer werdenden Einfluß der Subduktionskomponente innerhalb der Quellen und ist am niedrigsten bei SAT und am höchsten für LCT-MTL. Die gemessenen Wassergehalte der Schmelzeinschlüsse zeigen weder eine Beziehung zum Grad der Aufschmelzung noch zur Stärke des Slab Signals.
Themobarometrie mit Hilfe von Mineralzusammensetzungen zeigen, daß die Magmen aller drei Tephraeinheiten innerhalb der oberen Kruste bei einer Temperatur von 1100-1200°C gespeichert wurden (<500 MPa), was im Einklang mit geophysikalischen Beobachtungen steht. Die magmatische Differentiation durch Fraktionierung von Ol-Pl-Cpx-Mt Einsprenglingsphasen entwickelt sich jeweils leicht unterschiedlich in diesem Krustenbereich. MT-TIL erreichte dabei die am stärksten entwickelte Gesamtgesteinszusammensetzung. Hinsichtlich der Glaszusammensetzung zeigt SAT das höchst entwickelte Glas, gemischt mit primitiverem Glas. Eine Änderung von einer Olivin dominierten, zu einer viel stärker Plagioklas kontrollierten, Fraktionierung tritt in den MT-TIL und LCT-MTL Magmen auf. Dagegen zeigt die Fraktionierung bei niederen Drucken des SAT Magmas ungefähr konstante, gleiche Anteile an Olivin und Plagioklas. Diese Unterschiede zeigen geringe Variationen innerhalb des Wasserpartialdrucks an.
Das Gebiet um Zentral West Nicaragua ist sehr stark gefährdet bei vulkanischen Katastrophen, da es die höchste Bevölkerungsdichte des Landes hat und die großen Städte Managua, Granada und Masaya sowie Hauptlebensadern beinhaltet. Eine Risikoanalyse für die wichtigsten Bevölkerungszentren rund um die Masaya Caldera zeigt, daß bei einer vergleichbaren Eruption heute, Ticuantepe, Nindiri und Masaya die am stärksten gefährdeten Bezirke wären. Zusätzlich könnten auch noch La Concepción südwestlich der Caldera und die Hauptstadt Masaya, mehr als 15 km im Nordwesten in Mitleidenschaft gezogen werden. Das erneute Auftreten solcher hier beschriebenen Großeruption ist sehr wahrscheinlich in Zukunft. Trotzdem die Masaya Caldera kontinuierlich geophysikalisch überwacht wird, ist ein großes Problem, daß Vorboten und Mechanismen basaltischer plinianischer Eruptionen noch wenig verstanden werden und deshalb mehr an diesem Phänomen geforscht werden muß. Zusätzlich müssen Evakuierungspläne entwickelt werden welche die Möglichkeit ihres Auftretens und die darausfolgenden Konsequenzen berücksichtigen.

Resumen

El Complejo Volcánico Masaya en Nicaragua centro-occidental consiste en un antiguo volcán en escudo cuya parte central ha subsidido para formar una depresión caldérica oval de 6 x 11 km y más de 150 m de profundidad, que además alberga una serie de conos piroclásticos intra-caldéricos. La subsidencia de la caldera fue causada por una serie de erupciones basálticas altamente explosivas de tipo plinianas, phreatoplinianas y surtseyanas durante los últimos 6000 años. La primera erupción hace ~6 ka produjo la San Antonio Tephra (SAT), con un volumen total de 14 km^3. La segunda erupción hace 2.1 ka generó dos facies deposicionales con características internas y distribución distintas: La Concepción Tephra (LCT) al sur y la Masaya Triple Layer (MTL) al nororeste. El volumen total de ambas es 3.6 km^3. La tercera erupción hace 1.8 ka formó la Masaya Tuff (MT) y la sobreyacente Ticuantepe Lapilli (TIL), con un total de 10 km^3.

La SAT consiste de una sequencia inferior que alterna lapilli escoriáceo de caída y capas de ceniza (A1-A5), seguida por el evento de caída Pliniana más prominente que consiste en lapilli escoriáceo de morfología fluidal (A6) y un segundo evento de caída phreatopliniano con abundantes fragmentos líticos alterados hidrotermalmente. La parte superior de SAT está conformada por depósitos de oleadas piroclásticas de origen freatomagmático con laminación cruzada, tobas con abundante lapilli acrecional y una capa de caída superior bien seleccionada de lapilli denso. Durante la primera mitad de la erupción, la SAT evolucionó a través de varias eruptions subplinianas, interrumpidas por pulsos freatomagmáticos, hasta la erupción culminante (A6) de tipo pliniano. Durante este evento, el colapso del sistema hidrothermal permitió una interacción más fuerte del magma con agua externa, por lo cual la segunda parte de la erupción se volvió totalmente freatomagmática.

La LCT es una sucesión de 8 capas bien seleccionadas de lapilli escoriáceo y ceniza gruesa, intercaladas con depósitos freatomagmáticos de caída y oleadas que aflora al sur de la caldera Masaya. La MTL fue distribuida hacia el NW y se asimila a la LCT en que también consiste en capas de lapilli y ceniza bien seleccionadas separadas por tobas. La correlación de las distintas facies de LCT and MTL con base en sus características litológicas y geoquímicas permite dividir la sucesión combinada de LCT-MTL en 10 unidades principales (I-X), con diferente dirección de dispersión y mecanismos eruptivos. Direcciones de viento cambiantes y evidencia de pausas sugieren que el periodo eruptivo completo duró probablemente varias semanas o meses, alternando entre eventos plinianos y phreatomagmáticos que dominaron la segunda parte de la erupción, para dar paso al final de la eruption a la erupción phreatopliniana más intensa (X).

La MT es un depósito parcialmente endurecido, pobremente seleccionado y rico en ceniza, formado por oleadas piroclásticas de origen freatomagmático, que se extiende hasta una distancia de al menos 35 km de la fuente, cubriendo gran parte del suelo de la presente area de Managua. Las facies mediales se distribuyen radialmente y se caracterizan por la presencia de grandes antidunas, aunque estratificación cruzada puede ser trazadas hasta 20 km, distancia a la cual las oleadas se mantenían altamente energéticas. A mayores distancias, las nubes acompañantes de las oleadas fueron afectadas por los vientos, depositando un abanico de ceniza de caída hacia el NW. La TIL sobreyace directamente la MT y posee la misma composición química. Ella marca la fase final de la erupción del MT-TIL que fue menos influenciada por la interacción entre magma y agua que las altas columnas eruptivas que depositaron depósitos de caída de características freatoplinianas.

Las características distintivas de las tres tefras facilitaron la correlación con capas de ceniza distales encontradas en núcleos de perforación de sedimentos en el Pacífico, aunque esas correlaciones también fueron apoyadas por relaciones estratigráficas. Los volúmenes de tefra obtenidos son más realistas que los estimados únicamente con base en los datos en tierra. Mapas de isopletas e isopacas de las subunidades de cada capa de tefra fueron utilizadas para estimar alturas de la columna eruptiva y tasas de descarga de masa. Erupciones plinianas basálticas son generalmente consideradas como eventos exóticos, sin embargo son comunes en Masaya. Contenidos de agua de <3.4 wt% medidos en inclusiones vítreas son moderadas y no pueden explicar este comportamiento eruptivo, que puede ser mejor explicado por el acceso de agua externa que por cambios en la dinámica de desgasificación en el conducto.

Parámetros químicos indican que la composición de los magmas de Masaya se derivan de diferentes fuentes mantélicas. La fuente de SAT fue fuertemente modificada por componentes de subducción (alto Ba/La, U/Th), mientras que la fuente de LCT-MTL sufrió la menor modificación; MT-TIL presenta características intermedias. El cambio de fuentes mantélicas ocurrió en cortos periodos de tiempo de 10^2 a 10^3 años. El grado de fusión parcial (indicado por La/Yb entre otros) varía inversamente con el grado de modificación por subducción de la fuente, de forma tal que SAT presenta el menor grado de fusión parcial y LCT-MTL el mayor. Contenidos de agua medidos en inclusiones no muestran alguna relación con el grado de fusión o el enriquecimiento en indicadores de subducción.

Datos de termobarometría mineral muestran que los magmas que originaron las unidades de tefra fueron almacenados en un reservorio ubicado en la corteza superior (<500 MPa), de conformidad con observaciones geofísicas y a temperaturas entre 1100-1200°C. La diferenciación magmática por fraccionamiento de fenocristales de ol-pl-cpx-mt evolucionó un poco diferente en cada caso. MT-TIL alcanzó la composición más evolucionada de roca total, pero en SAT el vidrio más evolucionado aparece mezclado con vidrio menos evolucionado. Un cambio de fraccionación dominada por olivino a otra controlada fuertemente por plagioclasa ocurrió en los magmas de MT-TIL y LCT-MTL; mientras que fraccionación a baja presión del magma de SAT involucró ol+pl aproximadamente a proporciones constantes.

El centro-oeste de Nicaragua es un área altamente vulnerable a los desastres volcánicos, porque cuenta con la mayor densidad de población del país, incluyendo las grandes ciudades de Managua, Granada y Masaya, así como las principales líneas vitales. Un análisis de riesgo para los centros poblacionales principales alrededores de la caldera Masaya muestra que en caso de una erupción similar a las estudiadas ocurriera actualmente, las comunidades más vulnerables serían Ticuantepe, Nindirí y Masaya. Además, la población de La Concepción al suroeste de la caldera y la capital Managua, a más de 15 km al noroeste, podrían ser afectadas. La recurrencia de importantes erupciones como esas descritas podrían potencialmente ocurrir en el futuro. A pesar de que Masaya es contínuamente monitoreado, los mecanismos de las erupciones plinianas basálticas son pobremente comprendidos y posibles precursores se desconocen. Se requiere más investigación en erupciones basálticas plinianas y los planes de mitigación deben considerar la posibilidad y consequencias de su ocurrencia.

Contents

1 Introduction

1.1 Basaltic Plinian eruptions..... 1
1.2 Study area..... 2
1.2.1 Geological and tectonic setting of central-west Nicaragua..... 2
1.2.2 Masaya caldera complex..... 4
1.3 Objectives..... 5
1.4 Methodology..... 6
1.5 Thesis outline..... 7

2 Revised and refined tephrostratigraphy

2.1 Previous stratigraphic works 9
2.2 Methodology used for correlation..... 10
2.3 New stratigraphy for the Masaya tephras..... 11
2.3.1 The San Antonio Tephra (SAT)..... 12
2.3.2 La Concepción Tephra (LCT) and Masaya Triple Layer (MTL)..... 13
2.3.3 The Masaya Tuff (MT) and the Ticuantepe Lapilli (TIL)..... 13
2.3.4 Other units..... 13
2.3 Ages..... 14

3 The San Antonio Tephra

3.1 Clast components 16
3.2 Internal stratigraphy..... 16
3.2.1 Subunit A1 17
3.2.2 Subunit A2..... 17
3.2.3 Subunit A3..... 19
3.2.4 Subunit A4..... 19
3.2.5 Subunit A5..... 20
3.2.6 Subunit A6..... 20
3.2.7 Subunit A7..... 21
3.2.8 Subunit A8..... 21
3.2.9 Subunit A9..... 22
3.2.10 Subunit A10..... 22
3.2.11 Subunit A11..... 23
3.2.12 Subunit A12..... 23
3.2.13 Subunit A13..... 23
3.3 Lateral facies changes..... 24
3.4 Volume..... 26
3.4.1 Thickness distribution and volume..... 26
3.4.2 Distal tephra and total volume of the eruption..... 26
3.5 Eruption parameters..... 28

3.5.1 Eruption column height and wind speed..... 28
3.5.2 Mass eruption rates..... 29
3.5.3 Dispersal characteristics..... 31
3.6 Interpretation..... 32

4 La Concepción Tephra and the Masaya Triple Layer

4.1 La Concepción Tephra..... 35
4.1.1 Clast components..... 35
4.1.2 Internal stratigraphy..... 36
4.1.2.1 Subunit B0..... 38
4.1.2.2 Subunit B1..... 39
4.1.2.3 Subunit B2..... 40
4.1.2.4 Subunit B3..... 40
4.1.2.5 Subunit B4..... 40
4.1.2.6 Subunit B5..... 41
4.1.2.7 Subunit B6..... 43
4.1.2.8 Subunit B7..... 44
4.1.2.9 Subunit B8..... 44
4.1.2.10 Subunit B9..... 44
4.1.2.11 Subunit B10..... 46
4.1.2.12 Subunit B11..... 46
4.1.2.13 Subunit B12..... 47
4.1.2.14 Subunit B13..... 48
4.1.2.15 Subunit B14..... 48
4.1.2.16 Subunit B15..... 48
4.1.2.17 Subunit B16..... 48
4.1.3 Lateral facies changes..... 48
4.2 Masaya Triple Layer..... 51
4.2.1 Clast components..... 51
4.2.2 Internal stratigraphy..... 52
4.2.2.1 Subunit C1..... 53
4.2.2.2 Subunit C2..... 53
4.2.2.3 Subunit C3..... 55
4.2.2.4 Subunit C4..... 57
4.2.2.5 Subunit C5..... 57
4.2.2.6 Subunit C6..... 58
4.2.2.7 Subunit C7..... 58
4.2.2.8 Subunit C8..... 59
4.2.2.9 Subunit C9..... 60
4.2.2.10 Subunit C10..... 61
4.2.3 Lateral facies changes..... 62
4.3 Correlation between both units..... 66
4.3.1 Correlation of subunits B5 and C2..... 66

4.3.2 Proposed correlation 66
4.4 Volume 68
4.4.1 Thickness distribution 68
4.4.2 Volume 71
4.4.3 Distal tephra and total volume of the eruption 72
4.5 Eruption parameters 73
4.5.1 Eruption column height and wind speed 73
4.5.2 Mass eruption rates 77
4.5.3 Dispersal characteristics 78
4.6 Interpretation 80

5 The Masaya Tuff and the Ticuantepe Lapilli

5.1 The Masaya Tuff (MT) 83
5.1.1 Components 84
5.1.1.1 Fine fraction 85
5.1.1.2 Juvenile fragments 86
5.1.1.3 Lithic fragments 87
5.1.1.4 Accretionary lapilli 89
5.1.2 Bed forms 90
5.1.3 Facies variations 92
5.1.3.1 Vertical sequence 92
Subunit D1 94
Subunit D2 95
SubunitD3 96
Subunit D4 96
Subunit D5 96
Subunit D6 96
5.1.3.2 Facies changes with distance to the source 97
South and south-east sector 98
East, north and north-east sector 100
North-west 105
5.1.3.3 Discussion of facies variations 107
5.2 Ticuantepe Lapilli 108
5.2.1 Components 108
5.2.2 Internal stratigraphy 109
5.2.2.1 Subunit E1 109
5.2.2.2 Subunit E2 112
5.2.2.3 Subunit E3 112
5.2.2.4 Subunit E4 112
5.2.2.5 Subunit E5 112
5.2.2.6 Subunit E6 112
5.2.2.7 Subunit E7 112
5.2.3 Lateral facies changes 112

5.3 Volume..... 114
5.3.1 Thickness distribution and volume..... 114
5.3.1.1 Masaya Tuff..... 114
5.3.1.2 Ticuantepe Lapilli..... 115
5.4.2 Distal tephra and total volume of the eruption..... 116
5.4 Eruption parameters..... 118
5.4.1 Eruption column height and wind speed..... 118
5.4.2 Mass eruption rates..... 120
5.4.3 Dispersal characteristics..... 121
5.5 Interpretation..... 123

6 Geochemical characteristics of the Masaya tephras

6.1 Magma compositions..... 125
6.1.1 Major element compositions..... 126
6.1.2 Trace elements 128
6.1.3 Comparison with other deposits..... 131
6.1.3.1 Comparison with other Masaya-related rocks..... 131
6.1.3.2 Comparison with the Nejapa-Granada rocks..... 133
6.1.4 Geochemical variations in stratigraphic order..... 134
6.1.4.1 Bulk rock compositions..... 135
6.1.4.2 Glass compositions..... 136
6.1.4.3 Mineral chemistry..... 138
6.2 Vertical variations within the tephras..... 140
6.2.1 SAT..... 140
6.2.1.1 Bulk rock compositions..... 140
6.2.1.2 Glass compositions..... 141
6.2.1.3 Mineral compositions..... 144
6.2.2 LCT-MTL..... 145
6.2.2.1 Bulk rock compositions..... 145
6.2.2.2 Glass compositions..... 146
6.2.2.3 Mineral chemistry..... 149
6.2.3 MT-TIL..... 151
6.2.3.1 Bulk rock composition..... 151
6.2.3.2 Glass compositions..... 151
6.2.3.3 Mineral compositions..... 155
6.3 Origin and evolution of the magmas..... 157
6.3.1 Mantle sources..... 157
6.3.2 Variations in degree of partial melting..... 160
6.3.3 Modification during transport and storage..... 160

7 Magma chamber conditions

7.1 Pre-eruptive conditions..... 163
7.1.1 Water content..... 163
7.1.2 Temperature of crystallization..... 163
7.1.3 Pressure..... 167
7.1.4 Magma chamber conditions..... 168

8 Volcanic hazards

8.1 Volcanic hazards..... 169
8.1.1 Hazards from pyroclastic fall..... 170
8.1.2 Hazards from pyroclastic surges..... 170
8.1.3 Hazards from the Masaya caldera complex..... 170
8.2 Vulnerability of the area..... 171
8.2.1 Population..... 171
8.2.2 Buildings..... 174
8.2.3 Lifelines..... 175
8.3 Volcanic risk assessment..... 175
8.4 Discussion..... 177

9 Summary and Conclusions

9.1 Stratigraphy..... 179
9.2 Origin of the Masaya caldera..... 180
9.3 The generation of basaltic Plinian eruptions..... 181
9.4 Magmatic evolution..... 184
9.5 Volcanic hazards..... 185

Bibliography..... 187

Acknowledgments..... 195

Appendixes

Chapter 1

Introduction

1.1 Basaltic Plinian eruptions

Basaltic plinian volcanism is the most poorly understood type of basaltic activity and also the most dangerous due the rapid ascent rates of basaltic magma and wide dispersal of the tephra (Houghton et al. 2004). Plinian volcanism of basaltic composition is thought to be a rare phenomenon because basaltic magma mostly erupts in Strombolian, Hawaiian and Surtseyan fashion and as lava flows. Nevertheless, in the last two decades several examples of basaltic Plinian deposits have been reported in the volcanological literature, including the Fontana Lapilli and the Masaya Triple Layer or San Judas Formation of Masaya caldera, Nicaragua (Williams 1983b; Bice 1985; Wehrmann et al. 2006), the 122 BC eruption of Mount Etna, Italy (Coltelli et al. 1998), the 1790 AD Keanakakoi eruption of Kilauea, Hawaii (McPhie et al. 1990; Dzurisin et al. 1995; Mastin 1997) and the 1886 eruption of Tarawera, New Zealand (Walker et al. 1984; Sable et al. 2006).

Eruption mechanisms proposed for these deposits involve magma-water interaction (McPhie et al. 1990; Mastin 1997), high temperature and high density of the basaltic magma (Williams 1983b), interaction with a geothermal system (Walker et al. 1984), sudden decompression (Coltelli et al. 1998) or strong disequilibrium degassing (Wehrmann 2005). Houghton et al (2004) propose that conduit processes play a critical role in modifying the form of the eruptions and even with very high discharge, and presumably ascent rates, partial open-system behavior of basaltic melts becomes a critical factor that leads to development of domains of largely stagnant and outgassed melt that restricts the effective radius of the conduit. Present physical understanding of buoyant Plinian eruption columns requires high and relatively steady discharge rates, a high eruption temperature (as opposed to strong cooling by external water), and fine fragmentation of the magma to approach thermal equilibrium. No generally accepted model, however, has yet been found to explain how basaltic magmas fulfill these conditions.

The Masaya caldera complex in Nicaragua is a very remarkable volcano since it has been able to produce several basaltic Plinian events and high-volume surge deposits, as well as very fluid lava flows during the last 30 ka. Some pioneer works by Bice (1980,1985) and Williams (1983a, 1983b) gave an overview of the stratigraphy and geological history of the volcano. The Fontana Tephra has recently been revisited by Wehrmann et al. (2006), and Pérez and Freundt (2006) have shown that the younger succession at the caldera is more complicated than previously thought. There is still a lot of work to do in order to understand the driving mechanisms of basaltic Plinian eruptions in general, and what is so special about the Masaya volcano that it produced so many highly explosive basaltic eruptions.

1.2 Study area

1.2.1 Geological and tectonic setting of central-west Nicaragua

Nicaragua is part of the Central American Isthmus, where the subduction of the Cocos plate under the Caribbean Plate at a convergence rate of 70–90 mm/year (Barckhausen et al. 2001; DeMets 2001) results in a NW-SE trending volcanic front (Fig. 1.1). The actual volcanic front locates inside the Nicaraguan Depression, which is a NW-SE striking 45-50 km wide flat depression occupied by Lake Managua, Lake Nicaragua and the Pleistocene-Holocene volcanic centers. The depression extends to the NW, reaching the Pacific Ocean in the Gulf of Fonseca and is limited at the E by the so-called interior highlands (Ehrenborg 1987; Fig. 1.1). This depression has been previously interpreted as a graben or half graben (Weyl 1980, McBirney and Williams 1965, Cruden 1988, Weinbeg 1992), but more recent work argued it is merely a low-lying area between the central highlands and the Pacific coastal hills and not associated with large-scale tectonic structures (van Wyk de Vries 1993).

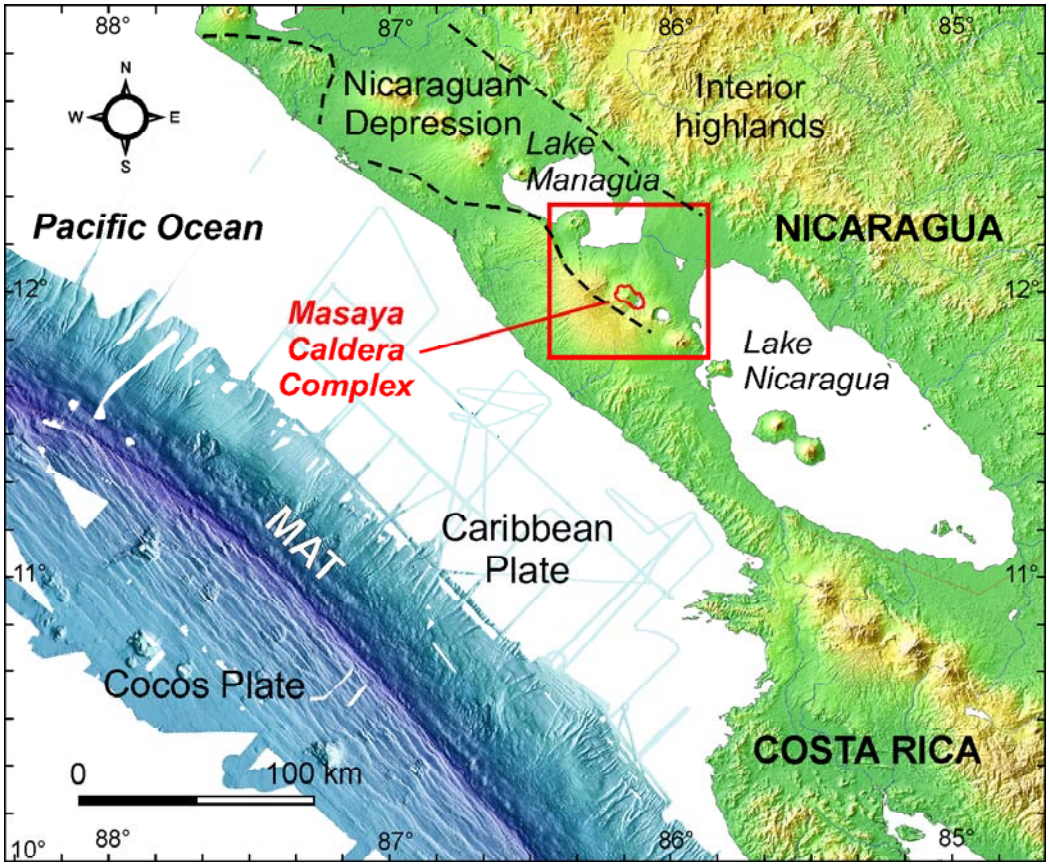

Figure 1.1: Map showing the geotectonic setting of western Nicaragua and northern Costa Rica. MAT is the Middle American Trench, marked by the darker blue area of the bathymetry. The black stippled line marks the boundary of the Nicaraguan depression after van Wyk de Vries (1993). The square encloses the study area shown in Fig. 1.2.

The area inside the depression located between the two lakes is the economical and social axis of the country, where the most populated cities are located and is surrounded by several highly explosive basaltic to rhyolitic volcanic complexes. The most important are from SE to NW: Mombacho, Apoyo, Masaya and Chiltepe (Fig. 1.2). In the western outskirts of Managua city there are an aligned series of pyroclastic cones and pit structures, the Nejapa-Miraflores alignment (Walker 1984). This group of volcanic edifices bound together with the Cofradía fault the Managua graben, the most active tectonic feature in Nicaragua (van Wyk de Vries 1993, Girard and van Wyk de Vries 2005).

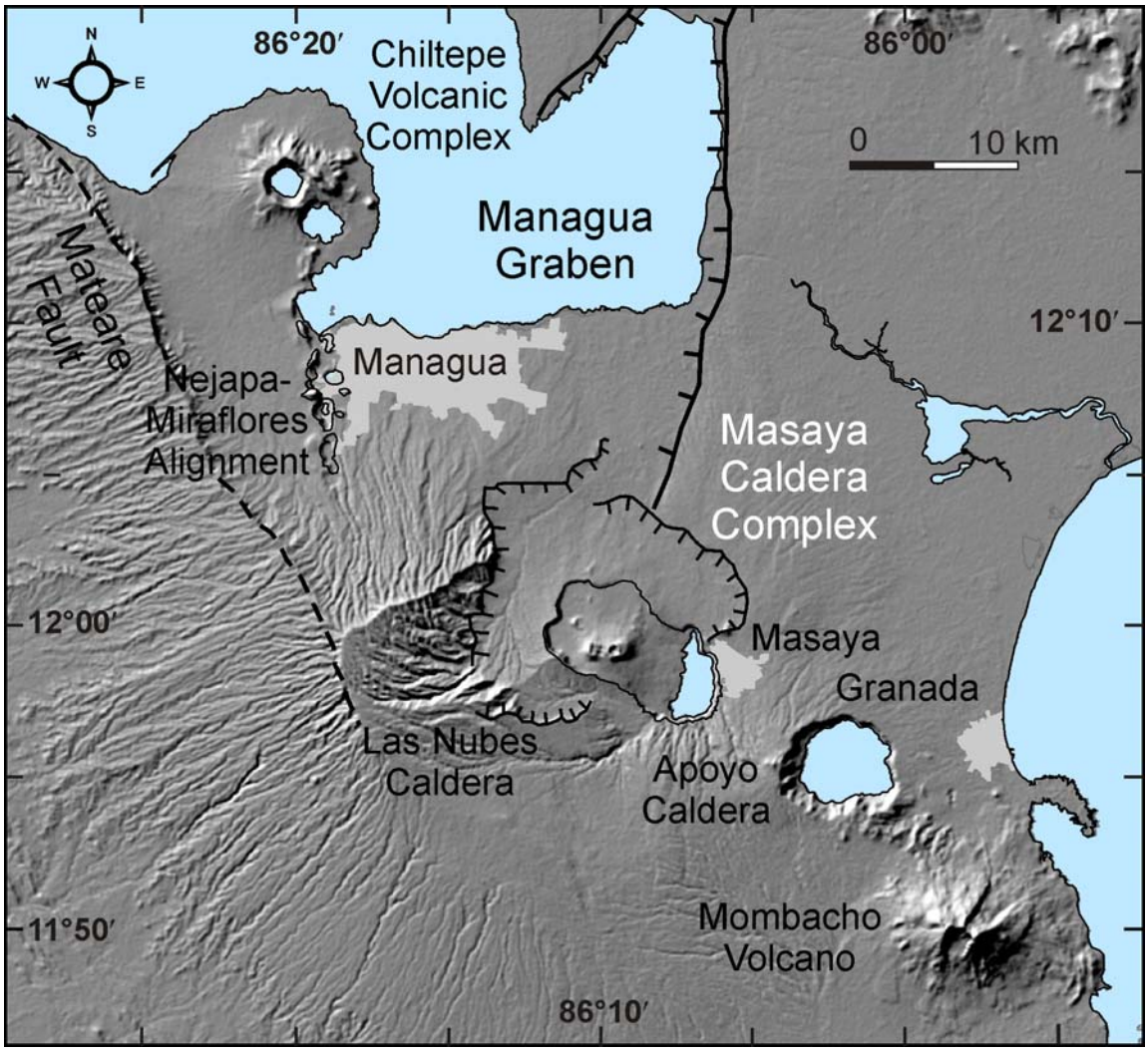

Figure 1.2: Study area showing the main volcanic edifices Mombacho, Apoyo Caldera, the Masaya Caldera Complex, the older Las Nubes Caldera, the Nejapa-Miraflores alignment pits and cones and the Chiltepe Volcanic Complex with its two volcanic lakes Xiloá and Apoyeque. The Managua graben and Las Nubes Caldera are indicated as after Sebesta (1997) and Girard and van Wyk de Vries (2005). The main cities Masaya, Granada and the capital Managua are located between the volcanic centers.

The basement of the area is thought to be Las Sierras Group, considered by Bice (1980) as a group of pyroclastic and epiclastic rocks mostly of mafic compositions with no clear relationship to any present volcanic structure. Radiometric ages of rocks from the upper Las Sierras Formation range in age from more than 100,000 years (Kuang 1971; Bice 1980) to 29,200 ± 800 yrs. B.P. (Williams, 1983a). Because of this wide age range, Williams (1983a) considered this formation to be an assemblage of many genetically unrelated rock units. More recently, Girard and van Wyk de Vries (2005) interpreted Las Sierras as a proto-Masaya volcanic system made up by basic ignimbrites erupted from the 25 km wide Las Nubes caldera enclosing the Masaya volcano (shown in Fig. 1.2).
Overlying these older rocks is the Managua Formation (Niccum 1976, Bice 1985; Kutterolf et al. in press), a thick tephra sequence intercalating rhyolitic and dacitic deposits of the Apoyo caldera and Chiltepe volcanic complex with basaltic deposits from the Masaya caldera.

1.2.2 Masaya caldera complex

The Masaya caldera complex is formed by a NW-SE elongated caldera 11 km long and 6 km wide, comprising the Masaya Lake at the SE rim and the post-collapse volcanic edifice, the so-called Santiago or simply Masaya volcano (Fig. 1.3), which developed within the caldera from eruptions along an arcuate series of vents (Williams-Jones et al. 2003).
Post-collapse activity produced the two main Masaya and Nindirí cones and several pit craters: Masaya, Santiago, Nindirí and San Pedro (Fig. 1.3). The currently active Santiago crater is believed to have formed in 1859 (McBirney 1956; Rymer et al. 1998) and it is characterized by an intermittent lava lake and an alternation of quiescent degassing with stronger periods of degassing (Williams-Jones et al. 2003). An energetic degassing phase through a lava lake took place in 1979, and the present degassing activity started in 1993 (Bulletin of the Global Volcanism Network 1993). Sandberg and Connor (2002) argue that the shallow magmatic system is in equilibrium with an apparently channelized groundwater body.
Masaya is one the most active volcanoes in Central America and it has been object of several geophysical and gas chemistry investigations. These investigations point out that Masaya caldera is underlain by a shallow upper crustal reservoir, which size has not been constrained. Gravity and degassing studies of the Masaya post-collapse cone (Williams-Jones, 2001) propose a 0.5 km^3 magma reservoir with convective removal of cooled and degassed magma and subsequent recharge by volatile rich magma from depth. Other studies propose a bigger reservoir ~10 km^3 slightly offset from the caldera (Connor and Williams 1990; Williams 1983a; 1983b; van Wyk de Vries 1993; Walker et al. 1993, Métaxian 1994).

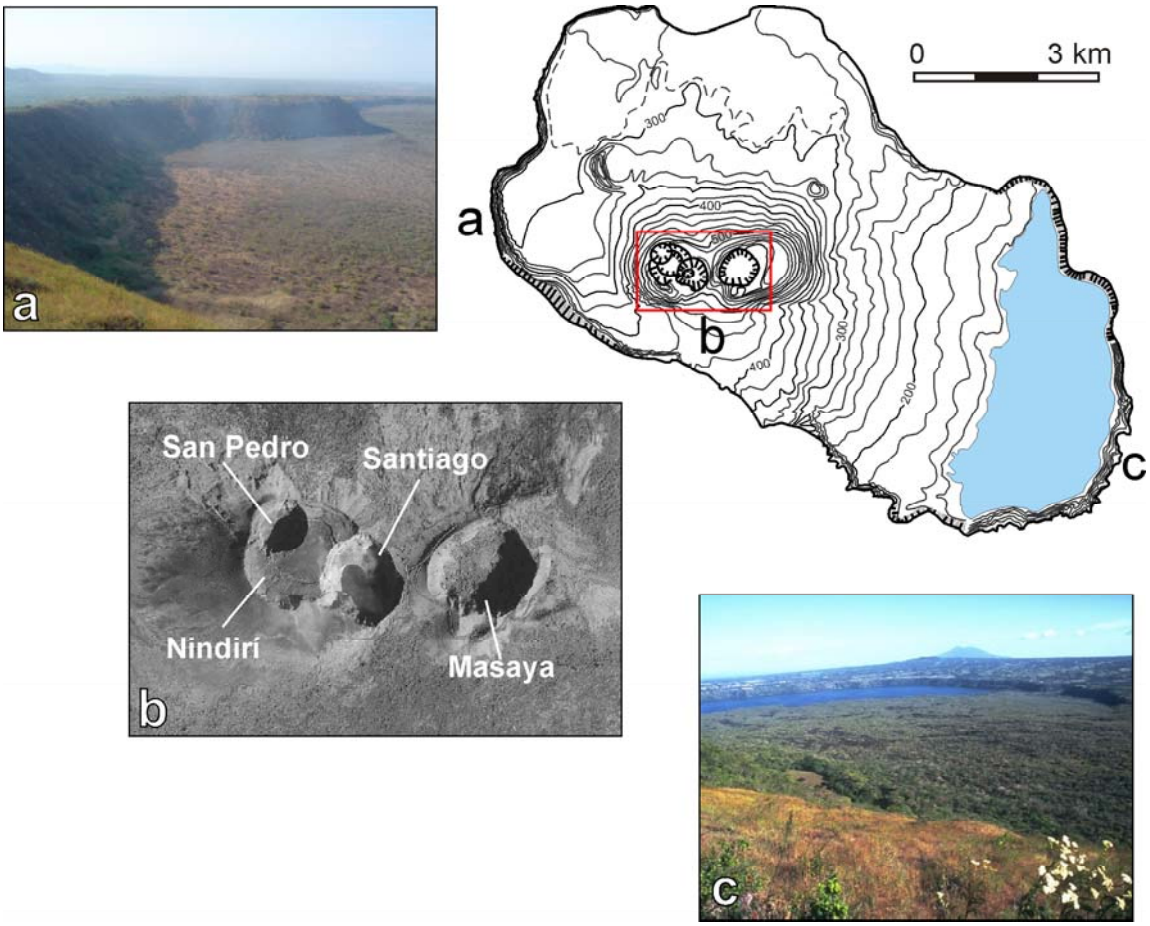

Figure 1.3: the Masaya Caldera Complex. [**a**] Photograph of the steep western portion of the caldera rim. [**b**] Detail view of the post-collapse edifice summit with its four pit craters (photo courtesy of NOAA). [**c**] Photograph of the Lake Masaya and the caldera rim, at the SE of the caldera; taken from http://volcano.si.edu. Masaya city just above the steep scarp and the volcano in the background is Mombacho.

1.3 Objectives

The main objective of this work is the identification and stratigraphy of Pleistocene to Recent highly explosive eruption deposits from the Masaya caldera complex, in order to determine the temporal and spatial evolution of the volcanic complex.
Secondary objectives also related with the main task include:

- Determine the stratigraphic sequence and changing eruption styles of multi-phase eruptions as a prerequisite to determine compositional gradients and variations in discharge rate.

- To map the areal thickness and grain size distributions of individual deposits (isopach and isopleth maps) in order to determine erupted masses, discharge rates and eruption column heights.

- Determine the magma composition and evolution within the last 6,000 years.

- Assessment of the volcanic hazards related to highly explosive eruptions from the Masaya caldera complex for the nearby population centres.

1.4 Methodology

The stratigraphic subdivisions and correlations are based on data of 239 outcrops around the Masaya caldera, studied in three field campaigns carried out in April 2003, April-May 2004 and April 2005. Correlations between outcrops were made using lithological criteria as well as geochemical data comparisons.

Tephra volumes were estimated using the isopach maps and the methods of Pyle (1989) and Fierstein and Nathenson (1992), by constructing a diagram of the ln of the isopach thickness and the square root of the area inside the isopach. The volume of pores and lithic fragments were subtracted from the total tephra volume and then converted to magma mass by multiplying the result by a density of 2700 kg/m^3. Tephra volumes include distal thickness data from marine gravity cores collected offshore Nicaragua during research cruises M54/2, M66/3a-b (RV METEOR) and SO173/3 (RV SONNE) (Kutterolf et al. submitted to G3); the stratigraphic correlation of marine ash layers with deposits on land is supported by chemical analyses, rates of sedimentation and relative age with respect to well-dated and correlated horizons.

Geometric measures from isopleth maps, based on the average of the five largest juvenile or lithic clasts, are used to estimate eruption column heights and discharge rates by comparison with the theoretical modeling results of Carey and Sparks (1986), Wilson and Walker (1987) and Woods (1988).

Batches of 2-3 lapilli of pre-determined bulk weight were mixed with loosely packed, ideally sorted coarse sand of known bulk density in a fixed-volume container and weighted. This allowed calculating their bulk volume and thereby the average bulk density and porosity with an uncertainty better than 5%, deduced from repeated measurements.

Thin sections made from all eruptive units provided textural characteristics and modal compositions necessary to understand petrogenetic processes and to constrain stratigraphic correlations. Bulk-rock concentrations of major and some trace elements were determined at IFM-GEOMAR by X-ray fluorescence analysis with an automated Philips X'Unique PW 1480 XRF spectrometer, using glass pellets made from finely ground sample powder mixed with lithium borate as fluidising agent. Trace and Rare Earth Elements from bulk rock were analysed at the University of Kiel with an Inductively Coupled Plasma Quadrupole Mass Spectrometer (ICP-MS; Agilent 7500cs and VG Instruments PlastaQuad1). Mineral, matrix and inclusion glass compositions were determined at IFM-GEOMAR with a Cameca SX50 wavelength dispersive electron microprobe at 15 kV accelerating voltage and a varying beam current of 10 (glass) to 50 nA (olivine). Laser Ablation Inductively Coupled Plasma Mass Spectrometry (LA-ICP-MS) at Frankfurt University (Finnigan VG PQII ELEMENT2 connected to a Merchantek UV-266/213 nm Laser) was used for the trace element chemistry of glass samples. Mineral, groundmass glass and whole-rock compositions were used to identify the composition and T-P conditions in the magma prior to eruption. Water content measurements in melt inclusions were made with Fourier-Transform infrared spectroscopy (FT-IR) at the Texas University at Austin.

The age of the deposits was determined by radiocarbon dating of charcoal at the Leibniz Laboratory for Radiometric Dating and Isotope Research at the University of Kiel. The samples were checked and mechanically cleaned under the microscope, afterwards sieved, and the dark organic-looking material <250µm was selected for further treatment. Conventional ^{14}C ages were calculated according to Stuiver and Polach (Radiocarbon 19/3 (1977), 355) with a $\delta^{13}C$ correction for isotopic fractionation based on the $^{13}C/^{12}C$ ratio measured by the AMS-system simultaneously with the $^{14}C/^{12}C$ ratio. The alkali extraction of the organic fraction (humic acid fraction) was precipitated with HCl, washed and dried, and afterwards also measured by the AMS-system.

1.5 Thesis outline

This work characterizes the deposits of the youngest explosive eruptions from the Masaya caldera in the last 6 ka, discussing the stratigraphy and correlation between these deposits as well as their geochemical characteristics to reconstruct magma chamber and conduit processes and to derive a hypothesis for the eruption mechanisms.
The dissertation consists of 9 chapters. The Introduction (chapter 1) addresses the location and geotectonic framework of the area and discusses why Masaya volcano is so particular, as well as the methodology and objectives of the work. The four following chapters (2, 3, 4 and 5) deal with the detailed stratigraphy and characteristics of the identified eruption deposits and eruptive parameters. Chapter 6 is dedicated to the chemical aspects in terms of vertical variations of the deposits and the magma composition and evolution in the last 6 ka. Chapter 7 deals with the magma chamber conditions prior and during the eruption like temperature and pressure of crystallization and water content. Chapter 8 is an assessment of the risk from a highly explosive eruption of the Masaya caldera complex for the surrounding areas. Finally the last chapter summarizes and discusses the derived results.

Preliminary results of this work have been consigned in the following publications:

Abstracts

- **Pérez W**, Kutterolf S, Freundt A (2005) The youngest explosive volcanic eruptions from the Masaya caldera complex (Nicaragua): Stratigraphy and volatile content. Sonderforschungsbereich - SFB 574 Retreat 13-15 August 2005

- **Pérez W**, Freundt A, Schmincke H-U, Kutterolf S (2006) Highly explosive basaltic eruptions from Masaya caldera complex, central Nicaragua, during the past 6,000 years: Stratigraphy and hazard aspects. EGU General Assembly, Geophysical Research Abstracts, Vol. 8, 07483

- Schmincke H-U, Freundt A, Kutterolf S, **Pérez W** (2005) Escaping from a powerful eruption –the 6000 year old human footprints at Acahualinca (Nicaragua). Lateinamerika Kolloquium, April 2005, Potsdam

- **Pérez W**, Freundt A, Kutterolf S (2007) Reconstruction of the 2,000 year old basaltic Plinian event from Masaya Caldera Complex (Nicaragua): the Masaya Triple Layer and La Concepción Tephra. Lateinamerika Kolloquium, April 2007, Kiel

- **Pérez W**, Freundt A, Kutterolf S (2007) Stratigraphic geochemical variations of the youngest explosive Masaya caldera complex tephras. Margins Workshop, June 2007, Heredia, Costa Rica

- Freundt A, Kutterolf S, **Pérez W**, Wehrmann H, Schmincke H-U (2007) CAVA magma production rates and volcanic hazards: Some aspects based on widespread tephras. Margins Workshop, June 2007, Heredia, Costa Rica

- Kutterolf S, Freundt A, **Pérez W,** Schmincke H-U (2007) Plinian volcanism along the ring of fire – Cyclicity and compositions from the long-term marine tephra record at the Central American Volcanic Arc (CAVA). Margins Workshop, June 2007, Heredia, Costa Rica

Peer-reviewed publications

- **Pérez W,** Freundt A (2006) The youngest highly explosive basaltic eruptions from Masaya caldera (Nicaragua): Stratigraphy and hazard assessment. In: Rose WI, Bluth GJS, Carr MJ, Ewert J, Patiño LC, Vallance J: Volcanic hazards in Central America. Geol Soc Amer Sp Pap 412:189-207

- Kutterolf S, Freundt A, **Pérez W**, Wehrmann H, Schmincke H-U Temporal succession and magnitudes of highly-explosive volcanic eruptions in west-central Nicaragua. J Volcanol Geotherm Res (in press)

Submitted or currently in preparation

- Kutterolf S, Freundt A, Schacht U, Mörz T, **Peréz W**, Wehrmann H, Bürk D, Schmidt M, Schmincke H-U Marine Tephras from explosive volcanism in Nicaragua - Implications for volcanology and marine science at the Pacific slope (submitted to G3)

- Kutterolf S, Freundt A, **Peréz W** Distal tephras offshore Guatemala and El Salvador - Source study and implications for distribution and erupted volumes (submitted to G3)

- **Pérez W**, Freundt A, Kutterolf S The Masaya Triple Layer: a 2000 year old basaltic Plinian event from Masaya caldera complex (Nicaragua)

Chapter 2

Revised and refined tephrostratigraphy

2.1 Previous stratigraphic works

The first geological study on volcanic rocks in Nicaragua was that of McBirney and Williams (1965), but this one was more related to the active volcanoes. The first attempt to establish a stratigraphic sequence in the Managua area was made by Niccum (1976), who differentiated the airfall pyroclastics overlying Las Sierras Group as the Managua series.

Bice (1980) made a much more detailed work on the Managua sequence which he defined as a series of basaltic to rhyodacitic airfall tuffs, ashes and lapilli layers, with sources at the nearby Apoyeque, Xiloá, Masaya and Apoyo volcanic centers. In total he identified four rhyodacitic deposits and three widespread basaltic ones (Fig. 2.1).

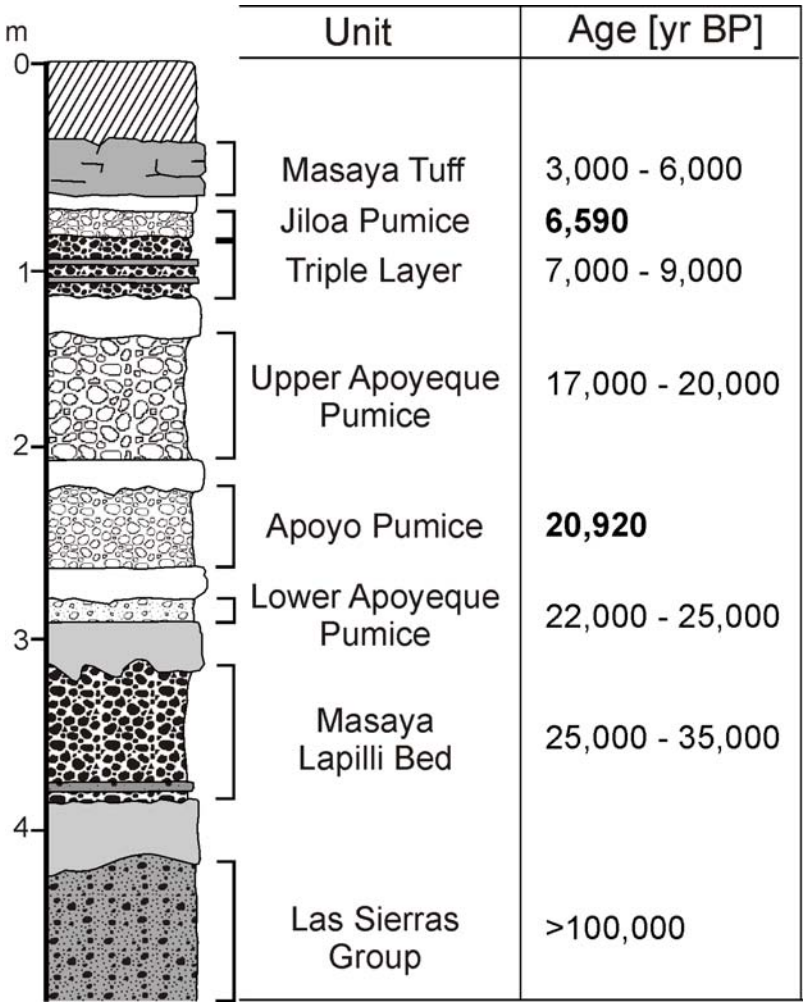

Figure 2.1: Stratigraphy of the Managua sequence of Bice (1980) with the ages he assigned to the units. Bold numbers denote absolute radiocarbon dates and the age ranges were estimated by stratigraphic relationship with the dated units.

Williams (1983a) in his work about the geology of the Masaya caldera complex studied three basaltic pyroclastic deposits in more detail:

[a] the older Masaya Lapilli Bed (Bice 1980; 1985) or Fontana Lapilli (Williams 1983b). This deposit was recently re-investigated and renamed as the Fontana Tephra by Wehrmann et al. (2006). She concluded that the source vent probably did not lie within the Masaya caldera but a few kilometers outside to the NW, what makes it part of Las Nubes caldera. The deposit is composed of well-sorted highly vesicular scoria lapilli of fallout origin and minor surge deposits limited to the most proximal exposures. The characteristics of the deposit suggest that it was a magmatic eruption not significantly affected by external water.

[b] the Masaya Triple Layer (Bice 1980; 1985) or San Judas Formation (Williams 1983b). Bice (1980; 1985) described the unit as two thin indurated tuffs sandwiched between three loose layers of coarse black ash, the reason why he assigned that name. He also mentioned that the deposit thickens towards Masaya caldera and becomes more complex, adding extra layers. Williams (1983a; b) described it as well-sorted, non-graded and composed of five to twelve scoria fall layers with a thickness between 0.5 to 1.5 m.

[c] the youngest Masaya Tuff (Bice 1980; 1985) or El Retiro Tuff (Williams 1983b), first reported by Krusi and Schultz (1979). It was later described by Bice (1980; 1985) as a thick widespread light tan poorly to moderately indurated, faintly layered to massive fine airfall basaltic tuff, with an average thickness between 20 and 50 cm and which constitutes the youngest large explosive deposit in the Managua area. Based on the chemical composition, petrographic similarities and field evidence, Bice (1980) stated that Masaya Tuff originated from the site of the present Masaya caldera and was probably genetically related to the collapse and formation of the caldera as it exists presently. He thought this fine grained indurated tuff in Managua city was the fine fall deposit equivalent of the base-surge facies at the Masaya caldera walls. Williams (1983a) described this unit as “pyroclastic surge deposits of unprecedented areal extent and volume; with a median grain size much coarser than any other measured before, as well as dune-forms and flow velocity of tremendous scale”.

2.2 Methodology used for correlation

Detailed sections made for the best outcrops of the total 239 were compared with other exposures in order to define the vertical sequence and the facies changes with distance to the Masaya caldera.

Correlations between outcrops were based on characteristics of the componentry (type of particle, shape, texture, vesicularity, crystallinity, mineral and lithic fragments content, among others), bed structures, relative succession, relative stratigraphic position, occurrence of large unconformities and the nature of intercalated sediments, as well as modal and chemical compositions. Geochemical data like whole rock, glass and mineral analysis were used for comparison between the units.

2.3 New stratigraphy for the Masaya tephras

The revised new stratigraphy of the Managua area resulting from this work and from Kutterolf et al. in press) is presented in Fig. 2.2.

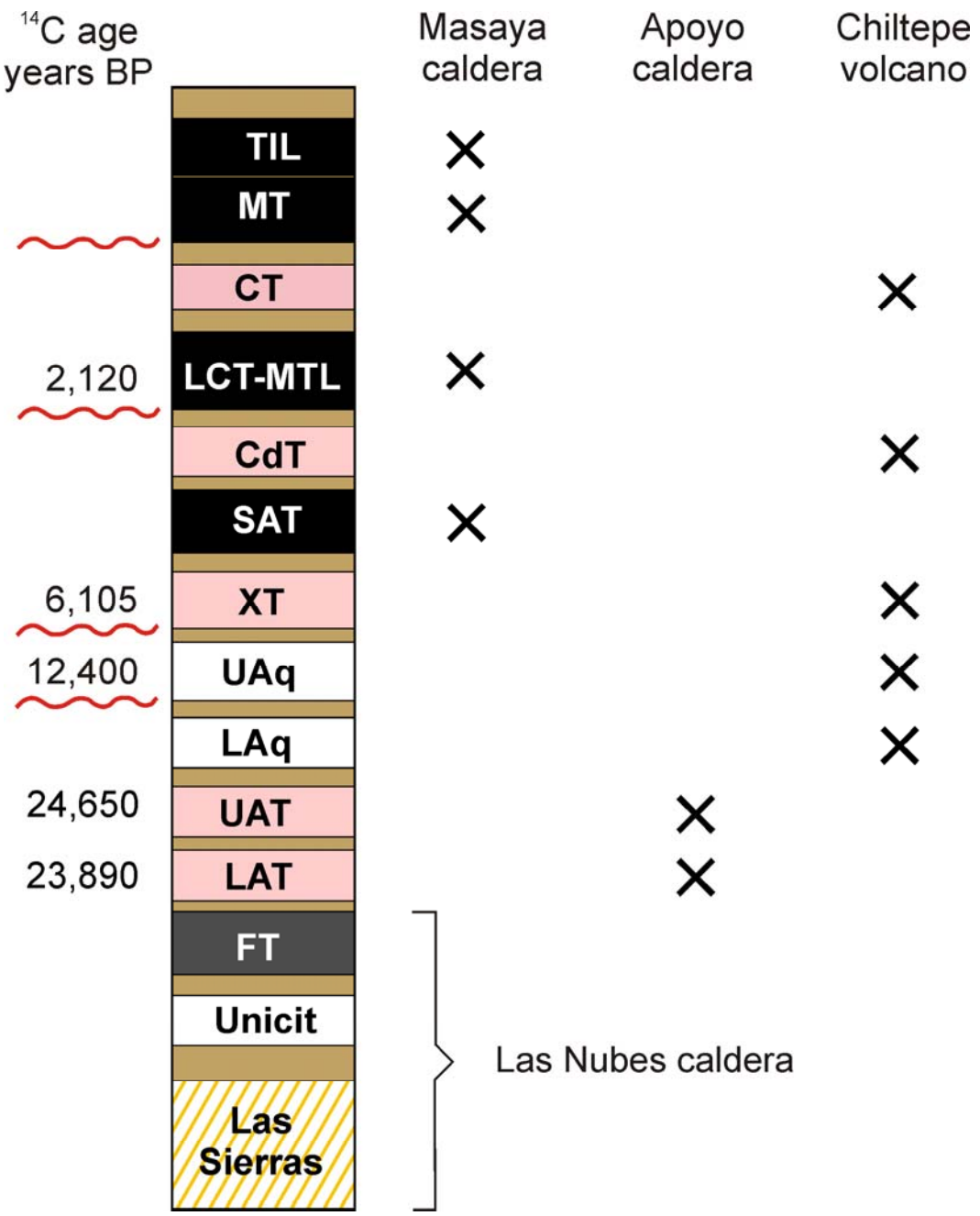

Figure 2.2: Stratigraphy of the Chiltepe-Managua-Masaya area based on this work and on Kutterolf et al. (in press). Black is used for basaltic tephra, dark-gray for basaltic-andesitic, white for dacitic, pink for rhyolitic and brown for paleosols. FT: Fontana Tephra, LAT: Lower Apoyo Tephra, UAT: Upper Apoyo Tephra, LAq: Lower Apoyeque Tephra, UAq: Upper Apoyeque Tephra, XT: Xiloá Tephra, SAT: San Antonio Tephra, LCT: La Concepción Tephra, MTL: Masaya Triple Layer, CT: Chiltepe Tephra, MT: Masaya Tuff, TIL: Ticuantepe Lapilli.

This work focuses on the stratigraphic succession of the highly explosive basaltic eruption deposits from the Masaya caldera complex of the last 6 ka. This time limit excludes the ca. 60 ka Fontana Tephra, which was already studied in detail by Wehrmann (2005). These younger deposits originated are grouped into three main eruptions: [1] the San Antonio Tephra (SAT), [2] La Concepción Tephra (LCT) and the Masaya Triple Layer (MTL), and [3] the Masaya Tuff (MT) with the Ticuantepe Lapilli (TIL). They were defined according to their stratigraphic position, bounded by unconformities or by dacitic and rhyolitic fallout deposits from the Chiltepe and Apoyo volcanic centers and by their chemical affinities. Members of the same group show the same chemical composition and plot in specific fields in several chemical diagrams (Fig. 2.3), supporting strongly the interpretation that they belong to separate eruptions.

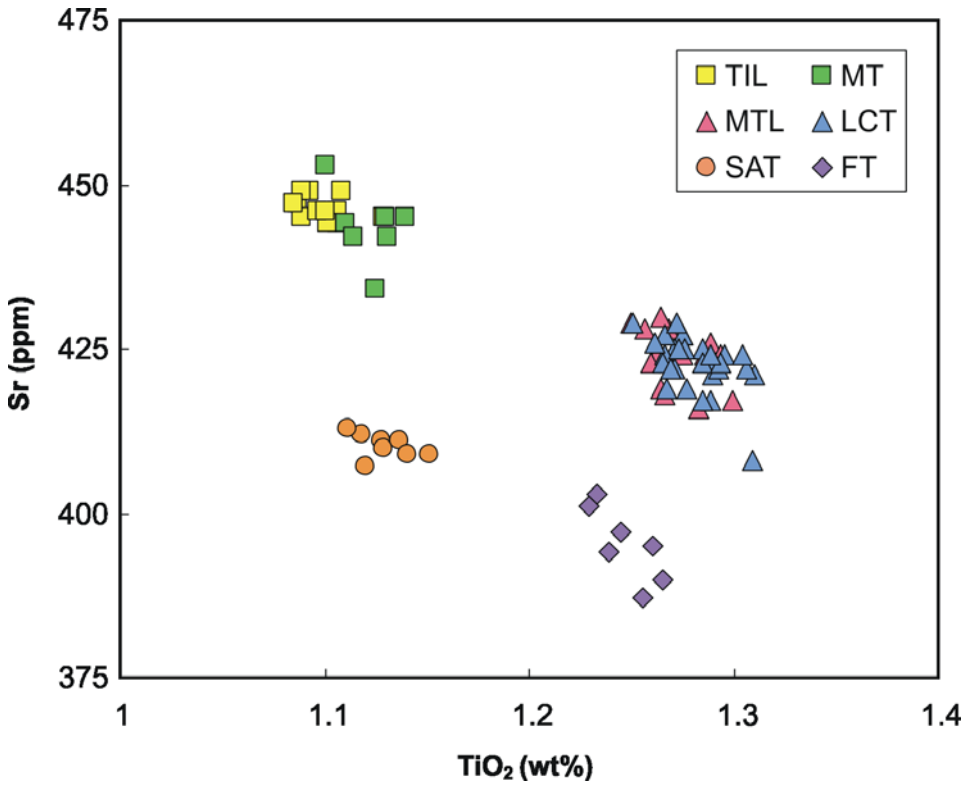

Figure 2.3: Diagram of Sr vs. TiO_2 contents of whole rock for the Masaya Tephras, showing that the deposits from different eruptions are compositionally distinct. Data for the ca. 60 ka old Fontana Tephra (FT) from Wehrmann (2005) are also included for comparison. Abbreviations used for the tephras are the same as in Fig. 2.2.

2.3.1. The San Antonio Tephra (SAT)

The San Antonio Tephra is reported here for the first time. It is the oldest basaltic Plinian deposit presently known to have doubtlessly erupted from the Masaya caldera. It comprises a lower succession of well-sorted scoria fall layers alternating with phreatomagmatic tuff beds, and an upper succession of pyroclastic surge deposits and accretionary-lapilli tuffs.

This unit underlies La Concepción Tephra and the Masaya Triple Layer from which it is separated by a thick paleosol and a regional erosive unconformity. At the NW of the caldera it is underlain by paleosols from the older Xiloá Tephra,

erupted from the Chiltepe volcanic complex (Kutterolf et al. in press), whereas to the E overlies pumiceous fall deposits originated at Apoyo caldera.

2.3.2 La Concepción Tephra (LCT) and Masaya Triple Layer (MTL)

At about 2 ka ago, another Plinian eruption at Masaya caldera produced the Masaya Triple Layer (Williams 1983b; Bice 1985). The re-investigation of this unit lead to the identification of two different facies which differ by their regional distribution and internal architecture: the Masaya Triple Layer to the NW, and La Concepción Tephra to the S. Despite the -at first sight- lithological differences they show identical chemical composition and they can be correlated, as will be shown in chapter 4.

To the NW, the MTL overlies a relief-forming regional erosional unconformity which together with intervening reworked tuffaceous deposits separate it from the older SAT. The MTL is overlain by the dacitic Chiltepe Tephra, in turn followed by the Masaya Tuff; all three are separated by intercalated reworked sediments and weathering horizons. S of the caldera, LCT overlies the SAT through an erosional unconformity and is overlain by the Masaya Tuff. This topmost contact is erosive and has carved different levels of LCT.

2.3.3 The Masaya Tuff (MT) and the Ticuantepe Lapilli (TIL)

The last big eruption from the Masaya caldera produced the Masaya Tuff, a huge phreatomagmatic pyroclastic surge deposit (Williams 1983a; Bice 1985). This eruption terminated in a stratified succession of well-sorted fallouts of vesicular and dense scoria, the Ticuantepe Lapilli.

The Masaya Tuff conformably overlies the Masaya Triple Layer, separated by a weathered massive fine-grained tuffaceous deposit containing scattered scoria or pumice fragments. Locally, it rests on an erosive unconformity cutting into La Concepción Tephra. In outcrops west of Managua city and near Chiltepe Peninsula, the Chiltepe Tephra separates the MTL and the MT. The Ticuantepe Lapilli directly overlies the Masaya Tuff without any sign of repose time in between but with a sharp contact. Near the volcano it is overlain by a grayish massive indurated tuff, an orange volcaniclastic deposit and younger Masaya deposits.

2.3.4 Other units

Williams (1983a) reports a basaltic ignimbrite exposed all around Masaya caldera underlying the Masaya Tuff, whose description fits with a fragmentary bomb-bearing deposit found along the road that crosses the southern rim of the caldera. However, the study of this specific deposit lies beyond the scope of this work and has to be carefully revised especially concerning to the transport and deposition mechanisms.

Several primary pyroclastic deposits are exposed only locally at the south of Masaya caldera and they have not been previously studied. Due to the limited exposures they could not be differentiated and characterized, but may be an important issue for the reconstruction of the caldera volcanic history. These local deposits are probably related to small phreatomagmatic eruptions that occurred the eastern caldera rim, which has a scalloped shape due to its intersection by several small steep-walled craters. There are also smaller less widespread deposits even younger than the TIL which are exposed mostly in the surroundings of the caldera, e.g. a well-sorted fluidal black lapilli rich deposit

cropping out at the road between Ticuantepe and the westernmost portion of the caldera rim.

2.3 Ages

The ages of the studied deposits were established primarily based on radiocarbon analysis of charcoal, plant material and/or carbon-bearing soil; or constrained by the stratigraphic position with respect to a directly dated unit (Table 2.1).

Table 2.1: ^{14}C ages for the Masaya Tephras and over- and underlying units

Sample	Unit	Type of sample	Age (yr BP)
KIA 18584	Masaya Triple Layer	Fossil plant material	2,120 ± 120
KIA 24438	Masaya Triple Layer	Fossil plant material	2,834 ± 112
KIA 18579	Xiloá Tephra	Charcoal in tephra	6,105 ± 30

The San Antonio Tephra could not been directly dated, due to the lack of charcoal or plant material in the deposits, but the maximum age was constrained by the dating of 6,105 years BP of charcoal from the underlying Xiloá Tephra (Freundt et al., 2006). The minimum age is constrained by the age of the 2,120 years BP-dated Masaya Triple Layer (see below), which overlies SAT through a paleosol and an unconformity. This means that the SAT must have been emplaced between ~2,500 and 6,000 years ago, probably around 6,000 years BP as suggested by sedimentation rates in cores at the Pacific off Nicaragua (Kutterolf et al. submitted).

No plant material for dating could be found in La Concepción Tephra, but in the Masaya Triple Layer. Two samples of fossil plant material in the MTL were dated, yielding ages of 2,120 ± 120 and 2834 ± 112 years BP. The first result is more confident and was taken as the age for the Masaya Triple Layer, much younger than the age of 6,500 years BP assigned by Bice (1980). Bice dated the Xiloá Tephra but then he correlated wrongly this pumice deposit with the one between MTL and MT, which actually corresponds to the Chiltepe Tephra.

Previous dates given for the Masaya Tuff include a 2,245 ± 150 years date made by Woodward-Clyde Consultants Inc (1975) for charcoal from a firepit above the Masaya Tuff. This agrees within error with the MTL date and suggest that the LCT-MTL, CT and MT-TIL were all erupted within a short period or time (~100-200 years). Dames and Moore Inc. (1978) published several ^{14}C dates from sites in Nicaragua, and got one date of 5,980±120 years from a peat layer at Tipitapa, overlying a deposit they assumed to be part of the Masaya Tuff. However, there is no evidence to support this correlation which would contradict all the other ages and stratigraphic data. Bice (1980) estimated the Masaya Tuff to be between 3,000 and 6,000 years old but this was a consequence of his erroneous correlation of the Xiloá Tephra as noted above. The new age result of 2120 years BP for the MTL indicates a much younger age for the Masaya Tuff than previously thought. The new age for the MT is now assigned to ca. 1,800 years BP, based on sedimentation rates at marine cores containing ash layers that were chemically correlated with the MT (Kutterolf et al. submitted).

Chapter 3

The San Antonio Tephra

The 6 ka old San Antonio Tephra is the oldest deposit found so far among the highly explosive Masaya caldera eruptions. It is exposed in a few outcrops to the NW, N and S of the Masaya caldera rim. The most complete exposures were found along the road from the San Antonio Sur village (type locality) through the Sierras Las Cuchillas hill up to Las Nubes village, near El Crucero (Fig. 3.1).

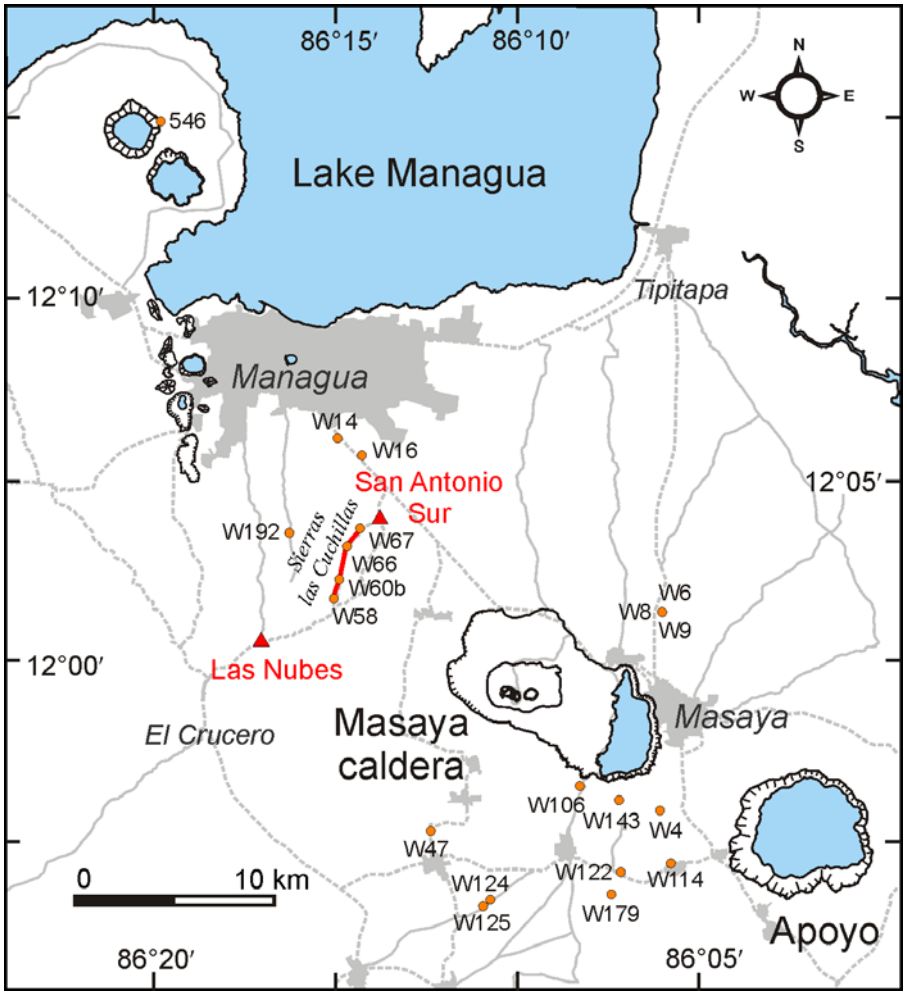

Figure 3.1: Exposures of the San Antonio Tephra, represented as orange dots. The road from San Antonio Sur and Las Nubes villages (marked in red) is the type locality, where the best outcrops with the complete sequence are exposed. The red line marks the location of the profile shown in Fig. 3.3.

3.1 Clast components

The juvenile fragments vary from fluidal, highly vesicular clasts, typical of Masaya products, to less vesicular, denser, round-shaped ones. The highly vesicular particles can have up to 90-95 vol.% of round vesicles in a sideromelane groundmass glass and contain very few phenocrysts or microlites. The denser particles are made by less vesicular (<40 vol.%) tachylitic glass, containing irregular-shaped voids and 1-5% of plagioclase, olivine and scarce cpx crystals. Some clasts are a mixture of sideromelane and tachylitic glass. The density ranges from 0.4-0.5 g/cm^3, for the most vesicular juveniles, to 1.5-1.6 g/cm^3 for the dense clasts.
The lithic content is highly variable, from almost none to 25-30 vol.% and some fragments are typically pinkish or yellowish due to hydrothermal alteration.

3.2 Internal stratigraphy

The limited available outcrops and the different degrees of erosion, which leave only portions of the stratigraphy exposed, complicated the definition and descriptions of the internal stratigraphy of the San Antonio Tephra.
In the most proximal outcrops at the NW sector of the caldera there is a lowermost sequence made up by an alternation of thin (<15 cm), well-sorted coarse-ash to fine-lapilli scoria fall beds and laminated tuffs, rich in fine ash (layers A1-A5; Figs. 3.2, 3.3).

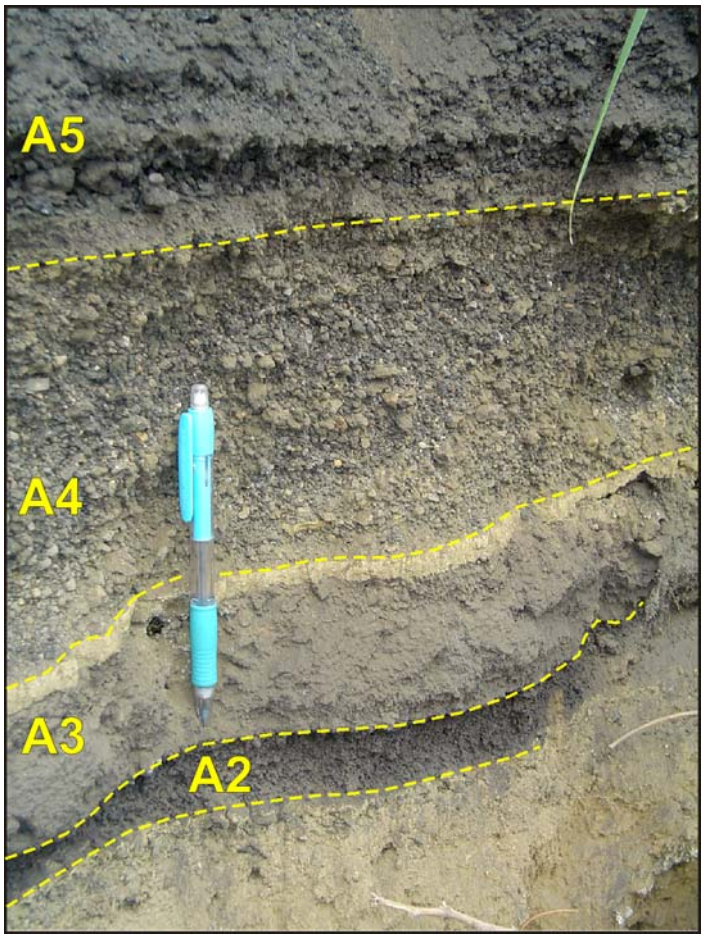

Figure 3.2: Photograph of the lowermost and middle sequence of the San Antonio Tephra. Subunit A1 is missing in the picture, appearing only in some sectors but thinning out laterally.

The middle part of the unit consists of the two most distinctive layers of the deposit, A6 and A7. A6 is a thick, well-sorted, fluidal lapilli fragments-bearing layer and A7 is a well-sorted, black lapilli layer with a high content of pinkish to yellowish hydrothermally altered lithic fragments. These two subunits allow the SAT to be recognized in the most distal exposures. Towards the top, the SAT sequence changes to finer-grained tuff beds with strong lateral variation of thickness and structures, as well as accretionary lapilli-rich tuffs and an uppermost well-sorted deposit of dense reddish lapilli (subunits A8-A13).
On the following pages, a detailed description is given for each layer of the San Antonio Tephra, including petrographic descriptions. This is based mostly on the exposures along the San Antonio Sur-Las Nubes road and especially in the outcrop W67, which is the most proximal locality with the complete SAT sequence exposed (Fig. 3.3).

3.2.1 Subunit A1

A1 is a well-sorted (σ~2), discontinuous thin layer of black, glassy, highly vesicular, fluidal fine lapilli (Φ_{avg} ~5 mm, Φ_{max} 20 mm) and minor coarse ash. It ranges in thickness from 1.5 to 4 cm. It is separated at the top from subunit A2 by a very thin (~0.5-1.5 cm) yellowish fine volcanic ash horizon. The juvenile fragments consist in highly vesicular and light particles, with densities between 0.5 to 0.7 g/cm^3, and less vesicular ones, with lower densities from 0.9 to 1.1 g/cm^3.
Microscopically, two types of juvenile fragments are present (Fig. 3.4). One is a highly vesicular, crystal-free, pale brown sideromelane glass with ~80-90 vol.% of round vesicles. The bubble dominating sizes are between 1.0-1.5 mm, but it also includes a second generation of smaller vesicles (0.1-0.2 mm). The other juvenile type is a less vesicular (~40 vol.%), darker brown sideromelane glass with round vesicles. The vesicles have an average size between 0.1 and 0.5 mm, but there are also scarce bigger ones with sizes up to 1 mm. It contains ~0.5 vol.% of plagioclase phenocrysts, microlites and rare olivine (Fig. 3.4).

3.2.2 Subunit A2

Subunit A2 is a very well-sorted (σ~1) layer of black, vesicular, round particles ranging in size from fine lapilli to coarse ash (Φ_{avg} ~1-5 mm, Φ_{max} 15 mm). The thickness varies from 3 to 8 cm at the most proximal studied outcrops.
Microscopically, it consists of three types of juvenile clasts (Fig. 3.5a-c):
[a] Highly vesicular (up to 60 vol.%) sideromelane clasts with a low crystal content (<2 vol.%, plag + ol + cpx as phenocrysts and microlites;
[b] A dominant population of black to dark brown, poorly to moderately vesicular tachylite (3-40 vol.% vesicles with sizes between 0.1-0.25 mm) with a variable crystal content (3-10 vol.%);
[c] Mixed clasts from both previous types, dense tachylite and highly vesicular sideromelane.
[d] The lithic fragments are microcrystalline basaltic lava fragments and hydrothermally altered ones.

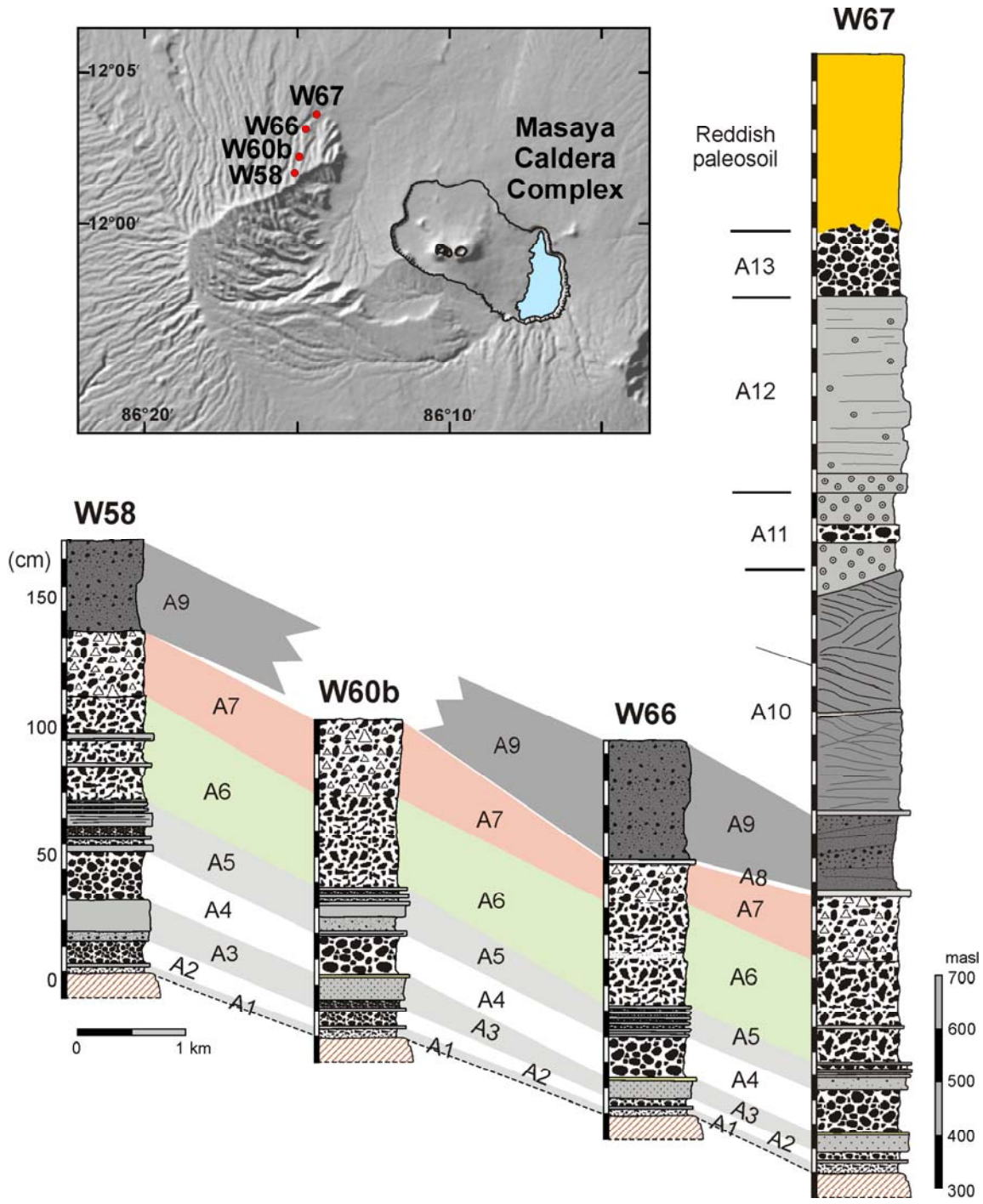

Figure 3.3: Proximal stratigraphy of the San Antonio Tephra along the road between San Antonio Sur and Las Nubes villages through the Sierra Las Cuchillas, the only place where the lowermost sequence A1-A5 is exposed. Note that the complete SAT sequence is only exposed at outcrop W67, located near the foot of the hills.

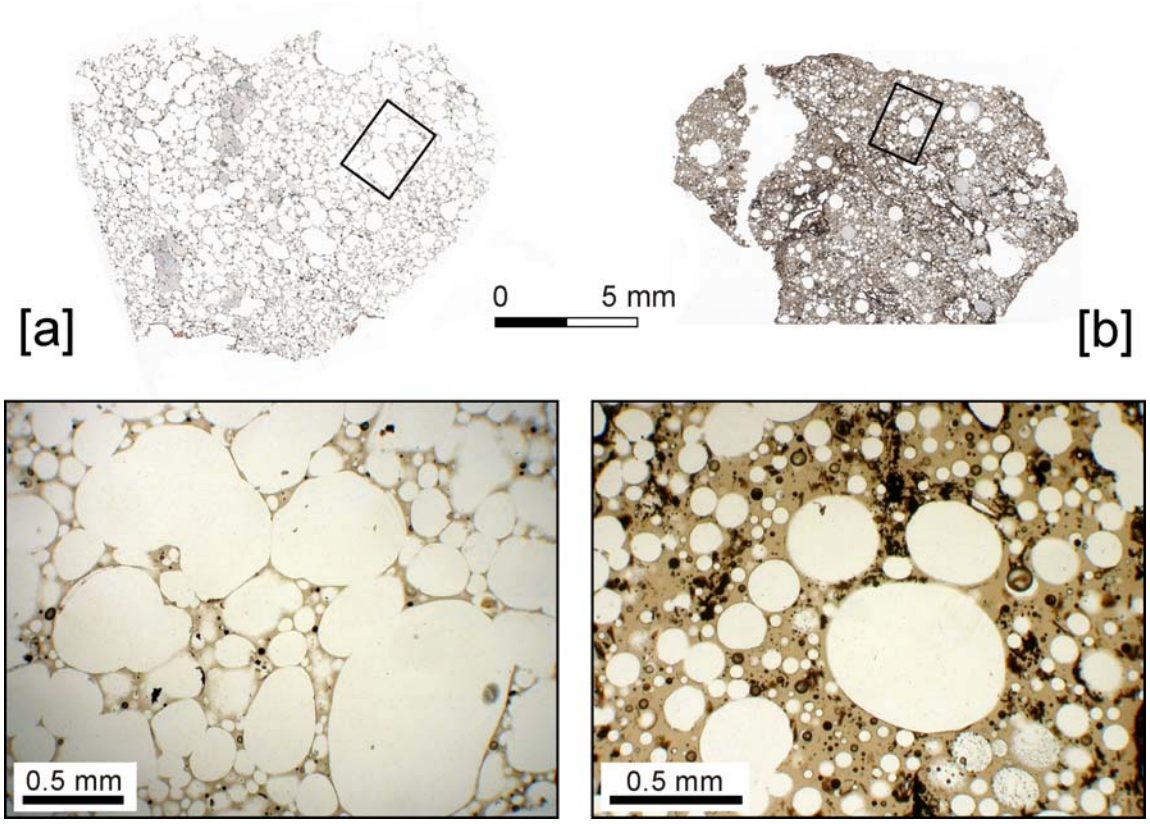

Figure 3.4: Microphotographs of the two types of juvenile clasts in A1. [**a**] highly vesicular, crystal-free, light brown sideromelane lapilli, containing large vesicles. [**b**] moderately vesicular, crystal-poor, darker brown sideromelane with two bubble generations, the smaller vesicles and few bigger ones (~0.1 mm).

3.2.3 Subunit A3

A3 is an indurated, grayish, fine tuff with some coarse ash layers, parallel bedding and leaf molds. The lowermost 2-3 cm of the bed consist of coarse ash-fine lapilli. The unit ends with a 1 cm indurated yellowish volcanic dust layer. The thickness varies from 7 to 16 cm.

3.2.4 Subunit A4

A4 is a thicker (~15-19 cm), well-sorted (σ~1.5-2) layer of vesicular, black, fine lapilli and around 20% of coarse ash size fragments. The maximum lapilli size is 20-25 mm. It contains 3-5 vol.% of hydrothermally altered lithic fragments with maximum sizes of 10-12 mm, some of them present as inclusions in the juvenile lapilli.

Microscopically, there are dense and vesicular juvenile fragments. The dense fragments have round shapes and consist of a mixture of moderately vesicular sideromelane and tachylite with ~40% vesicularity. The vesicles are small and irregularly-shaped and ranging in size from ~0.08 mm to 0.16 mm. The vesicular clasts can be of two types: one is highly vesicular, crystal-free pale brown sideromelane glass, with 85 vol.% of vesicles, ranging in diameter from 0.05 to 4.75 mm (0.5 mm avg). The other is a slightly less vesicular dark brown sideromelane with ~60 vol.% of irregular-shaped vesicles and ~5 vol.% of crystals (plag + ol). They have densities between 0.7-1.0 g/cm^3.

The lithic fragments (~5 vol.%) are basaltic lavas (plag+cpx+mt), some black fragments which look like preexistent tachylite clasts, hydrothermally altered fragments and palagonitized tuffs.

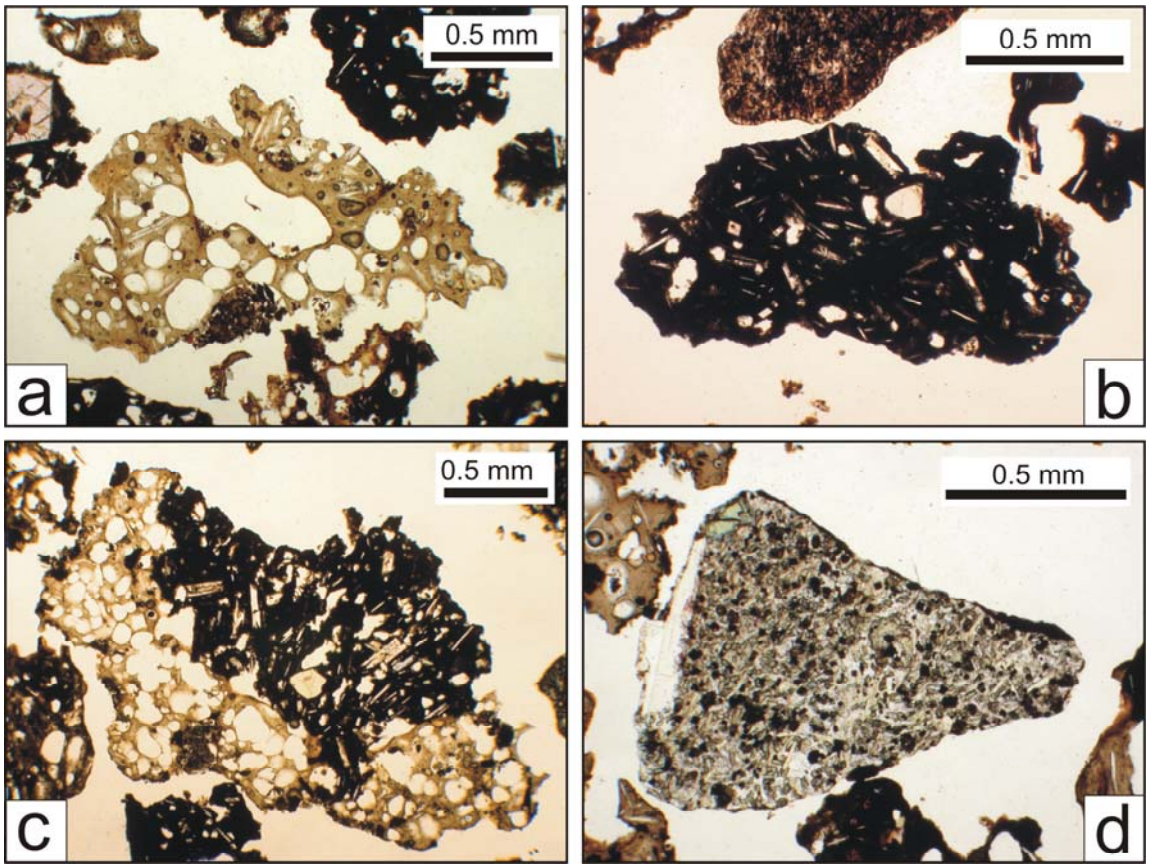

Figure 3.5: Microphotographs of the three main types of juvenile fragments and a lithic fragment in subunit A2. [**a**] sideromelane vesicular clasts, [**b**] tachylitic crystal-rich clasts, [**c**] mixed clast, and [**d**] basaltic lithic fragment common in the subunit.

3.2.5 Subunit A5

This is a bedded deposit, alternating dark gray indurated fine ash tuffs (mostly <1 cm thick) with loose black vesicular fine lapilli to coarse ash layers (up to 4 cm thick). The observed thickness ranges between 11 and 19 cm.

3.2.6 Subunit A6

A6 is a well-sorted, extremely loose layer, made of glassy highly vesicular fluidal-shaped black lapilli, which can be found in all of the outcrops together with subunit A7. It has <1 vol.% lithic fragments (Fig. 3.6). The thickness diminishes from 40 cm at the most proximal outcrops found, to less than 5 cm at 30 km from Masaya caldera. At the most proximal exposures three layers can be differentiated: a basal fluidal-shaped fine lapilli, a whitish to black fine ash layer (1-2 cm thick) in the middle, and a well-sorted, thicker, highly vesicular, fluidal-shaped, black lapilli layer.

Microscopically, the juvenile fragments are of two types: vesicular tachylitic glass and highly vesicular sideromelane. The vesicular tachylite contains 60-65

vol.% of round vesicles and scarce crystals (1-2 vol.% of plag + ol). The highly vesicular sideromelane clasts are the dominant type in the deposit, they contain ~70 vol.% of large round vesicles, 0.05-3.5 mm in size, and minor amounts of plag + ol + cpx crystals (<1 vol.%). The highly vesicular clasts have a density of 0.4-0.6 g/cm^3 and the denser ones of 0.8-1.2 g/cm^3.

3.2.7 Subunit A7

The contact between A6 and A7 is marked by the sudden appearance of a high amount (25-30 vol.%) of lithic fragments, most of them hydrothermally altered (Fig. 3.6). A7 is also a well-sorted (σ~2) deposit, with reverse grading, consisting of highly vesicular black lapilli ((ρ~0.7-0.8 g/cm^3) but mostly of denser fragments (ρ~1.1-1.4 g/cm^3). Some of them have aerodynamic shapes and/or bread-crust rims.

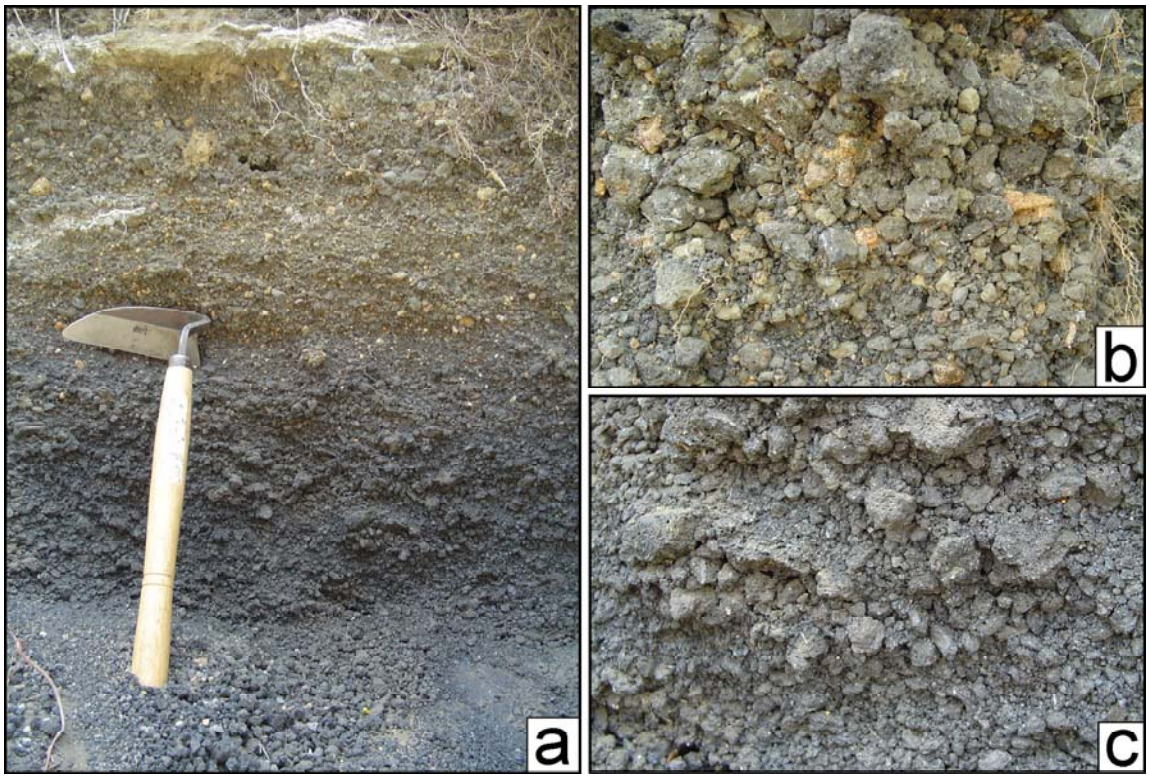

Figure 3.6: [**a**] The contact between subunits A6 and A7 is marked by the sudden appearance of a high amount of yellowish to pinkish lithic fragments. [**b**] Detail of subunit A7 with the high amount of hydrothermally altered lithic fragments and dense juveniles. [**c**] Detail of subunit A6, showing the fluidal shapes of the juvenile particles and the almost absence of lithic fragments in the deposit.

3.2.8 Subunit A8

A8 is a 3 cm massive hardened whitish tuff layer.

3.2.9 Subunit A9

This is a poorly sorted (σ~4), loose, fine-grained deposit. It is dominated by black coarse to fine ash, with a minor amount of highly vesicular, fluidal-shaped lapilli (Φ_{max}~25 mm, ρ~0.5-0.8 g/cm^3) and ~1-2% of yellowish angular lithic fragments. It exhibits faint cross-bedding and the thickness varies from 20-30 cm.

3.2.10 Subunit A10

Subunit A10 is formed by at least two main fine-grained deposits with dune structures and cross-bedding, separated by an indurated tuff. The lower dune level is less consolidated, it consists of three smaller dune sections alternating lapilli and ash-rich horizons, with internal lamination (Fig. 3.7). It shows striking thickness variations, e.g. from 40 to 15 cm in a 10 m wide outcrop. The light gray indurated fine tuff that separates both deposits changes in thickness from 6 cm to 0.5 cm at the crest of the lower dune deposit. The upper dune level is more indurated, and finer-grained than the lower one. It shows well-developed planar bedding in dune structures and laminations and a wave length of 3 m.

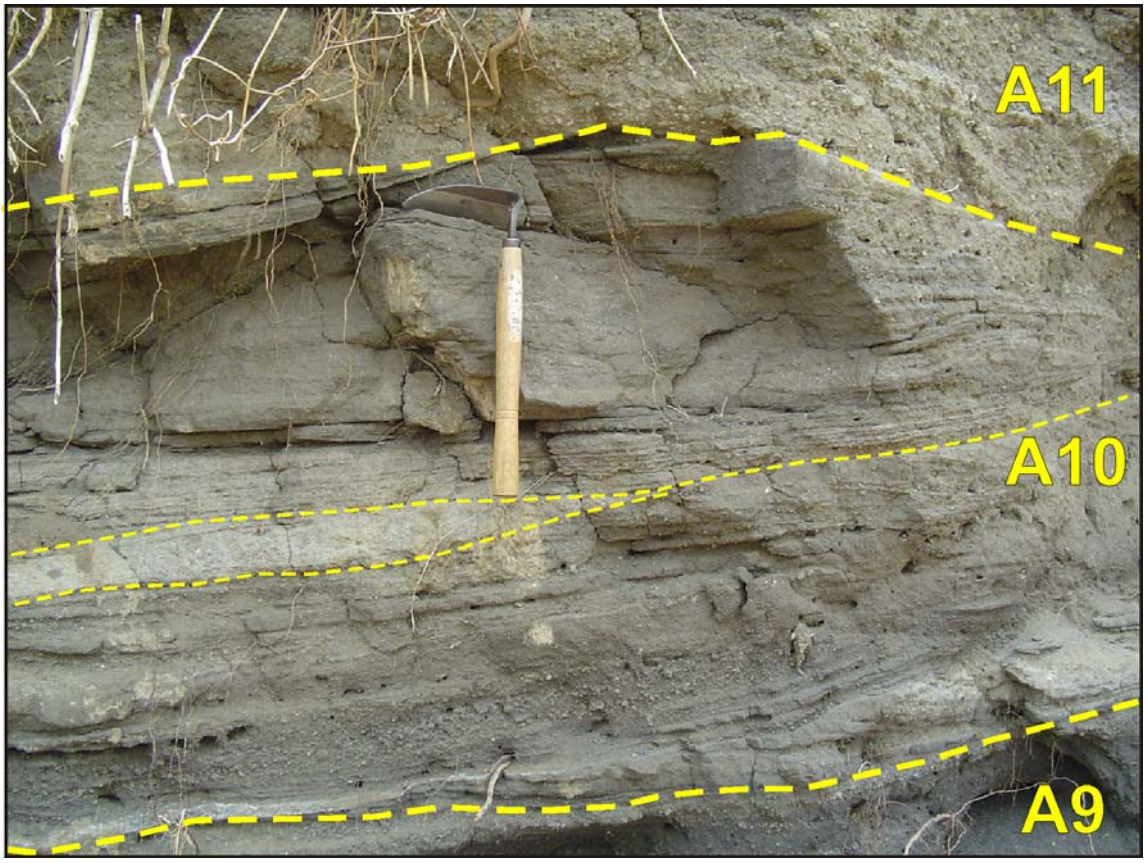

Figure 3.7: Subunit A10 limited by the dashed yellow lines and showing the different dunes. The contact between the lower and the upper dune is marked by the presence of a thin hardened tuff, which thins out from left to right. The scraper used as scale is 30 cm long.

At exposures S of the Masaya caldera, this subunit appears as a cross-bedded yellowish indurated tuff with striking thickness changes (from 3 cm to 18 cm at the same outcrop).
The density of the juvenile fragments varies from 0.6-0.8 g/cm^3 for the most vesicular clasts, to 1.2-1.5 g/cm^3 for the denser ones.

3.2.11 Subunit A11

A11 consists of two fine, accretionary lapilli-rich, ash layers sandwiching a well-sorted black vesicular lapilli (Φ_{max}~34 mm) layer with ~3% of lithic fragments.

3.2.12 Subunit A12

The lowermost part consists of a highly indurated grayish fine tuff, but most of the deposit is a very altered fine-grained, planar-bedded, grayish tuff with accretionary lapilli and low angle cross-bedding. The maximum observed thickness is 80 cm NW from the caldera, but at one exposure S it reaches 50 cm and it looks massive with faint planar bedding.

3.2.13 Subunit A13

The topmost deposit of SAT is an altered, well-sorted, reddish lapilli deposit. The lapilli fragments are vesicular and dense, mostly coated by yellowish fine ash. It can be found in several exposures at the S and NW of the caldera. It changes gradually to a thick yellowish-reddish paleosol (~75 cm maximum observed thickness) which underlies a regional unconformity (Fig. 3.8).

Figure 3.8: Major erosional unconformity between SAT and LCT, covering around 4000 years. The outcrop is located S of the Masaya caldera, along the street between Masatepe and Catarina.

3.3 Lateral facies changes

The lateral facies variation of the SAT deposit with increasing distance from the caldera rim at the NE, S and SE is shown in Fig. 3.9. The section at the NW of the caldera is not included since most of them were already shown in Fig. 3.3. To the NW the deposits extend farther away towards Managua city have been found as far as Chiltepe Peninsula, more than 30 km away from the Masaya caldera. At these distal exposures the unit is reduced to a thin fine black vesicular lapilli layer 5-15 cm thick, sandwiched between paleosols and underlying an unconformity. The upper 2-3 cm contain tiny pinkish lithic fragments, corresponding to subunit A7.

At the NE, in a quarry at one side of the road between Masaya and Tipitapa, it is possible to find the SAT overlying the Apoyo pumice deposits and underlying MT (outcrops W6, W8 and W9 in Fig. 3.1). The lowermost subunits are missing there, but subunit A6 is thick (~40 cm) and shows fluctuations in grain size, giving it a layered appearance. A7 is also present, but thinner than at the NW, and is overlain by a fresh lithic-rich deposit of up to 40 cm. Subunit A9 appears only locally in the quarry, but massive fine planar bedded tuffs, which may be the lateral equivalent of the surge deposits, are present always at the top (Fig. 3.9). The SAT in this locality is eroded, appearing as a black lapilli lens (layer A6-A7) and immediately overlain by the Masaya Tuff.

At the outcrops S of the caldera, the thickest subunits of SAT can be recognized, but the lowermost sequence is also missing. In this sector there are several other minor local deposits, which complicate the stratigraphic reconstruction. Distal exposures at the S show both subunits, A6 and A7, with thickness <10 cm, overlain by a fine black ash with faint cross-bedding (subunit A9) and a massive structure-less to faintly cross-bedded fine grayish tuff with a well-sorted lapilli layer in between (A10-A12; Fig. 3.9). At the top, there is a reddish to yellowish paleosol with floting scoria fragments, possibly belonging to subunit A13.

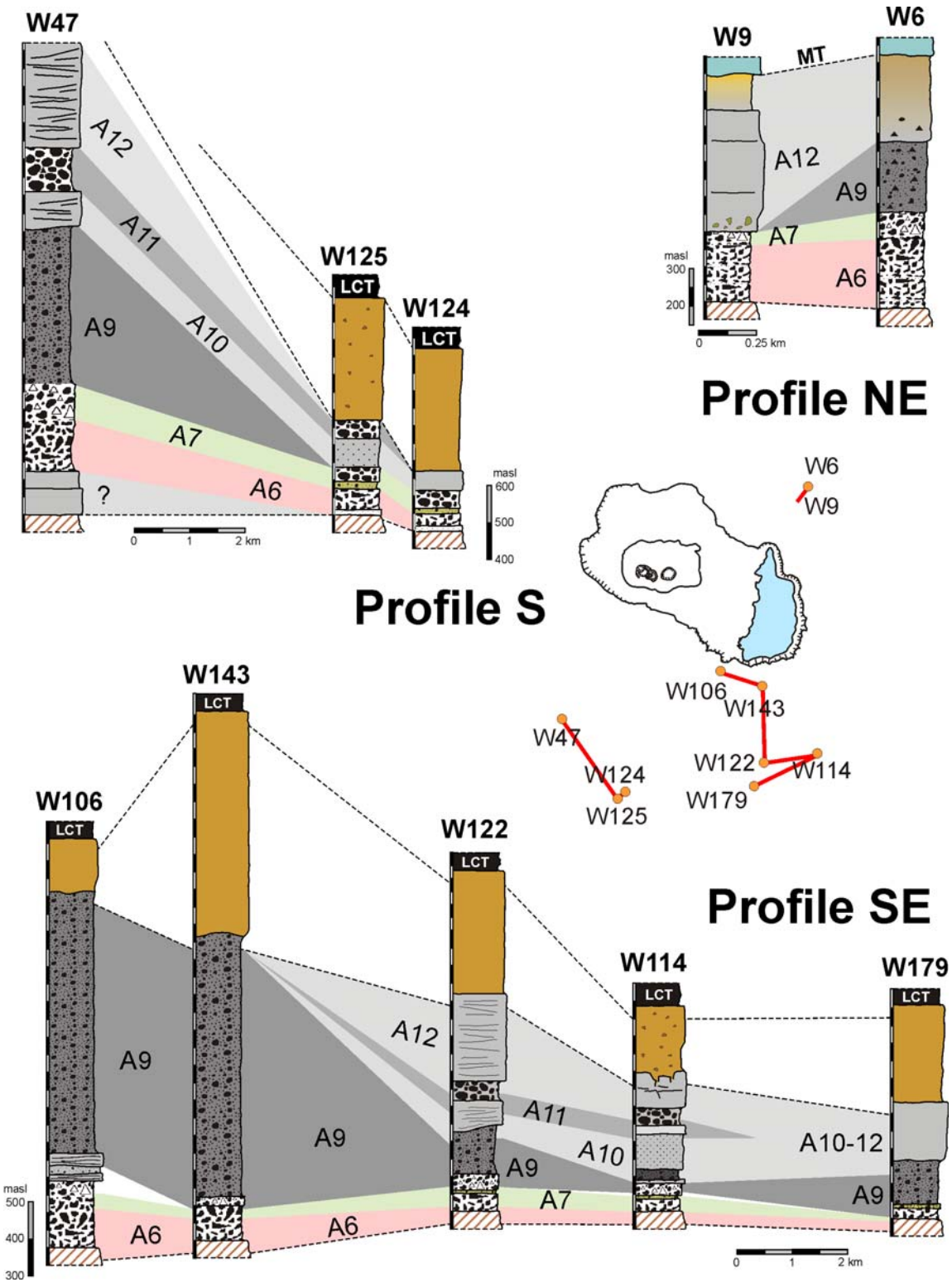

Figure 3.9: Correlation profiles of the SAT in different directions from the Masaya caldera. The upper subunits (A9-A12) are better exposed at the S and SE of the caldera but not at the NE.

3.4 Volume

3.4.1 Thickness distribution and volume

The limited amount of exposures for the San Antonio Tephra, together with the erosion which affected the deposits, do not allow to construct a whole-deposit isopach map for the SAT. It was only possible to map thickness distributions for the fallout subunits A6 and A7 (Fig. 3.10), because subunits A1-A5 are only exposed at the NW of the caldera, whereas the sequence A8-A12 also crops out in a very few localities S of the caldera. The isopachs of the subunit A6 show a dispersion axis to the NW, whereas those of A7 are concentric. Both suggest a vent at the northern part of the caldera.

The volume for both subunits was calculated following the method of Pyle (1989) and yielded 0.37 km^3 for A6 and 0.16 km^3 for A7. The dense rock equivalent volumes (DRE) are 0.1 km^3 and 0.05 km^3, respectively.

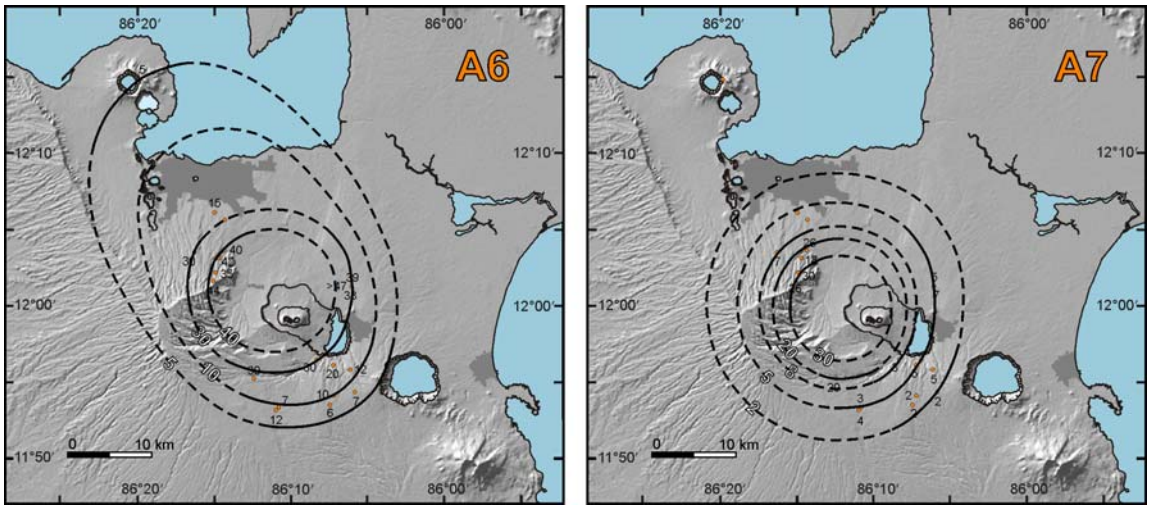

Figure 3.10: Isopachs maps for subunits A6 and A7 of the San Antonio Tephra. Isopach contours are in cm. Orange dots indicate the site of the measurement. Cities are represented in dark gray.

3.4.2 Distal tephra and total volume of the eruption

During cruises M54/2, M66/3a-b and SO173/3 several gravity cores containing mafic ash layers were collected at the Pacific Ocean, offshore Nicaragua. Some of these mafic ash layers were correlated with the Masaya Tephra units (Kutterolf et al. submitted). The criteria used for the correlation were: stratigraphic relationships with already correlated felsic tephra (e.g. Chiltepe Tephra; Kutterolf et al. submitted), location of the core in comparison to the dispersion axis on land, pelagic sedimentation rates and most important the chemistry of the glass. The cores are located at the continental slope and at the incoming plate.

Ten of these mafic marine ashes were correlated with the SAT (Fig. 3.11), 6 located at the continental slope and 4 in the incoming plate. They were found at variable depths below the sea floor, ranging from 4 cm to 325 cm and are intercalated with pelagic sediments.

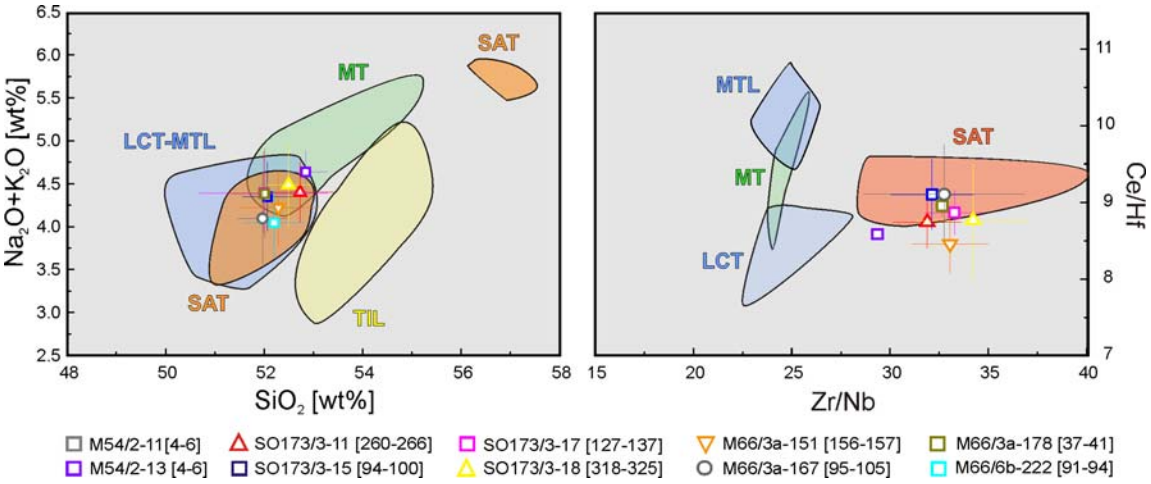

Figure 3.11: Example of the chemical correlation between the marine ash layers and the glass composition of the Masaya Tephra units. Symbols represent the mean value from all measurements of a sample, with the corresponding standard deviation.

The layers correlated with SAT vary in thickness from 1 cm to 10 cm. They were used to reconstruct the distal thickness distribution for the San Antonio Tephra shown in Fig. 3.12.

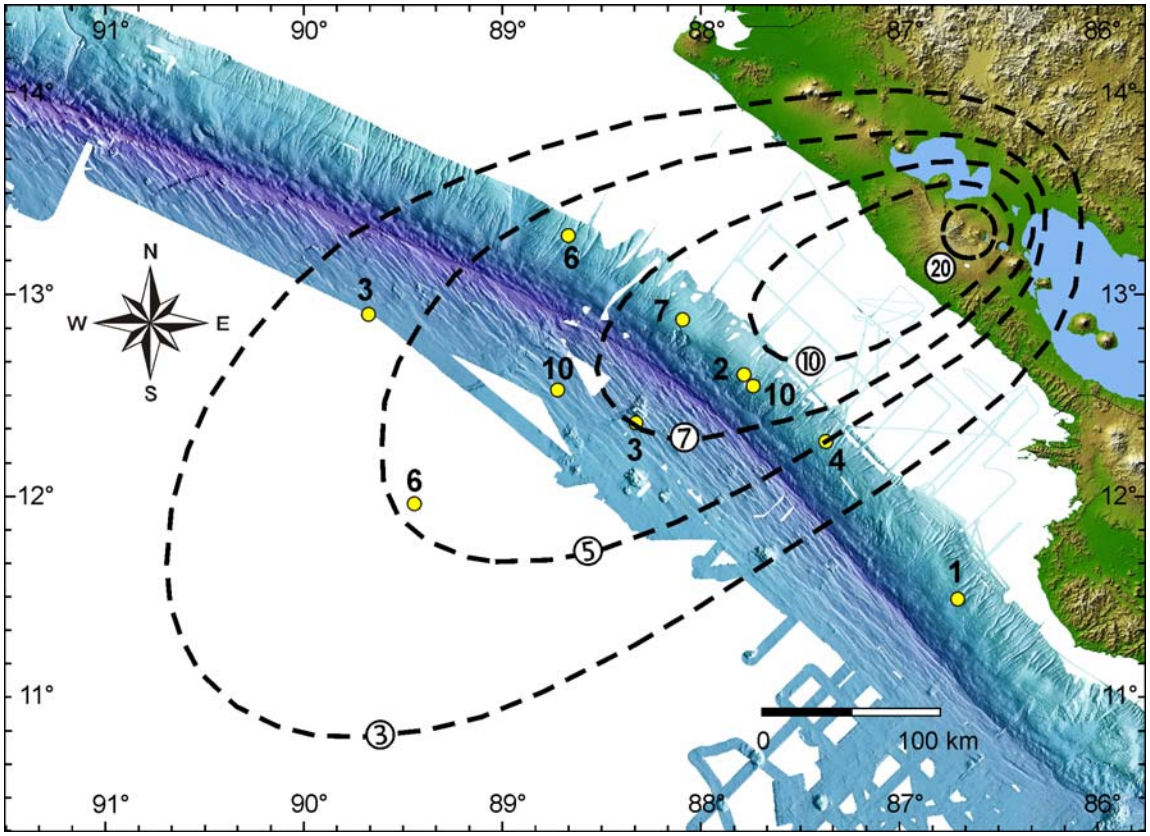

Figure 3.12: Isopachs in centimeters for the San Antonio Tephra whole deposit. The isopachs on land are mainly based on subunits A6 and A7. The yellow dots give the location of the gravity cores containing the correlated ash layers and the numbers correspond to the thickness of the layer.

A new total volume calculation with the method of Pyle (1989) results in ~14 km^3 for the whole SAT deposit. This is 22 times more volume than the previously calculated one, based only on the distribution on land of the main subunits A6 and A7.

3.5 Eruption parameters

3.5.1 Eruption column height and wind speed

The juvenile (MP) and lithic fragments (ML) isopleths for the subunits A6 and A7 were constructed based on the average of the five biggest clasts found in the studied outcrops. The limited amount of outcrops and data made it difficult to construct well-constrained contours for both units (Fig. 3.13).

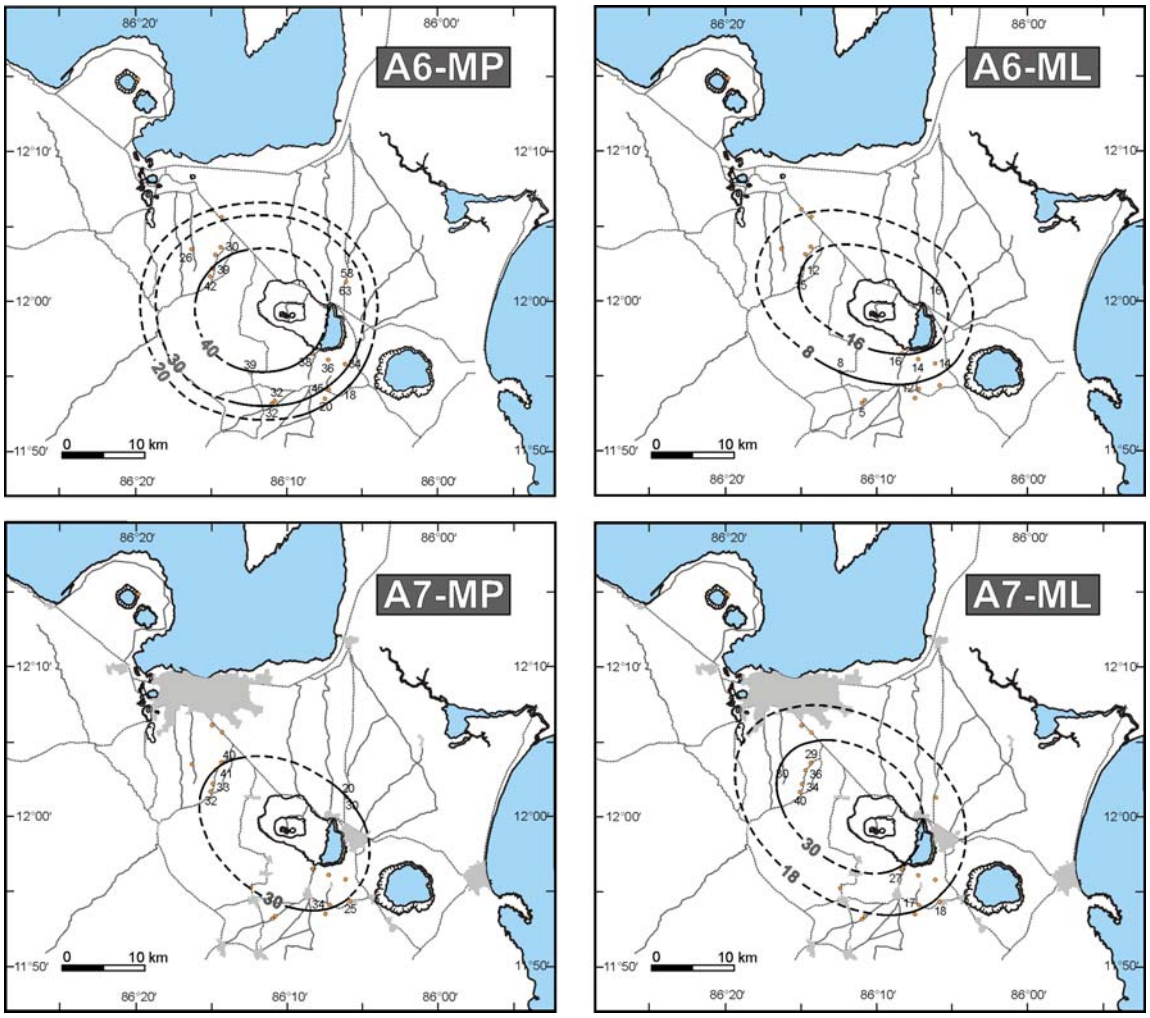

Figure 3.13: Isopleth contours in mm for subunits A6 and A7 of the San Antonio Tephra. Maximum juvenile (MP) isopleths and maximum lithic fragment (ML) isopleths for subunit A6 [above]. Maximum juvenile (MP) isopleths and maximum lithic fragment (ML) isopleths for subunit A7 [below].

The eruption column heights were estimated comparing the downwind and crosswind ranges of the maximum clast, calculated from the isopleth maps of Fig. 3.13, with theoretical modeling results of Carey and Sparks (1986). Even though the isopleth maps are not so well constrained, the results are very uniform and range from 21 to 29 km, with an average column height of ~24 km for both eruptions (Fig. 3.14). The wind speed estimation is around 7 m/s, but the ML isopachs for the subunit A7 indicate higher velocities up to 30 m/s.

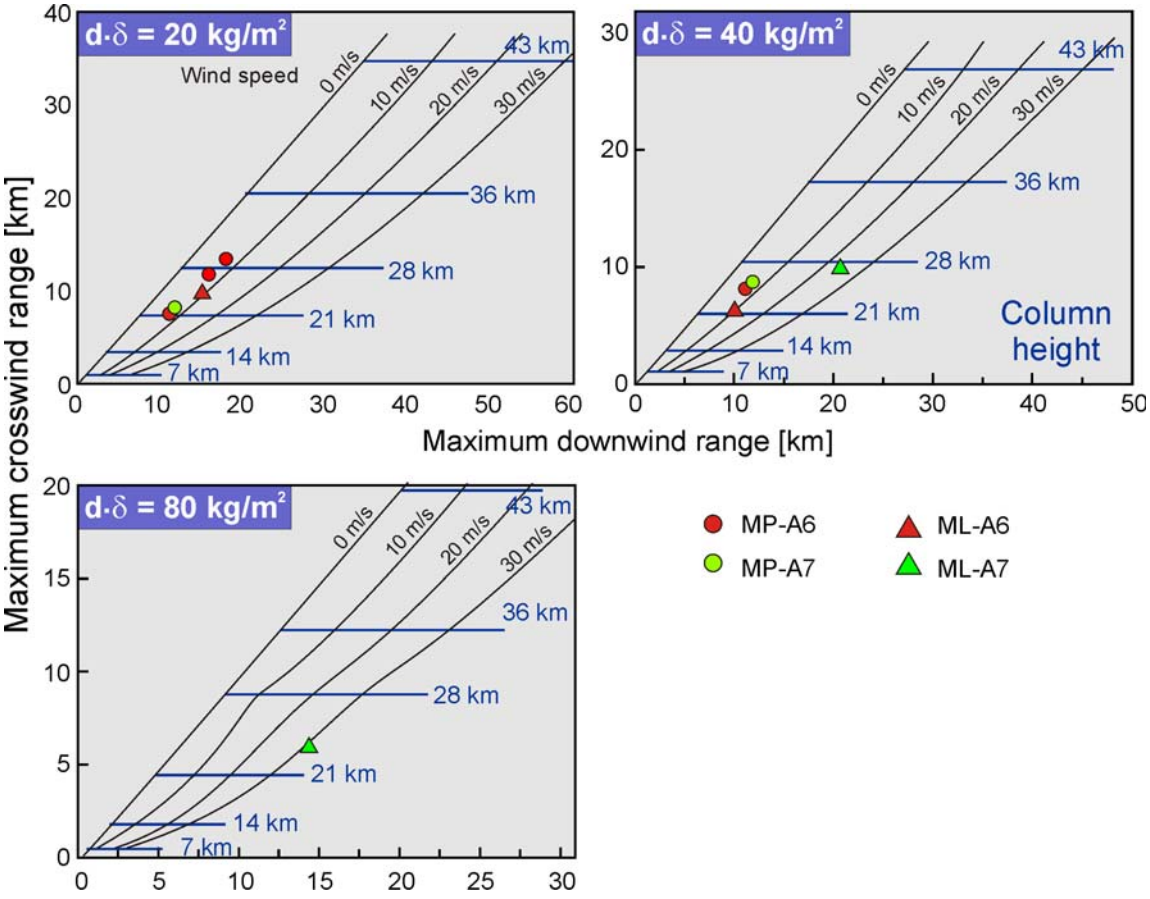

Figure 3.14: Crosswind range versus maximum downwind range for the MP and ML isopleths for subunits A6 and A7 of the SAT. The blue lines indicate column height in km and the black curves are wind speed in m/s, both taken from Carey and Sparks (1986).

3.5.2 Mass eruption rates

The mass flux for the two main eruptions of the San Antonio Tuff ranges between 10^7-10^8 kg/s, although only one data point lie above the dashed line and yields $3x10^7$ kg/s (Fig. 3.15). Results below the dashed line are less reliable since the model applied by Wilson and Walker (1987) used a velocity profile that did not capture lateral velocities in the higher part of the eruption column.
The derived mass flux and column heights can be checked for consistency by comparison with the model curves of Woods (1988), as shown in Fig. 3.16. The ranges in column height and the resulting mass flux 10^7-$7x10^7$ kg/s are illustrated as darker blue areas.

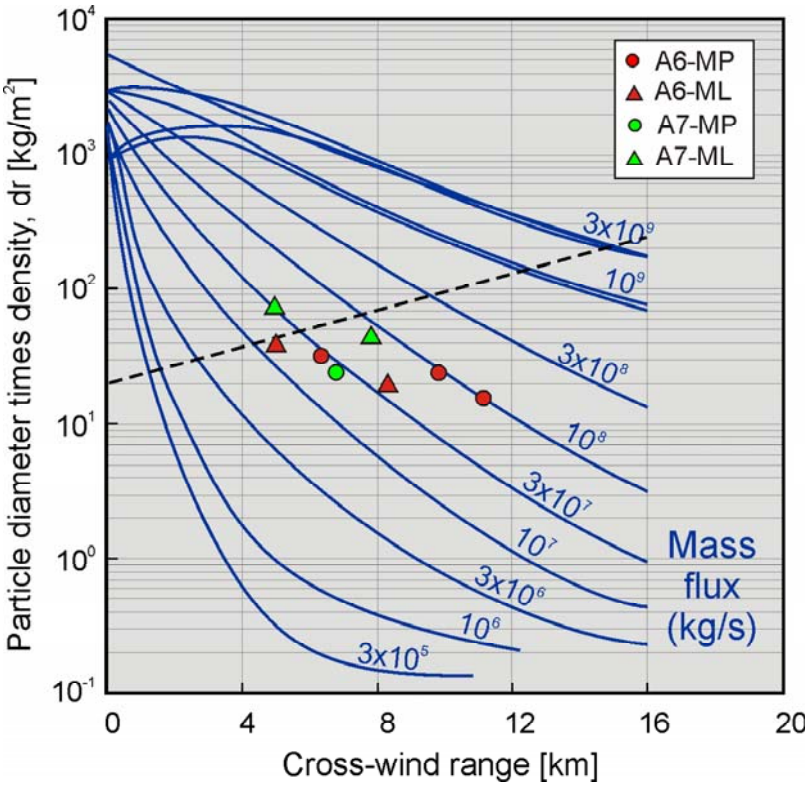

Figure 3.15: Discharge rate of the eruptions forming subunits A6 and A7, based on the diagram of Wilson and Walker (1987).

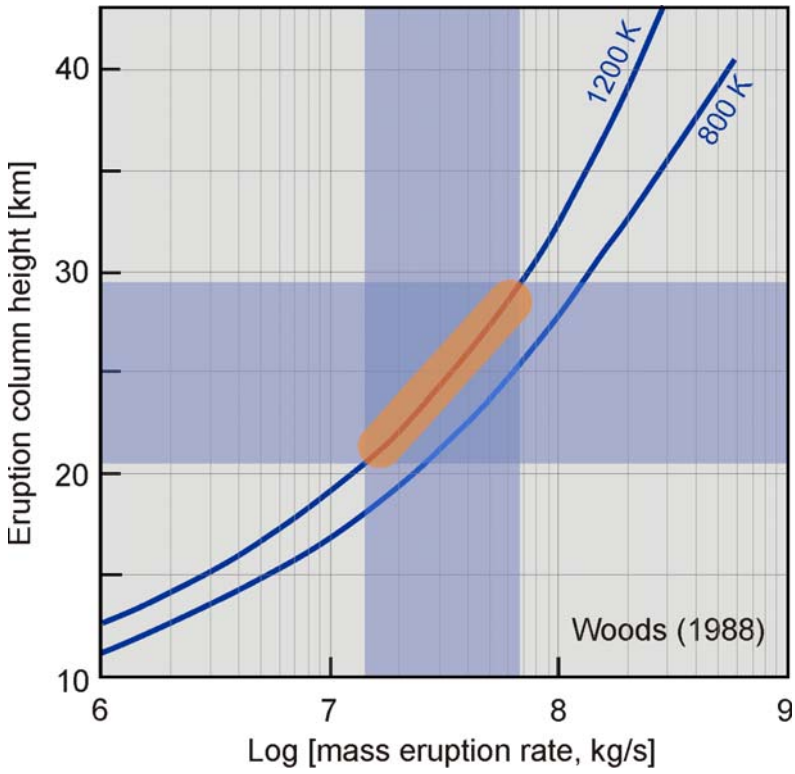

Figure 3.16: Eruption column height vs log of the mass eruption rate with the temperature lines of Woods (1988).

3.5.3 Dispersal characteristics

A plot of the ln isopach vs square root of the area enclosed by the isopach for the SAT subunits A6 and A7 is presented in Fig. 3.17. The fields were taken from Houghton et al. (2000), and they show the distribution of typical eruption types from the literature. The subunits A6 and A7 plot in the fields of Plinian and Subplinian-Phreatoplinian, respectively. Subunit A6 has indeed Plinian characteristics, whereas subunit A7 has evidence of external water influence and a Subplinian dispersal, so it could be classified as Phreatoplinian. It is clear anyway that they were very powerful eruptions.

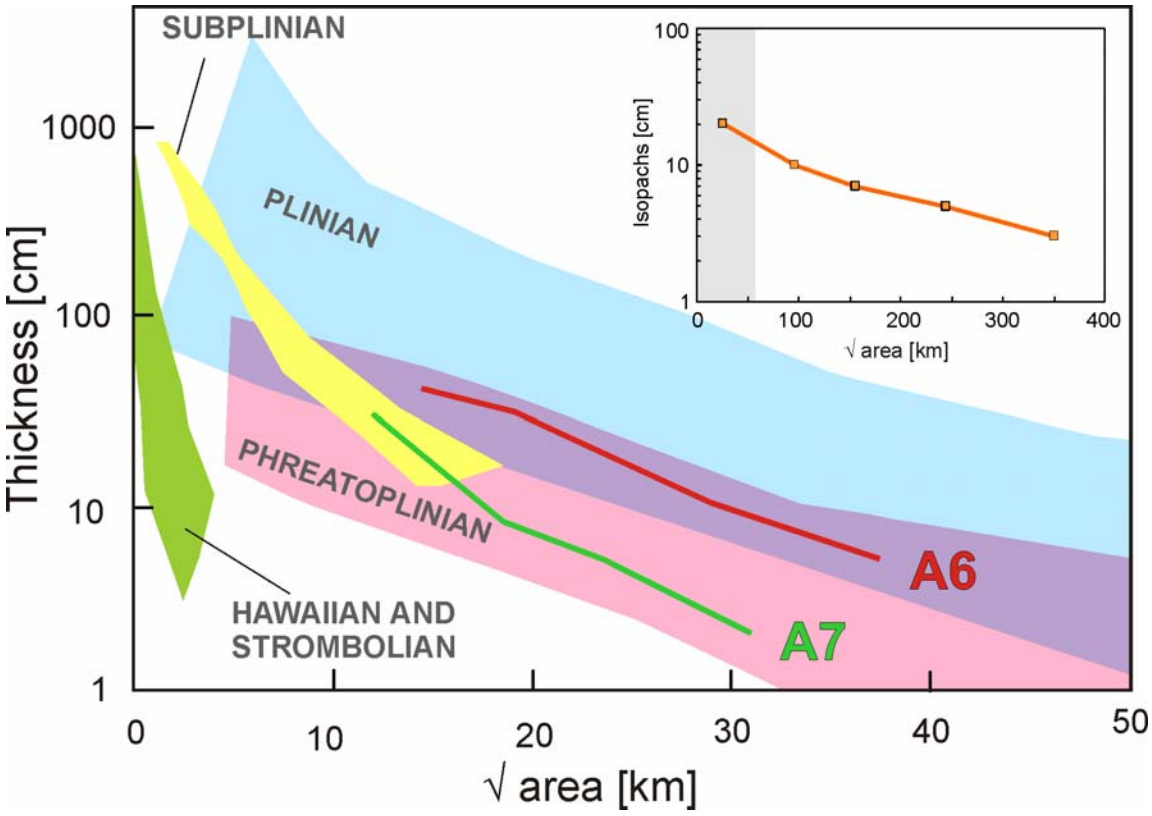

Figure 3.17: Diagram ln isopach vs square root of the area enclosed by the isopachs for the SAT subunits. The fields of Hawaiian and Strombolian, Plinian, Subplinian and Phreatoplinian were taken from Houghton et al. (2000). The inset at the top right corner shows the same diagram but in a larger scale, in order to plot the whole deposit data, considering the marine tephra layers correlated with SAT.

Another way to determine the type of eruptions is using the classification scheme of Pyle (1989). This diagram uses the parameter bt or thickness half-distance which describes the rate of thinning of the deposit, and the half-distance ratio (bc/bt). The parameter bc is the clast half-distance, which describes the rate of clast size decay with the distance.
Typical bt values range between 1 and 10 km for the proximal portion of the deposits, not taking distal tephra in account (Houghton et al. 2000). The value of bt for the San Antonio Tephra is 4.2 km for subunit A6 and 2.7 km for A7.

The lack of enough data on maximum clast sizes for these subunits difficult the estimation of the parameter bc and was only possible to get a value of 11.8 km for SAT-A6. Figure 3.18 shows the Pyle's classification scheme for SAT-A6, which clearly exhibits Plinian distribution characteristics.

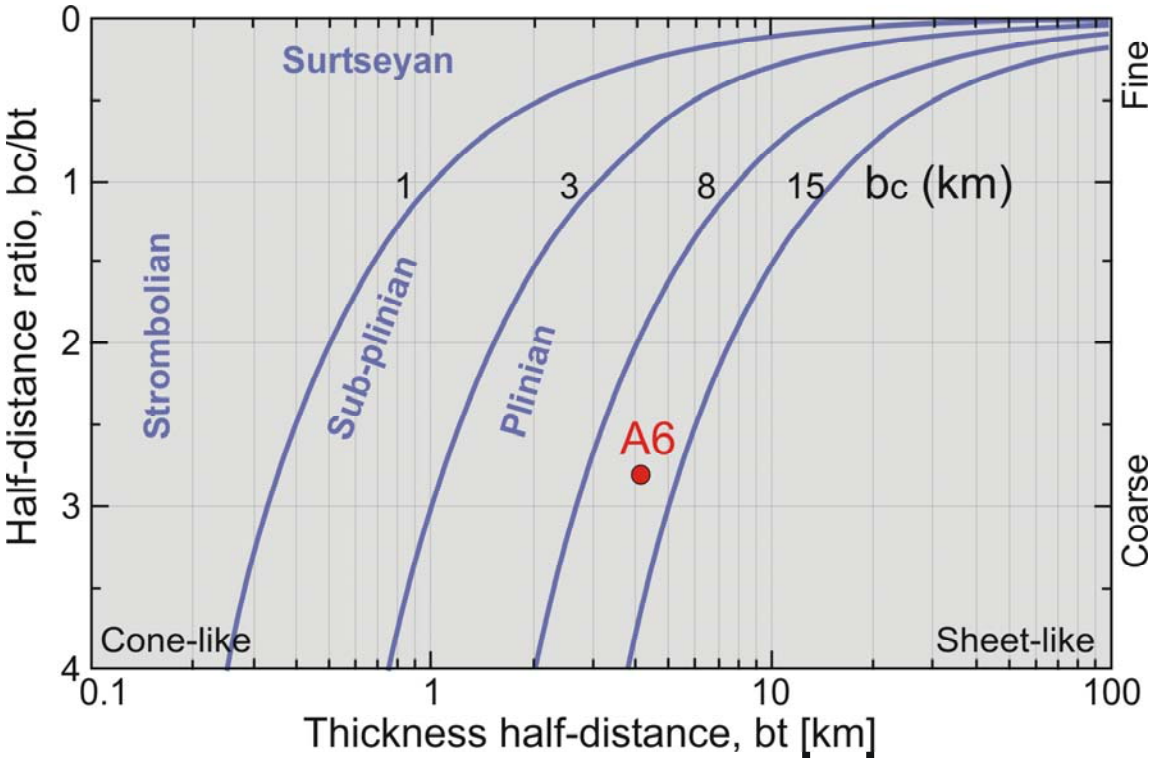

Figure 3.18: Classification scheme of Pyle (1989) based on the thickness half-distance vs half distance ratio for the subunit SAT-A6.

3.6 Interpretation

The eruption sequence for the San Antonio Tephra is summarized in Fig. 3.19. The lowermost sequence of the San Antonio Tephra (A1-A5) is interpreted as the fall deposits of magmatic eruptions, interrupted by short phreatomagmatic pulses, mainly ejected towards the NW of the caldera. The biggest magmatic eruption of the SAT, started with several pulses forming a thin layered deposit (subunit A5), and continued with the Plinian eruption of subunit A6, which had an eruption column of 24 km height (section 3.6). The eruption suffered minor changes in intensity as reflected by the changes in grain size of the deposit. As a response to the sudden evacuation of a high amount of magma (~0.4 km^3) a change occurred as suggested by the high amount of hydrothermalized lithic fragments of layer A7. This change might have been a conduit collapse or vent widening which also probably allowed the entrance of limited water in the system, accelerating the fragmentation process and created a range of clasts with a wide range of density and vesicularity.

From this point on, the system remained unstable with continuous access of water which produced phreatomagmatic eruptions which generated surges (subunit A10) and also fall deposits rich in accretionary lapilli. The eruption terminated with the deposition of the topmost fallout layer A13, which could

have been like a strombolian eruption with dense and vesicular reddish juvenile fragments.
As seen, phreatomagmatic phases persisted throughout the eruption of this tephra and dominated its terminal phase; it seems likely that external water also affected to some extent some of the well-sorted scoria-fall layers, as suggested by the different ranges of vesicularity and density of clasts in the same deposit.

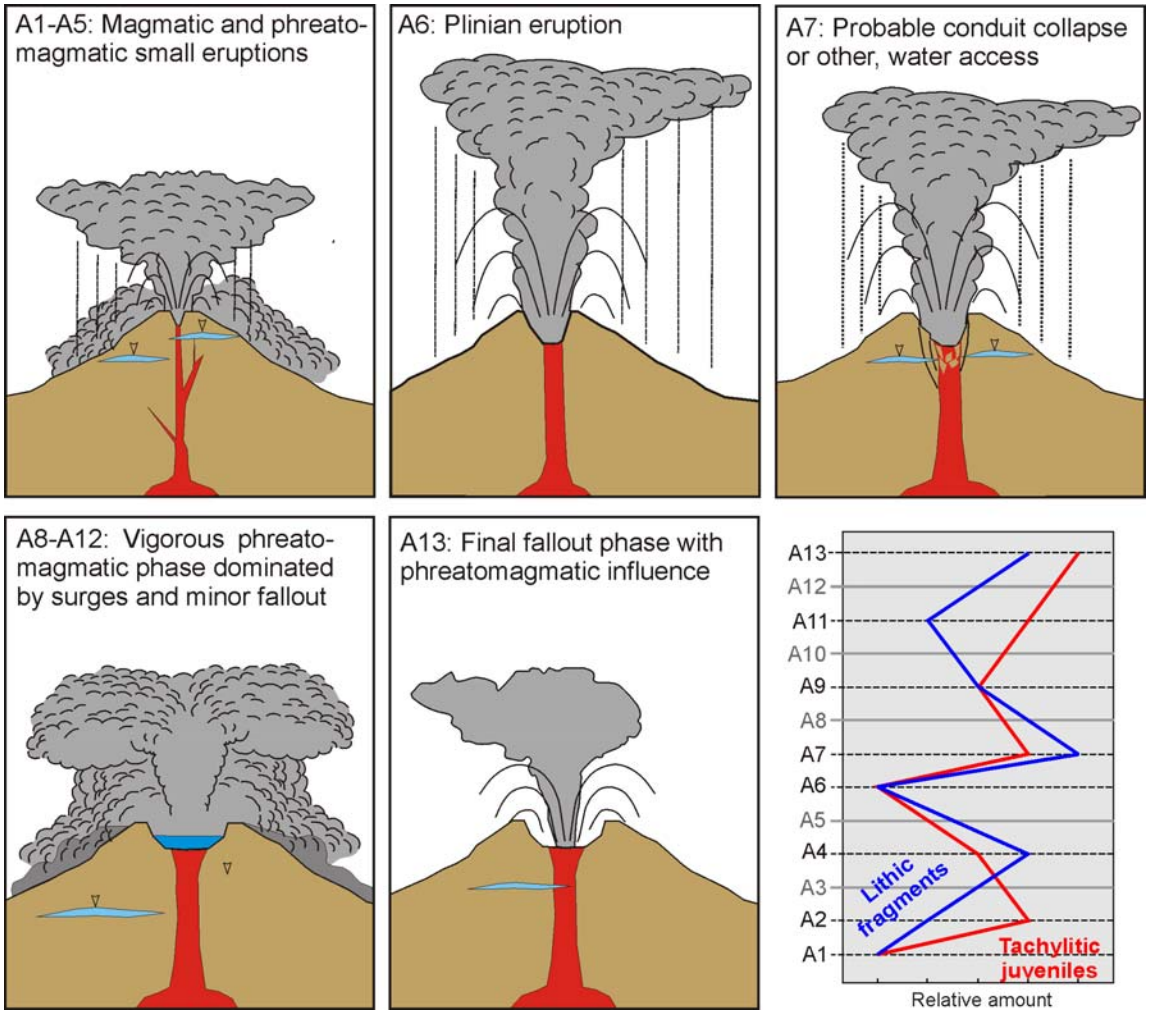

Fig. 3.19: Model for the eruption sequence of the San Antonio Tephra. The blue color is used for ground- and surface water. The diagram at the bottom right shows the abundance of lithic fragments and dense juveniles in the different subunits.

Chapter 4

La Concepción Tephra and the Masaya Triple Layer

Bice (1980) was the first to describe a deposit in the Managua area consisting of "two thin indurated gray tuffs sandwiched between three 5-10 cm loose layers of coarse black ash" and named it the Masaya Triple Layer. He also mentioned that the unit thickens toward Masaya caldera and becomes more complex, adding extra layers. Williams (1983a; b) described this deposit as well-sorted, non-graded, and composed of five to twelve scoria fall layers, with a thickness between 0.5 to 1.5 m.
South of the Masaya caldera, a basaltic tephra occurs at the same stratigraphic level as the Masaya Triple Layer, overlying the San Antonio Tephra and underlying the Masaya Tuff. Some of these outcrops were interpreted by Williams (1983a) as proximal facies of the MTL. However, detailed logging of the outcrops around the Masaya caldera revealed that, the deposits at the south have a different internal architecture and hence do not simply correlate with the MTL. This southern tephra was therefore called La Concepción Tephra (LCT) by Pérez and Freundt (2006), referring to the most complete section exposed near the village of La Concepción (known as La Concha). Ongoing work has now revealed the genetic relationship between the MTL and the LCT, and this will be discussed below, after first introducing the two deposits separately.

4.1 La Concepción Tephra

La Concepción Tephra is a succession of well-sorted scoria lapilli and ash layers interbedded with poorly sorted tuffs, that crops out to the south and east of the Masaya caldera (Fig. 4.1). It overlies the San Antonio Tephra above a thick paleosol and a regional unconformity, and is overlain by the Masaya Tuff above another erosional unconformity.

4.1.1 Clast components

The juvenile fragments range from highly vesicular (>80 vol.% vesicles), fluidal-shaped, lapilli achneliths with a density as low as 0.25 g/cm^3 to a poorly vesicular (<40 vol.%), round, black lapilli with an average density of ~1.6 g/cm^3. Microscopically, the first group is mostly composed of dark brown sideromelane and sometimes of black tachylite with 40-80 vol.% round vesicles whereas the denser lapilli consist of black tachylitic glass with 7-20 vol.% vesicles with mostly irregular shapes and minor round ones. The juvenile fragments sometimes contain xenoliths of basaltic lavas and of older dense tachylitic fragments. The phenocryst content is relatively low (~2-5 vol.%) and consists mainly of sparse plagioclase phenocrysts with abundant melt inclusions and olivine; the sideromelane and tachylitic groundmass contains plagioclase and olivine microlites. Basaltic lava country rock fragments with various textures are also present in small amounts (<1-3 vol.%).

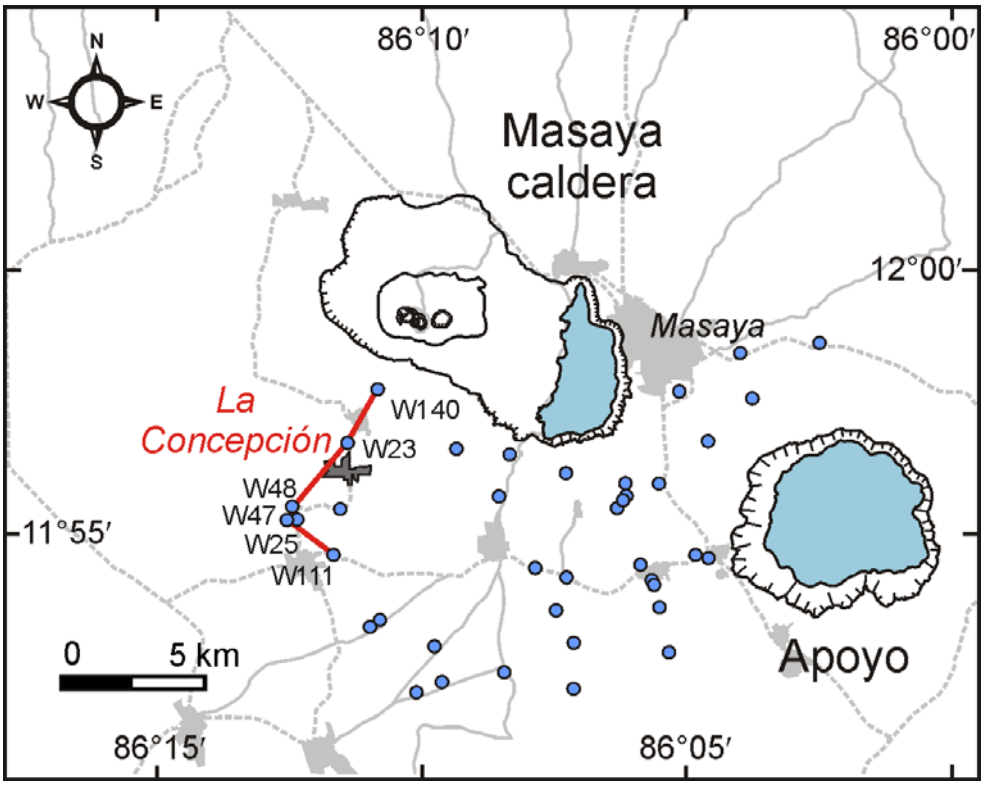

Figure 4.1: Location of the studied outcrops for La Concepción Tephra. The type locality W23 is located near the village La Concepción (or La Concha), which is marked in dark gray in the map. The red line is the profile shown in Fig. 4.2.

4.1.2 Internal stratigraphy

La Concepción Tephra is composed of 8 well-sorted, black, scoria lapilli to coarse-ash layers (B1, B3, B5, B7, B9, B11, B14, B16), intercalated with tuff beds (B2, B4, B6, B8, B10, B12, B13, B15; Fig. 4.2). The lower part of the sequence is dominated by lapilli layers whereas the upper part by tuff beds.

The well-sorted layers B1, B3 and B5 are composed of highly vesicular black lapilli to coarse-ash, with small amounts of basaltic lava country rock fragments (~1-3%). Layer B5 is the thickest lapilli bed, vaguely stratified by vertically alternating grain size, composed of fluidal-textured lapilli and ash particles, and hence is a useful marker bed in all outcrops. Above B5, the well-sorted layers consist of highly vesicular and dense scoria lapilli, with the fraction of denser clasts increasing upwards in the sequence, as well as the amount hydrothermally-altered lithic fragments.

The tuff beds are mostly grayish and cemented, except B4 which is less indurated, relatively well-sorted, fine grained and parallel laminated. Other tuffs (B2, B6, B8, B10) are fine-grained massive beds; some of them contain accretionary lapilli, armored lapilli, dispersed glassy scoria fragments and plant molds. The uppermost tuffs (B12, B15) are thicker, poorly-sorted, with low angle cross-bedding, dune-structures and laterally changing thickness. Layer B13 is a bed of fine ash rich in accretionary lapilli.

The following is a detailed description of each layer based mostly on the proximal exposures.

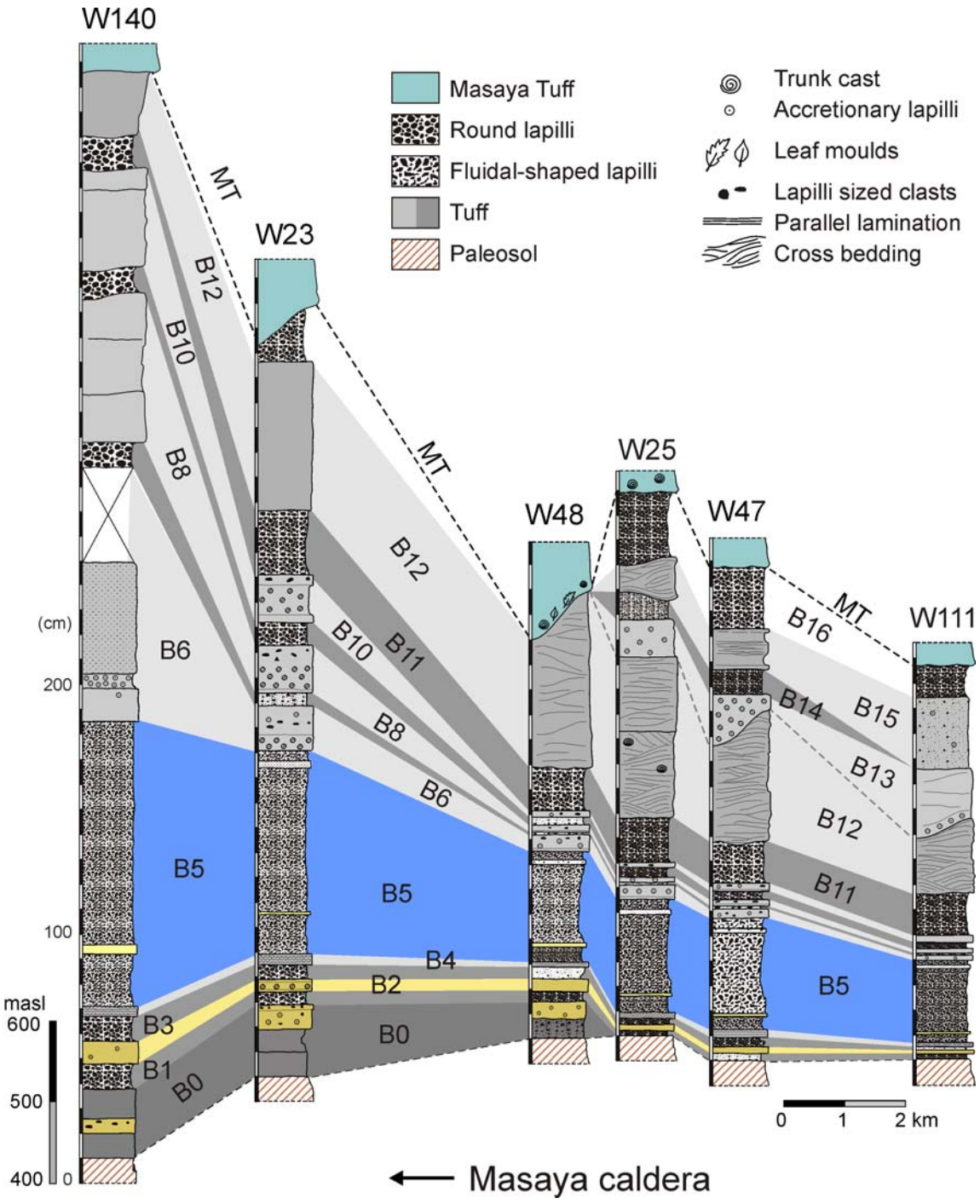

Figure 4.2: Stratigraphy of La Concepción Tephra at the most proximal exposures southwards of the caldera. The profile line is shown in Fig. 4.1. Note the different degrees of erosion displayed by the outcrops, with the Masaya Tuff lying unconformably over it.

4.1.2.1 Subunit B0

In a few proximal outcrops <6 km from the caldera rim, some ash deposits can be found at the bottom of the sequence. They are presumably phreatomagmatic deposits of smaller events with limited dispersion that occurred as precursors of the LCT eruption. The deposits consist of two basal fine ash layers and an accretionary lapilli tuff at the top. At the outcrop W23, where this subunit is well exposed, three layers can be distinguished (Fig. 4.3): B01 is a loose light gray fine ash, but in some parts there are some clusters or ash aggregates. B02 is a poorly sorted light gray fine ash layer with medium to coarse ash in the middle. B03 is a yellowish indurated fine tuff with accretionary lapilli as well as scarce fragments of black vesicular scoria lapilli. The upper part is more cemented than the rest and contains hydrothermally altered clasts and plant remains.

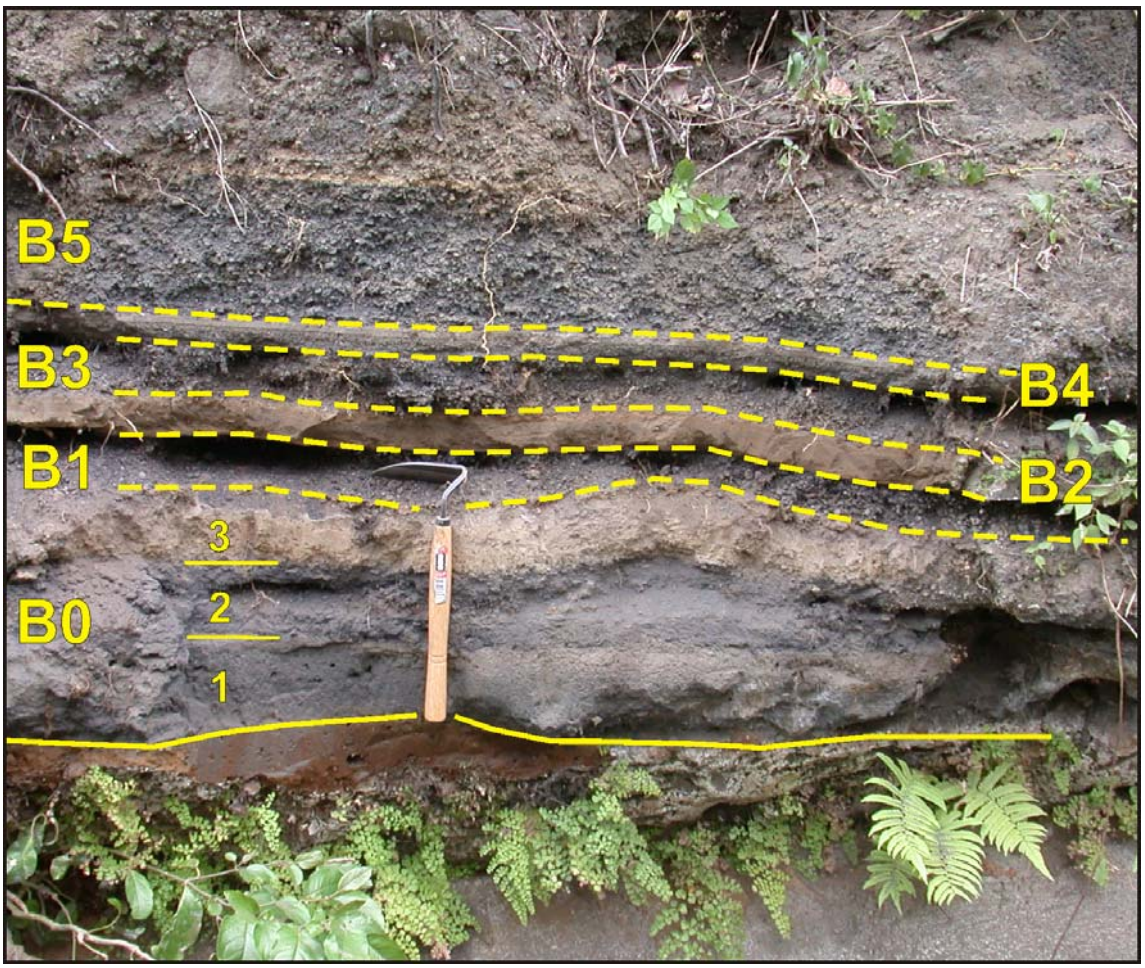

Figure 4.3: Lower contact of La Concepción Tephra at the proximal outcrop W23, 3 km south of the Masaya caldera rim. This is one of the few places where the subunit A0 can be found.

4.1.2.2 Subunit B1

It is a well-sorted (σ~1.5), black lapilli unit (Fig. 4.4), ranging in thickness from 10 cm at 1 km from the caldera rim to 2 cm at 7.5 km distance. The juvenile fragments are mostly moderately vesicular, round-shaped lapilli with a bread-crust texture, but there is also a minor amount of highly vesicular glassy lapilli. The clasts range in density from 0.8 to 1.35 g/cm^3.

Microscopically, it consists only of tachylitic glass with different degrees of vesicularity. There are vesicular clasts with ~40-50 vol.% of mostly round vesicles (0.6 mm in average but could be as big as 1.4 mm, Fig. 4.5a) and denser clasts with ~7-17 vol.% of irregular-shaped very small (0.08 mm in average) voids (Fig. 4.5b). The mineral content is dominated by large plagioclase phenocrysts (up to 1.5 mm, Fig. 4.5c) and less common olivine and augite, as well as plagioclase microlites at the groundmass. The lapilli fragments contain small lava xenoliths and curiously they are always surrounded by a large void space (Fig. 4.5d). Probable the surface of the lithic served as nucleation site during heterogeneous bubble nucleation.

At the base of the layer abundant lithic fragments (>5 vol.%) can be found, mostly hydrothermally altered or palagonitized. The biggest and more common ones are angular lavas with Mn oxides patches. A minor amount of gabbroic plutonic lithic fragments can also be found.

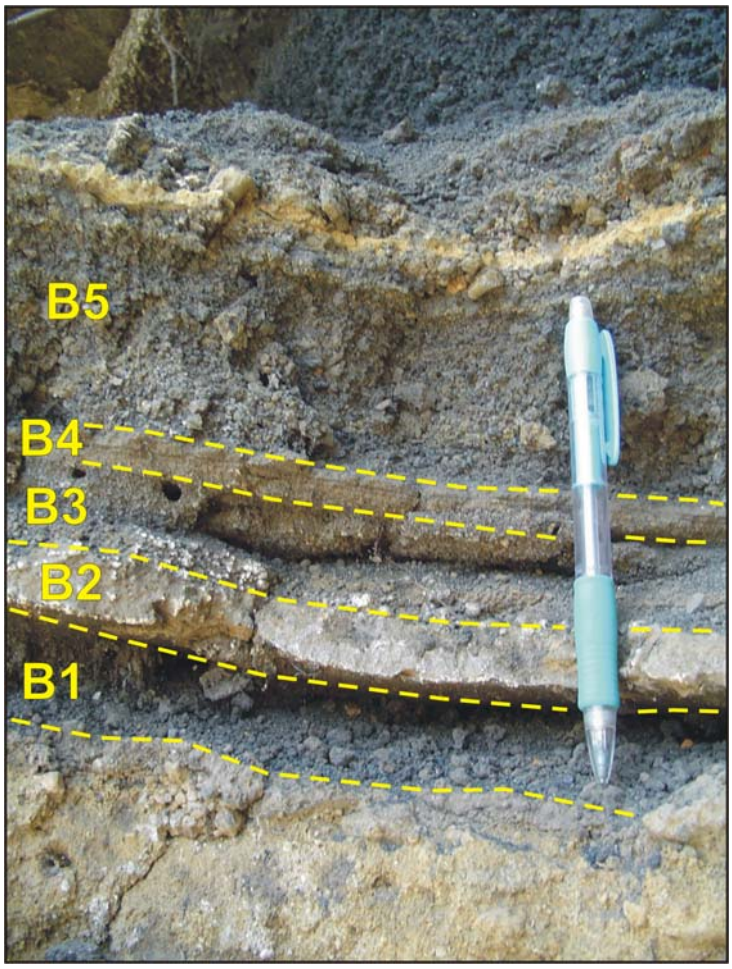

Figure 4.4: Lower sequence of La Concepción Tephra from subunit B1 to B5. The subunit B0 does not crop out here. The locality lies approximately 5.5 km to the south from Masaya caldera rim. B1 overlies the yellowish-reddish paleosol at the top of the San Antonio Tephra.

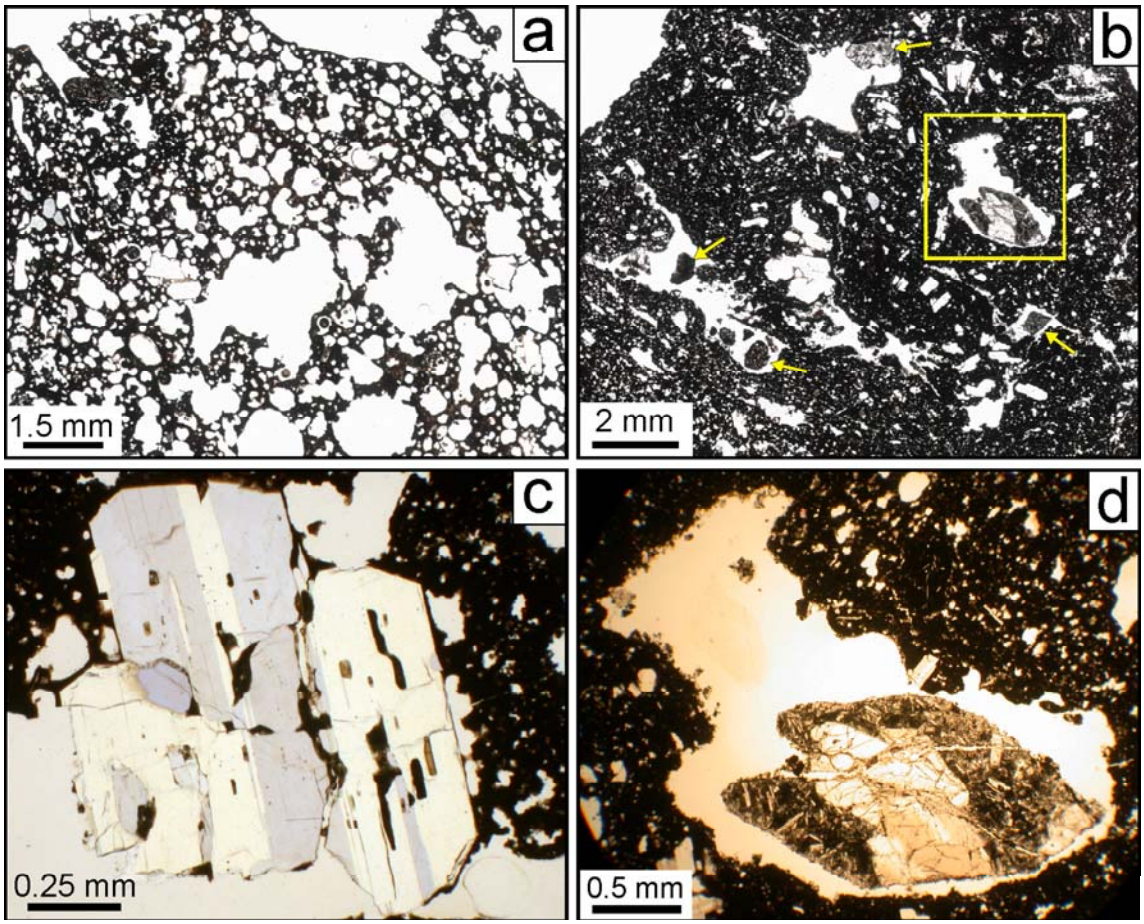

Figure 4.5: The two dominant types of juvenile particles at the subunit LCT-B1: [**a**] vesicular tachylitic fragments and [**b**] dense tachylitic fragments. [**c**] Large plagioclase phenocryst. [**d**] Lithic fragment in a void.

4.1.2.3 Subunit B2

This is a yellowish indurated fine tuff (Figs. 4.3, 4.4), containing very fine accretionary lapilli (2-3 mm diameter), concentrated at the lower part of the tuff but also a few disseminated in the rest of the tuff. The top is faintly laminated and contains plant molds (grass leaves).

4.1.2.4 Subunit B3

Subunit B3 is similar to B1 but with finer grained lapilli and contains a smaller amount of lithics (1-2 vol.%), most of them with hydrothermal alteration. It is moderately sorted and the juvenile lapilli fragments are poorly vesicular, with small lithic fragment inclusions. Most of juveniles are dense (~1.50 g/cm^3) and have round-shapes.

4.1.2.5 Subunit B4

It is a parallel laminated tuff, weakly indurated (Figs. 4.3, 4.4). It appears as a basal coarse-ash laminated tuff and a very fine thinly laminated top. The fine-grained top layer has a light gray to cream thin layer which has a higher proportion of lithic ash, and also dark gray layers, made mostly by glassy ash.

The ash particles consist mainly of poorly to non-vesicular glass, but there is about 3~5 vol.% of highly vesicular achnelith-shaped fragments and an important proportion of hydrothermal lithics. Sometimes there are some "load structures" affecting the parallel lamination, which can be an indication that the fine ash was wet during emplacement.

4.1.2.6 Subunit B5

Layer B5 is the most distinctive and thickest lapilli layer of the LCT, composed of fluidal-textured lapilli achneliths and ash particles, and hence is a useful marker bed in all outcrops (Fig. 4.6). It is a well-sorted (σ=1~2) black highly vesicular lapilli deposit, separated by a light yellowish thin layer of fine ash and vaguely stratified by vertically alternating grain size (Fig. 4.7).

The glassy fluidal-shaped juvenile fragments are very aphyric (<2 vol.% of euhedral plagioclase phenocrysts) and consist of highly vesicular sideromelane glass containing 45-80 vol.% of round-shaped vesicles. The density varies between 0.5 and 0.8 g/cm^3, but the most vesicular lapilli can have a density as low as 0.25 g/cm^3 and denser fragments ~1 g/cm^3.

The lithic content is very low (<1 vol.%) and the few present ones are small (<12 mm maximum size) and hydrothermally altered.

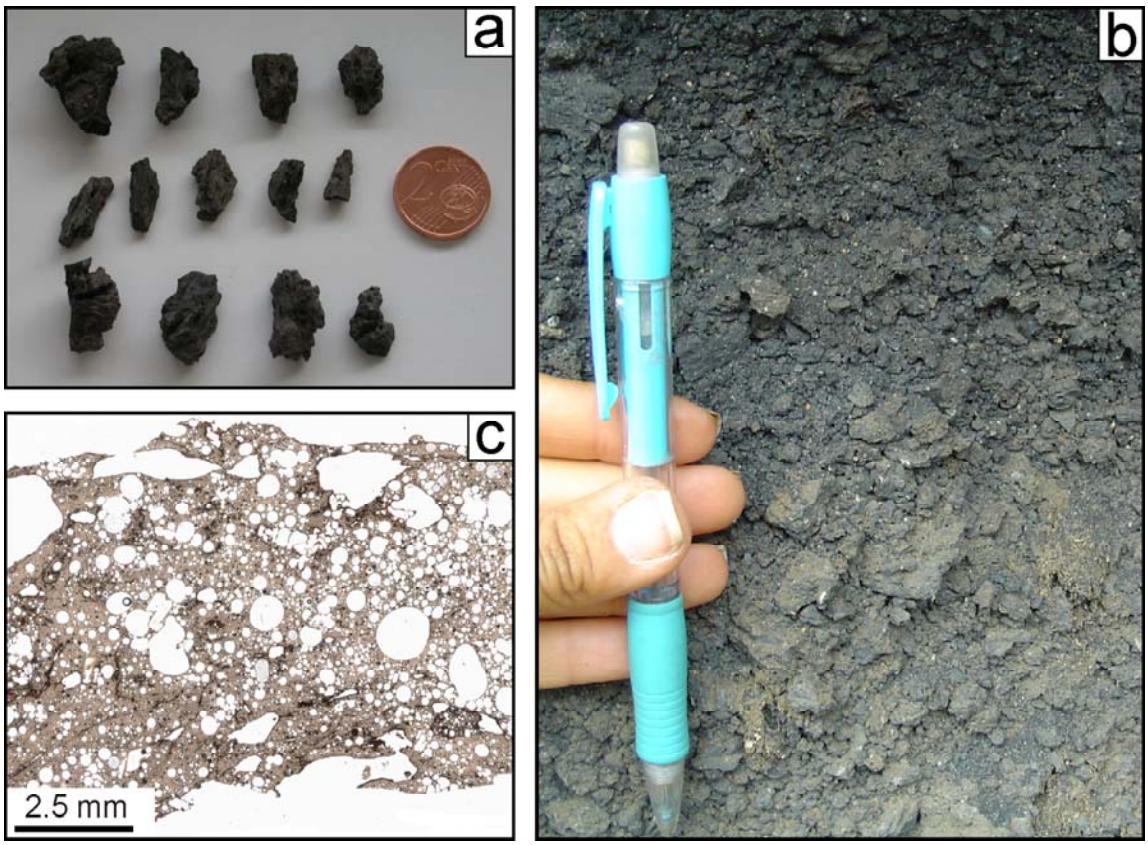

Figure 4.6: Photographs of the juvenile particles of subunit B5. [**a**] Single particles with fluidal shapes and glassy surfaces. [**b**] Whole deposit how it looks at the outcrops. [**c**] In thin section, as highly vesicular brown sideromelane glass.

The total thickness of the unit decreases from 115 cm at 1 km from the vent to 12 cm at 10 km, where it appears as a single thin layer of achnelith-shaped fine lapilli. It can also be subdivided in different layers (Fig. 4.7):

[a] Highly vesicular, glassy black, faintly laminated, moderately good sorted lapilli layer with some amount of juvenile components in the ash fraction and very few lithics. Most of the juvenile fragments have elongated or contorted shapes similar to Peleé's tears, and are called achneliths; others have glassy surfaces and elongated tubular vesicles and ~20 vol.% have a high amount of rounded globular vesicles reticulites.

[b] Yellowish volcanic fine ash layer of around 1 cm thick (reaches 4 cm at 1 km from the caldera rim), shown in Figs. 4.4 and 4.7a.

[c] Is the thickest layer (reaching at least 90 cm in the proximal areas) and nearly similar to [a] with some differences regarding better sorting at the top, increase of the maximum grain size, and a higher content of lithics (~1 vol.%). It shows also important vertical variations in the grain size, with a slightly laminated layer consisting of fine lapilli to coarse ash at the bottom and changes to well-sorted lapilli in the rest of the layer. The lapilli fragments are mostly glassy with a density ranging from 0.7 to 0.8 g/cm^3 and in some cases reaching 1 g/cm^3.

[d] Finer-grained glassy medium ash layer, slightly laminated, but also harder than the loose lapilli of the underlain and overlying layers.

[e] Similar to [a] and [c].

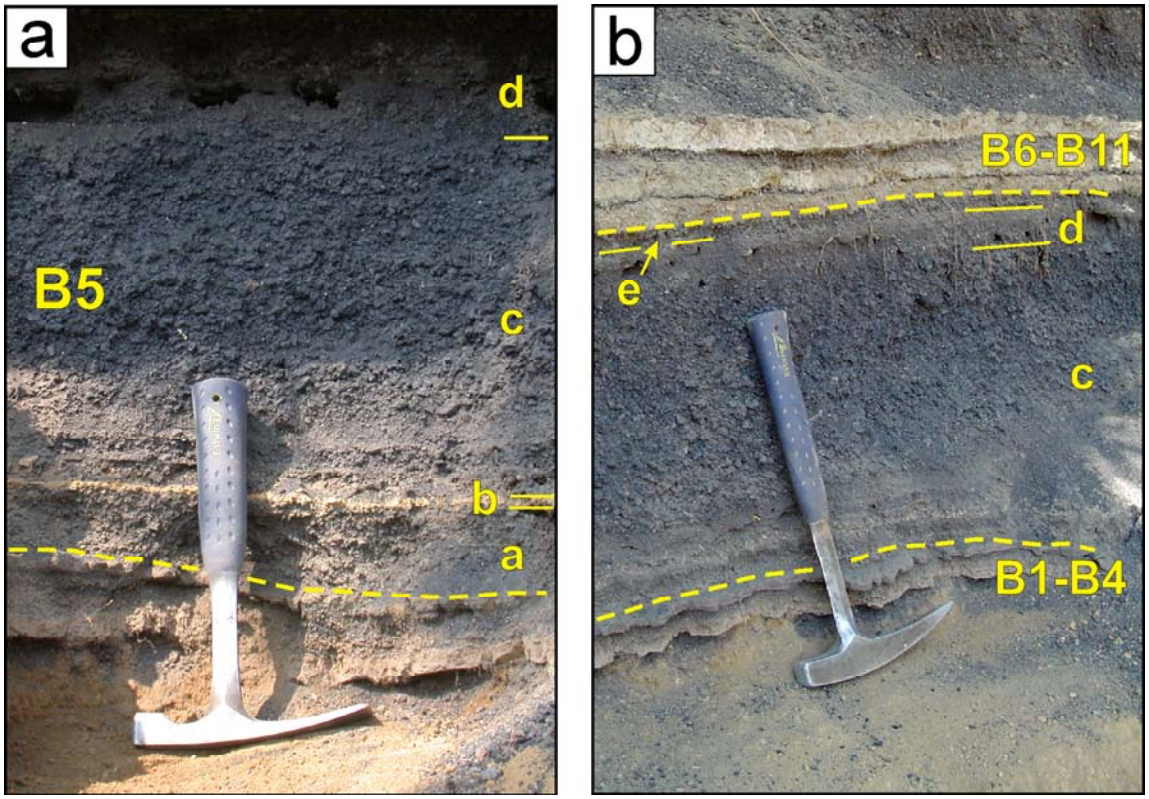

Figure 4.7: Internal sequence of the subunit B5 at [**a**] 5 km and [**b**] 7.5 km from Masaya caldera. The yellowish volcanic ash of subunit B5b is not present at the second locality, but appears as a fine ash layer. The variations in grain size of the deposit are an indication of fluctuations in the eruptive column.

4.1.2.7 Subunit B6

It is a grayish indurated tuff, separated in two sections: the lower part is finer grained with accretionary lapilli and the upper one is coarser, with cross bedding structures of fine lapilli to coarse ash, as shown in proximal exposures. In the medial exposures it appears as a fine indurated tuff with vesicular lapilli at the bottom and a laminated medium to fine ash with scarce accretionary lapilli at the top. The ash particles are made of highly vesicular and dense glass, as well as some hydrothermal altered lithic fragments and plagioclase crystals. It is characterized by a rapid decrease in thickness, from around 60 cm at 1 km distance from the vent to 2 cm at 7 km. Already 3 km away from the vent it is only a 20 cm tuff.

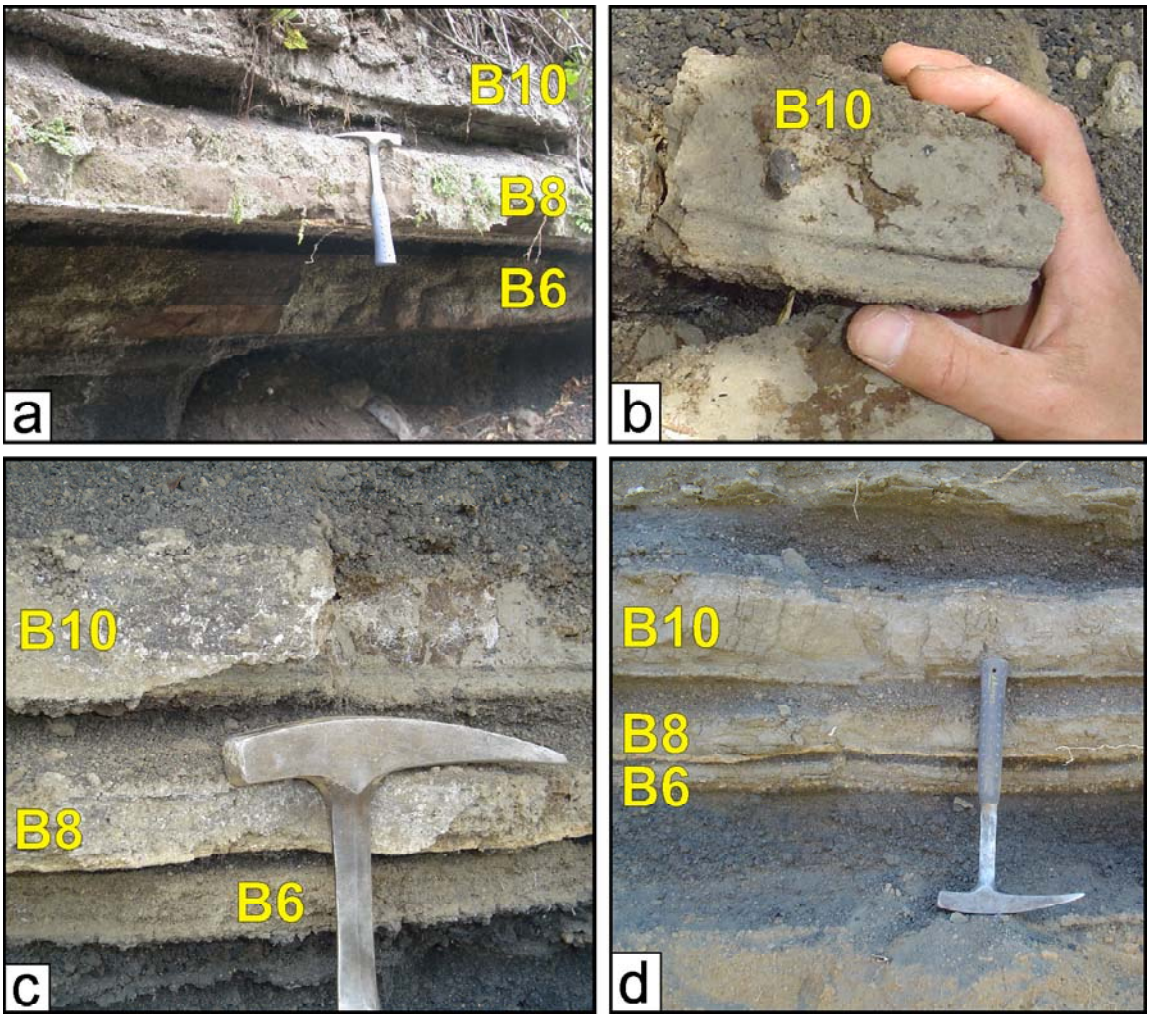

Figure 4.8: Photographs of the tuff sequence B6-B10 with the intercalated well-sorted fall deposits. [**a**] At an outcrop 3 km S from the rim where they are several cm thick, [**b**] zoom of the tuff B10 showing the lower laminated part at 5.5 km S of the caldera. [**c**] The three tuffs at 7.5 km S of the caldera rim and [**d**] 1 km SE from the Masaya caldera rim.

4.1.2.8 Subunit B7

Well-sorted, black, fine lapilli layer, which decreases in grain size to coarse ash in a distance of 7 km. Most of the juvenile fragments are glassy and highly vesicular, with a density 0.9-1 g/cm^3, but ~5-10 vol.% of them are dense (ρ~1.5 g/cm^3) and poorly vesicular. The clasts show mostly round shapes and typical achnelith shapes like those of the Unit B5 are lacking. Microscopically, the juvenile particles are a mixture of black tachylite and light brown sideromelane (Fig. 4.9), with a vesicularity of 50-60%. The vesicles in the tachylitic glass are commonly irregular-shaped, whereas the vesicles in the sideromelane glass are mostly round (Fig. 4.9). The deposit contains less than 1% of lithic fragments, some of them are hydrothermalized but also non-altered.

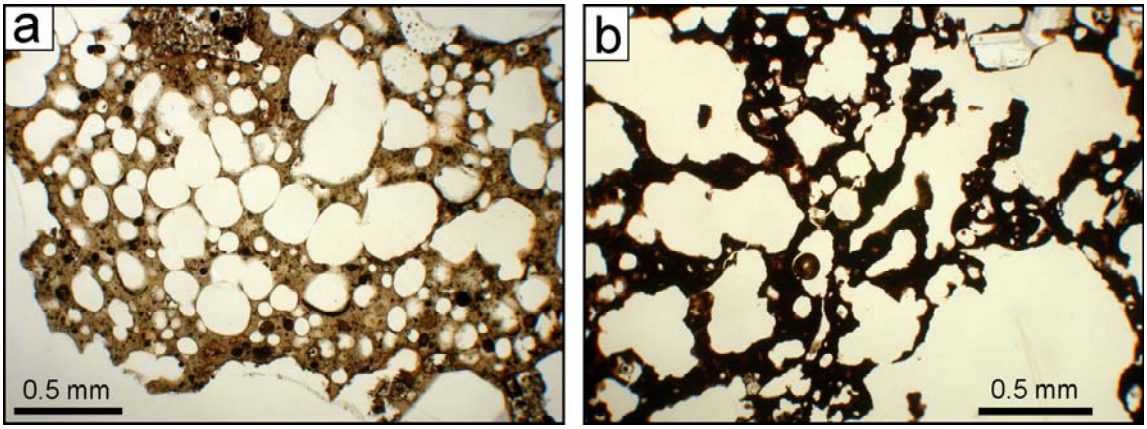

Figure 4.9: Different glass types present forming the juvenile clasts of the subunit LCT-B7. Both microphotographs are from the same lapilli fragment. [**a**] Brown sideromelane glass with 52 vol.% of round vesicles and [**b**] Black tachylite with a slightly higher vesicularity (62 vol.%), but the vesicles exhibit irregular and elongated shapes.

4.1.2.9 Subunit B8

B8 is an indurated tuff and has a maximum thickness of 60 cm at the proximal facies (~1 km from the vent). It shows dune structures and cross bedding, alternating coarse and fine lapilli layers at the bottom. In the medial facies, it appears as a 20 cm tuff with a 1 cm yellowish fine ash at the bottom, overlain by an indurated fine tuff with accretionary lapilli and floating glassy clasts. The top is a highly indurated/cemented light gray fine tuff.

4.1.2.10 Subunit B9

It is a black, moderately-sorted, highly vesicular to dense lapilli layer, coated with fine ash and ~1 vol.% of lithic fragments. The juveniles are mainly poorly vesicular with round shapes and a density of ~1.20-1.35 g/cm^3. About 10 vol.% of the juveniles are highly vesicular, with a lower density 0.9-1.10 g/cm^3. It reaches a maximum thickness of 10 cm at proximal exposures, and a minimum of 2 cm, observed 7 km away from the vent. Microscopically, it has three types of fragments, highly vesicular brown to pale brown sideromelane, vesicular tachylite and dense tachylite (Fig. 4.10). The dense tachylitic clasts are the dominant ones in the deposit. The lithic fragments are mostly reddish to orange with brown steins and a pearly luster.

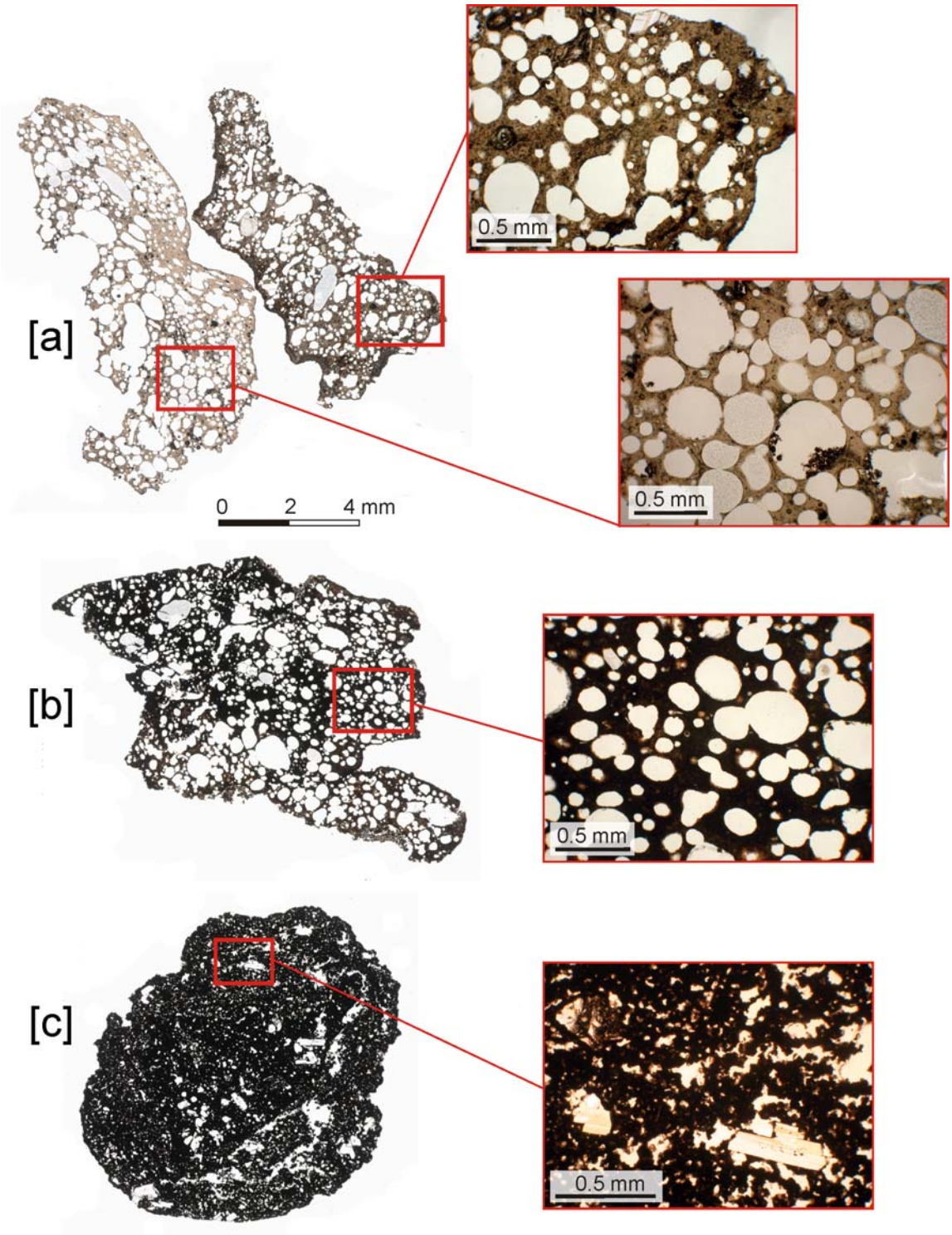

Figure 4.10: Types of lapilli fragments of the subunit LCT-B9: [**a**] highly vesicular sideromelane (~43-48%vol. vesicles), [**b**] vesicular tachylite with ~40 vol.% round vesicles and [**c**] dense tachylite, where the vesicularity consist in irregular-shaped voids (~16%vol.).

4.1.2.11 Subunit B10

It is an indurated grayish tuff that reaches a maximum thickness of 40 cm at 1 km from the vent but thins rapidly to only 2-3 cm at 6 km. At the most proximal exposure occurs as a bedded, poorly sorted, coarse tuff. It shows floating lapilli fragments at the base, a fine to medium tuff with dune structures at the middle portion and a highly indurated tuff at the top. At medial exposures S or SE from the caldera rim, it consists of an indurated grayish cross bedded tuff with coarse ash and fine lapilli at the bottom and a fine tuff with accretionary lapilli at the top (Figs. 4.8, 4.11). At distal exposures to the S and SW, it appears as a few cm indurated tuff with accretionary lapilli, slightly laminated at the bottom.

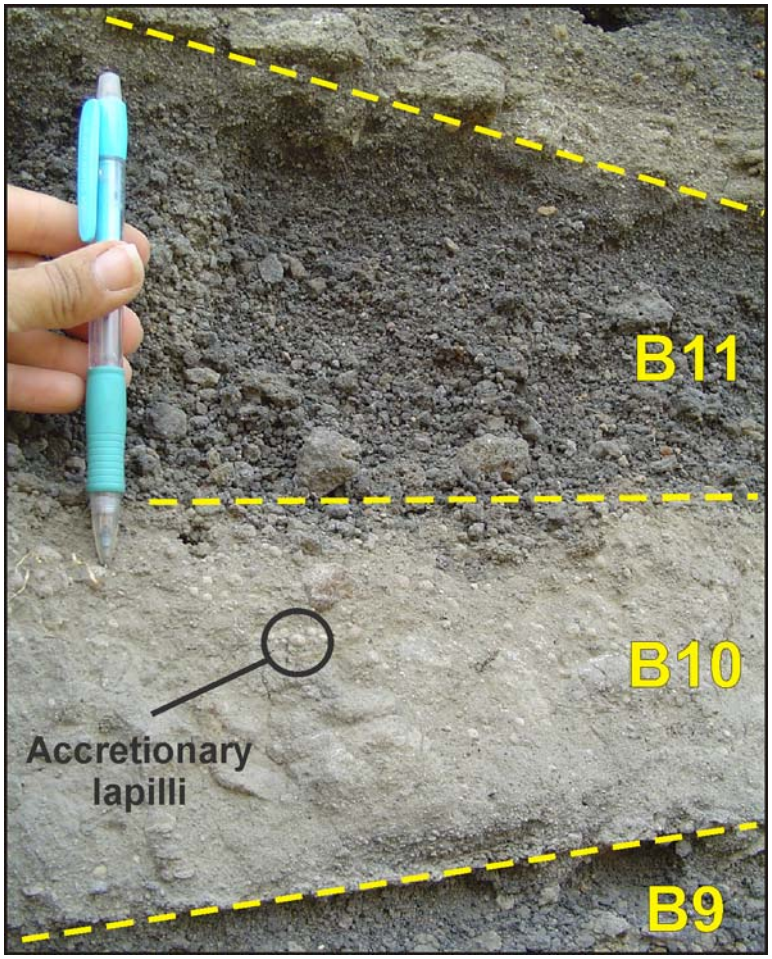

Figure 4.11: Photograph of the subunits LCT-B10 and LCT-B11 at an exposure 1 km SE of the caldera. Subunit B10 has a coarser bottom and a top part rich in accretionary lapilli (marked on the picture).

4.1.2.12 Subunit B11

It is a black, well-sorted, poorly to moderately vesicular lapilli layer, with a minor amount (~20 vol.%) of highly vesicular particles (Fig. 4.11). The dominant clast type are moderately vesicular lapilli, with a density of 0.8 g/cm^3. The denser juvenile fragments have an average density of 1.2 g/cm^3 (can be as high as 1.6 g/cm^3), they exhibit mostly spherical shapes and are coated with fine ash. The highly vesicular clasts have lower densities of ~0.65 g/cm^3 in average.
Microscopically, the juvenile clasts consist of tachylitic glass and minor sideromelane, both coexisting in the same clasts and exhibiting a wide range of vesicularities. The moderately vesicular clasts have a vesicularity ~30-45% whereas the dense ones ~17-20%. The amount of phenocrysts is higher than at

the underlying subunits (~10 vol.%) and consist mostly of large plagioclase and minor olivine.
The lithic content is relatively high, 3~5%, and contains similar reddish pearl-lustered lithics to those of the Unit B9, but also vesicular lavas and plutonic fragments.

4.1.2.13 Subunit B12

It comprises at least two main indurated tuff beds of lapilli to medium ash with cross-bedding and well-developed dune structures. The lowermost unit (35 cm thick at the most proximal outcrop) is coarser grained, and has elongated cavities aligned in different directions, which are molds of branches and trunks. The upper bed is a low angle cross-bedded finer deposit (fine to medium ash), with a maximum observed thickness of 30 cm. At more distal exposures (7.5 km from the caldera) it looks like a massive indurated grayish tuff with cross bedding at the bottom (Fig. 4.12a) and at the most distal outcrops it appears as a massive yellowish soft tuffaceous deposit.
The tuff is poorly-sorted with angular ash to fine lapilli-sized fragments (~0.1 to 4 mm) of mostly dense angular sideromelane and tachylitic glass, a minor amount of vesicular sideromelane, crystals of plagioclase, olivine and augite. It also contains lithic fragments (basaltic lavas, tuffs, among others), small accretionary lapilli and armored lapilli (Fig. 4.12b-h). The bigger lapilli-sized fragments are mainly lavas of different textures and dense juveniles.

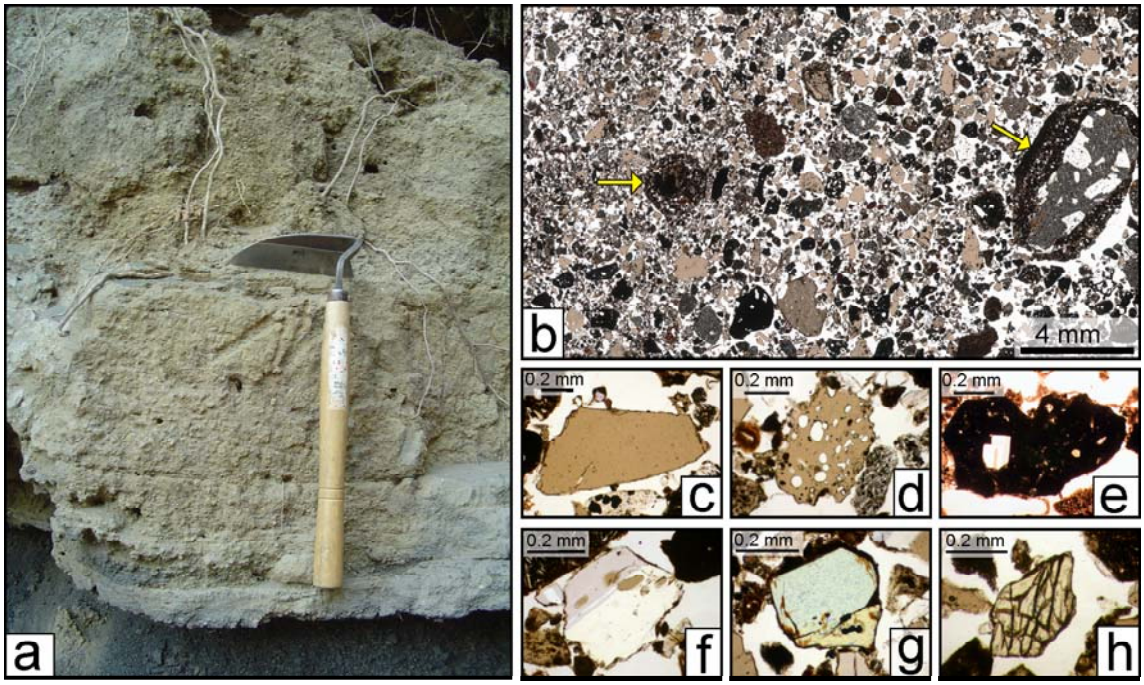

Figure 4.12: [**a**] Photograph of the B12 tuff at mesoscopic scale, where the cross bedding can be distinguished. [**b**] Microphotograph of the tuff, the two yellow arrows point out to accretionary lapilli (left) and armored lapilli (right). The other pictures are examples of the main components of the tuff: [**c**] angular sideromelane fragment; [**d**] vesicular sideromelane and a small lithic fragment near the lower right corner; [**e**] dense tachylitic fragment; [**f**] plagioclase with melt inclusions; [**g**] olivine and [**h**] augite.

4.1.2.14 Subunit B13

It is a grayish accretionary lapilli-rich fine tuff, with ash-coated scoria fragments of fine lapilli size. It changes the thickness even at the same outcrop because it filled the topography left by the dunes of the underlying subunit B12. The maximum observed thickness is 15 cm, at the outcrops W25 and W48 located ~6 km from the caldera rim (see Fig. 4.2).

4.1.2.15 Subunit B14

B14 is a relatively well-sorted (σ~1.5) coarse ash to fine lapilli layer, made up by vesicular and dense juvenile fragments coated with fine ash and showing faint cross-bedding. The maximum observed thickness is 18 cm at 6 km from the caldera rim. In thin section, the juvenile fragments are completely formed by moderately vesicular (35-50 vol.%) tachylitic glass with cores of dense tachylite (~8 vol.% voids) and large plagioclase phenocrysts (up to 3.5 mm).

4.1.2.16 Subunit B15

This subunit is a gray to yellowish, indurated, fine to coarse ash tuff, with scattered accretionary lapilli and vesicular lapilli-sized fragments. It shows cross-bedding and lapilli-rich lenses and it is limited at the base and top by light gray cemented tuff horizons (0.5-1 cm in thickness). At the outcrop W25 it shows an undulated bedding, changing in thickness lateraly from 9 to 17 cm across a distance of 2 m (Fig. 4.2).

4.1.2.17 Subunit B16

This upper moderately well-sorted lapilli layer consists of vesicular and dense black scoria fragments and lithic fragments, some of them hydrothermally altered. At proximal exposures it has a maximum thickness of up to 25 cm and decrease to 10 cm at a distance of 9 km from the caldera rim. The juvenile fragments range from highly vesicular light particles with density as low as 0.4 g/cm^3, to moderately vesicular lapilli (ρ~ 0.6-0.7 g/cm^3), which are the most common particle type making ~80% of the juveniles, and minor dense fragments with densities of 1.1-1.5 g/cm^3. The scoria maximum size ranges from 50 mm 5 km away from the caldera to 34 mm at 9 km.

Microscopically, the juvenile fragments consist of moderately vesicular (20-30%) tachylite with mostly irregular-shaped vesicles and minor round ones, similar to those of the subunit B7 shown in Fig. 4.9b. They also have large plagioclase phenocrysts (up to 2 mm), olivine and basaltic lithic fragments.

4.1.3 Lateral facies changes

The upper contact of the LCT is commonly eroded to a variable degree. At some localities it is overlain by a thick overburden of a clayey material, whereas at others it is deeply incised by an erosional unconformity filled by the Masaya Tuff. Most of the exposures show the succession from B1 to B11 and a little part of B12 in a massive deposit and just a few of them show the complete sequence (Fig. 4.13).

The most striking lateral facies change occurs in the subunits B6, B8 and B9 (Figs. 4.12, 4.14). At proximal exposures, 2 km from the caldera rim, these units appear as thick (up to 60 cm), cross-bedded tuffs, whereas at outcrops located at >5 km from the caldera they appear as thin (2-20 cm), massive, accretionary lapilli-rich, structure-less indurated tuffs.

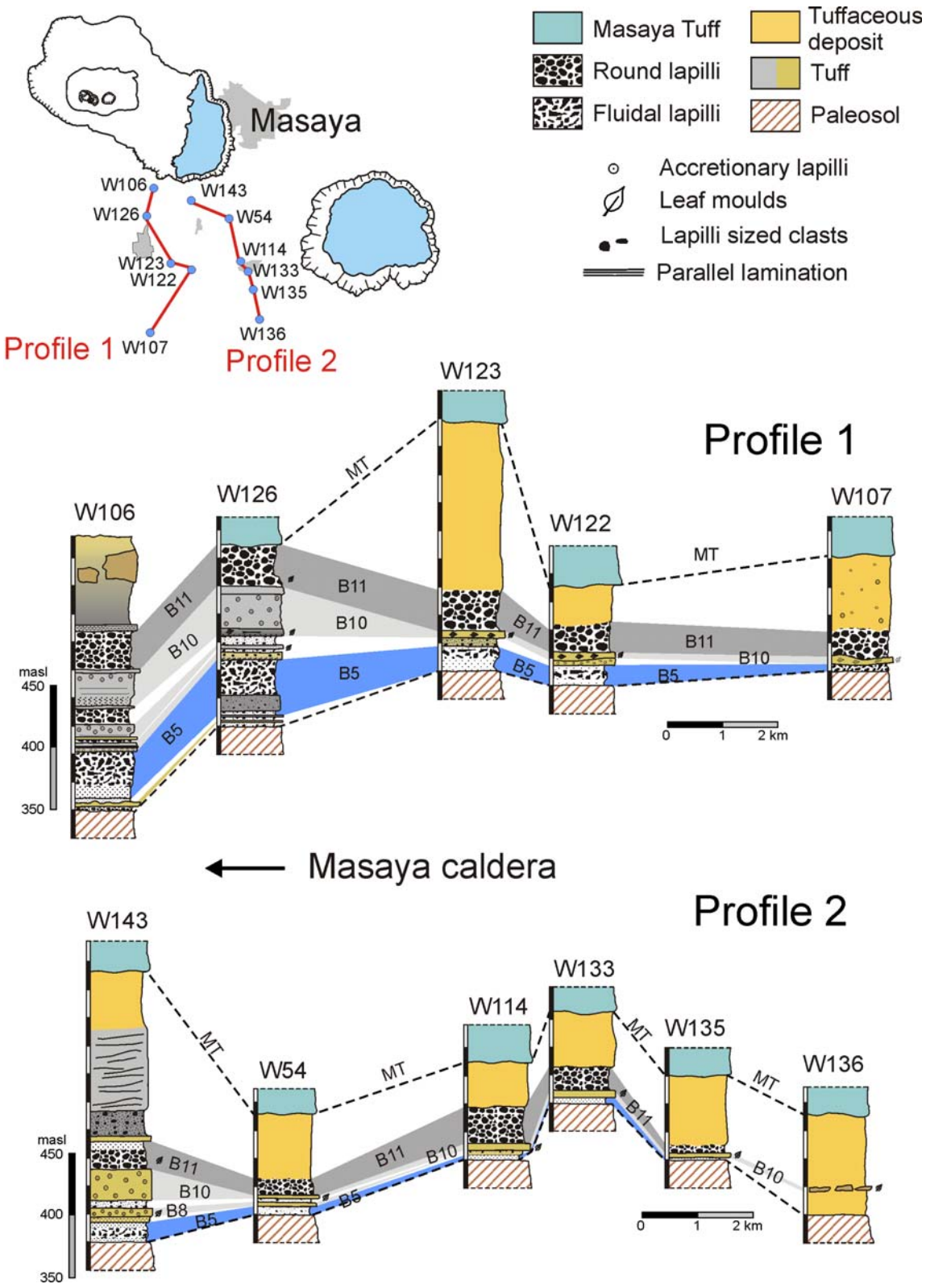

Figure 4.13: Stratigraphic variations of La Concepción Tephra with distance to the Masaya caldera rim, shown in two profiles.

With increasing distance from the vent the fall layer B7 and tuffs B6 and B8 thin out. In the most distal localities the LCT appears as a 10 cm deposit consisting of only three layers: a lower well-sorted fluidal fine lapilli deposits, followed by a hard undulated thin tuff with leaf molds at the base, and a well-sorted lapilli layer (Fig. 4.14). All are overlain by a ~25 cm massive altered reddish deposit.
At proximal areas to the south of the caldera, near Masatepe, the tuff of subunit B11 is thicker than the underlying ones (B7 and B9), and with abundant accretionary lapilli, similar to the characteristic subunit C7 of the Masaya Triple Layer (Fig. 4.12).

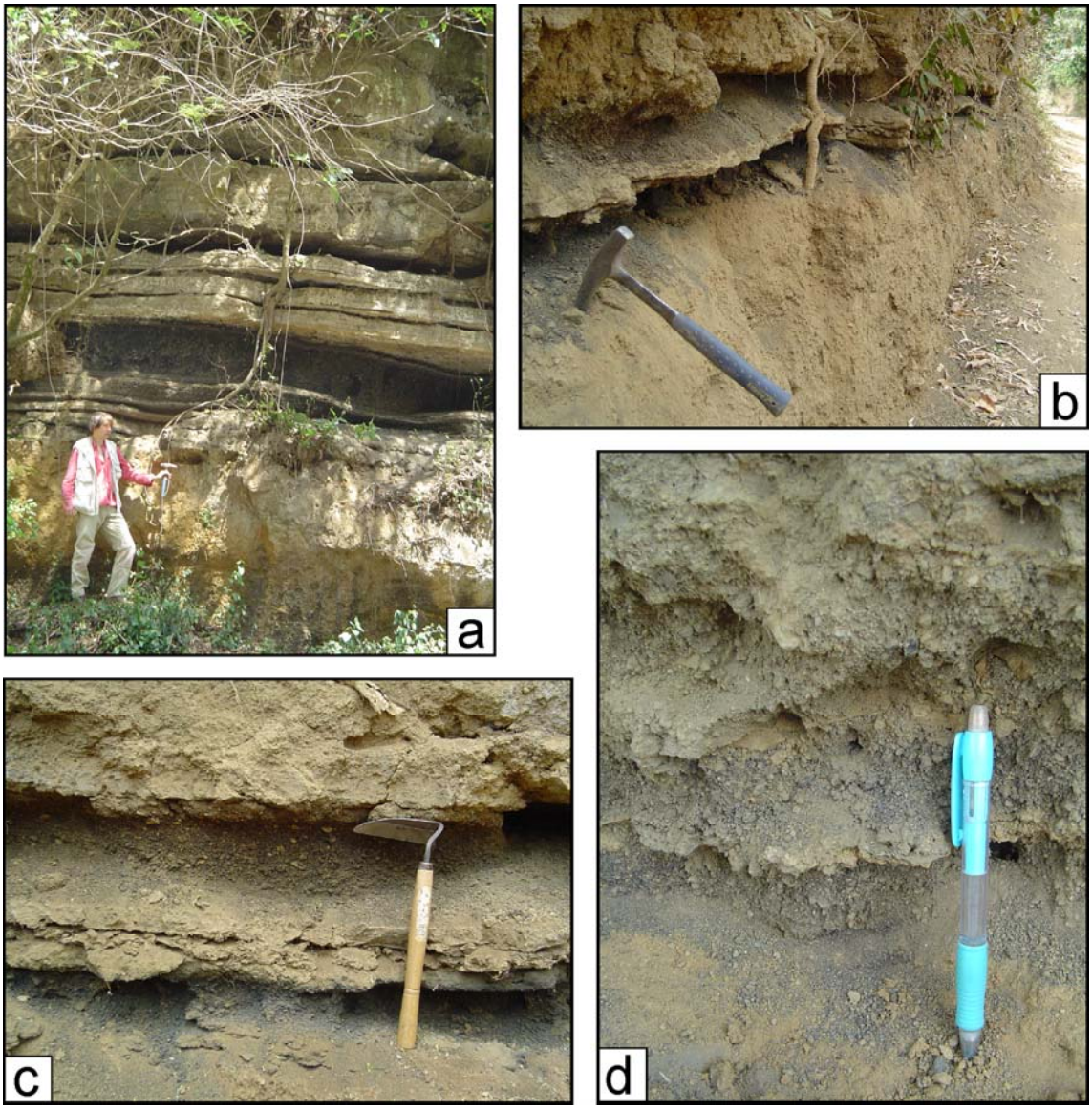

Figure 4.14: Photographs showing proximal to distal variations of the LCT. [**a**] At 3 km S of the caldera, where almost all the subunits are present. [**b**]-[**c**] At 9 and 9.5 km S of the caldera respectively, showing how the tuff subunits B6-B8-B10 merge, the two lower ones tend to dissapear and only a single tuff remains. [**d**] At 2.5 km to the SE of the Masaya caldera rim, consisting only by two fine lapilli layers separated by a tuff.

4.2 Masaya Triple Layer

The Masaya Triple Layer is a deposit consisting of well-sorted black scoria lapilli, coarse ash layers and grayish indurated tuffs. It crops out in numerous exposures to the NW from Masaya caldera, between El Crucero, Managua and as far NW as Ciudad Sandino (Fig. 4.15). This unit overlies the San Antonio Tephra by a paleosol and an erosive unconformity, and it is separated from the overlying Chiltepe Tephra by a yellowish massive reworked tuffaceous deposit. No trace of the MTL could be found to the NE and SW of the caldera, although underlying and overlying units do occur in these areas. This suggests that there was little or no deposition of MTL rather than strong erosion removing the deposit.

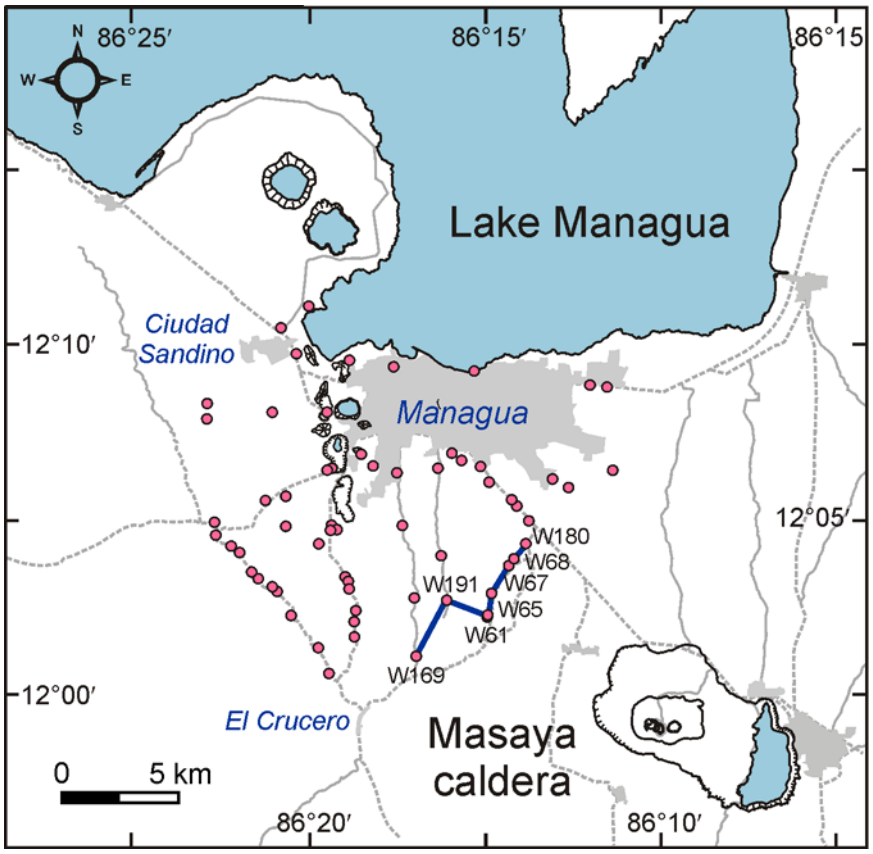

Figure 4.15. Location of the studied outcrops for the Masaya Triple Layer. The blue line is the proximal profile shown in Fig. 4.16. The main cities mentioned in the text are marked in blue.

4.2.1 Clast components

The juvenile fragments vary from highly vesicular to dense round-shaped scoria lapilli, with a wide density range between 0.4 and 2.3 g/cm^3. Both types and intermediate members occur not only in different layers but can also be present at the same deposit.

Microscopically, the clasts consist of highly to moderately vesicular (70-40%) sideromelane and tachylite with round vesicles, as well as dense (1-4% porosity) tachylite with irregular-shaped voids and a higher microlite content. Both types can also occur in the same clast. The mineral content is <1-5 vol.% of

plagioclase, olivine and clinopyroxene phenocrysts. The amount of clinopyroxene phenocrysts increases stratigraphically upwards in the MTL. The lithic fragments are mainly basaltic lava and gabbro.

4.2.2 Internal stratigraphy

The Masaya Triple Layer is mainly a fall deposit formed by 7 major beds of black well-sorted scoria lapilli to coarse-ash (C1, C2, C3b, C4, C6, C8 and C10 in), separated by 4 major (C3a, C5, C7, C9) and several minor tuff layers (Fig. 4.16). The lowermost lapilli layers (C1, C2) contain highly vesicular and fluidal scoria particles; some of the other layers (C3b, C4, C6, C8, C10) can have a minor amount of these fluidal lapilli but are characterized by relatively round-shaped denser scoria lapilli and higher contents of lava lithic fragments.

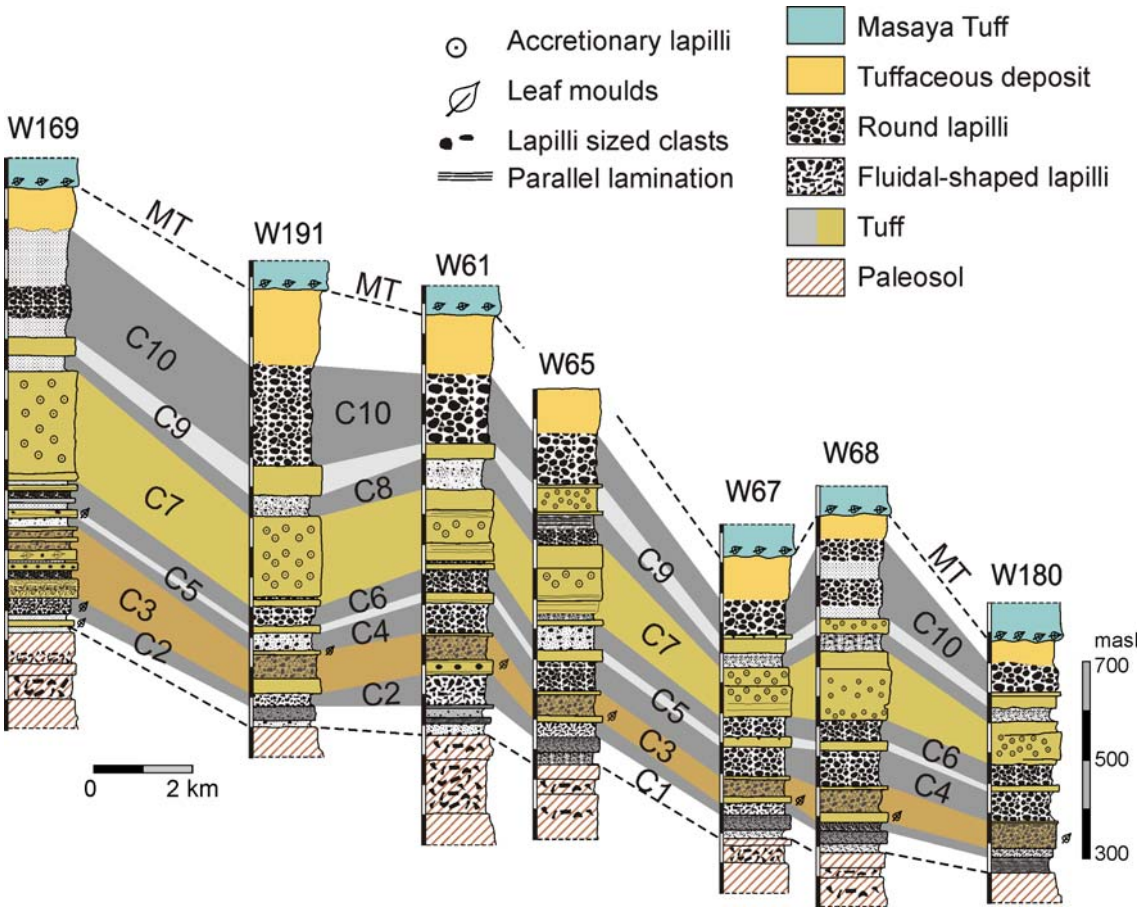

Figure 4.16: Stratigraphy of the Masaya Triple Layer at the most proximal exposures NW of the caldera. The profile line and location of the outcrops is shown in Fig. 4.15.

The massive tuff layer C7 contains accretionary lapilli and is thicker than the other tuff beds, reaching a maximum thickness of 40 cm in the most proximal exposures, ~10 km distance from the caldera. The tuff beds C5 and C9, as well as some of the minor thin tuff beds, have desiccation cracks on their upper surfaces, which is an indication of wet emplacement and of repose time between the different depositional events. Most of these tuff beds appear as thin massive

indurated tuffs in the distal facies. In the medial facies, they exhibit parallel lamination, and in the proximal facies each corresponds to a sequence of thin lapilli to ash layers.
The following is a detailed description of each layer in the succession and their petrographic characteristics. They were identified based on the study of 88 outcrops, mostly on those at proximal areas (Fig. 4.16).

4.2.2.1 Subunit C1

C1 can be subdivided into two parts. C1a is a non-consolidated, highly vesicular, well-sorted, black coarse-ash to fine lapilli layer and C1b is a harder, black to purple, laminated finer-grained layer of medium to coarse-ash tuff, which frequently contains a very thin yellowish discontinuous fine layer rich in plant material.
The juvenile fragments are mostly highly to moderately vesicular with a density between 0.6 and 1.1 g/cm^3, contain phenocrysts of plagioclase (Φ~1-2 mm) and olivine and reddish small (~1 mm) lithic xenoliths.

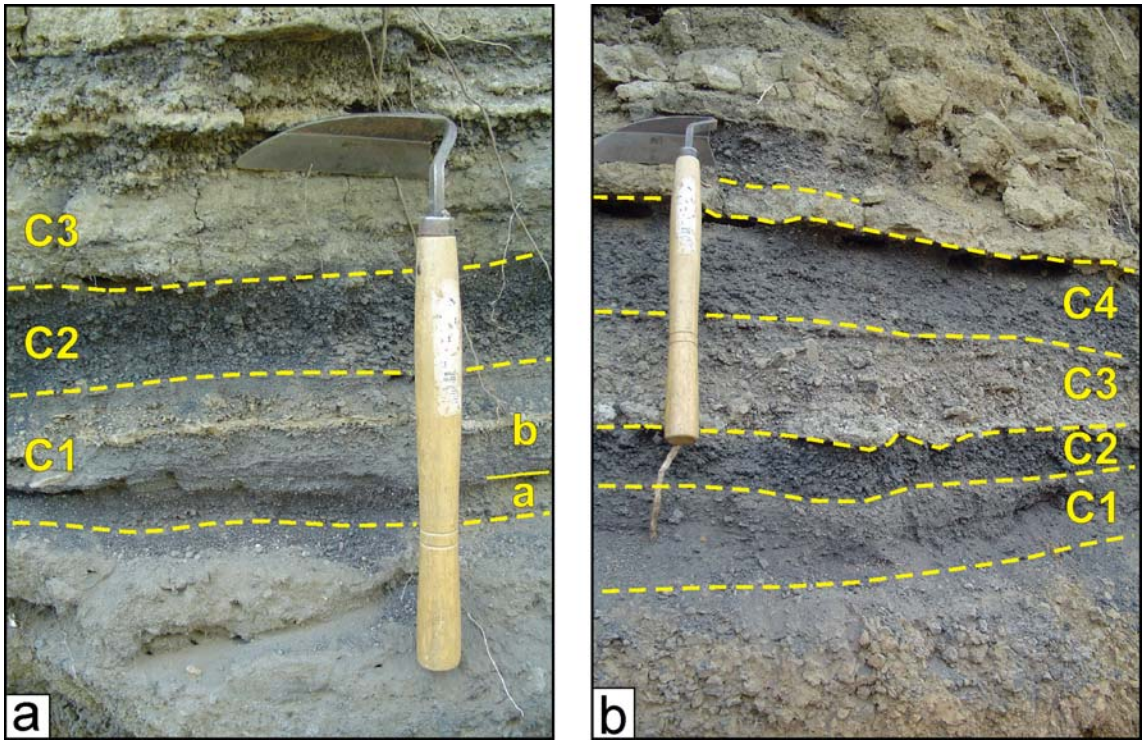

Figure 4.17: Photographs of the lowest portion of the Masaya Triple Layer showing subunits C1, C2 and C3. [**a**] At outcrop W169, 10 km WNW of the caldera rim, the layers a and b of C1 are well exposed. [**b**] At outcrop W65, 7.5 km NW from the caldera, C1 is only a laminated tuff.

4.2.2.3 Subunit C2

It is a well-sorted, highly vesicular lapilli layer with <1 vol.% of lithic fragments. At proximal outcrops reaches a maximum thickness of 5 cm, but at medial-distal sections (>13 km to the NW of Masaya caldera) it turns into a ~1 cm thick black ash layer (Fig. 4.17).

The juvenile fragments are light, moderately to highly vesicular, fluidal, glassy scoria lapilli with round large vesicles (up to 8 mm Φ), as well as plagioclase and olivine phenocrysts. It can be easily recognized in the field due to the morphology of the juvenile components with their fluidal shapes and the stratigraphic position. The density of the fragments is ~0.6 g/cm^3 for the most vesicular ones and ~0.9-1.1 g/cm^3 for denser less vesicular particles.
A thin section of an ash sample from a medial outcrop (Fig. 4.18a) shows that the dominant particle type is moderately vesicular (30-40%) elongated sideromelane (Fig. 4.18b, c), although some highly vesicular (~70% vesicularity) fragments are also present. Less than 20% of the fragments are poorly to moderately vesicular tachylite (~0.5-30% vesicularity; Fig. 4.18d,e). The mineral content is represented by plagioclase phenocrysts with abundant glass inclusions, olivine and minor clinopyroxene.

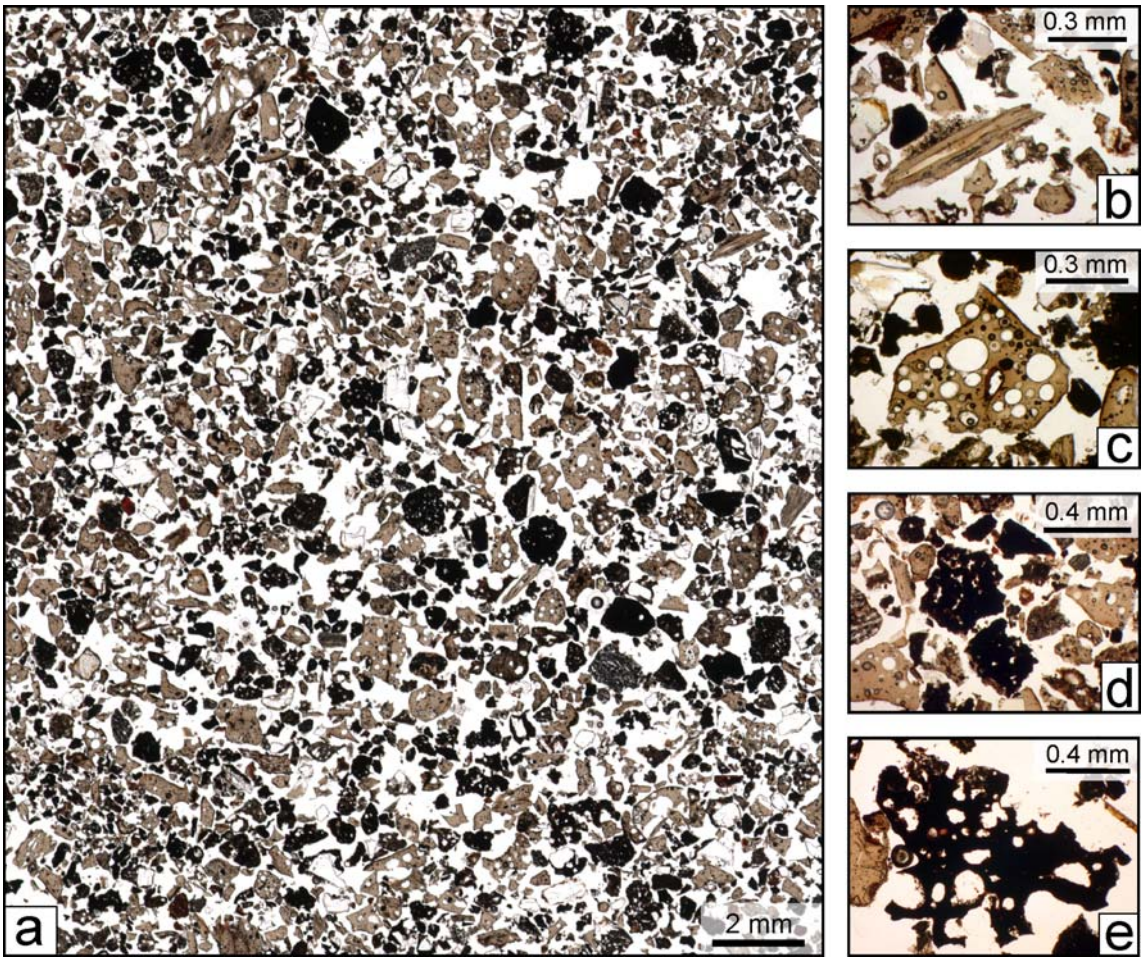

Figure 4.18: Thin section of the subunit C2 at a locality 11.5 km NW from the caldera rim, where it consists mostly of sideromelane coarse ash. [**a**] Overview of part of the section where the proportion of the different components can be appreciated. Detail of the components: [**b**] elongated sideromelane, [**c**] vesicular sideromelane, [**d**] dense tachylite, and [**e**] vesicular tachylite.

4.2.2.3 Subunit C3

This subunit appears at medial facies as an intermediate to poorly-sorted, normal-graded layer with vesicular to dense lapilli and lithic fragments (some hydrothermally altered) and ~30% of coarse ash matrix. It contains abundant molds of plants (Fig. 4.19). In some of the exposures it is possible to differentiate three main layers: a fine yellowish indurated tuff with leaf molds at the base, a relatively well-sorted layer of vesicular to dense lapilli and lithic fragments in a matrix of coarse ash, and a topmost hard thin tuff with desiccation cracks at the surface.

At some proximal exposures, like at the outcrop shown in Fig. 4.19a, C3 consists of several layers, intercalating tuffs and lapilli beds. The maximum observed thickness is 23 cm.

The juvenile fragments are mostly round dense lapilli (1.8-2.3 g/cm^3), but there is a minor proportion of vesicular lapilli with a density of ~1.3 g/cm^3 and even fluidal-shaped particles, all coated with brownish fine ash (Fig. 4.20a, b4). They have inclusions of reddish small lithic fragments (1-2 mm) and plagioclase phenocrysts.

Microscopically, the fragments are a mixture of vesicular sideromelane with 40-60 vol.% of round bubbles and vesicular tachylite, 35-55 vol.% of irregularly-shaped vesicles (Fig. 4.20b, c). The minerals are large melt inclusion-bearing plagioclase phenocrysts and subhedral olivine.

The lithic fragments content is high (~5-15 vol.%) and consist of angular dense aphyric basaltic lavas and hydrothermally altered reddish to yellowish fragments.

Plant remains from this subunit were used to obtain the radiocarbon date of the MTL of 2120 ± 120 years BP (Pérez and Freundt 2006).

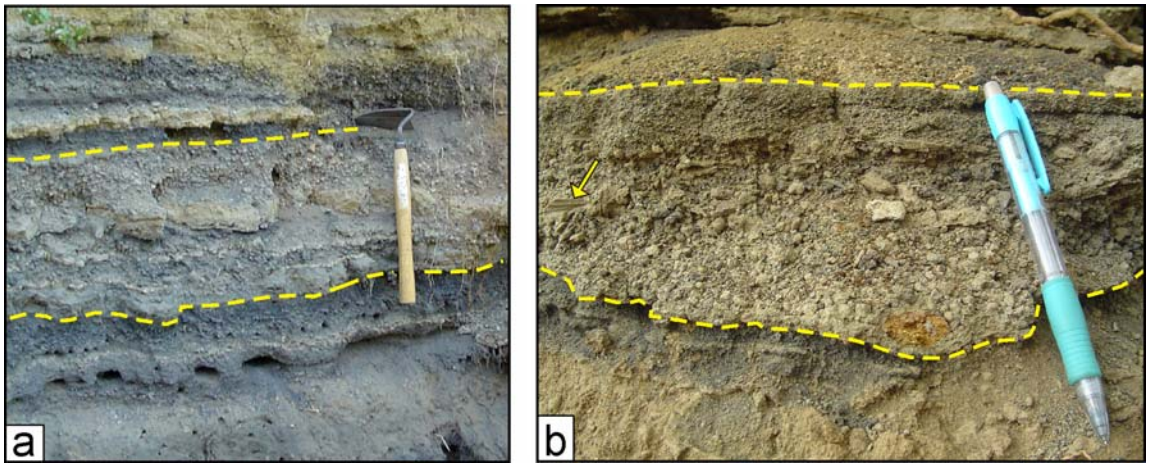

Figure 4.19. Subunit C3 of the Masaya Triple Layer. [**a**] In a proximal outcrop, 10 km WNW from the caldera, where the subunit is constituted by several layers. [**b**] In a medial exposure, 13 km NW the caldera, with its typical appearance of a single relatively poorly-sorted layer with plant molds (like the one indicated by the arrow).

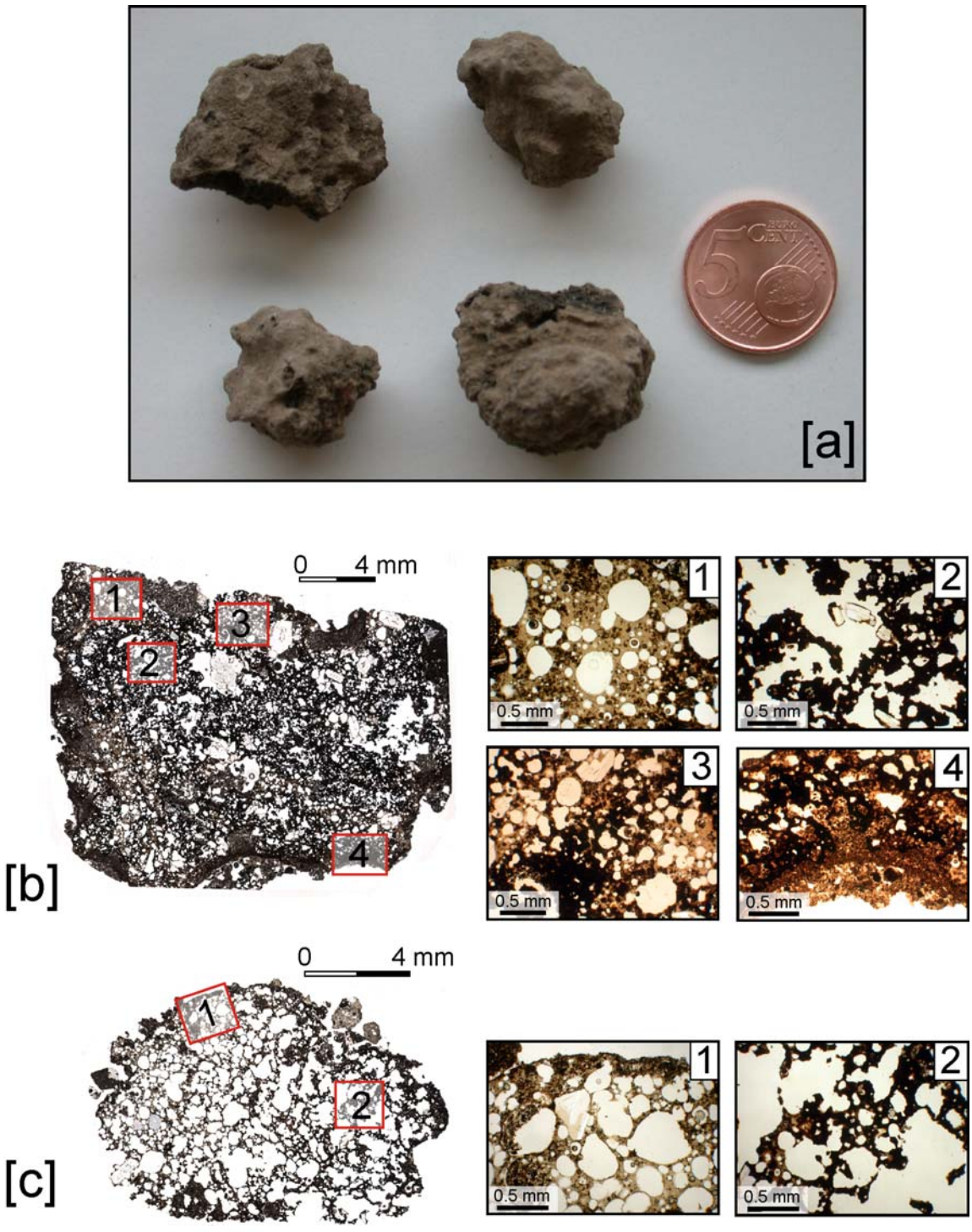

Figure 4.20. Juvenile fragments of the subunit C3. [**a**] Dense and vesicular lapilli, coated with brownish fine ash. [**b**] Dense lapilli made of a mixture between sideromelane and tachylite (1-3), the fine ash rim can be seen in (4). [**c**] vesicular lapilli made up by sideromelane (1) and tachylite (2) with 65 and 55 vol.% of vesicles, respectively.

4.2.2.4 Subunit C4

C4 is a well-sorted, slightly normal-graded, black, vesicular lapilli layer with <3% of lithic fragments (Fig. 4.21). The grain size decreases to the coarse ash fraction at distances greater than 13 km from the caldera. The maximum observed thickness is 12 cm at 7 km to the NW of the Masaya caldera rim (Fig. 4.21a).

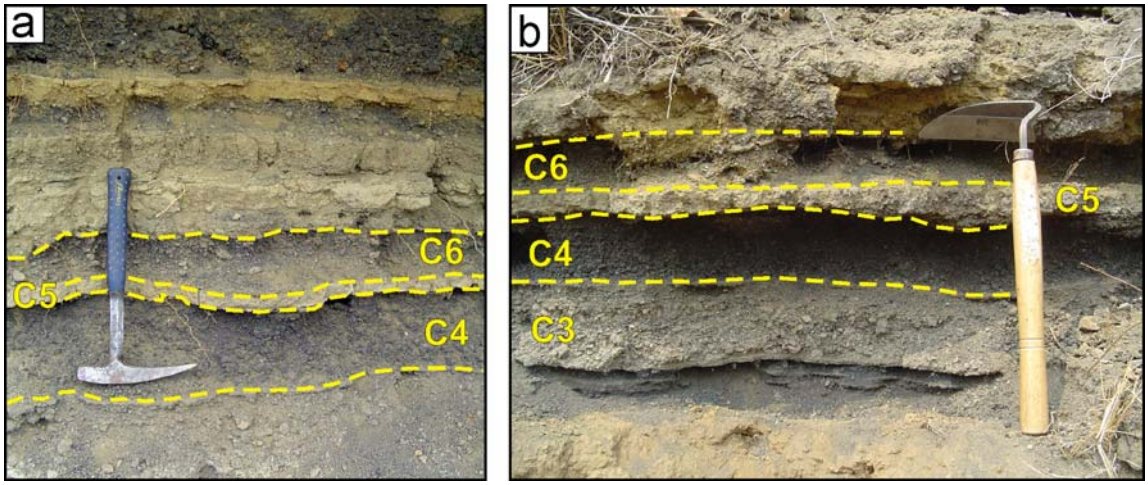

Figure 4.21. Middle portion of the MTL made up by the two well-sorted lapilli/coarse ash layers C4 and C6 separated by a brownish indurated tuff (C5) at exposures [**a**] ~7 km and [**b**] 10 km to the NW of the caldera.

The juvenile fragments are mostly highly vesicular with a density between 0.6-0.8 g/cm^3 but there is a minor fraction of slightly denser ones, up to 1.3 g/cm^3. Both types contain large plagioclase phenocrysts and minor olivine (mostly forming glomeroporphyritic clots with plagioclase), as well as lithic xenoliths of a few milimeters size.

Microscopically, the clasts are a mixture of mostly vesicular tachylite (40-50% vesicularity) and lesser vesicular sideromelane, present only at the rim of the clasts (Fig. 4.22). It also contains plagioclase phenocrysts, scarce olivine and clinopyroxene.

4.2.2.5 Subunit C5

The C5 layer is an indurated grayish to yellowish tuff (Fig. 4.21). At proximal outcrops contains scattered floating small vesicular lapilli, leaf molds and cross-bedding at the base. At other outcrops, farther than 10 km from the caldera, it is a thin 0.5-1 cm thick tuff with desiccation cracks at the top and sometimes with a coarse ash laminae at the bottom. The maximum thickness observed is 4.5 cm at 7.5 km distance from the caldera, but it thins out to 1 cm and then disappears.

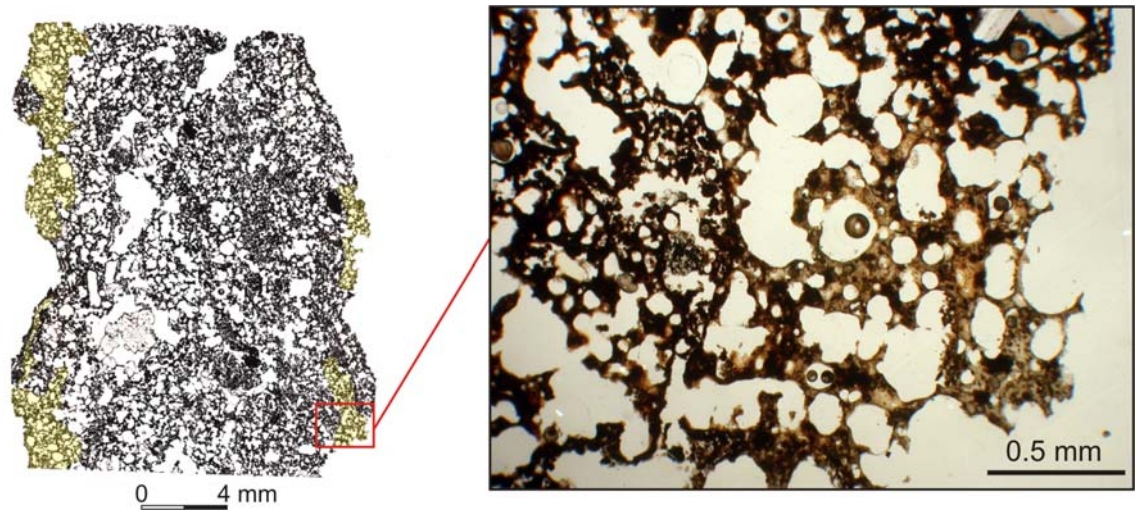

Figure 4.22. Typical clast of the subunit MTL-C4 consisting mostly of vesicular tachylite and a lesser amount of vesicular sideromelane at the rims (areas highlighted in yellow), showing a detail of one of these areas.

4.2.2.6 Subunit C6

It is a well-sorted scoria lapilli layer with <5 vol.% of mostly hydrothermally altered lithic fragments (Fig. 4.21). At medial exposures (>12 km from the caldera rim) the grain size decrease to medium-coarse ash.

The juvenile fragments exhibit a wide range of vesicularites, but the dominant particles are highly vesicular glassy and light ones with a density between 0.6 and 0.9 g/cm^3. There are also moderately vesicular fragments and a minor proportion of denser lapilli (~1.3 g/cm^3). A thin section of the coarse ash fraction within the subunit revealed that the juvenile fragments consist mostly of vesicular to dense tachylite (~10-30% vesicularity) and minor vesicular sideromelane (~40% vesicularity).

4.2.2.7 Subunit C7

It is a thick yellowish tuff with abundant accretionary lapilli (diameters 2-10 mm) and scarce armored lapilli. It reaches a maximum thickness of 40 cm at the most proximal exposures (Fig. 4.23a). It has an internal stratification, with levels containing some floating lapilli or coarse ash fragments, with variable amounts of accretionary lapilli, or hardness (soft to indurated). In some outcrops it looks massive but in others it exhibits some planar bedding (Fig. 4.23b-d).

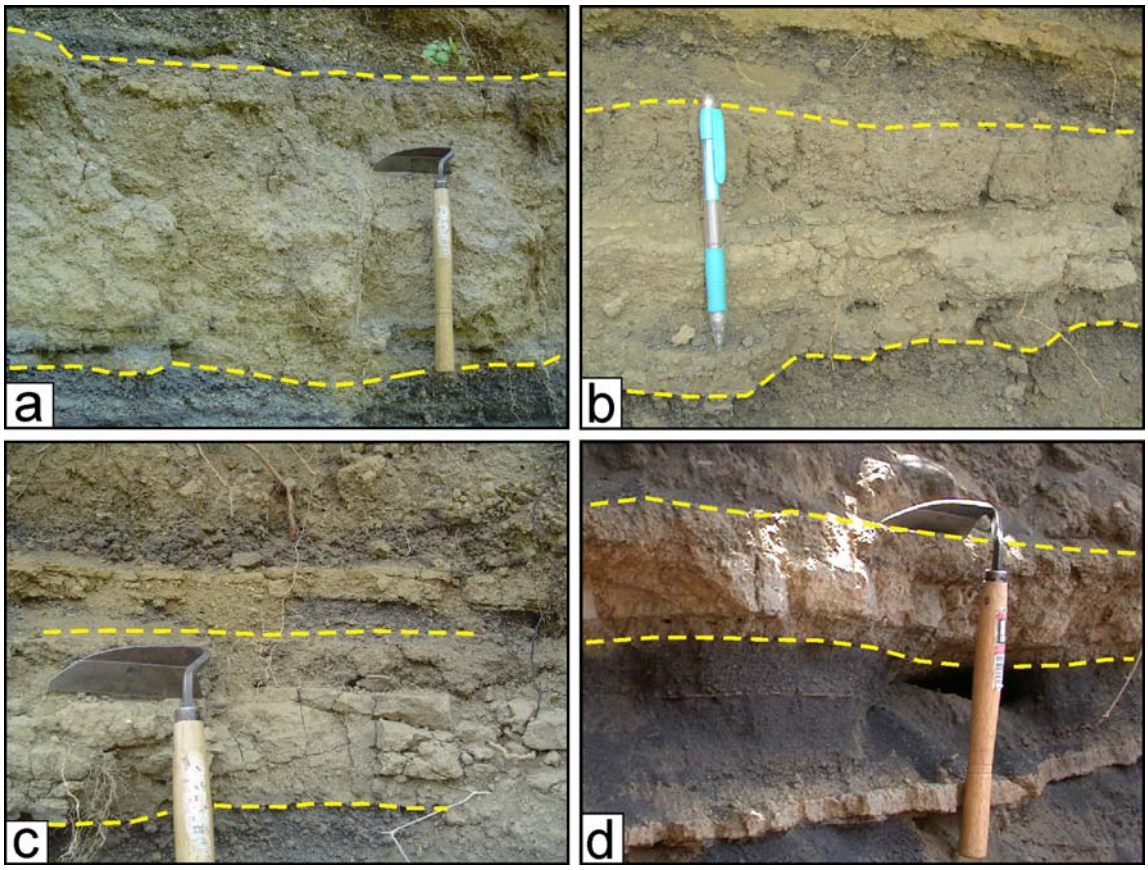

Figure 4.23. Subunit C7 of the Masaya Triple Layer at proximal exposures 10 km and 7 km to the NW of the Masaya caldera where it reaches thickness of 40 cm and 24 cm respectively [**a**, **b**] and at farther locations where it decreases to 16 cm and 14 cm [**c**, **d**].

4.2.2.8 Subunit C8

It is a well-sorted coarse to medium ash layer with a minor amount of fine lapilli (<2 cm in size) and ~2% of hydrothermal altered lithic fragments. In some outcrops it has a consolidated parallel bedded part at the middle of the layer.

The juvenile fine lapilli particles are moderately vesicular, with densities ranging from 0.7 to 1.1 g/cm^3.

In thin section, the ash fraction consists mostly of dense to poorly vesicular (1-12%) tachylitic glass and a minor amount of dense, angular sideromelane fragments with olivine and plagioclase microlites (Fig. 4.24). There are also ash-sized particles consisting of plagioclase, olivine and clinopyroxene crystals and rare basaltic lithic fragments (<<1%).

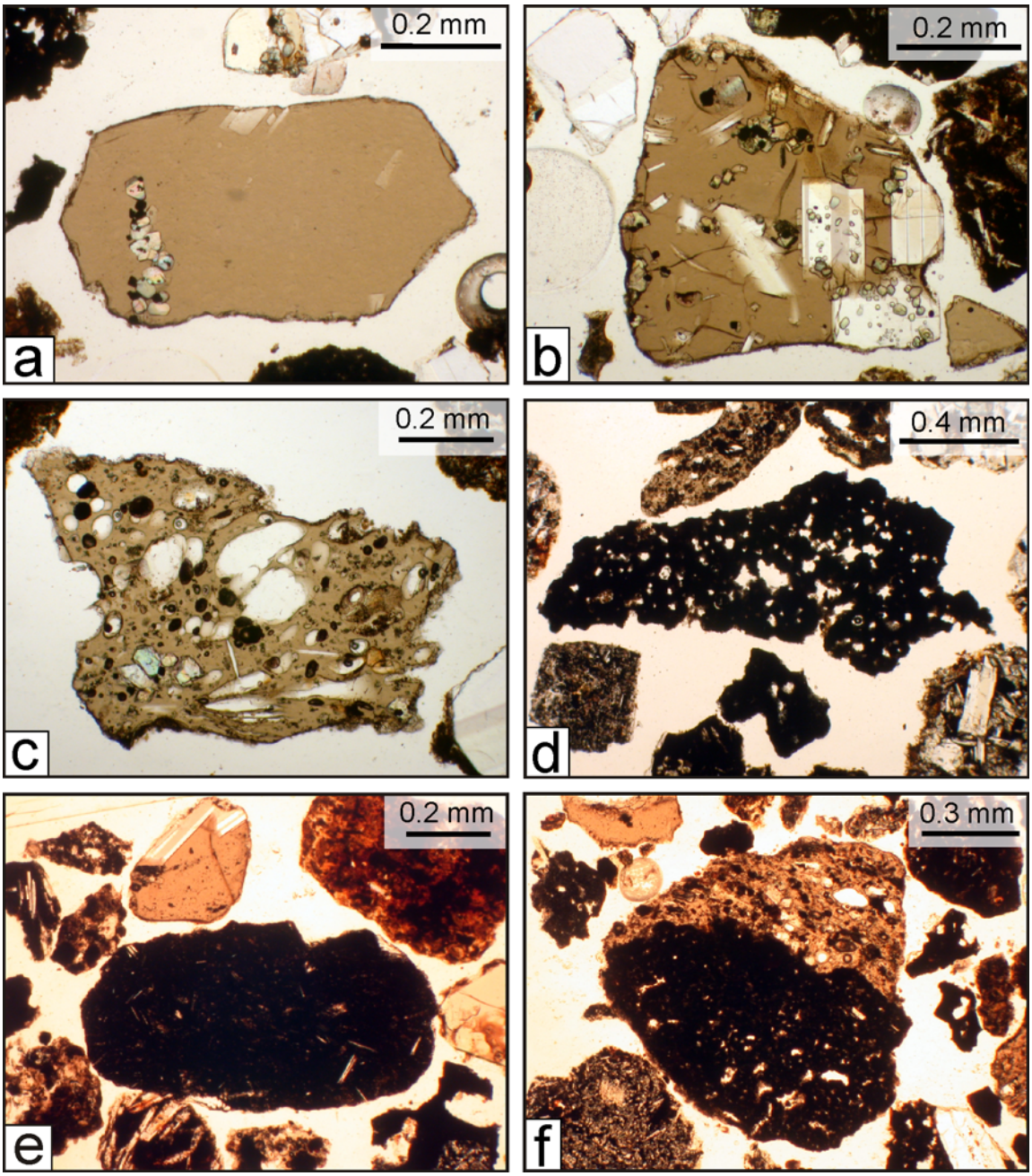

Figure 4.24. Main types of ash particles forming the subunit MTL-C8: [**a**] angular dense sideromelane clast with a few small olivine microlites, [**b**] crystal-rich sideromelane fragment, [**c**] vesicular sideromelane, [**d**] vesicular tachylite, [**e**] dense tachylite with plagioclase microlites and [**f**] mixed clast of vesicular sideromelane and tachylite.

4.2.2.9 Subunit C9

This is an indurated fine tuff with accretionary lapilli and small floating lapilli fragments. At the top there is a thin (0.5 cm) hardened level with desiccation cracks (Fig. 4.25). In some outcrops it has an undulated stratification and variable thickness.

Figure 4.25. Desiccation cracks at the top of the subunit C9. The cover of the camara used as scale has a diameter of 3 cm.

4.2.2.10 Subunit C10

It is a well-sorted deposit of vesicular and dense lapilli with ~5 vol.% of lithic fragments, some of them hydrothermally altered (Fig. 4.26). It is the thickest and coarsest lapilli layer of the MTL, with a maximum observed thickness of 36 cm at 10 km to the NW of the caldera, decreasing to 3 cm near Ciudad Sandino (25 km from the Masaya caldera). At medial exposures it normally shows reverse grading, but at proximal outcrops it is variable (e.g. coarsest grain in the middle of the bed or two reverse graded layers like at W68, Fig. 4.16). The maximum observed size for the juvenile fragments is 6.5 cm at ~8 km to the NW of the Masaya caldera.

The lapilli fragments consist mostly of round denser lapilli (1.3-1.7 g/cm^3), with scarce plagioclase phenocrysts and xenoliths, but there is also a small fraction of moderately vesicular lapilli with a density of 0.8-0.9 g/cm^3. Microscopically they consist of tachylite with some vesicular sideromelane portions having large melt inclusion-bearing plagioclase and euhedral altered olivine phenocrysts.

The lithic fragments are mostly of basaltic lavas, especially a light grayish type with plagioclase phenocrysts.

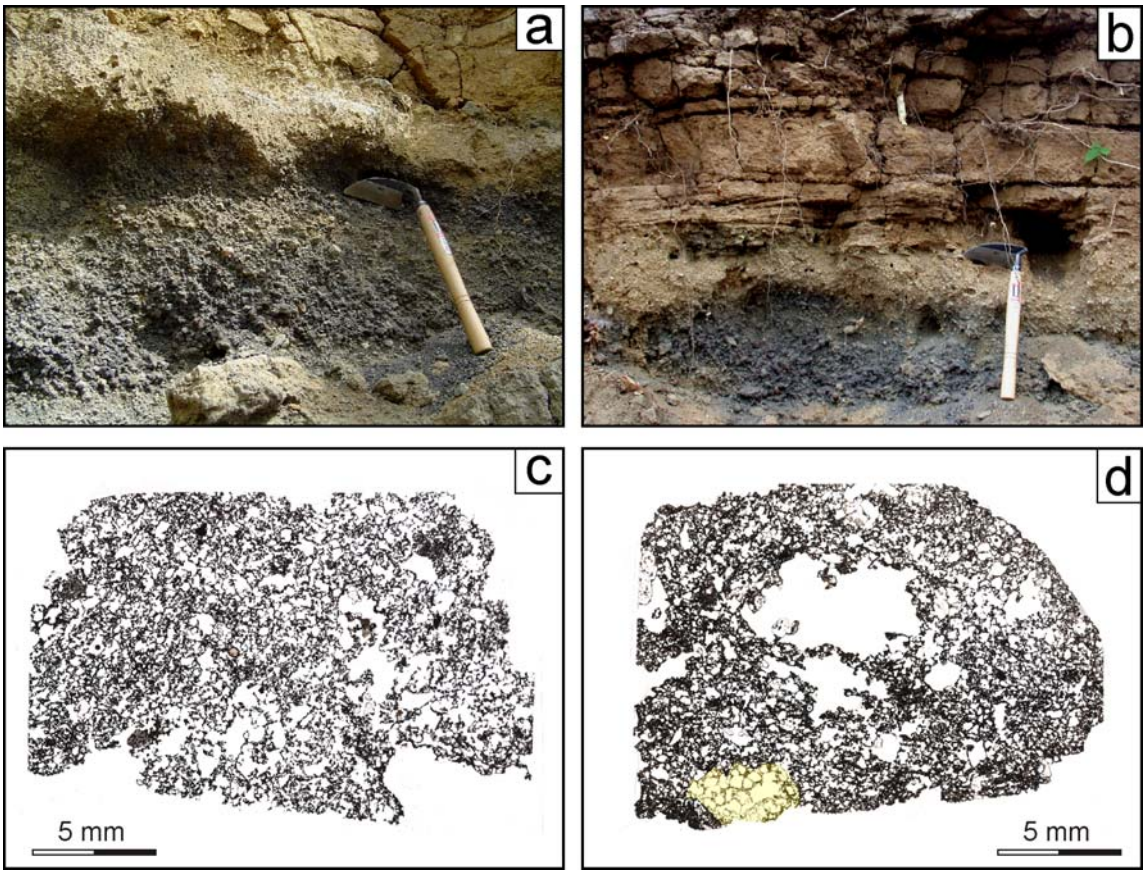

Figure 4.26. The thickest and coarsest lapilli layer of the Masaya Triple Layer, the subunit C10, overlain by a yellowish deposit with lapilli fragments. [**a**] at 9.5 km NW of the caldera and [**b**] at 11.5 km. [**c**] Thin section of a juvenile clast made up completely by vesicular tachylite. [**d**] Other type of clast, consisting mostly of tachylite but with domains of vesicular sideromelane (highlighted in yellow) and transitional zones mixing both glass types.

4.2.3 Lateral facies changes

Figure 4.27 shows the lateral stratigraphic changes of the Masaya Triple Layer to the NW with increasing distance from the Masaya caldera.

No outcrops could be found within the first 5 km of distance from the Masaya caldera rim. The most proximal outcrops are those located along the road from San Antonio Sur to Las Nubes at 7 to 7.5 km from the caldera and also at exposures near Las Nubes (W169 and W191 in Fig. 4.15), where the MTL reaches its maximum observed thickness (Fig. 4.28a). At these proximal exposures the stratigraphy is more complex and some of the subunits are composed of several beds, e.g. subunit C1 is made up by at least three beds and subunit C3 also consist of 3 to 5 beds at 7-10 km from the caldera (Figs. 4.27 and 4.28a). Also some tuffs like C5 and C9 show some cross bedding at the bottom and the thick tuff of subunit C7 consists of several beds with different contents of lapilli-size clasts, accretionary lapilli and with parallel bedding (Figs. 4.16, 4.27).

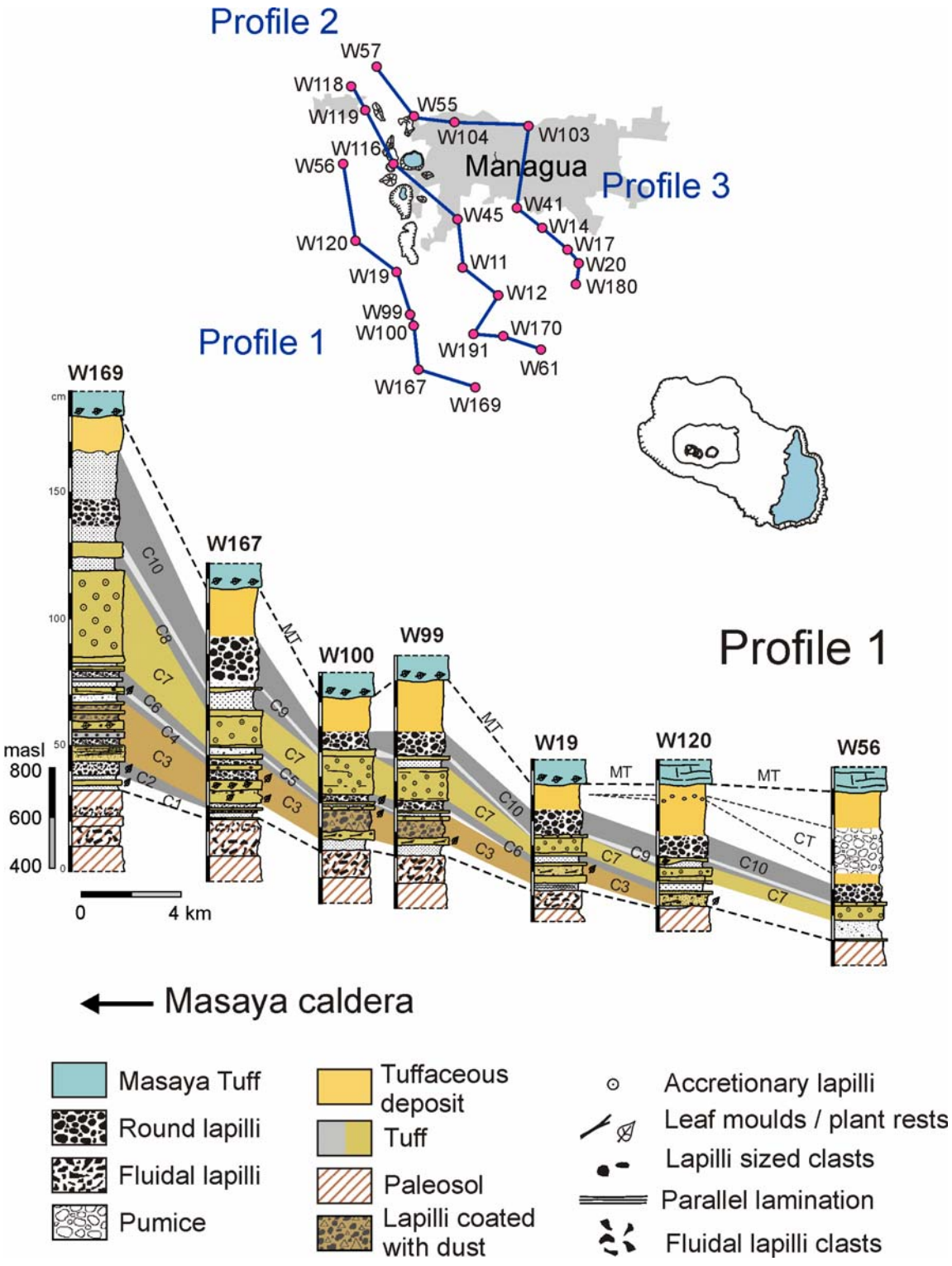

Figure 4.27: Stratigraphic variations of the Masaya Triple Layer with increasing distance from the Masaya caldera rim, shown in three profiles. At distal exposures the Chiltepe Tephra (CT) appears between the MTL and the Masaya Tuff (MT) and thickens in direction to Chiltepe Peninsula.

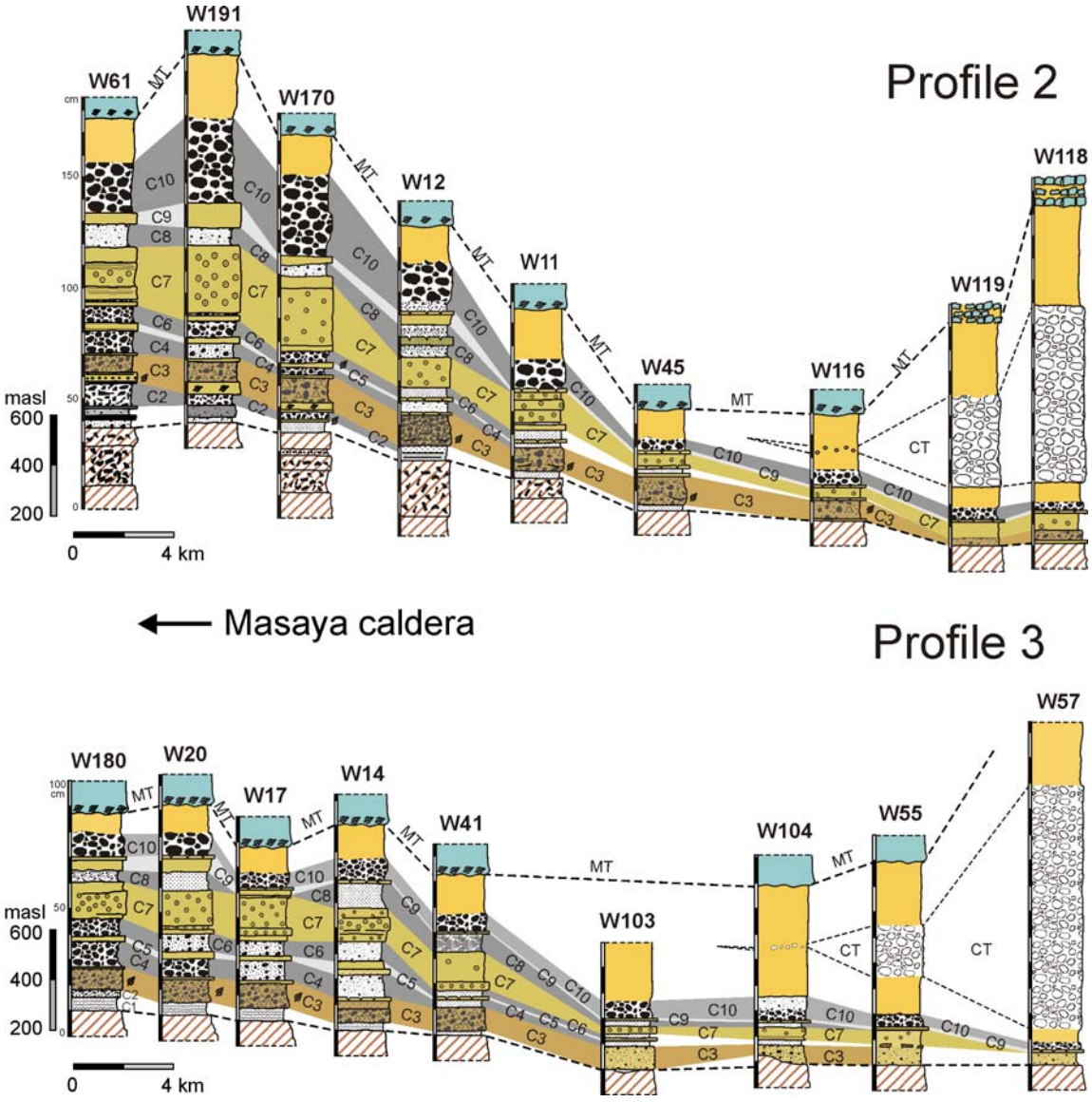

Continuation...

At exposures between 15-20 km from the caldera, the stratigraphy gets simpler. C1 and C2 can no longer be distinguished, both appearing as a ~1 cm fine black ash layer with fluidal ash particles. The well-sorted subunits C4, C6 and C8 decrease in thickness with distance and, near Managua, C6 disappears or merges with C4 (Fig. 4.28d). The tuff layers frequently contain plants remains and molds at the proximal areas but not farther away.

The different subunits of the MTL also thin out towards the north and west of the caldera, away from the general dispersion axis. At the westernmost outcrops the MTL has a different appearance and looks like a tuff-dominated sequence (Fig. 4.28e), which together with the degree of alteration/weathering of the rocks (they are located at the side of Masaya's degassing plume direction) make the correlation difficult.

At distances beyond 25 km from the caldera, the only recognizable subunits are C3, due to the plant molds content, a yellowish fine deposit with small clasts similar to C7, a thin hard tuff which can be correlated with C9 and the lapilli subunit C10 (Fig. 4.28f). Some of the tuff layers do not extend to great distances so that the stratigraphic succession gets simpler away from the vent, but some others like C9 are preserved due to their hardness, permitting the reconstruction of the succession. In some distal outcrops to the north, near the Managua International Airport, the only recognizable characteristic of the MTL is a 1 cm thick indurated tuff.

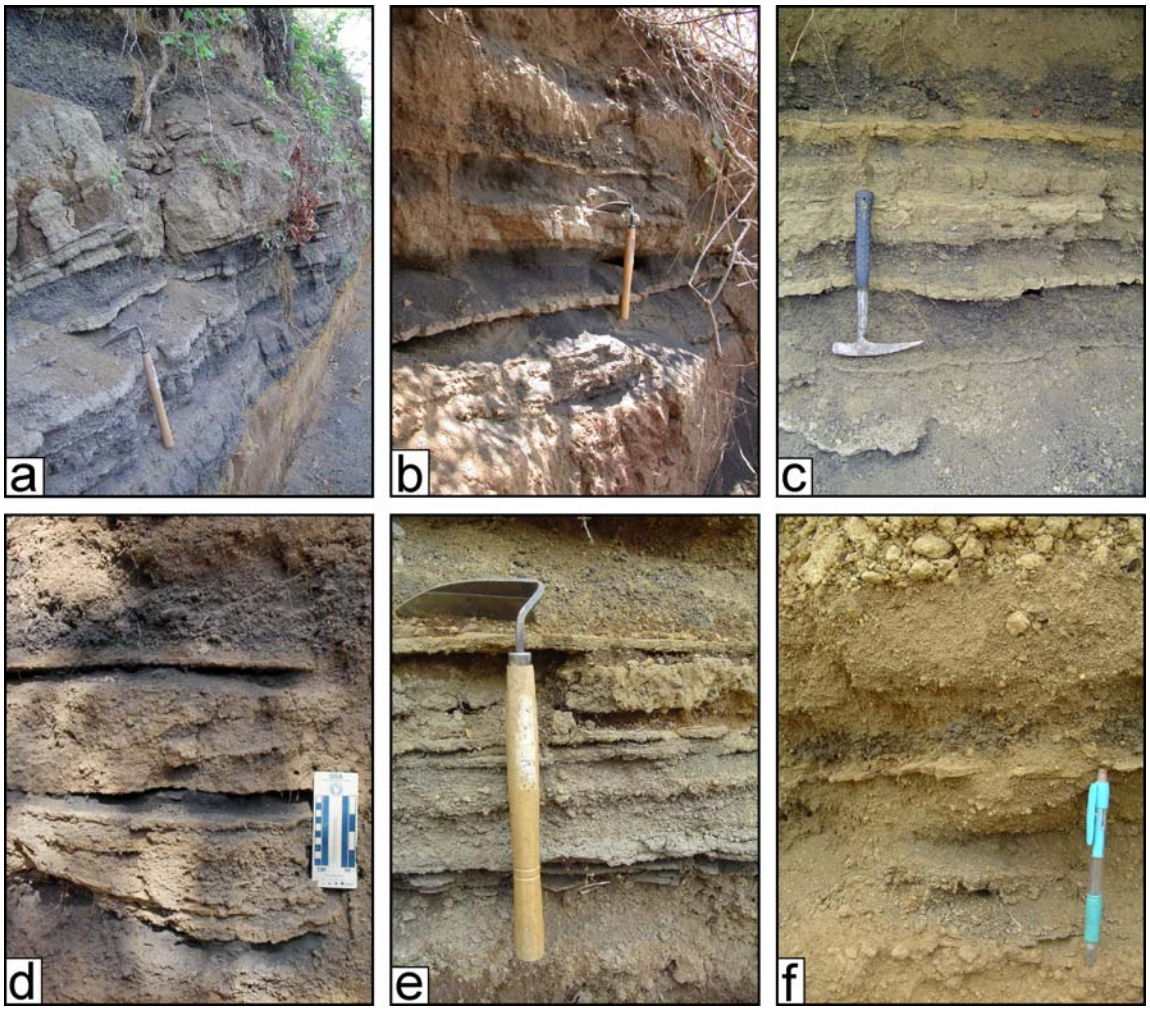

Figure 4.28: Photographs showing proximal to distal variations of the MTL, at different distances from the Masaya caldera. [**a**] at 9.5 km to the NW, where the MTL reaches its maximum thickness and the stratigraphy is more complex, showing some of the subunits composed of several beds. [**b**] Outcrop W14, 11.5 km from the caldera, with the complete stratigraphy as it has been described before. [**c**] W67 at 7.5 km from the caldera rim. [**d**] W45 at 15 km, the subunits C1 and C2 appear as a single few cm thick layer of fine black ash. [**e**] Outcrop W19 at the western side of Managua, where the deposit is alterated and looks dominated by tuffs because they are more resistent to the erosion. [**f**] Distal exposure near Ciudad Sandino, with a very simplified stratigraphy composed by subunits C3, C7, C9 and C10.

4.3 Correlation between both units

The different internal architectures of La Concepción Tephra and the Masaya Triple Layer do not allow to easily correlate individual layers, particularly because there are no linking outcrops at the SW and NE of the caldera between the distribution areas. That was the reason why Pérez and Freundt (2006) treated them as different deposits, although they occupy the same stratigraphic position between the San Antonio Tephra and the Masaya Tuff. Since the time of writing that paper, chemical analyses have been completed in the hope to use compositional zonation as a tool to facilitate correlations. However, bulk rock, glass and mineral compositions of both tephras overlap completely within narrow ranges of both, major and trace element concentrations. Although this compositional identity supports the interpretation that the two tephras are actually two facies of a deposit from the same eruption, the compositional variations found in each single layer are as wide as in any other layer and the whole deposit. In other words, there is no compositional zonation that could be used for correlation. Then, the shape and texture of juvenile particles remain as the best criterion to attempt a correlation between the two facies.

4.3.1 Correlation of subunits B5 and C2

These two subunits are prominent in their respective facies because of their high content of highly vesicular, fluidally-textured elongated achneliths. Masaya volcano has repeatedly produced such scoria particles in eruptions ranging from the ca. 60 ka Fontana Tephra (Wehrmann et al. 2006) to the recent products of the active Santiago crater. Such lapilli also occur in several layers of the LCT-MTL sequences. However in the LCT, layer B5 is outstanding because it is the thickest fallout deposit and almost exclusively composed of achneliths lapilli. Layer C2 in the MTL is only a thin fallout deposit but conspicuous because it also is composed almost exclusively of such juvenile particles. Therefore the correlation between LCT-B5 and MTL-C2 is used in this work as a starting point to correlate the other layers.

4.3.2 Proposed correlation

The new subunits introduced (I to X) group LCT and MTL layers according to their lithologic and petrographic properties in the most proximal (and therefore most complete) outcrops, starting with subunit II formed by LCT-B5 and MTL-C2. The combined stratigraphy agrees with the overall upward increase in denser juvenile particles and hydrothermally altered lithics observed in both facies. Each new subunit has been checked for consistency in the resulting areal thickness and grain-size distributions. As a result, the following is proposed as the most plausible correlation scheme between LCT and MTL (Table 4.1, Fig. 4.29).

The well-sorted lapilli fallout layers of both facies, above LCT-B5 and MTL-C2, are correlated to yield subunits IV (B9, C4), VI (B11, C6), VIII (B14, C8) and X (B16, C10). Fallout of the subunit VIII shows locally variable faint parallel or cross-bedding; this may indicate that fallout emplacement was affected either by contemporaneous weak surges or by near-surface wind. Subunit I consists of layers B1 to B4 which thin to the NW and merge to layer C1, which contains a horizon rich in plant material resembling B2. In similar fashion, layers B6 to B8 (Fig. 4.8) combine to layer C3 (Fig. 4.19) in the NW and form subunit III.

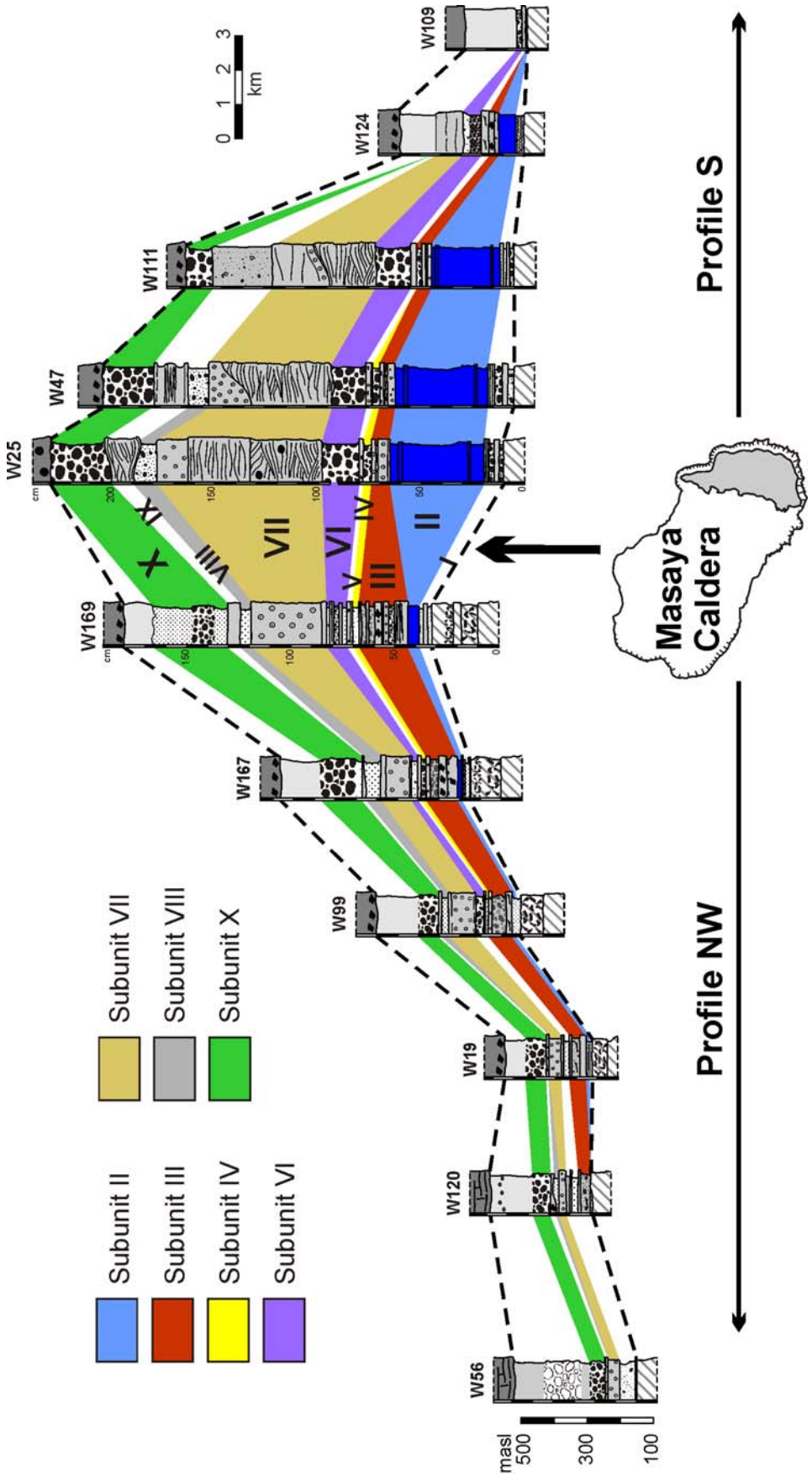

Figure 4.29. Proposed correlation between La Concepción Tephra and the Masaya Triple Layer based on the marker beds B5 and C2 (highlighted in blue). As indicated, the left profile -MTL- is towards the NW of the caldera and the right one –LCT- is to the S. The thick black arrow points out the position of the caldera with respect to the profiles. The orange line at the bottom marks the boundary with the soil and the upper greenish one the upper boundary with the Masaya Tuff

Subunit V combines the tuff beds B10 and C5. Subunit VII is a surge deposit (B12) capped by a tuff rich in accretionary lapilli (B13) which form a single thick accretionary-lapilli-rich tuff (C7) in the NW, where the surge became too weak to form cross-bedding. Subunit IX (B15, C9) has characteristics of an ash-rich surge that expanded more strongly to the NW and was weaker to the S but the deposit is everywhere capped by an indurated thin fine-ash layer, the final wet fallout from the surge cloud (Fig. 4.25).

Table 4.1 New correlated subunits between the LCT and MTL

New proposal	LCT	MTL
Subunit I	B1, B2, B3, B4	C1
Subunit II	B5	C2
Subunit III	B6, B7, B8	C3
Subunit IV	B9	C4
Subunit V	B10	C5
Subunit VI	B11	C6
Subunit VII	B12, B13	C7
Subunit VIII	B14	C8
Subunit IX	B15	C9
Subunit X	B16	C10

4.4 Volume

Preliminary data of the volume, distribution, erupted mass, magnitude and volcanic explosivity index (VEI) treating the LCT and MTL separately were given by Perez and Freundt (2006). Maximum column heights and mass discharge rates of 18-26 km and 3-7 x 10^7 kg/s were calculated for the LCT, respectively, whereas the MTL yielded 22-29 km maximum eruption column height and mass discharge rates between 6 x 10^7-1.5 x 10^8 kg/s at wind speeds of ~20 m/s (Kutterolf et al. in press). Here the emphasis is on the respective values for individual subunits, using distribution data based on the above correlation, in order to understand the temporal evolution of the eruption.

4.4.1 Thickness distribution

The isopach maps for the correlated fallout subunits I, III, IV, VI, and X all show a dispersion axis towards the NW, in direction to Managua city (Fig. 4.30). Accordingly, decay rates, elongation and axis orientation vary between subunits, indicating changing wind conditions. One exception is the concentric circular pattern exhibit by the thickness distribution of subunit II. This type of pattern is an indication that the eruption column was not affected by wind (Carey and Sparks 1986).

It is emphasized that the lack of outcrops to the SW and NE of the caldera does not allow to constrain isopach patterns more precisely. Moreover, the paucity of proximal outcrops also inhibits a precise determination of the vent position, although all isopachs maps agree with a vent inside the Masaya caldera, possibly beneath the modern Masaya intra-caldera cone.

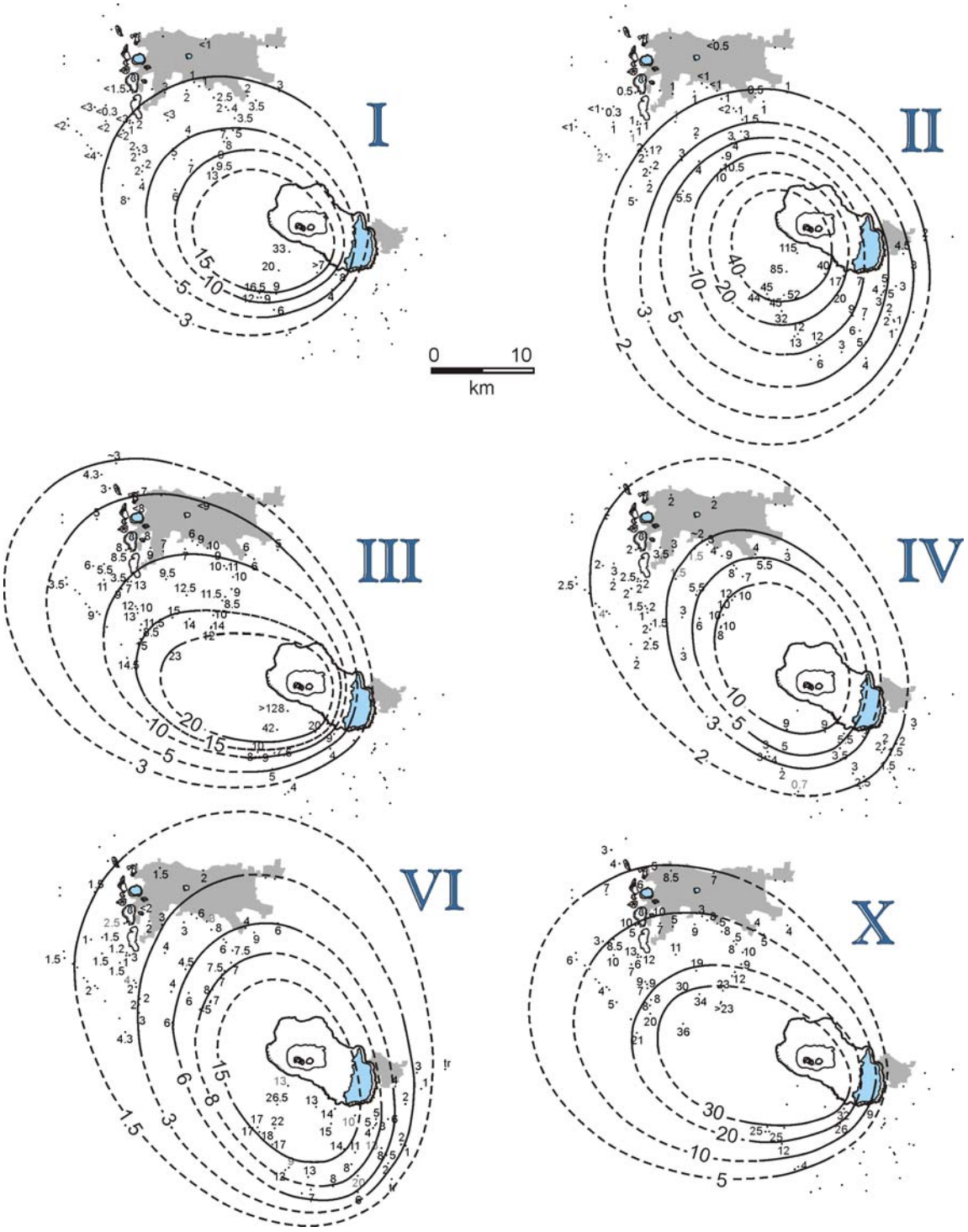

Figure 4.30: Isopachs maps for the main fall subunits I, II, III, IV, VI and X of the correlated LCT-MTL. Isopach contours are in cm and the discontinuous segments represent areas with no data. The cities of Managua and Masaya are represented in gray.

The tuff subunits have a more irregular distribution, as shown by the isopach maps for the tuffs V, VII and IX of Fig. 4.31. When comparing the thickness of the tuffs with the topography, it is clear that the pyroclastic surges did not deposit only in low flat areas, but actually produced significant deposits at the lee side of the hills of Las Sierras volcano, west of the Masaya caldera.
Thickness data for subunits VIII to X are particular scarce closer to, and to the S of the caldera, due to strong post-emplacement erosion. That is the reason why the respective isopach maps remain incomplete in these areas.

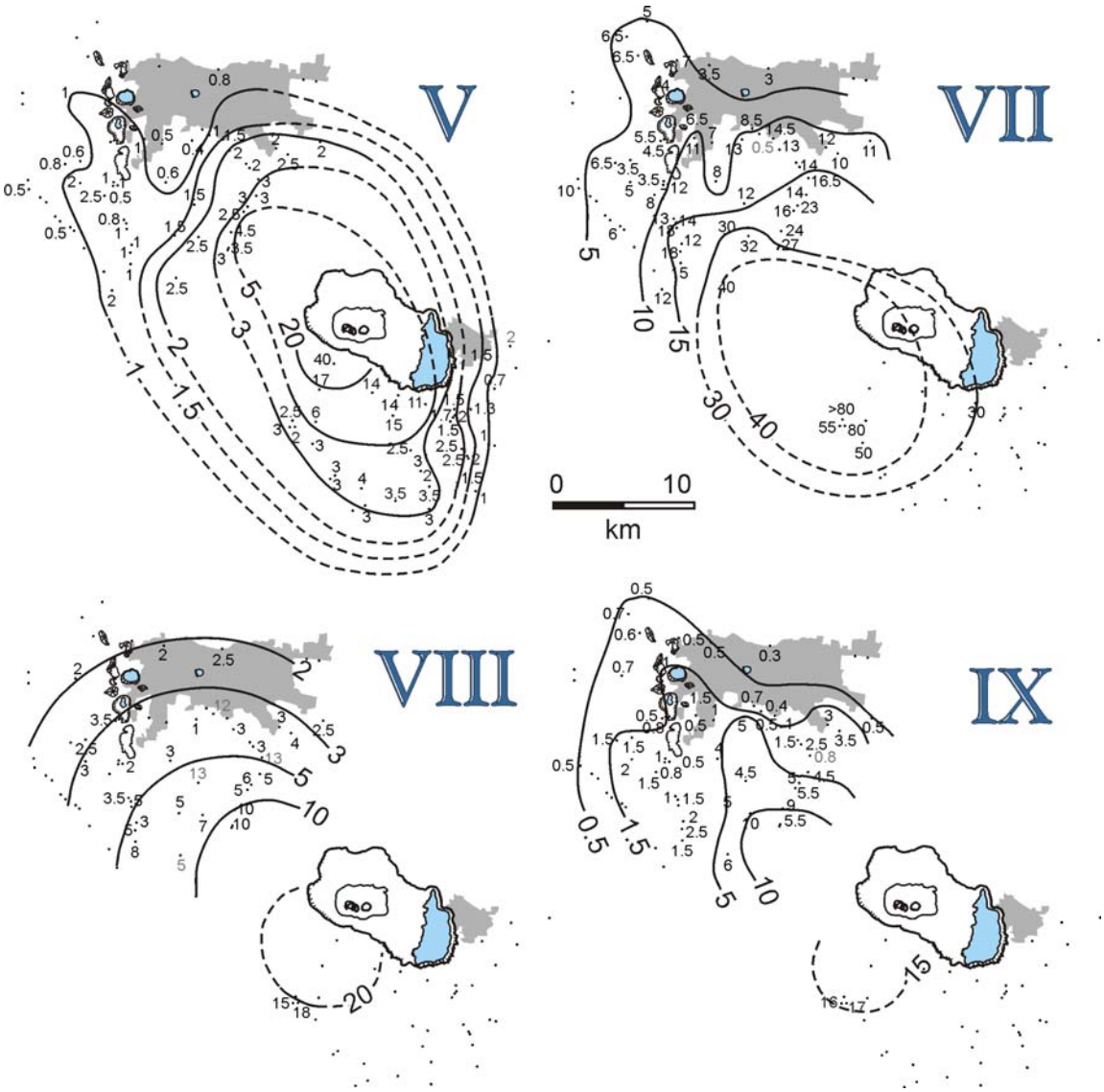

Figure 4.31: Isopachs maps for the tuff subunits V, VII and IX and the fall VIII of the correlated LCT-MTL. Isopach contours are in cm and the discontinuous segments represent areas where there was no data available. The cities of Managua and Masaya are represented in gray.

4.4.2 Volume

Volumes for both bulk-deposits separately were calculated by Pérez and Freundt (2006) as 0.2 km^3 for LCT and 0.7 km^3 for the MTL, respectively. The individual volumes of the LCT subunits, calculated with the method of Pyle (1989), range between 0.004 and 0.128 km^3. This upper limit corresponds to the main subunit B5. The volume of the upper subunits B12-B16 could not be estimated due to the lack of exposures. The single subunits of MTL yield volumes between 0.017 and 0.13 km^3. The most voluminous events of the Masaya Triple Layer are the thick tuff C7 and the uppermost lapilli layer C10 with bulk volumes >0.1 km^3 (Table 4.2).

The bulk volume for each subunit from I to X was calculated based on the isopach maps shown in Figs. 4.30 and 4.31 and applying the method of Pyle (1989). The new bulk volumes range between 0.02 and 0.22 km^3 (Table 4.2) and are equivalent to erupted masses between 10^{10} kg and 10^{11} kg for the single subunits. The biggest events were the fall subunits II, III and X.

These new subunit volumes add up to a whole deposit volume for the LCT-MTL eruption of 0.86 km^3. This is almost the same as the sum of the separate LCT and MTL deposit volumes of 0.88 km^3, determined by Pérez and Freundt (2006).

Table 4.2. Comparison of the volume calculated of the single subunits of the LCT and MTL with the new volumes of the correlated subunits I-X

Proposed complete stratigraphy			La Concepción Tephra		Masaya Triple Layer	
Subunit	Volume (km^3)		Subunit	Bulk volume (km^3)	Subunit	Bulk volume (km^3)
	Bulk	DRE				
I	0.068	0.028	B1	0.010	C1	0.030
			B2	0.007		
			B3	0.010		
			B4	0.012		
II	0.115	0.038	B5	0.128	C2	0.017
III	0.125	0.102	B6	0.019	C3	0.092
			B7	0.004		
			B8	0.016		
IV	0.052	0.025	B9	0.014	C4	0.040
V	0.037	0.015	B10	0.027	C5	0.019
VI	0.099	0.038	B11	0.074	C6	0.048
VII	0.018	0.007	B12-13	?	C7	0.131
VIII	0.076	0.030	B14	?	C8	0.040
IX	0.046	0.018	B15	?	C9	0.022
X	0.219	0.115	B16	?	C10	0.119
Total	**0.856**	**0.416**	**Total**	**0.322**	**Total**	**0.560**

4.4.3 Distal tephra and total volume of the eruption

Two ash layers found in cores drilled offshore Nicaragua during the Meteor cruise M54/2 and Sonne SO173/3 were correlated with the LCT-MTL. Both cores are located at the continental margin of the Middle American Trench. Examples of the chemical correlation based on the glass composition are shown in Fig. 4.33. Other criteria, e.g. stratigraphic position of other dated and correlated ash layers, were also used.

The core M54/2-2 was collected at the slope ~150 km away from the Pacific shore of Nicaragua where the ash layer has a thickness of 6 cm. The core SO173/3-18, is also located at the slope, <50 km from the other one. There the correlated ash layer is 4 cm thick.

Considering these distal deposits, an isopach map for the whole LCT-MTL deposit was constructed (Fig. 4.33). The obtained minimum volume of 0.86 km^3 of the bulk LCT-MTL deposit on land was complemented with the new calculations including the data of marine layers. Using the method of Fierstein and Nathenson (1992), the LCT-MTL eruption yielded a total volume of 3.6 km^3. (1.2 km^3 DRE).

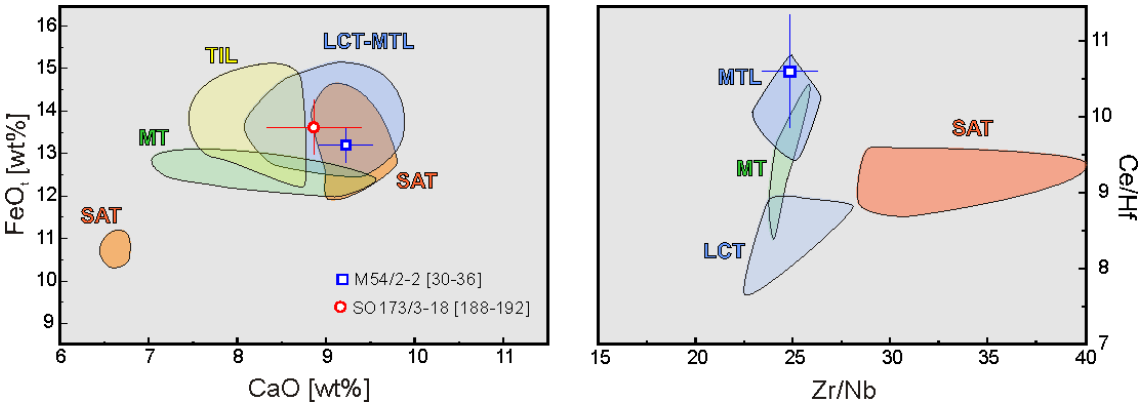

Figure 4.32: Examples of the chemical correlation between the glass of the Masaya Tephra (SAT, LCT-MTL, MT-TIL) and the two marine ash layers found at the continental slope offshore Nicaragua. Symbols represent the mean value from all measurements of a sample, with the corresponding standard deviation.

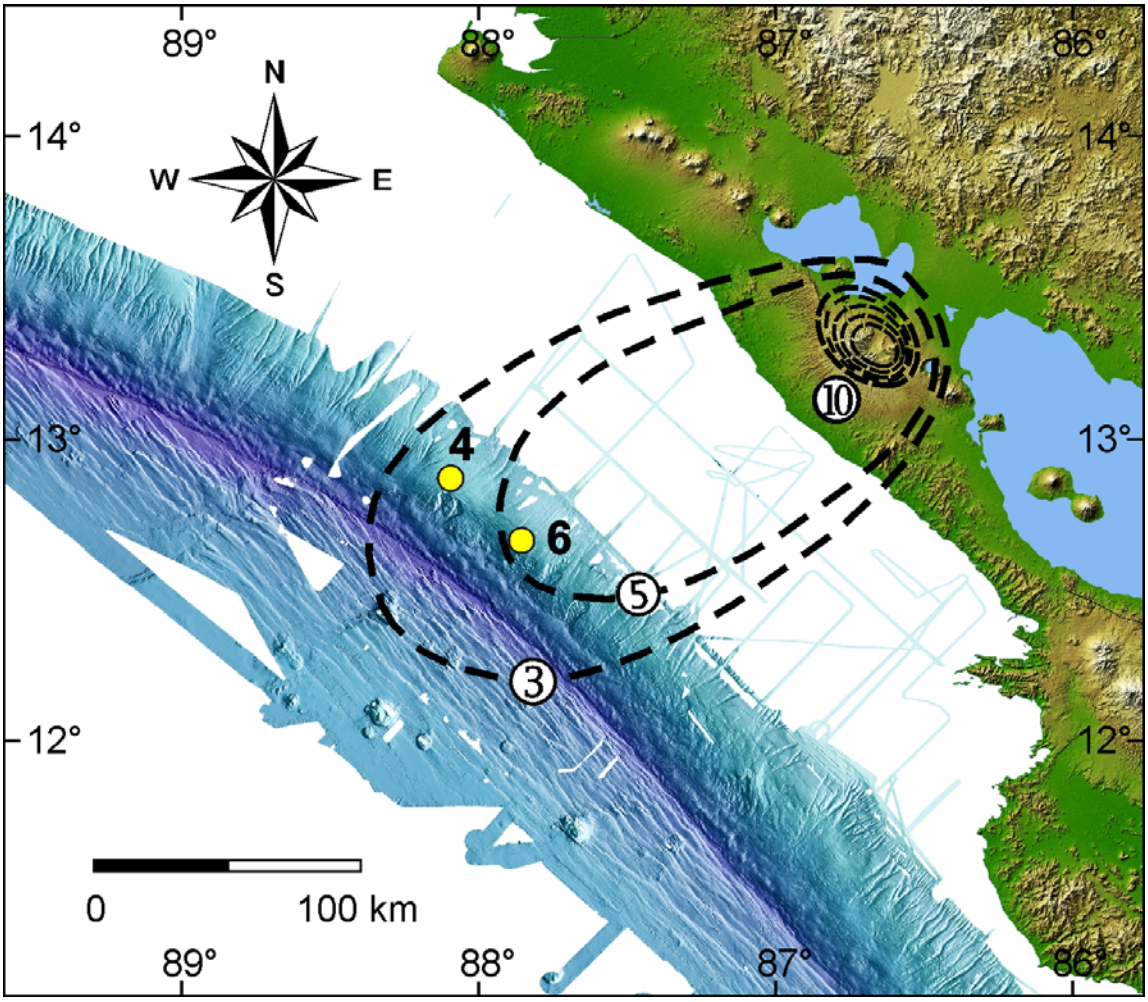

Figure 4.33: Isopachs in centimeters for La Concepción Tephra-Masaya Triple Layer whole deposit. The dots give the location of gravity cores at the Pacific Ocean off Nicaragua indicating the thickness of the layer.

4.5 Eruption parameters

4.5.1 Eruption column height and wind speed

The isopleth maps necessary for the comparison with established numeric models for eruption columns were constructed for the maximum juvenile (MP) and lithic fragments (ML) of the fall subunits II, III, IV, VI, VIII and X of the correlated LCT and MTL (Fig. 4.34).

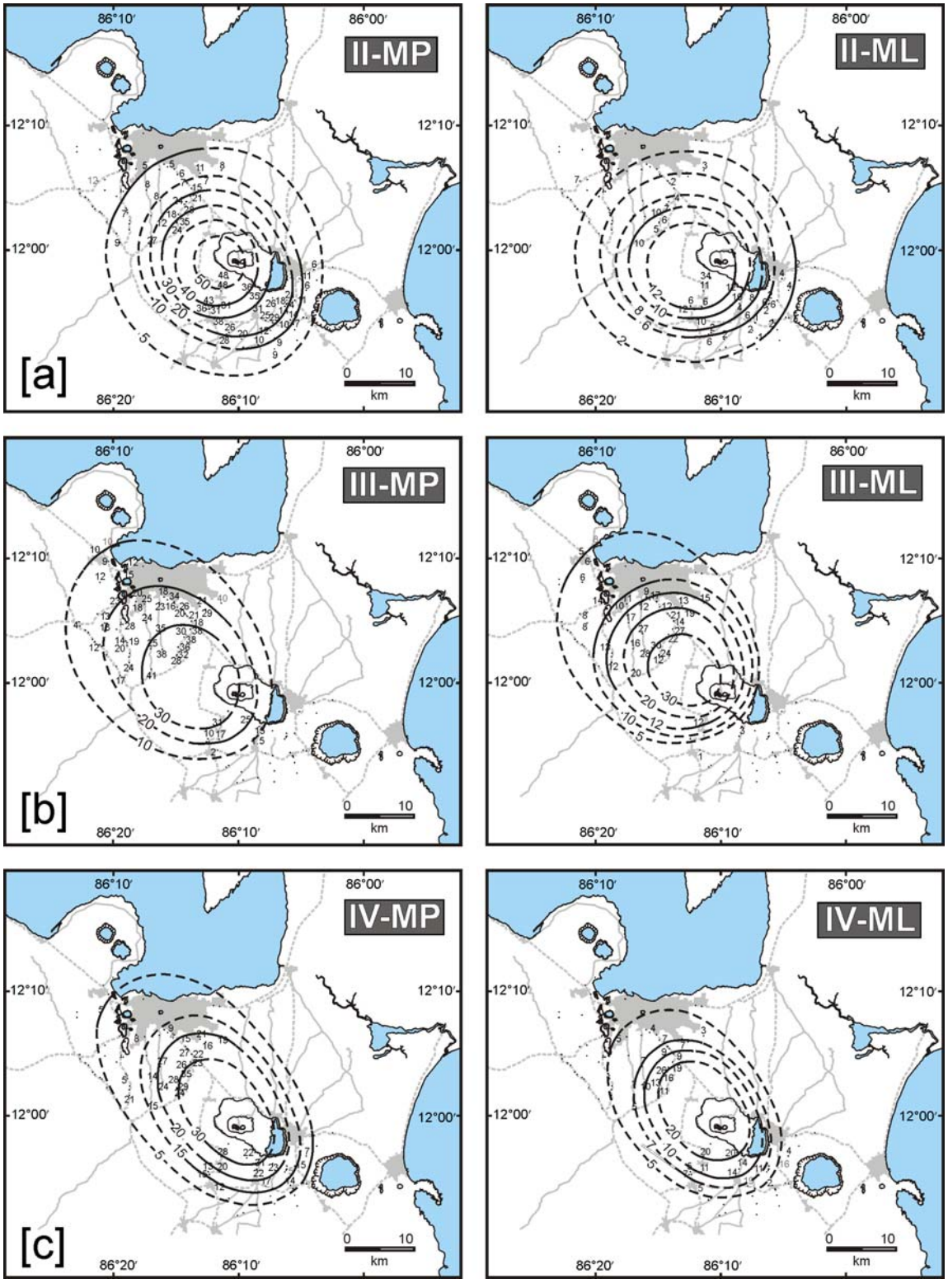
II-MP
II-ML
III-MP
III-ML
IV-MP
IV-ML
[a]
[b]
[c]
86°10′
86°00′
12°10′
12°00′
86°20′
0 10
km

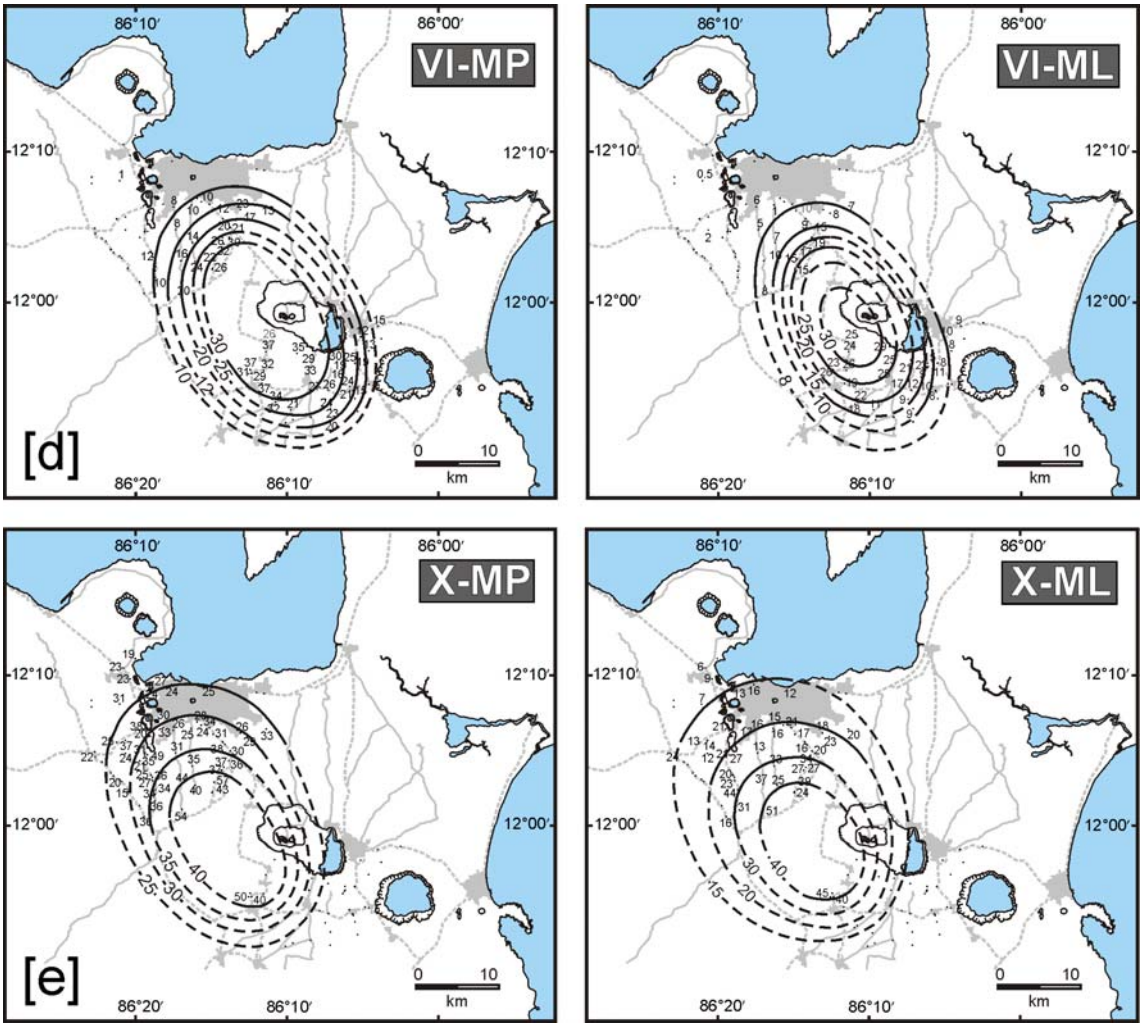

Figure 4.34: Isopleth contours in millimeters of maximum juvenile (MP) and maximum lithic fragment (ML) for the main fallout subunits of the correlated La Concepción Tephra and the Masaya Triple Layer. [**a**] Subunit II, [**b**] Subunit III, [**c**] Subunit IV, [**d**] Subunit VI, and [**e**] Subunit X.

Using the diagrams of Carey and Sparks (1986) shown in Figs. 4.35 and 4.36, the height of the columns of the eruptions forming the LCT-MTL fallout subunits were estimated in 15 to 28 km. The subunit II had an average column height of ~22 km, III had ~24 km, IV ~21 km, VI ~22 km and subunit X ~24 km (Fig. 4.35). The wind speeds show changes during the course of the eruption, the subunit II had very weak winds of <2 m/s, as indicated also by the concentric MP and ML isopleths, then the following subunits III, IV and VI show mostly around 10 m/s or slightly higher and the topmost subunit X had higher wind speeds of ~20 m/s. This may reflect wind strengths varying with time but, considering the differences in column height, it may also indicate wind strength changing with height in the atmosphere.

The larger a clast and the closer to vent it was deposited, the lower the height to which it was carried in the eruption column. This is illustrated, for example, by the data for subunit X in Fig. 4.35. Such data suggest that most material deposited within 5-10 km from vent did not reach stratospheric heights but may have been affected by tropospheric wind of different direction. This may explain why the isopach pattern of subunit III has a westward direction proximally before turning toward NW, or why subunit VI proximally extends to the S while the main fan is directed to the NW. On the other hand, distal isopachs of the surge deposits, representing distal fallout from drifting surge clouds, extend to the NW, suggesting that tropospheric and stratospheric wind directions were similar. According to present-day wind data (cf. Kutterolf et al. in press), such conditions prevail during July and August in the rainy season of Nicaragua.

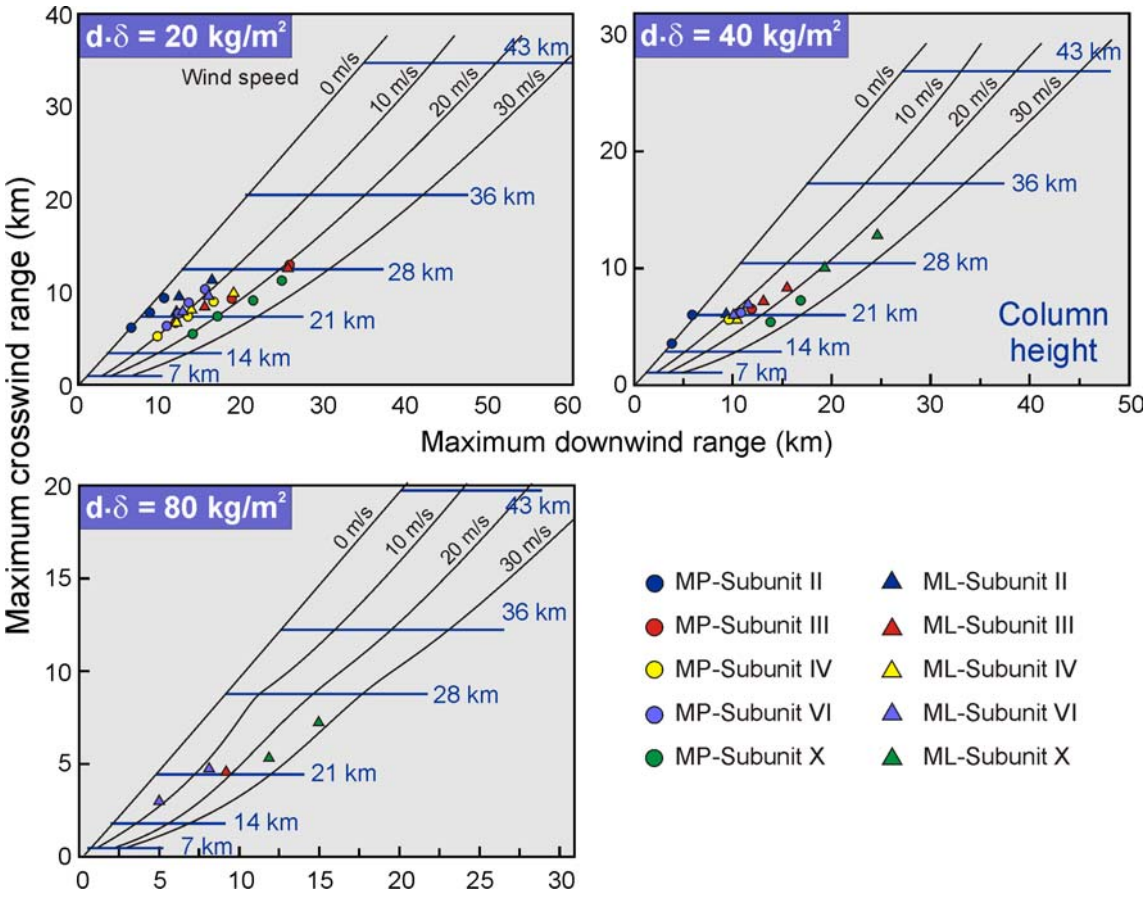

Figure 4.35: Crosswind range versus maximum downwind range for the MP and ML isopleths for subunits II, III, IV, VI and X of the LCT-MTL. The fields are those from the Carey and Sparks (1986) models. Most of the values locate between 20 and 24 km in average and the different subunits show different winds speeds.

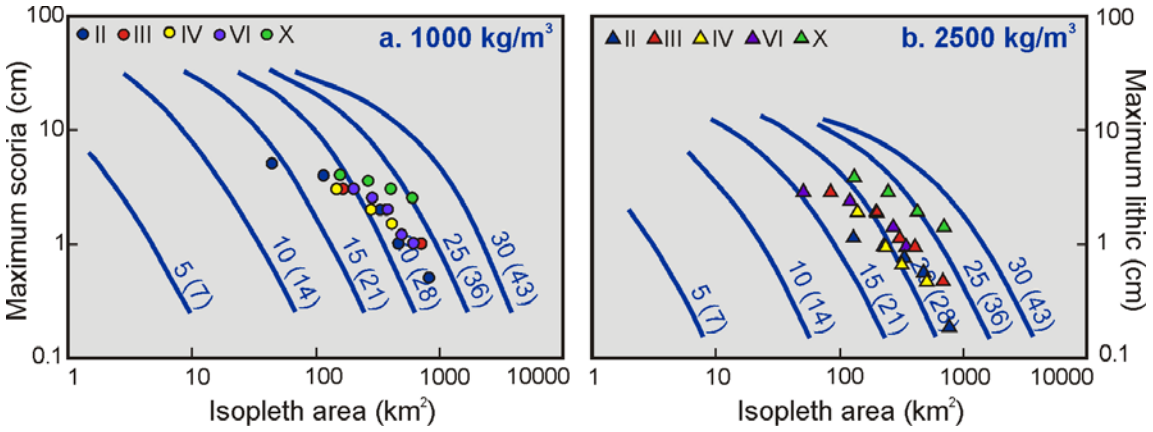

Figure 4.36. Isopleth area versus maximum clast size of scoria and lithic fragments for the fall subunits of the LCT-MTL. The trend lines are from Carey and Sparks (1986) and the values refer to the level of neutral density, H_B, where the plume the same density as the surrounding atmosphere has and in parentheses the top of the plume H_T, governed by the momentum of the plume.

4.5.2 Mass eruption rates

Data of the cross wind range and maximum clast size of lithic and scoria fragments were plotted in the diagram of Wilson and Walker (1987), in order to estimate discharge rates for the eruptions forming the LCT-MTL fallout subunits (Fig. 4.37). Although the subunits III, IV, VI and X plot between the curves of 10^6 to 10^7 kg/s and the subunit II between 10^7-10^8 kg/s, these results are uncertain because they locate below the dashed line. The only trustable value is given by the maximum scoria of subunit II, and yields a mass discharge rate between $3x10^6$ –10^7 kg/s for that event.

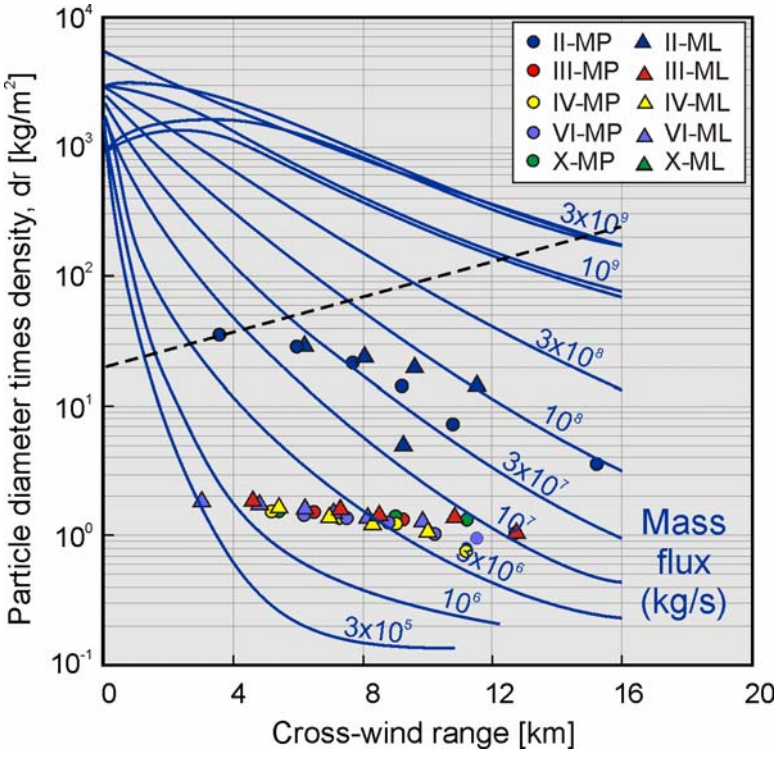

Figure 4.37: Discharge rate of the eruptions forming subunits II, III, IV, VI and X of the LCT-MTL, based on the diagram of Wilson and Walker (1987).

Such a mass discharge rate for the subunit II, suggests the eruption was a very fast event lasting a couple hours.
The model of Woods (1988) allows to estimate discharge rates from the column height data. Projecting estimated average eruption column height for each subunit onto the 1200 K curve in Fig. 4.38, yield mass rates of ~1-2 x 10^6 kg/s. The results obtained by other approaches for subunit II were also tested, plotting the column height ranges and the mass rate obtained with the method of Wilson and Walker (1987), the result is shown as a blue area in Fig. 4.38. The mass rate obtained is lower than predicted by the model of Woods (1988).

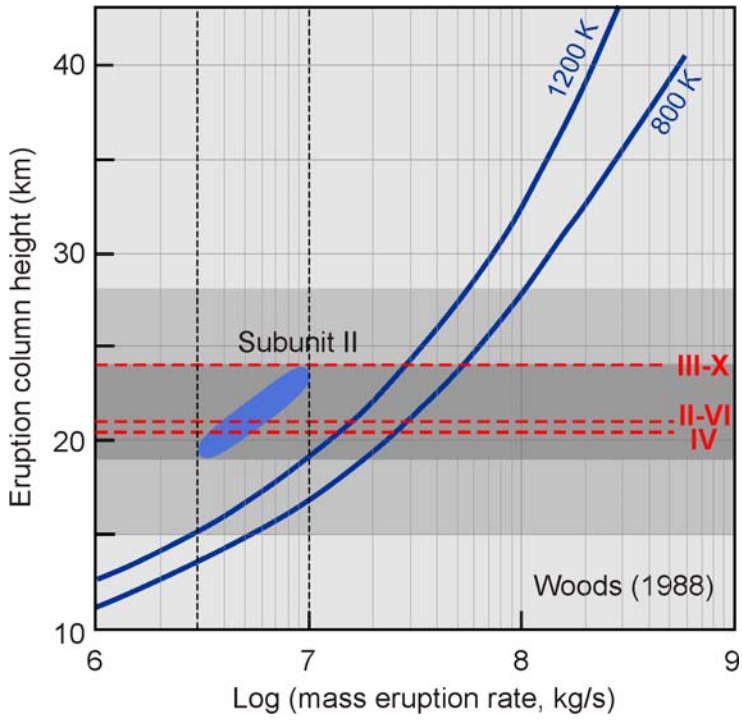

Figure 4.38: Eruption column height versus log of the mass eruption rate with the temperature lines of Woods (1988). The light gray area is the overall range in column height results of all subunits, whereas the darker gray is only for subunit II. Red dashed lines are the average eruption column height for the fall subunits II, III, IV, VI and X. See text for explanation.

4.5.3 Dispersal characteristics

The plots of the natural logarithm of isopach thickness versus the square root of the area enclosed by each isopach, for the correlated fall subunits, can be used not only for volume calculations but also as a way to classify them according to their dispersal characteristics by comparison with well-known eruptions (Fig. 4.39).
Using the fields of Houghton et al. (2000) for different types of eruptions, the fallout subunits of LCT-MTL mostly plot inside the Phreatoplinian field. Subunits II and IV can be considered as Plinian eruptions, due to their grain size and in most cases their little to inexistent interaction with water. Subunits VI and X are coarse grained and have Plinian distributions, nevertheless the juvenile fragments shape and density and especially the relative amount of lithic

fragments in the deposit suggest also external water influence (Phreatoplinian). Subunit III shows evidences of a strong water influence in the eruption (e.g. relative poor sorting, clasts coated with fine ash, abundant lithics, tuff layers intercalated in proximal exposures) and therefore should be classified as Phreatoplinian.

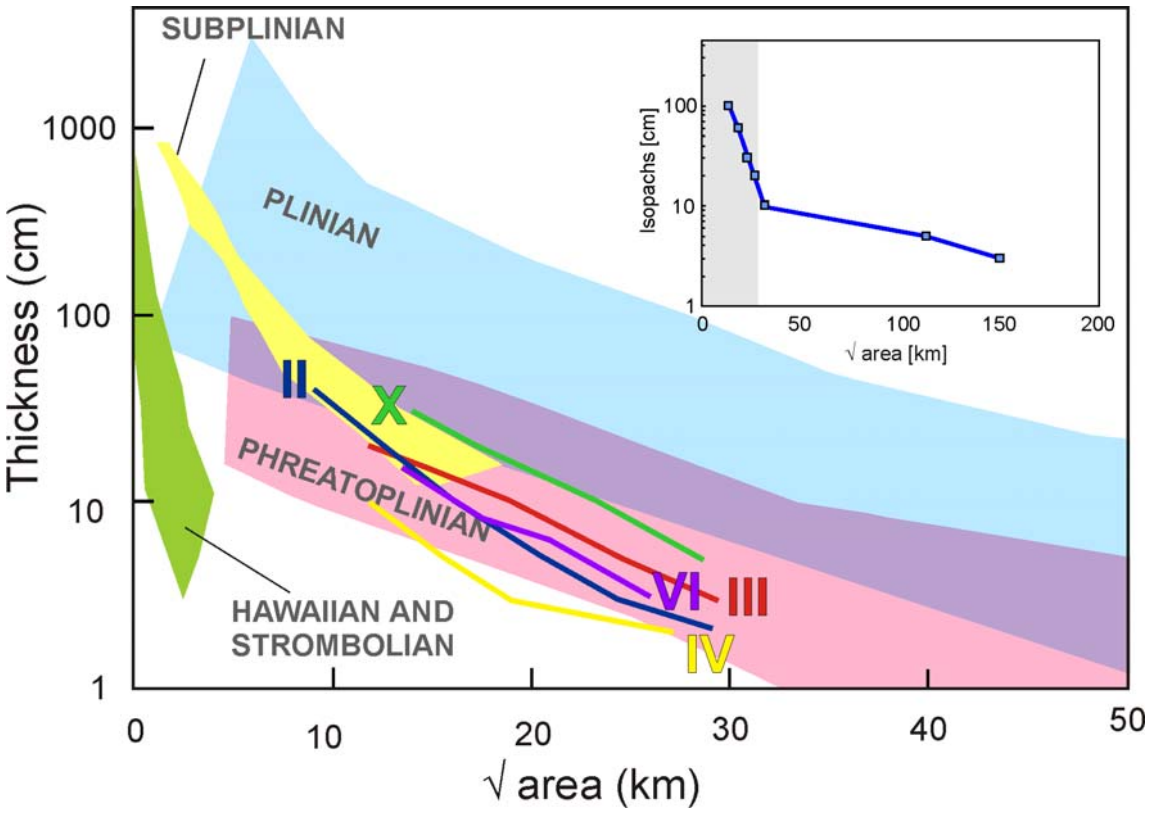

Figure 4.39: Diagram ln isopach vs square root of the area enclosed by the isopachs for the LCT-MTL fallout subunits. The fields of Plinian, Subplinian and Phreatoplinian eruptions are from Houghton et al. (2000). The inset at the top right corner shows the same diagram but in a bigger scale of the whole deposit, considering the marine tephra layers.

The half distance thickness parameter b_t (after Pyle 1989) for these subunits range between 2.6 and 3.9 km, whereas the half distance b_c ranges between 6 and 18 km. In the discrimination diagram of Pyle (1989) the subunits plot clearly in the Plinian field (Fig. 4.40).

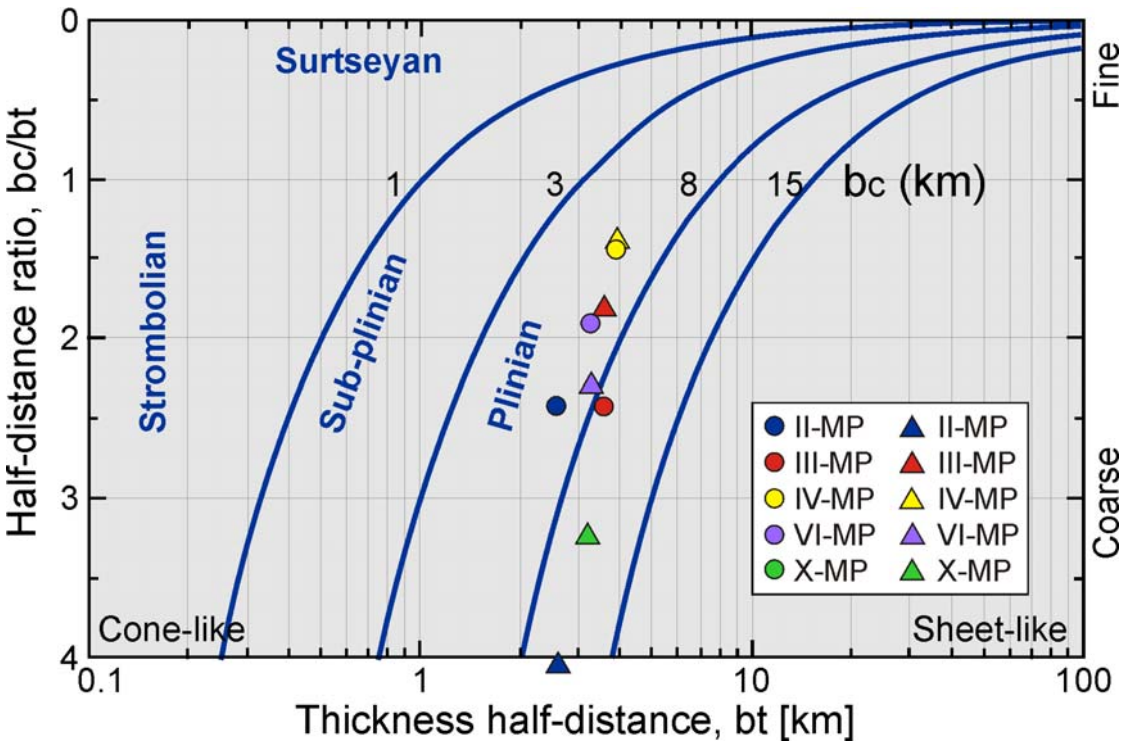

Figure 4.40: Classification scheme of Pyle (1989) based on the thickness half-distance versus half distance ratio for the main fall subunits of the LCT-MTL.

4.6 Interpretation

The reconstruction of the eruption giving rise to La Concepción Tephra-Masaya Triple Layer deposit is summarized in Fig. 4.41 and table 4.3. In general, it can be concluded that La Concepción Tephra and the Masaya Triple Layer are the product of a spasmodic eruptive period which alternated subplinian to plinian events with phreatomagmatic explosions.

Table 4.3. Summary of the parameters for the main fallout eruptions of the LCT-MTL

Sub-unit	V[1] DRE (km^3)	Mass (kg)	Column height (km)	Wind speed (m/s)	MDR[2] (kg/s)	Dura-tion (hours)	Type
II	0.038	$3.79x10^{10}$	~21-24	<2	10^7-10^8	~1	Plinian
III	0.102	$1.02x10^{11}$	~24	~10	10^6-10^7	3-28	Phreatoplinian
IV	0.025	$2.46x10^{10}$	~21-22	~10	10^6-10^7	<1-7	Plinian
VI	0.038	$3.83x10^{10}$	~21-22	~10	10^6-10^7	1-11	Phreatoplinian
X	0.115	$1.15x10^{11}$	~25-26	~20	10^6-10^7	3-32	Phreatoplinian

Explaining notes: [1]V=volume, [2]MDR=Mass discharge rate

The eruption started with phreatomagmatic precursor activity, producing ash fall with a limited distribution, the subunit B0, exposed only at some of the most proximal localities of the LCT facies, south of the caldera. The main eruptive period started with minor fall eruptions of phreatomagmatic origin and minor surges and became more magmatic with time (**subunit I**). This period includes an opening vent eruption, as suggested by the high lithic content at the base of the lowermost layer (LCT-B1), followed by a phreatomagmatic pulse (layer LCT-

B2) which generated a surge that carried vegetation, and overlying well-sorted black lapilli and ash layers of magmatic fall deposits. This magmatic smaller eruptions culminated with the eruption of **subunit II**, forming a Plinian eruption that evacuated 0.038 km^3 of fresh non-degassed magma and formed a column of 20-24 km height and lasted for ~1 h. The eruptive column changed its intensity with time as reflected in the fluctuations in the grain size of the deposit but it was almost not affected by wind. The characteristic fluidal shape of the lapilli fragments (achneliths) within subunit II suggests the eruption of a hot low viscosity magma. The lack of lithic fragments in this subunit indicates that there was no significant interaction of the magma with groundwater.

The **subunit III** was mostly phreatomagmatic, forming surges which destroyed and carried along the vegetation. There were also fallout events of Plinian character, which formed an eruptive column ~24 km high but may have not been so stable and partly collapse forming minor surges. When the availability of water at the conduit walls ceased, another magmatic Plinian eruption occurred (**subunit IV**), that lasted a couple hours and ejected 0.025 km^3 of a mixture of fresh non-degassed and degassed magma in a column rising up to 21-22 km.

Subunit V was of phreatomagmatic nature and formed surges that flowed mainly towards the south whereas the finer fraction flew towards the NW. After the deposition of this unit there was a major break in the eruptive period, which is indicated by the presence of desiccation cracks at the top of the tuff.

After the break the system recovered again and produced another Plinian eruption, **Subunit VI**, which was in part similar to the preceding one (IV), with a similar column height, mass discharge rate and just a slightly higher volume. The water gained again access to the system and produced the most important phreatomagmatic event of the whole eruption, the **subunit VII**. This activity was characterized by thick surge deposits formed by flows towards the S and the associated ash cloud moved with the wind towards the NW, forming thick fine ash deposits rich in accretionary lapilli. A fine-grained phreatomagmatic event - **subunit VIII**- followed the activity and formed a deposit with relatively good sorting but faint cross bedding, suggesting a fallout origin with a minor lateral transport component. The next event was also dominated by phreatomagmatic surges of widespread distribution, the **subunit IX**. The deposit exhibits a very small thickness (max. observed 20 cm) and at the upper surface has also desiccation cracks, as an indication of a second major break in the eruptive events. These breaks may not have lasted more than a few days, since there is no evidence of erosion.

The **subunit X** was the final and most vigorous event of the whole eruption. The characteristics of the deposit like the shape of the juvenile fragments and the high amount of lithic clasts, some of them hydrothermally altered, suggest the eruption was triggered by magma-water interaction. The ~0.1 km^3 of mostly degassed magma interacted with groundwater at the conduit, causing a Phreatoplinian eruption reaching a maximum eruptive column of 26 km high.

The eruptive column formed by this event was the highest of the LCT-MTL eruptive period, higher than those of earlier magmatic phases., and was also affected by stronger winds, probably because it reached higher atmospheric levels. It had a mass discharge rate between 10^6-10^7 kg/s, which means it might have lasted from 7 hours to 3 days.

An important conclusion derived from the reconstruction of the subunit X is that some breaks in activity may be misinterpreted as the end of the eruption,

while in fact, vigorous renewal of activity occurred. Rather than activity gradually declining, the vast eruption pulse was the most violent, due to magma-water interaction.

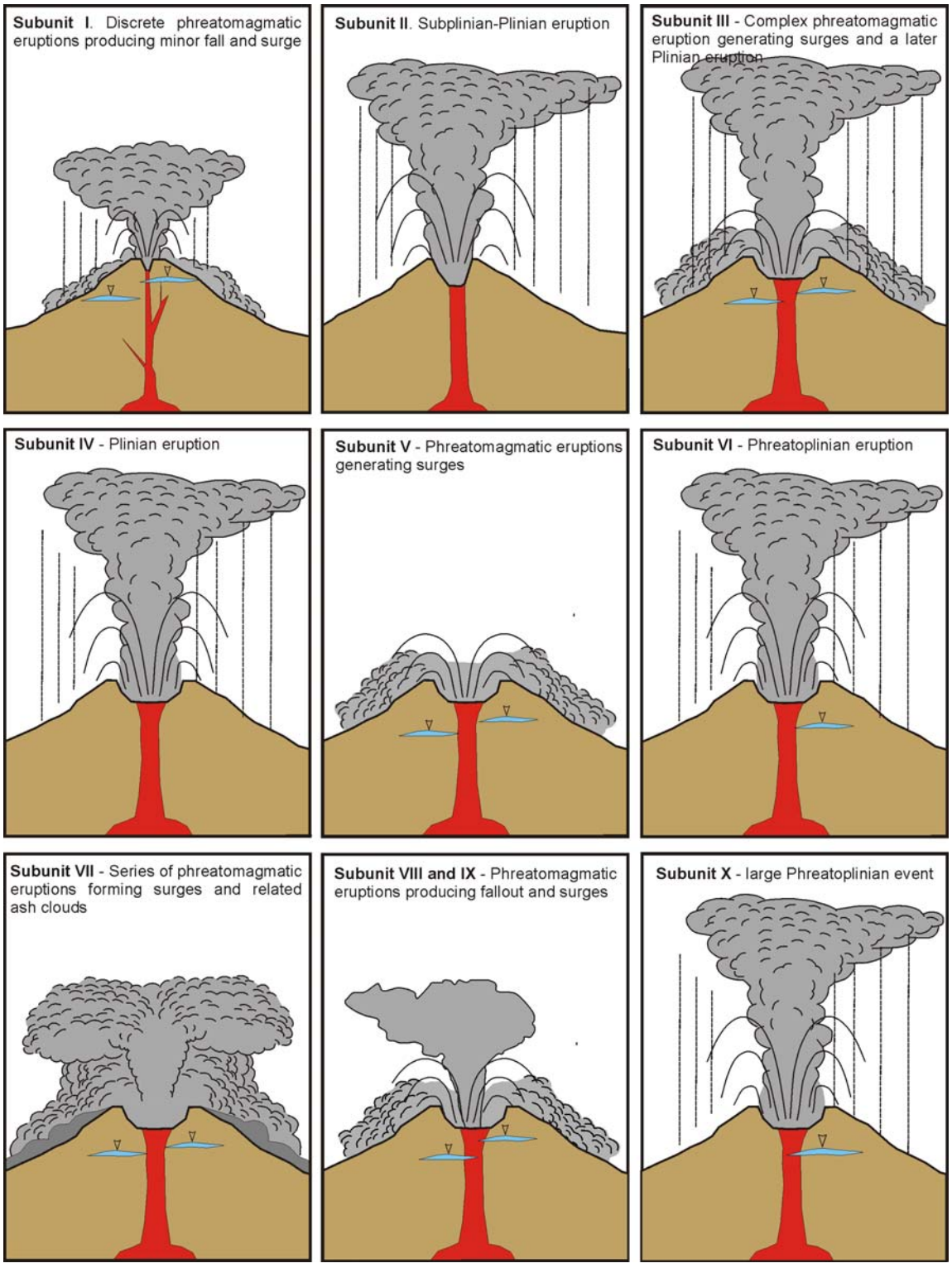

Figure 4.41 Simplified model of the LCT-MTL eruption, showing the main 5 Plinian and Phreatoplinian eruptions interrupted by surge-forming phreatomagmatic activity. Blue lenses represent ground water influence.

Chapter 5

The Masaya Tuff and the Ticuantepe Lapilli

The first report on the Masaya Tuff was made by Krusi and Schultz (1979). It was later described by Bice (1980; 1985) as a thick widespread light tan poorly to moderately indurated, faintly layered to massive fine airfall basaltic tuff, with an average thickness between 20 and 50 cm which constitutes the youngest large explosive deposit in the Managua area. Based on the chemical composition, petrographic similarities and field evidence, Bice (1980) suggested that Masaya Tuff came from the site of the present Masaya caldera and was probably genetically related to the collapse and formation of the caldera as it exists presently. He thought this fine-grained indurated tuff in Managua city was the fallout equivalent of the base-surge facies at the Masaya caldera walls. Williams (1983a) described this unit as pyroclastic surge deposits of unprecedented areal extent and volume; with a median grain size much coarser than any other measured before, as well as dune-forms and flow velocity of tremendous scale.
The Ticuantepe Lapilli has only been briefly mentioned by previous authors and no name had been assigned to this unit. It is presumed that this unit could be the “upper black lapilli” of Collins et al. (1976), which was sampled by Bice (1980) and correlated with the Masaya caldera deposits. Williams (1983a) stated that the surges (MT) grade up to scoria and ash fall deposits at the top of the section but did not present any data in his work.

5.1 The Masaya Tuff (MT)

The Masaya Tuff is a grayish, partly indurated tuff deposit that extends radially from the Masaya caldera complex, reaching a maximum distance of at least 35 km to the NW (Fig. 5.1). It conformably overlies the Masaya Triple Layer to the NW, separated by a yellowish weathered massive fine-grained tuffaceous deposit containing scattered scoria or pumice fragments, but locally it rests on an erosive unconformity cutting into La Concepción Tephra towards the S (Fig. 5.2). In outcrops west of Managua city and near Chiltepe Peninsula, the Chiltepe Tephra separates the MTL and the MT. This indicates that deposition of the Masaya Tuff occurred some time after the eruption of the Masaya Triple Layer <2000 years ago, and hence much more recently than the 3000 to 6000 years estimated by Bice (1980).

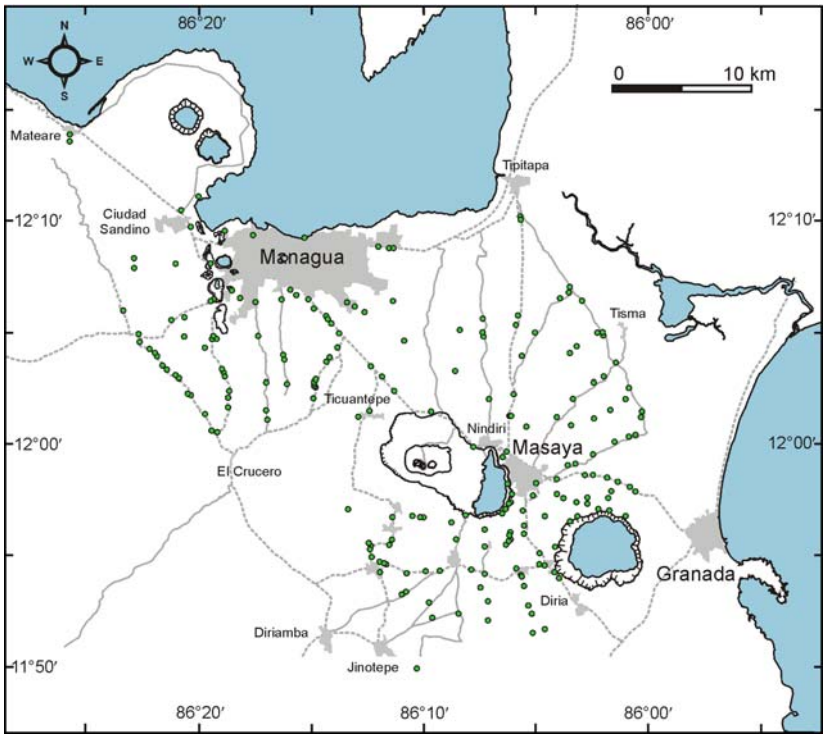

Figure 5.1: Map showing the distribution of the studied sites of the Masaya Tuff.

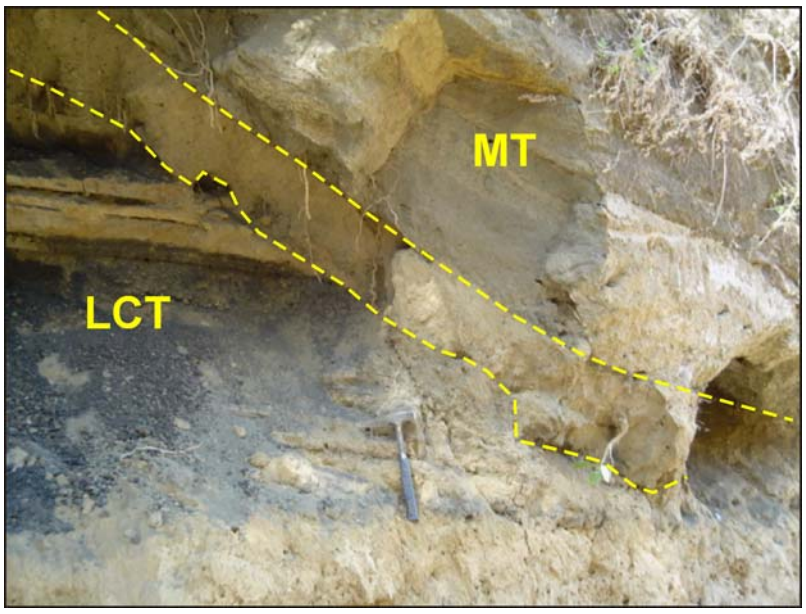

Figure 5.2: Unconformity between La Concepción Tephra (LCT) and the Masaya Tuff (MT), S of the Masaya caldera. The massive yellowish deposit in between seems to be reworked.

5.1.1 Components

The MT is a relatively poorly-sorted (σ>3) grayish deposit, composed mainly of vitric fine ash and dust with 5-20 vol.% of lapilli to block-sized fragments of juvenile and pre-existent material and abundant accretionary lapilli. The juvenile fraction consists mostly of dense aphyric fragments and in a minor amount vesicular lapilli, both with scarce plagioclase and olivine phenocrysts. The lithic fragments are mafic lavas of different textures and some plutonic rocks.

5.1.1.1 Fine fraction

The fine fraction of the Masaya Tuff consists mostly of fine lapilli (not larger than 4 mm), ash and volcanic dust (Fig. 5.3).

The larger particles with sizes between 1-5 mm exhibit a great variation in type (sideromelane, tachylite, mingled clasts of both, lithic fragments; Fig. 5.3a-d), vesicularity (dense to highly vesicular), shape (angular to round) and crystallinity (microlite-poor to microlite-rich). These particles are frequently coated by a thin fine ash film.

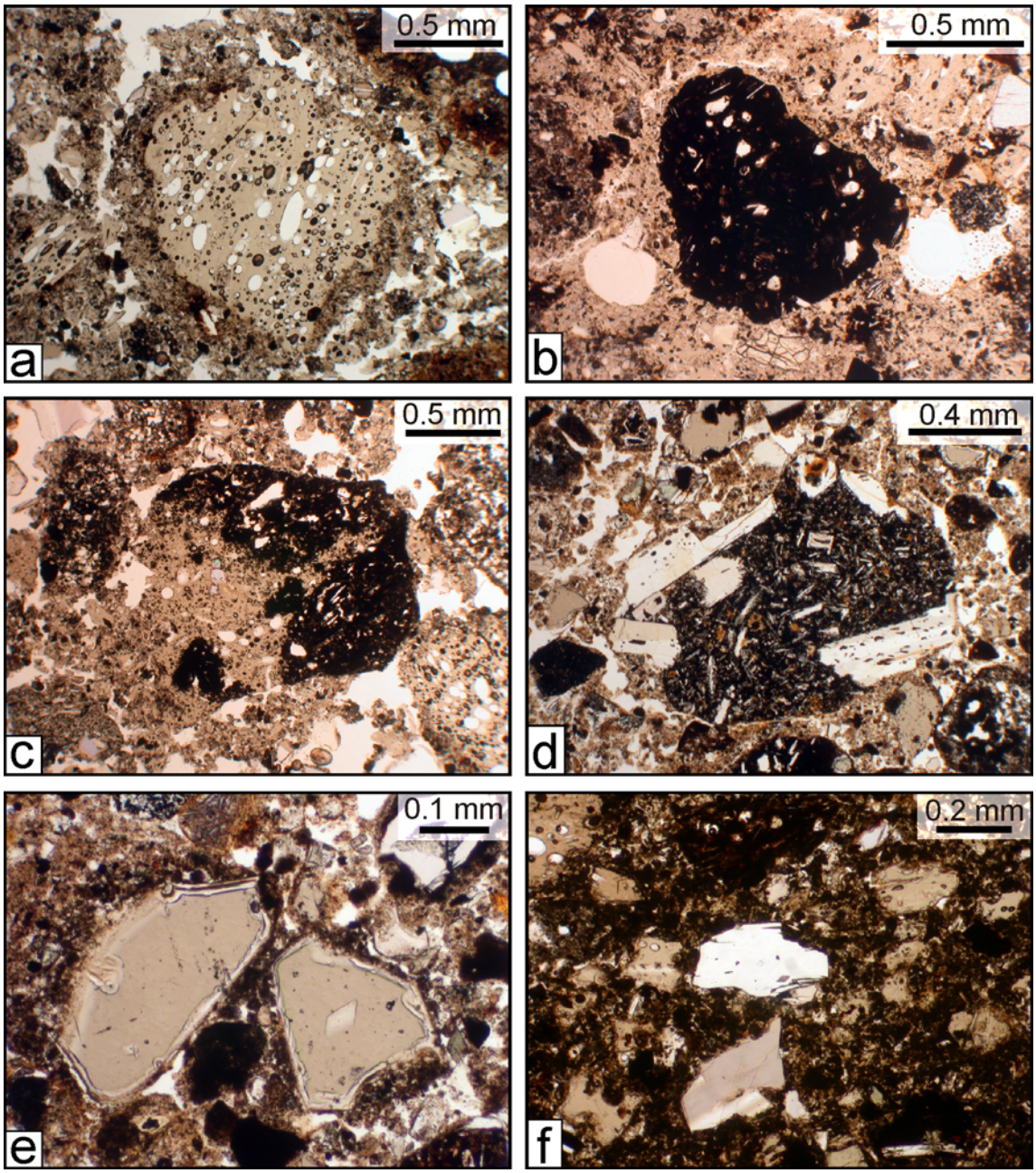

Figure 5.3: Fine fraction particle types of the Masaya Tuff: coarse ash sized fragments of different types [**a**] sideromelane, [**b**] tachylite, [**c**] mixed and [**d**] lithic, [**e**] dense angular sideromelane fragments. [**f**] Finest clasts made up mainly by sideromelane, crystals and clay.

The medium to fine ash fraction is dominated by angular dense sideromelane fragments, but there is also few vesicular particles, crystals (mostly plagioclase but also minor pyroxene and olivine, with euhedral to anhedral shapes) and small lithic fragments (Fig. 5.3e). The finest ash material, with a size smaller than 0.1 mm, consists of angular dense sideromelane, clay and crystal fragments (Fig. 5.3f).

5.1.1.2 Juvenile fragments

There are two dominating types of juvenile material of the Masaya Tuff: dense (~1.5-1.9 g/cm^3) glassy fragments with ~1 vol.% of crystals (mostly plagioclase) and light vesicular aphyric fragments (Fig. 5.4). The vesicular fragments exhibit a density of ~0.6-0.8 g/cm^3, are commonly round and are preferentially found in well-sorted lenses in dune structures. These round shapes could be due to abrasion during turbulent transport. There are also minor amounts of dense crystal-rich fragments and highly vesicular, glassy lapilli.

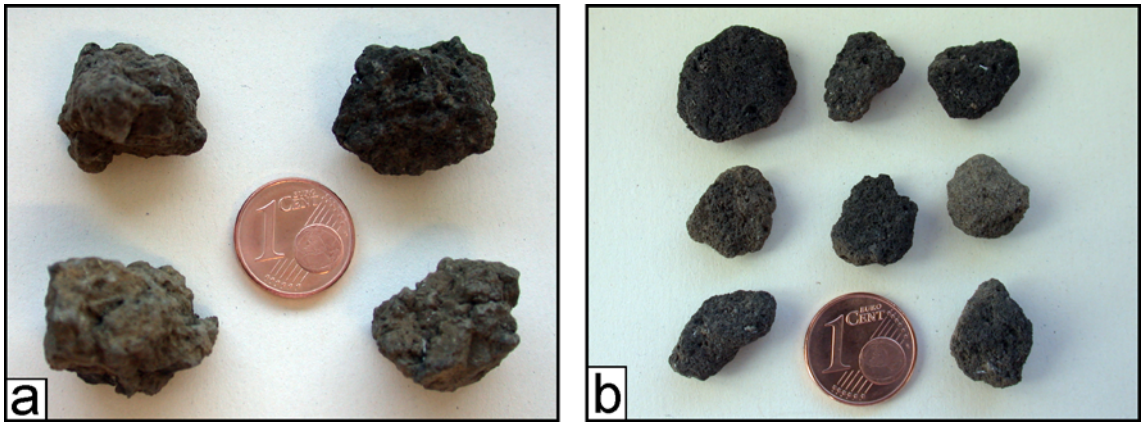

Figure 5.4: Main types of juvenile fragments in the Masaya Tuff. [**a**] dense fragments coated with volcanic dust and with cauliflower shape, and [**b**] round-shaped vesicular lapilli.

Microscopically, most of the juvenile fragments consist of tachylite although with large variations in vesicularity, but also few sideromelane or mingled fragments have been found. Typically, most of the Masaya Tuff juvenile clasts have xenoliths from lavas and altered denser glass fragments.

The highly vesicular clasts are mostly made by tachylitic glass with scarce plagioclase microlites and ~40-80 vol.% of irregular-shaped vesicles with sizes ranging from 0.1-1.5 mm and even maximum sizes up to 6 mm (Fig. 5.5a). The phenocrysts make up less than 1 vol.% and consist mostly of plagioclase but also minor olivine and rare clinopyroxene.

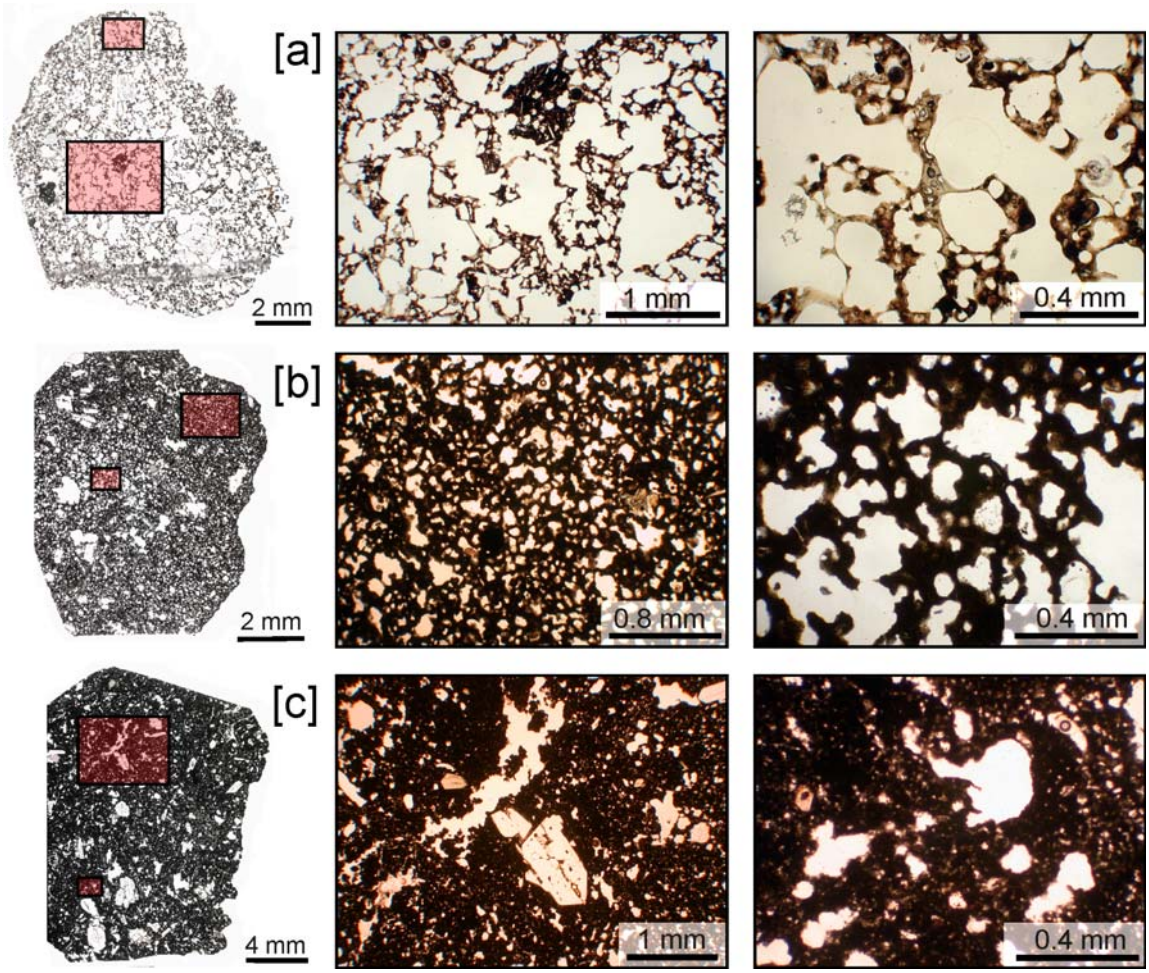

Figure 5.5: Main types of juvenile fragments at the Masaya Tuff and detail of them at different scales for comparison: [**a**] highly vesicular, [**b**] moderately vesicular and [**c**] dense fragments.

The moderately vesicular fragments (20-40% of vesicularity) are also consist of tachylite or mingled glass with spherical and irregular-shaped vesicles with average sizes between 0.2-0.5 mm, but with minimum sizes of ~0.08 mm and maximum of ~2 mm (Fig. 5.5b). They have higher phenocryst contents (1-3 vol.%) of pl+cpx+ol+mt.
Dense fragments are tachylitic with less than 20 vol.% of vesicles, sometimes with irregular shapes but mostly spherical (0.04-0.5 mm) and with phenocryst contents up to 10 vol.% (Fig. 5.5c). The microlite content varies from scarce plagioclase needles to 40 vol.% or more of pl+cpx+mt.

5.1.1.3 Lithic fragments

The lithic fragments in the MT deposit are mostly mafic lavas but there are also some plutonic ones, found in particular outcrops. The lavas, mostly basaltic, show different textures and mineral content. The most common types are aphyric dense black lavas, but there are also other types like aphyric vesicular lavas or afanitic-porphyritic lavas with ~10 vol.% of phenocrysts (mostly plagioclase, minor olivine and rare pyroxene, Fig. 5.6a-c). A minor lava type

seem to be more felsic, with a higher content of crystals (~15 vol%, pl+px) in a light gray groundmass.

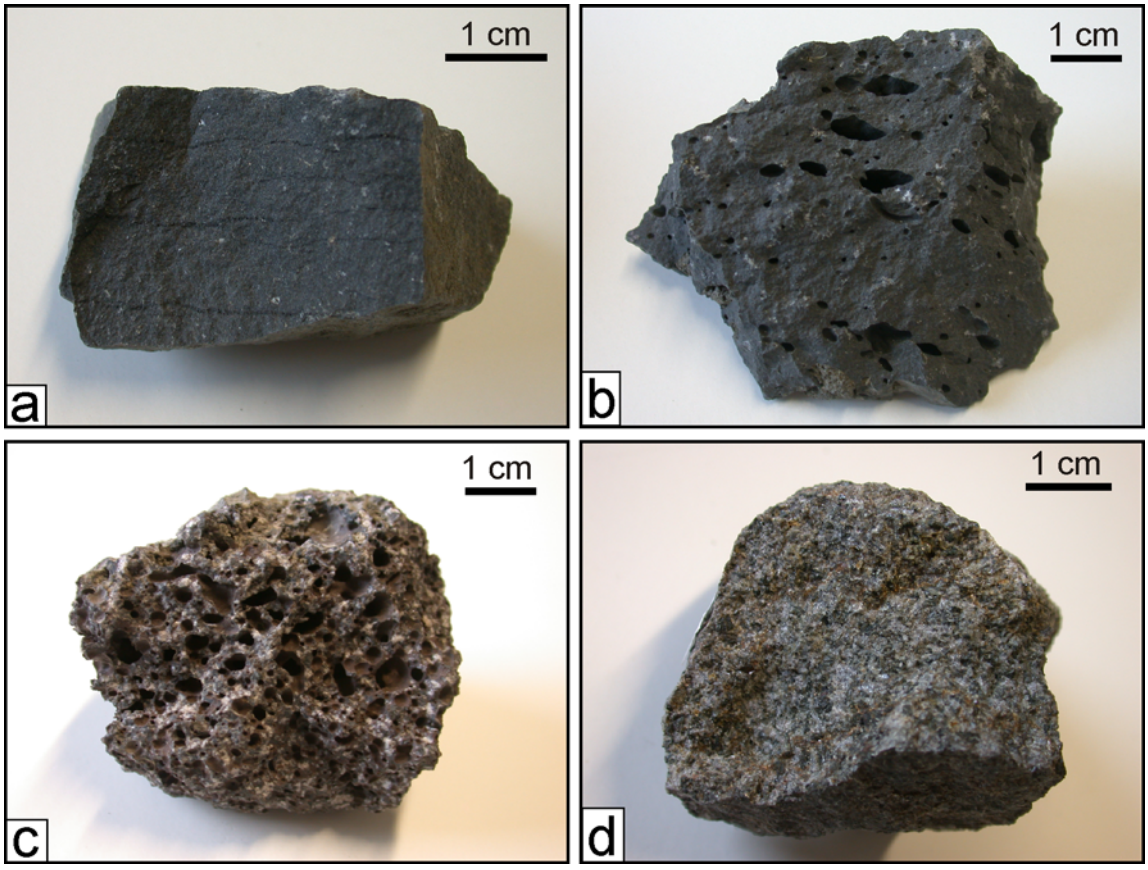

Figure 5.6: Types of lithic fragments commonly found in the Masaya Tuff deposits: [**a**] dense aphyric dark lava, [**b**] vesicular aphyric lava, [**c**] vesicular lava with plagioclase phenocrysts and [**d**]. plutonic rock from an outcrop 3 km N of the caldera.

The plutonic fragments like the one in Figure 5.6d have been found in certain outcrops in proximal areas between 2-3 km from the caldera rim. In hand specimen the rocks are crystalline and very similar, just with slight differences in the amount of the different mineral phases and crystal size. A thin section of one of the samples (Fig. 5.7) revealed that they are formed mostly by strongly zoned plagioclase (~75 vol.%, Fig. 5.7c) and clinopyroxene (~20 vol.%), as well as minor amounts of magnetite and olivine. Also there are some sericite, oxides and brownish and fibrous alteration minerals in between the crystals (Fig. 5.7d).

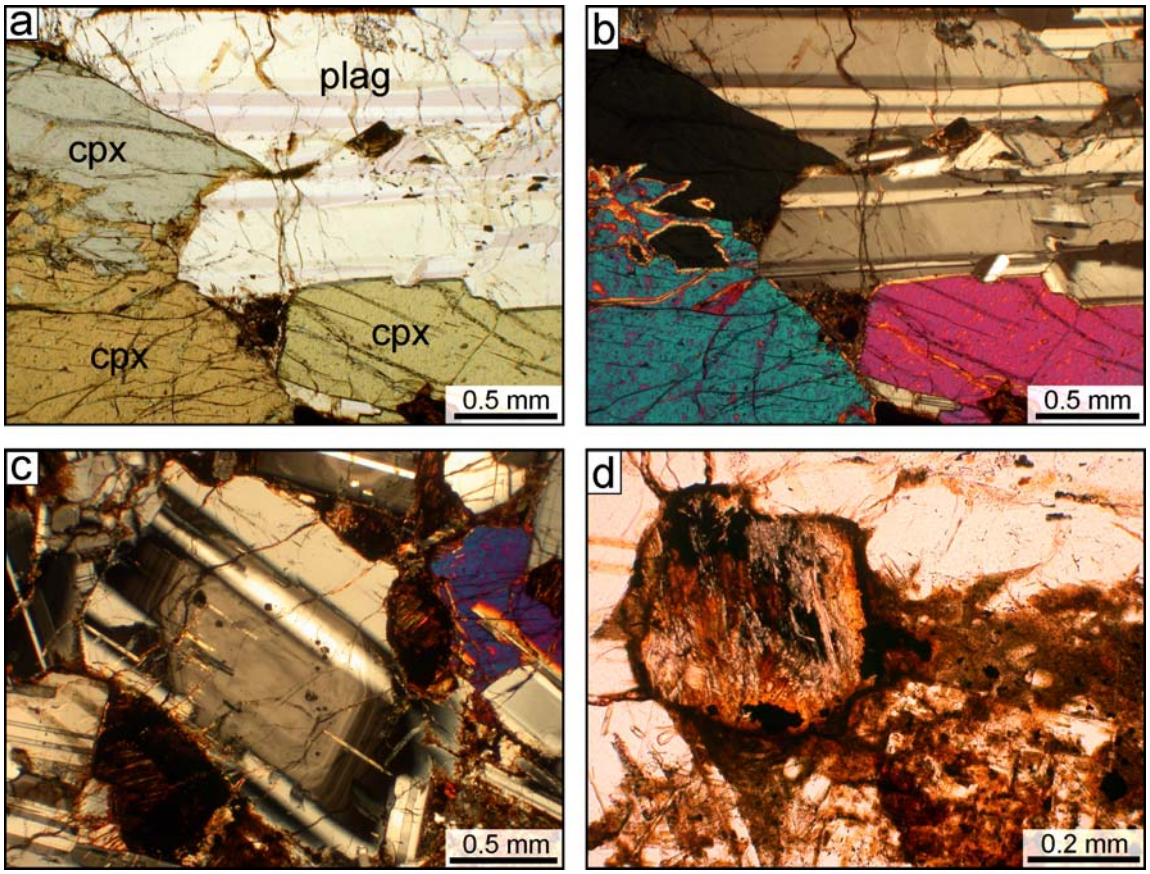

Figure 5.7: Microphotographs of a plutonic lithic fragment inside the MT. [**a**]-[**b**] Main mineral phases present at parallel nicols and crossed nicols, respectively. [**c**] Strongly zoned plagioclase phenocryst. [**d**] Alteration minerals in spaces between the phenocrysts.

5.1.1.4 Accretionary Lapilli

As mentioned before, accretionary lapilli are very abundant in the fine grained beds of the Masaya Tuff; mostly at the upper plane bedded portion of the deposit and at the middle part, but can be also found as fine tuffs at the top or inside of cross-bedded or dune sequences. Some beds have 5-10 vol.% of accretionary lapilli but others can have as much as 30-40 vol.%. Their sizes range mostly from 3 to 10 mm but can reach up to 30 mm and their shapes are mostly spherical and few deformed ones.

In some planar beds the accretionary lapilli have normal grading, e.g. lapilli with ~15 mm in diameter are at the bottom and those <5 mm at the top, whereas in other outcrops the accretionary lapilli are concentrated only at the top of the bed.

Thin sections of accretionary lapilli from the MT reveal several aspects about their internal structure. All accretionary lapilli seen at the Masaya Tuff are rim-type following the nomenclature of Schumacher and Schmincke (1991). Few accretionary lapilli are fine-grained and lack a marked layered concentric structure, showing a subtle grain size decrease from the core towards the outer rim (graded rims), from ~300 μm to <10 μm (Fig. 5.8a). However most of the MT accretionary lapilli show a well-developed concentric structure (multiple rims). The coarse grained core is made by medium to coarse ash (300-400 μm)

of dense sideromelane and crystal fragments. The rim is very fine grained material (<20-10 μm) which a thickness ranging from 0.2 to 0.7 mm (Fig. 5.8b, c). Some of the accretionary lapilli can include few spherical vesicles inside (Fig. 5.8b).

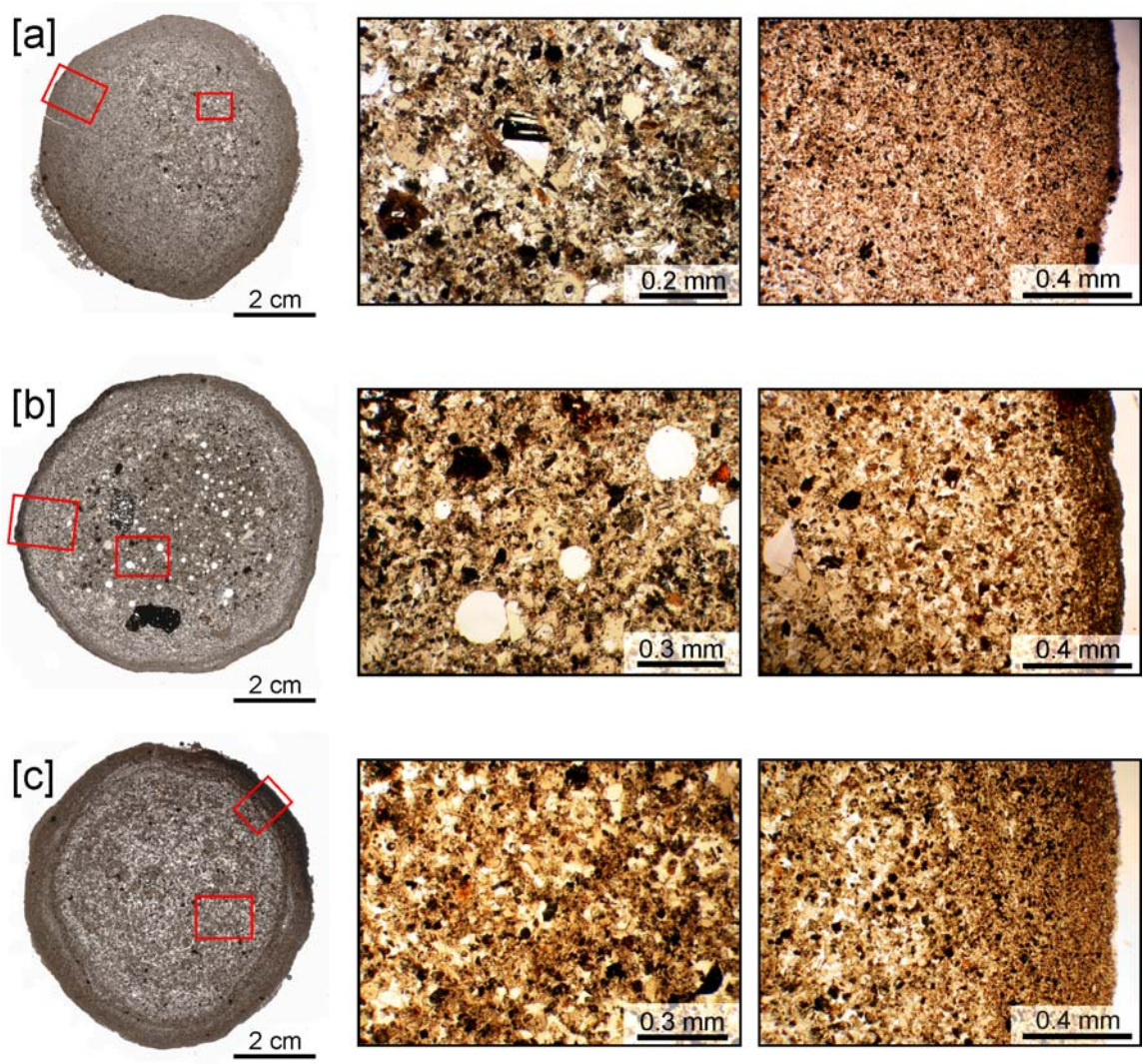

Figure 5.8: Examples of the rim-type accretionary lapilli found at the Masaya Tuff. [**a**] The grain size decreases in a gradational way from the core to the rim. [**b**] Lapilli with a dark thin (0.2 mm) rim of fine material and spherical vesicles at the core. [**c**] Thick rim (0.7 mm).

5.1.2 Bed forms

Three main types of bed forms are common in the Masaya Tuff: cross bedding, dunes and planar bedding. The cross bedding and dune structures are typical of the lower section of the tuff at distances not farther than 10 km from the caldera, whereas planar bedding is mostly present at the upper part of the deposit and dominates the sequence at distal exposures.

The cross bedding has mostly low angle bedding and is present not only as planar bounded beds but also as lamination inside a single bed. It can be crude or well-developed.

The dunes of the MT are mostly regressive like the ones shown in Fig. 5.9a, c and are actually antidunes. Measured wavelenghts range from 16 m at 5 km to the NW to 2.7 m at 8.5 km E of the caldera. Some dunes show sets of cross lamination bounded by erosive surfaces inside the same dune; most of them have gentle angles at the stoss side (~5°). The internal lamination or cross bedding has also low angles, not higher than 10°.

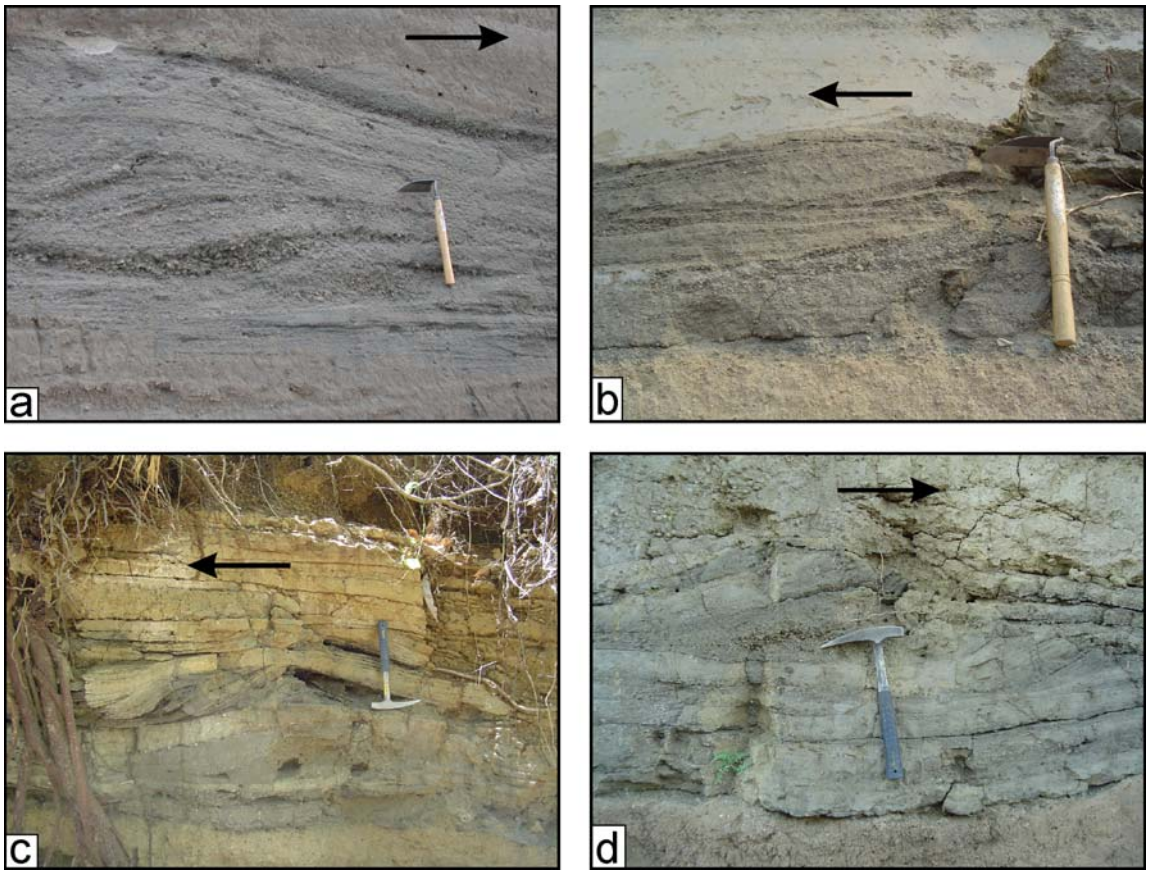

Figure 5.9: Examples of dunes of the Masaya Tuff. [**a**] Well-developed antidunes at 5 km NW from the caldera. [**b**] Low angle cross bedding inside a dune 8.5 km E of the caldera. [**c**] Planar beds bounding small regressive antidunes at ~450 m above sea level south of Managua, over 100 m above the general caldera rim level. [**d**] Planar bedded dunes, also regressive in an outcrop near Catarina, ~6 km SE of the Masaya caldera. The white arrow points out to the flow direction.

In average the planar beds are 15-30 cm thick, but they can also be as thin as 5 cm (Fig. 5.10b). They are massive, sometimes with some faint gradation, and have mostly planar parallel surfaces at the bottom and top, although they also thin out or have wedge shapes (Fig. 5.10a, c, d). At distal exposures sometimes the lower planar beds have internal cross bedding whereas upper planar beds contain accretionary lapilli like at the outcrop shown in Fig. 5.10b.

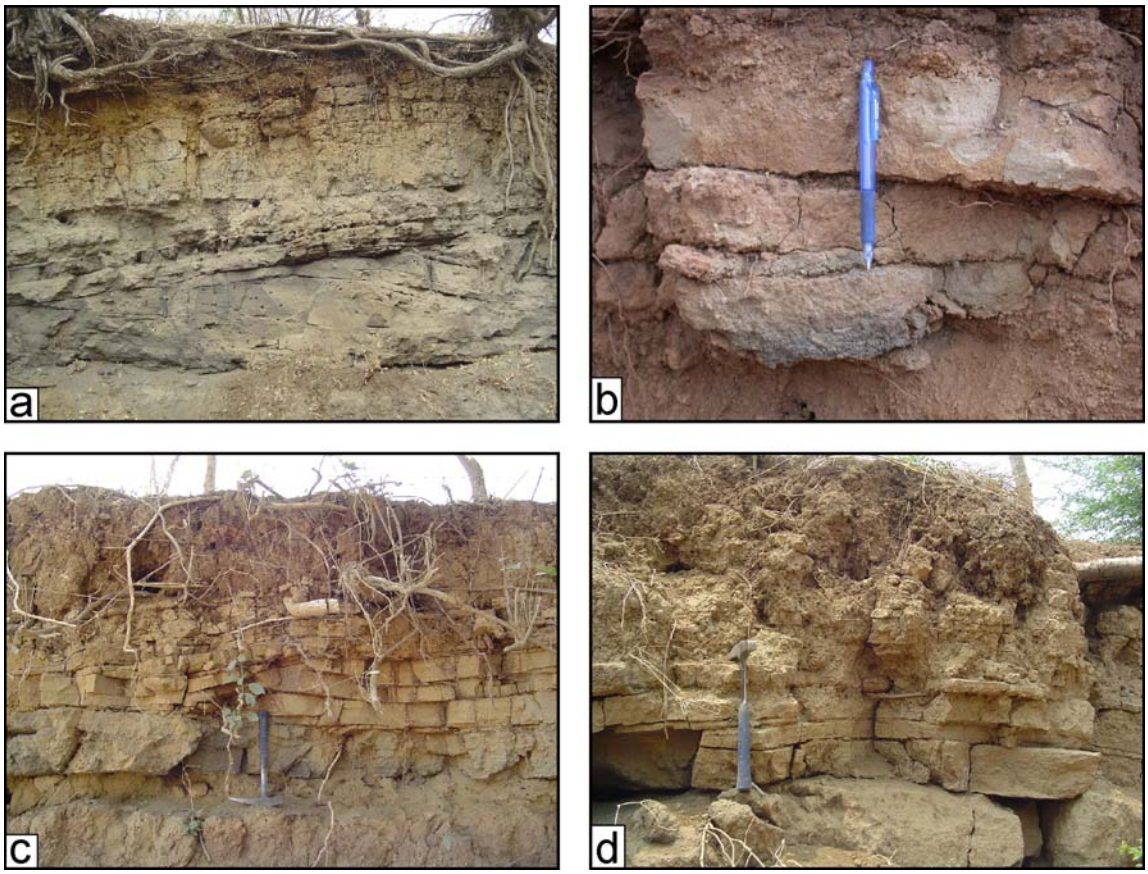

Figure 5.10: Planar beds at the top and distal exposures of the Masaya Tuff: [**a**] Planar undulated beds. [**b**] Planar beds with a bottom showing some cross bedding and at the top accretionary lapilli. [**c**] Coarse-grained thicker bed at the bottom overlain by thin very fine beds. [**d**] Typical parallel planar beds at distal exposures ~10 km NE of the caldera.

5.1.3 Facies variations

5.1.3.1 Vertical sequence

At proximal exposures, <1 km to the NE of the caldera rim, the base of the Masaya Tuff is represented locally by a 15-60 cm thick basal breccia. The breccia consists of mostly dense and glassy dark gray angular basaltic lava fragments, but also of plagioclase-rich or vesicular lavas. Nevertheless, at most of the outcrops, especially at medial localities, the lower contact of the Masaya Tuff is characteristically marked by an almost continuous horizon of leaves and plant molds, which facilitate the recognition of the tuff (Fig.5.11). The horizon where the molds can be found is made of angular, dense, glassy fine lapilli (Φ~1-5 mm), and is commonly found S and SE of the Masaya caldera. At most proximal outcrops it is common to find cylindrical cavities which are actually molds of thin trunks or branches.

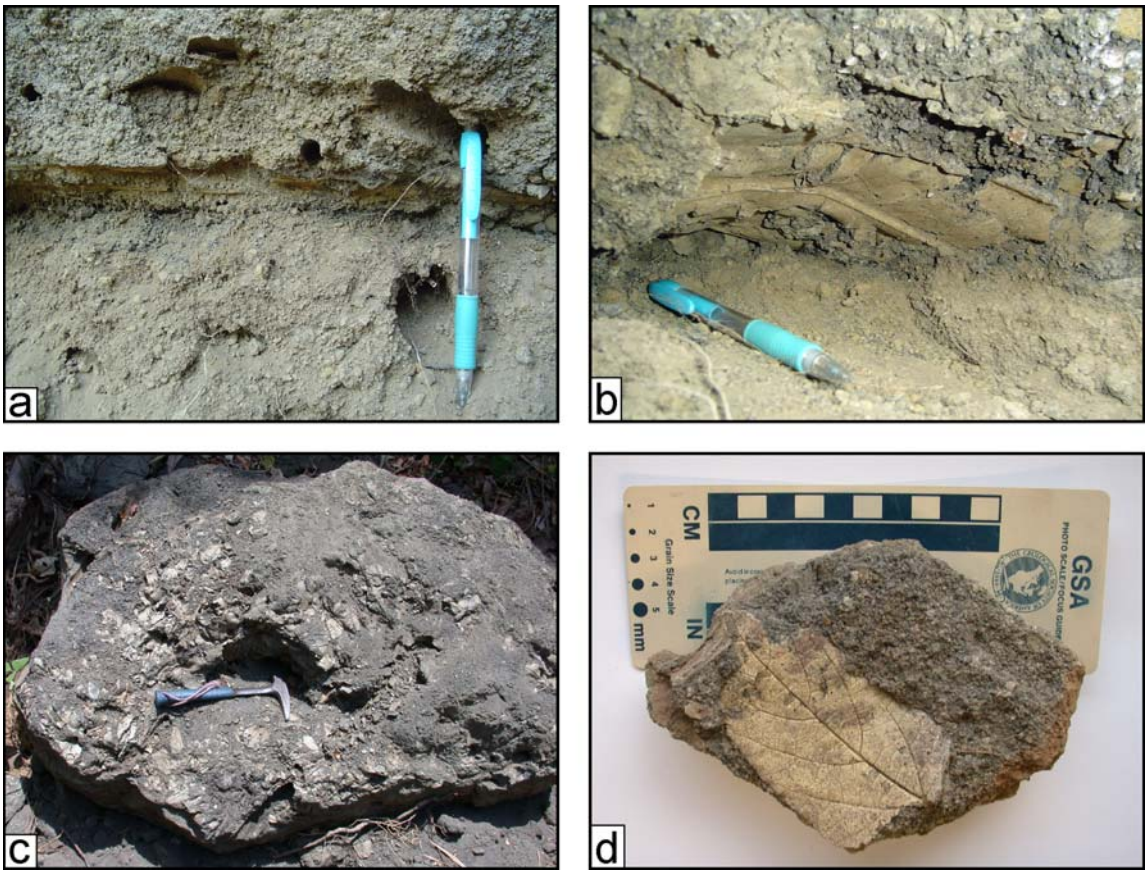

Figure 5.11: Photographs of the lower contact of the Masaya tuff characterized by abundant leaf molds: [**a**]-[**b**] Show the horizon at the outcrop, [**c**] Block of the basal part of the tuff showing the high amount of the vegetal rests and [**d**] is a detail of a leaf mold in a hand specimen.

The most complete simplified sections of the Masaya Tuff are exposed 3 km to the N and 4 km to the east from the caldera rim and they were used to subdivide the MT sequence into six units (D1 to D6) based on grain size, structures and bedforms (Fig. 5.12). In general there is an overall fining upward in grain size culminating in the fine-ash planar-bedded tuff D6.
Subunits D2, D3 and D6 occur all around the caldera, D1 and D4 just towards the east and north and D5 only at the northern sector.

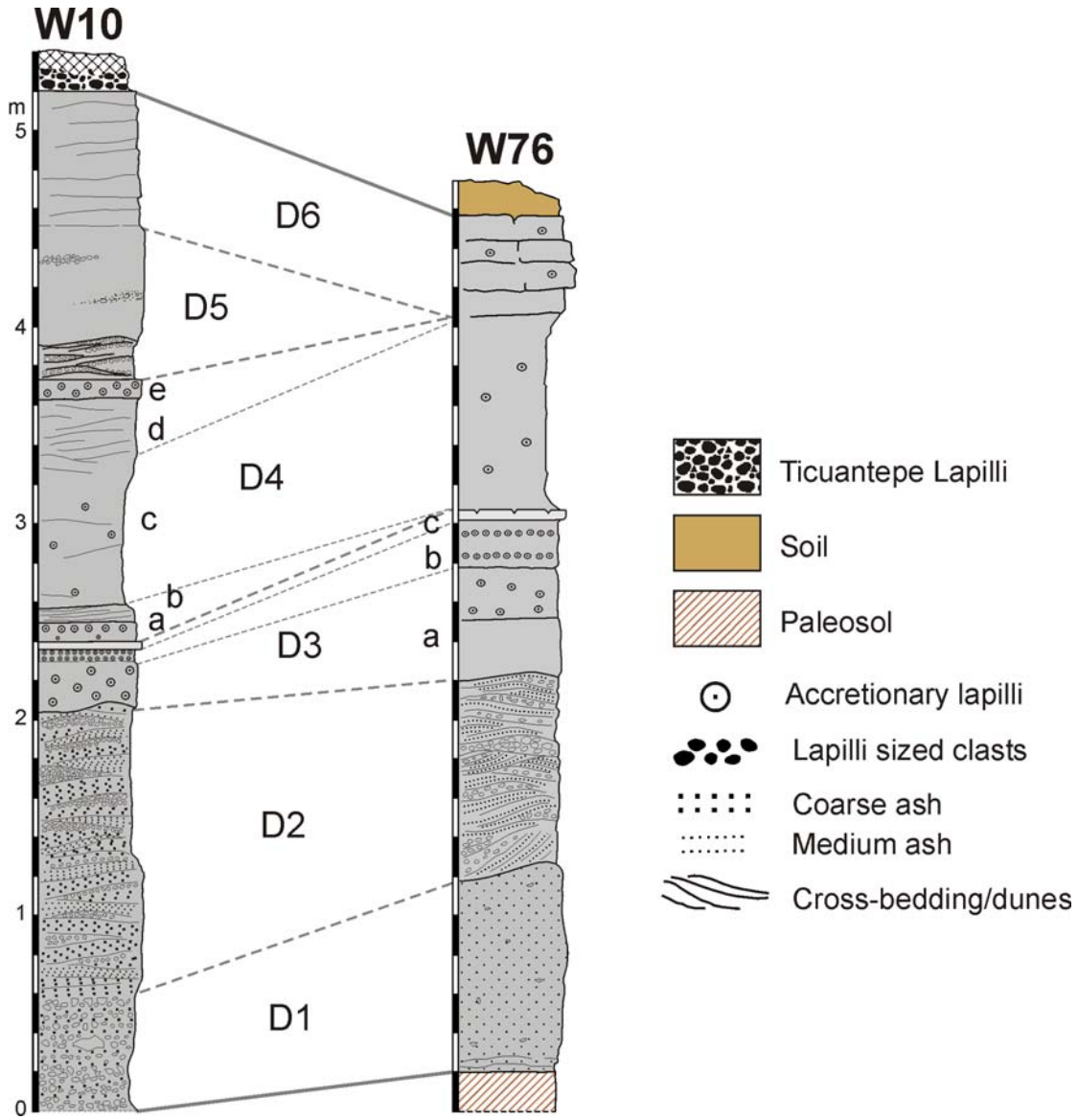

Figure 5.12: Vertical variations and subunits of the Masaya Tuff based on the outcrops W10 located 3 km to the North of the caldera rim, at a quarry along the road between Masaya and Tipitapa and outcrop W76, 4 km to the east of the caldera.

Subunit D1

Subunit D1 is a coarse-grained deposit, consisting of lapilli, coarse ash and even blocks (Fig. 5.12), or floating lapilli in a finer poorly-sorted matrix. At outcrops to the north of the caldera it appears like a loose breccia with a crude bedding (Fig. 5.13a), but in several outcrops towards the east and southeast, it is extremely indurated and has a consistency similar to concrete (Fig. 5.13b). In road cuts east of the caldera this concrete-like layer is a lateral equivalent to the lower dune of the subunit D2 closer to the vent.

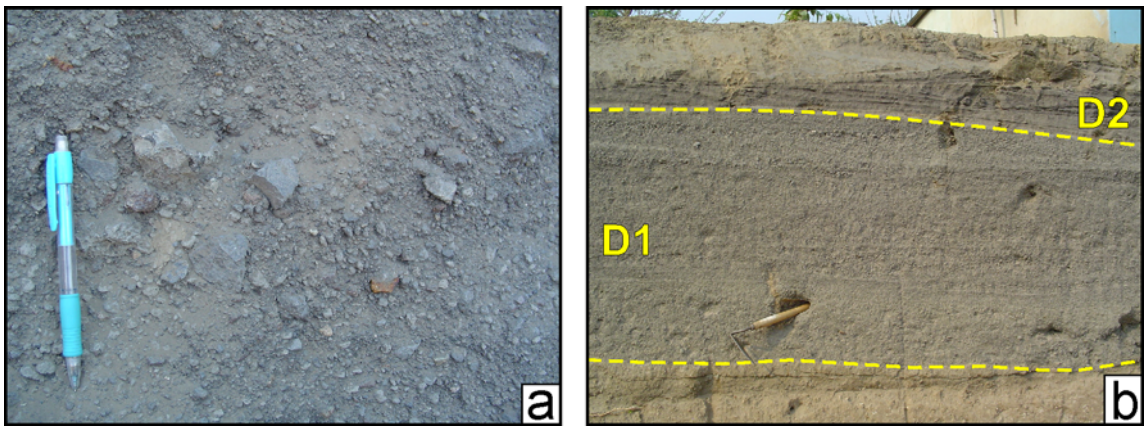

Figure 5.13: Subunit D1. [**a**] At the outcrop W10 north of the Masaya caldera where it appears like a relative loose breccia. [**b**] Concrete-like subunit D1 to the east of the caldera. The cavity where the scraper is inside is a mold left by a branch or a small tree trunk.

Subunit D2

This deposit is overlain by several layers with cross-bedding and dune structures that range in grain size from lapilli to ash. It contain lenses of well-sorted, round and abraded scoriaceous lapilli, as well as denser angular juveniles and lithic fragments (Fig. 5.12, 5.14a). The cumulative thickness reaches 15 m and at the lowermost dune it is common to find molds of branches or trunks of small trees, wrapped around by hardened tuff.

At outcrops toward the east of the caldera up to three main dune events can be differentiated, separated by hardened tuffs (Fig. 5.14b).

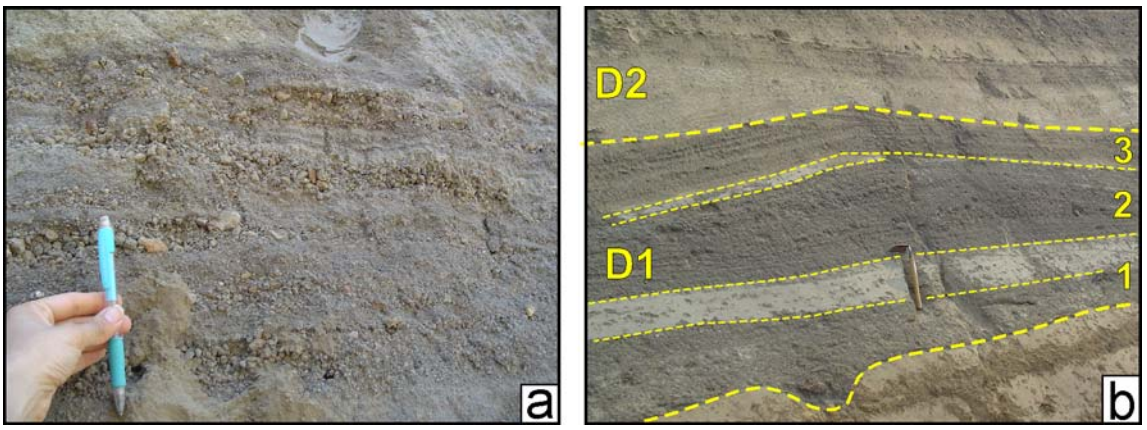

Figure 5.14: Subunit D2. [**a**] Good sorted lapilli lenses at subunit D2. [**b**] The 3 main dune events separated by fine-grained light gray tuffs. In this outcrop the lowest dune already looks a little like the concrete-like subunit D1.

Subunit D3

At the top of the D2 dunes there is a planar-bedded fine ash layer containing relatively large accretionary lapilli (up to 20 mm; D3a in Figs. 5.12, 5.15). It ends up with a fine soft layer (D3b) with abundant and tiny (<5 mm) accretionary lapilli concentrated at the top and bottom of the bed and a very hard fine tuff with desiccation cracks at the topmost pointing out to a major break in the eruptive sequence (D3c, Fig. 5.15).

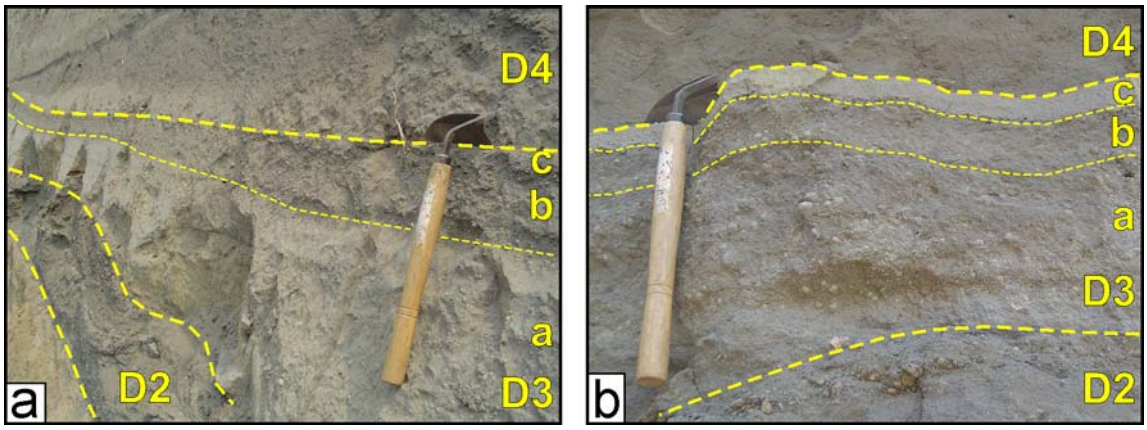

Figure 5.15: Subunit D3. [**a**] Beds D3a-c-f at an outcrop. [**b**] Detail of the subunit showing the accretionary lapilli bearing bed D3a, a thin D3b with very small accretionary lapilli and the light gray hardened tuff D3c.

Subunit D4

It is characterized by a massive fine-grained soft tuff with accretionary lapilli which erodes easily and forms a back-weathered relief. At the outcrop W10 it starts with a thin indurated tuff overlain by a cross bedded interval (D4a,b respectively; Fig. 5.12), followed by a soft tuff (D4c) and is overlain by another cross bedded interval and an indurated accretionary lapilli bearing tuff (D4d,e; Fig. 5.12).

Subunit D5

The unit D5 only occurs at the northern sector of the caldera and consists of a cross bedded lapilli tuff which becomes finer upwards.

Subunit D6

This subunit is a package of fine-grained planar beds with accretionary lapilli which dominate the top and distal parts of the deposit (Fig. 5.10). It has a variable thickness and probably in some outcrops has been eroded. At medial-distal outcrops it is possible to find some lamination of the lowermost beds, but they are mostly massive fine grained and structure-less.

Towards the NW, the sequence is much more complex so it cannot be so easily correlated. In the flat area from the caldera rim to Managua (near Ticuantepe) the tuff is thicker and consists of several dunes intercalated with fine-grained deposits with accretionary lapilli (Fig. 5.16). The subunits distinguished in Fig. 5.12 cannot be really correlated with the sequence there.

Figure 5.16: Images of the most complete and proximal outcrop of the MT, located 4.5 km NW of the caldera, along the main road Managua-Masaya. Note the dunes and wavy structures along the road cut. [**a**] NE wall of the road. [**b**] Detail of the dune at the left side of [a]. [**c**] SW wall, to the right is direction to Managua city.

5.1.3.2 Facies changes with distance to the source

Although with some local variations, there is a general facies distribution with increasing distance from the source in the different directions. The proximal facies of the Masaya Tuff are locally represented by a dense-clast breccia at the base, occurring only within ~1 km from the caldera rim. In these areas the dune and cross bedding structures are well developed.

At the medial facies at ~5-10 km from the caldera, the dune and cross-bedding subunit is much thinner and is located mostly at the lower portion of the tuff, capped by a sequence of several indurated planar bedded tuffs with accretionary lapilli. The distal facies (>15 km to the NW and ~10 km to the N, NE, E, SE and S) are represented exclusively by an indurated, 10 to 50 cm thick planar stratified fine ash deposit.

The following is a detailed description of the sequence at the different directions and distance from the caldera rim. The location of the profiles described is shown in Fig. 5.17.

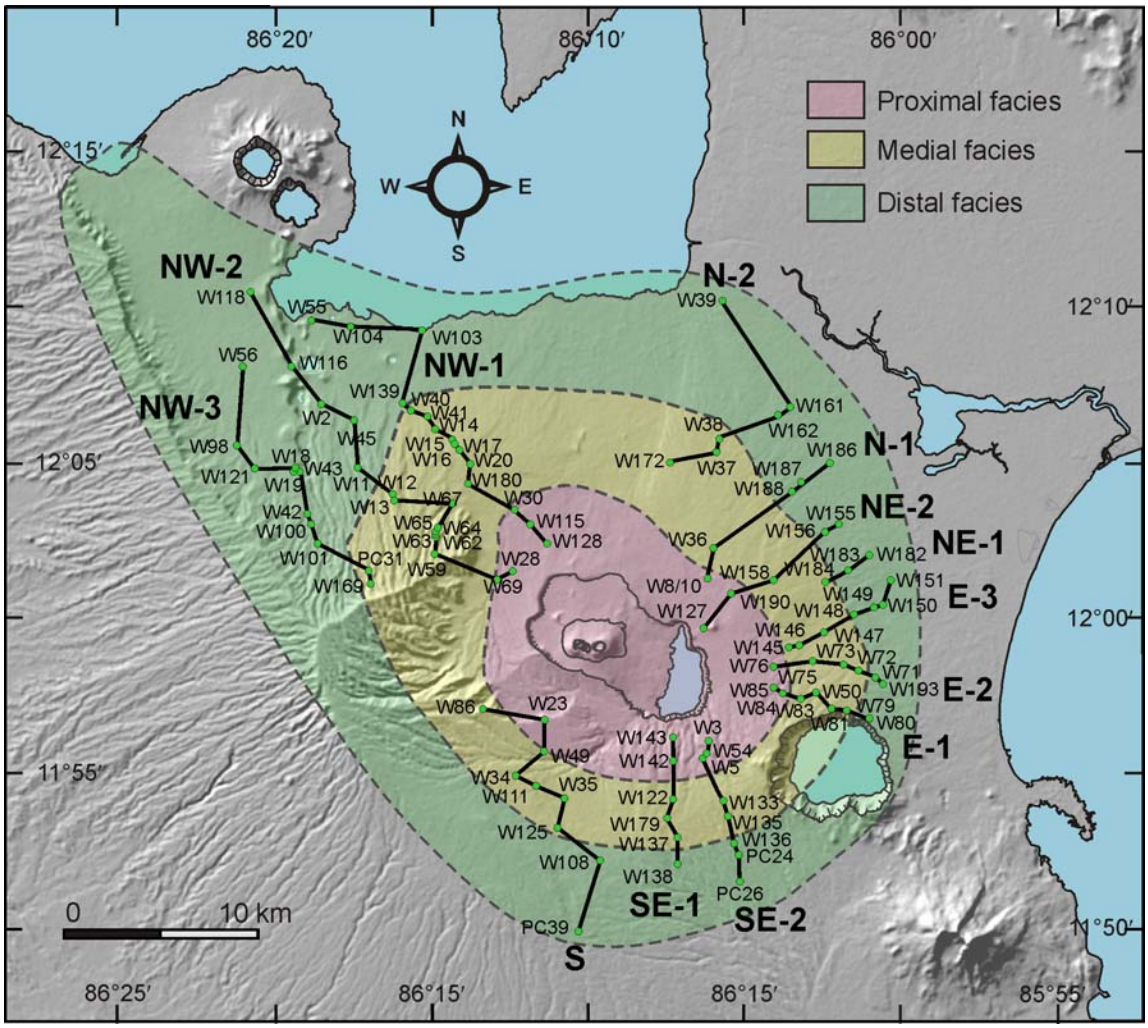

Figure 5.17: Profiles and facies distribution of the Masaya Tuff around the Masaya caldera. Note that towards the W and SW no outcrops of the MT were found and between profiles NW-1 and N-2 just a few small ones which do not show much detail.

South and south-east sector

Towards the south of the caldera, the lower part of the tuff is a massive, well-cemented, relative coarse-grained tuff with abundant plant molds; overlain by a cross bedded and dune sequence of lapilli and ash and even blocks in proximal exposures (Fig. 5.18). The upper part is dominated by a thick sequence of planar bedded fine-grained tuffs with accretionary lapilli. At exposures 9 km from the vent, the cross bedded lower portion is still present but thinned as well as the planar package. The most distal exposures consist only of a few planar beds that are massive with no structures at all (Fig. 5.18).

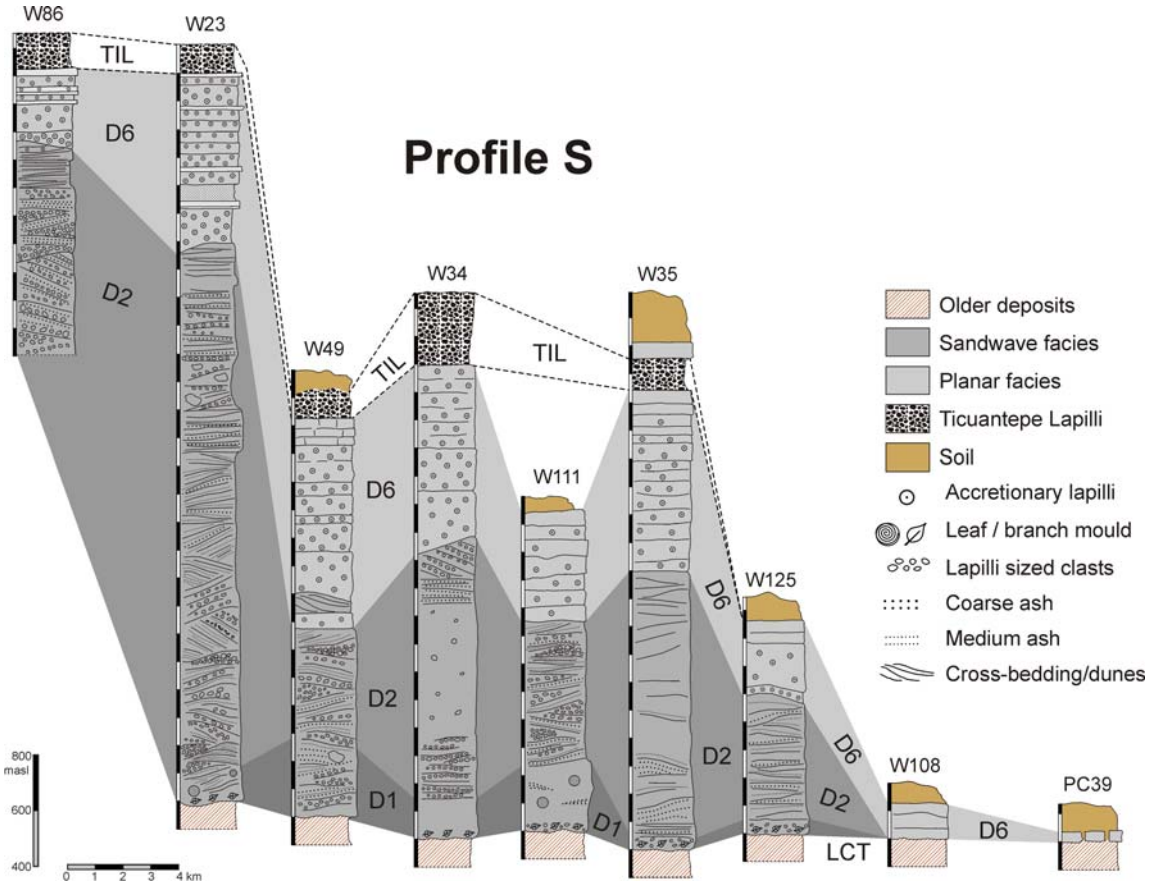

Figure 5.18. Profile south of the Masaya caldera showing the different facies of the MT present towards this direction and sandwiched between La Concepción Tephra and the Ticuantepe Lapilli. The correlation of the lowest subunit D1 is not so clear in some of the outcrops.

The sequence towards the SE is pretty similar to that south of the caldera, consisting of subunits D1, D2 and D6 (Fig. 5.19), with the difference that the massive subunit D1 is thicker than at exposures to the south. Here, the cross-bedded and dune-bearing subunit D2 is well exposed, reaching a maximum thickness of >1 m and at distal exposures (e.g. outcrop W136, Fig. 5.19) it shows planar wavy bedding. The overlying planar subunit D6 is consistently absent at the outcrops nearest the caldera rim, probably due to erosion. In one outcrop (W142), it was possible to recognize the soft massive deposit of D4 and parts of D3. The Ticuantepe Lapilli does not crop out at this side of the caldera.

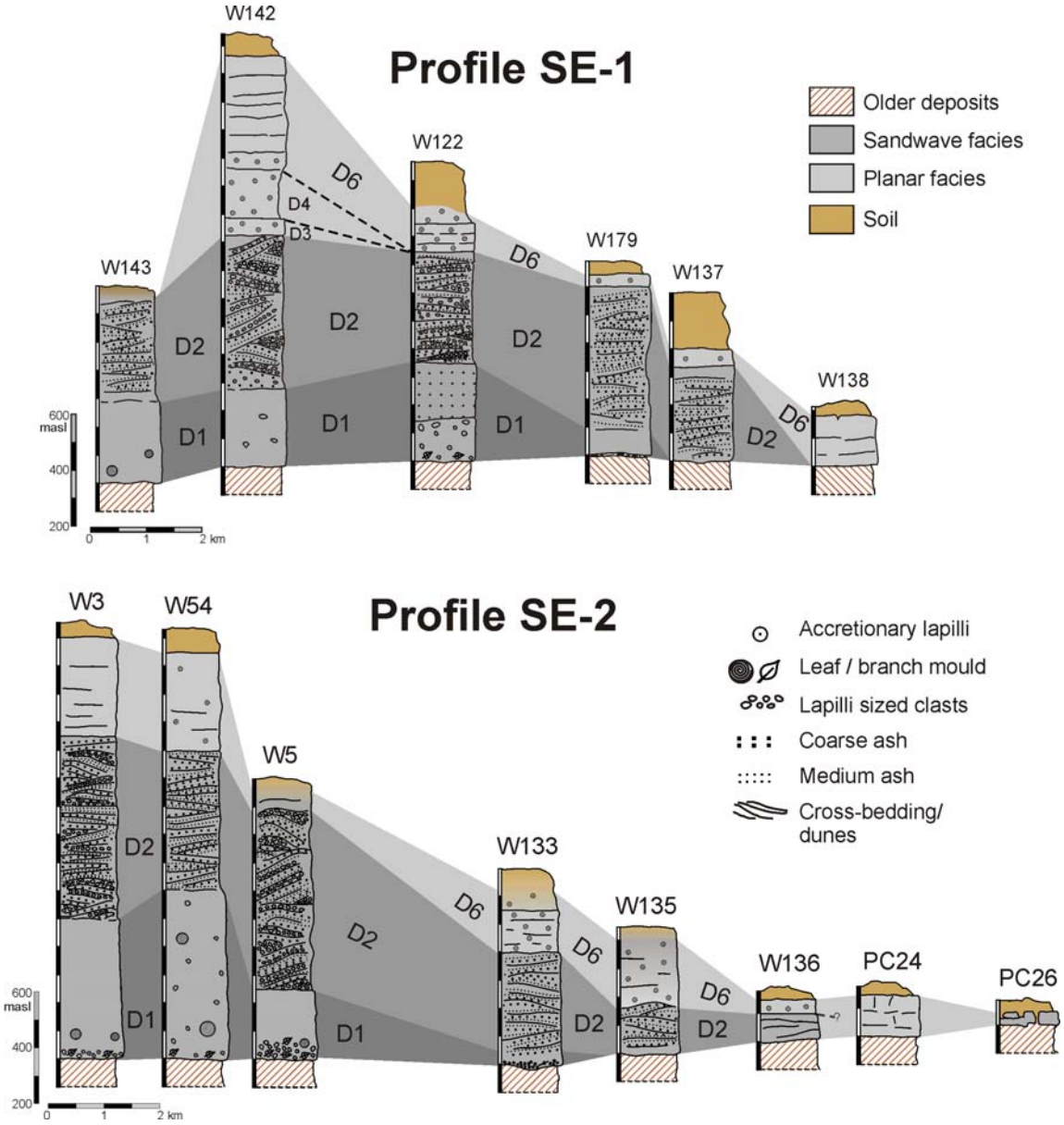

Figure 5.19: Profiles south-east of the Masaya caldera showing the different facies of the MT present towards this direction. Both profiles are pretty similar and it is possible to note that at the nearest outcrop to the caldera the subunit D6 is missing, probably due to erosion.

East, north and north-east sector

The MT sequence towards the east is illustrated in the three profiles shown in Fig. 5.20, which differ from each other. The sequence at profile E1 is very similar to that exposed at the SE of the caldera, showing a massive, coarser grained lower deposit (D1) at the more proximal outcrops, and the cross-bedded or dune interval (D2) overlain by a fine-grained planar tuff (D6).

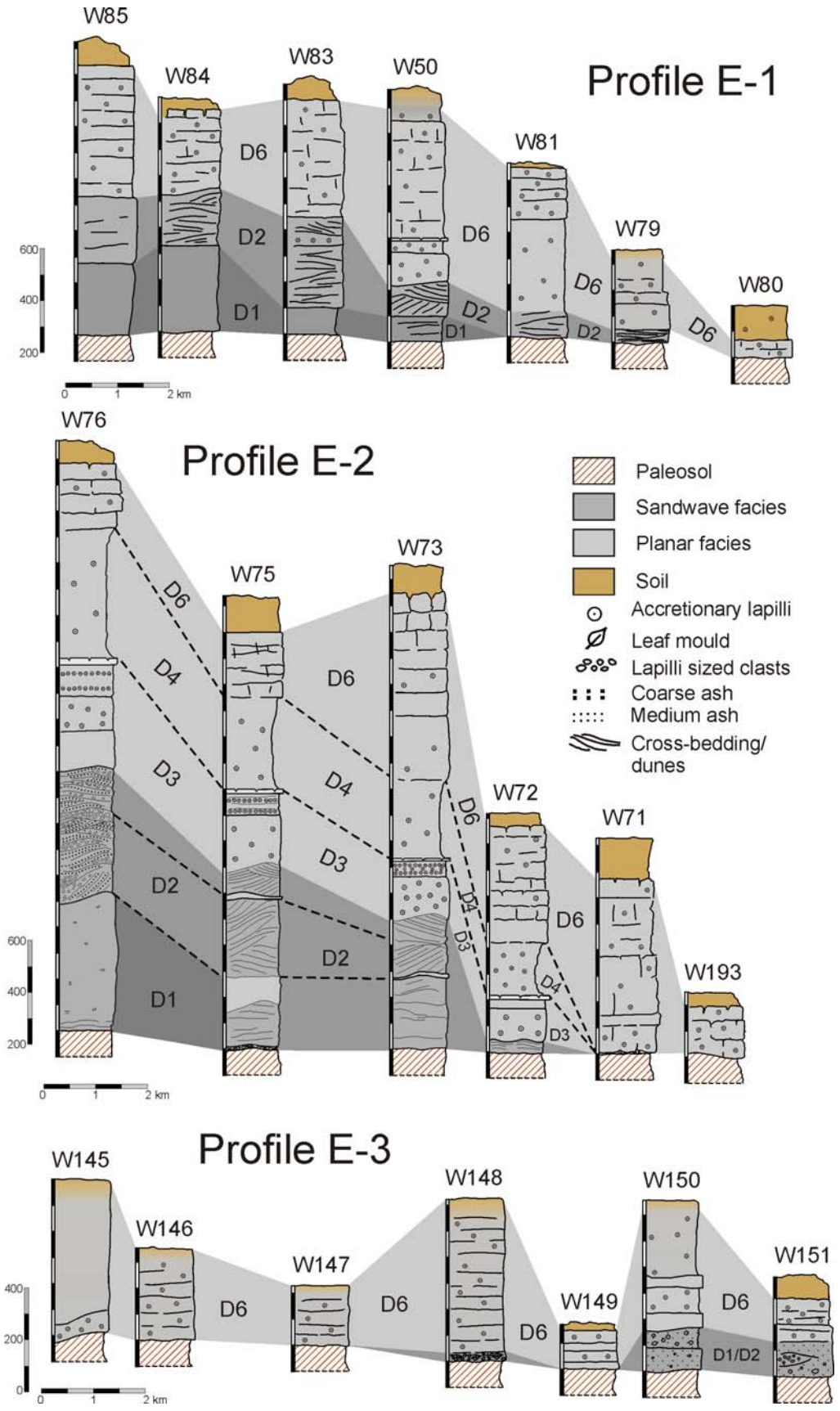

Figure 5.20: Profiles east of the Masaya caldera showing the different facies of the MT present towards this direction. Profile E-2 is the most complete showing almost all of the different MT subunits and their changes with the distance from the caldera rim.

The most complete section of the Masaya Tuff is the profile E2, which was exposed along the road Masaya-Granada as a result of the widening of the Inter-American Highway in April 2005. There it was possible to asses the facies changes with increasing distance to the source and five of the main six subunits of the MT could be recognized.
At the most distal outcrop (W193, ~11 km from the caldera rim), the MT is only a 40 cm tan indurated planar tuff with scattered accretionary lapilli (Fig. 5.20). At ~10 km (W71), the tuff is thicker (130 cm) and still consists of only planar bedded fine tuffs with accretionary lapilli. In contrast to W193, there is a fine thin layer of 1-2 cm of fine, glassy, dense and vesicular lapilli with no fine ash at the very bottom (Fig. 5.21). This layer has been also found in areas to the SE of the caldera and is interpreted as a blast deposit. At ~9.4 km (W72) most of the sequence is already present, with a lower 10 cm level of cross-bedding to undulated bedding (D2) overlain by a thick massive accretionary lapilli tuff, a thin layer very rich in small accretionary lapilli and a thin 4 cm hardened tuff with desiccation cracks at the top (D3). The soft massive tuff of D4 is also present, overlain by a ~1 m of planar beds. At 8.5 km (outcrop W75) the lower subunit D1 is much coarser and is formed by two main dunes, a lower coarser one dominated by dense juveniles and with abundant plant molds and an upper dune better bedded and with layers of round vesicular lapilli, both separated buy a fine 2-3 cm hard tuff. At 6.5 km from the caldera, at the outcrop W76, the subunits remain basically unchanged, except for D1 which is now build up by three main dunes, separated by very fine-grained indurated tuffs (Fig. 5.20). The lower dune is coarser grained and the lamination is faint, whereas the upper dunes are better bedded. The most proximal exposure lies at 4 km from the caldera rim (outcrop W76 at Fig. 5.20) and there the subunit D1 is exposed at the base as 1 m of massive poorly sorted concrete-like deposit overlain by well-bedded thick dunes (D2). It is not possible to distinguish single dunes like in outcrop W75. Profile E3 is different from the other profiles, exhibiting a smaller thickness of the MT (<1.2 m) and is clearly dominated by the planar bedded facies (Fig. 5.20).

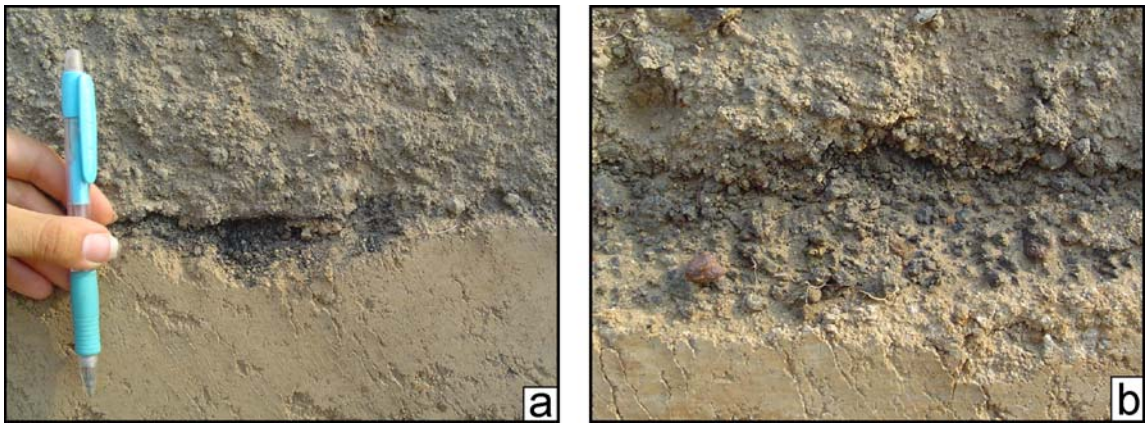

Figure 5.21: Photographs [**a**-**b**] of the fines depleted basal deposit (blast) at the base of the Masaya Tuff, in an outcrop 10 km E from the Masaya caldera.

The NE area of the caldera is characterized by the presence of the subunit D5, which does not crop out at other areas around the caldera. The profile NE-2 shows the coarser-grained, cross-bedded subunit D2 at the lower part, overlain by a thinned (max. 15 cm thick) subunit D3. Subunit D5 resembles subunit D2, but it has a higher stratigraphic position and is finer-grained and in some cases slightly cemented. The planar bedded topmost subunit D6 reaches here a thickness of ~1 m (Fig. 5.22).
At the short medial-distal profile NE-1, there is a cemented coarser grained planar bed at the bottom which is similar to the concrete-like subunit D1. This layer might represent the distal equivalent of subunits D1+D2. The subunit D5 is also present but much thinner, reaching a maximum thickness of only 30 cm and it is overlain by the fine beds with accretionary lapilli of subunit D6 (Fig. 5.22).

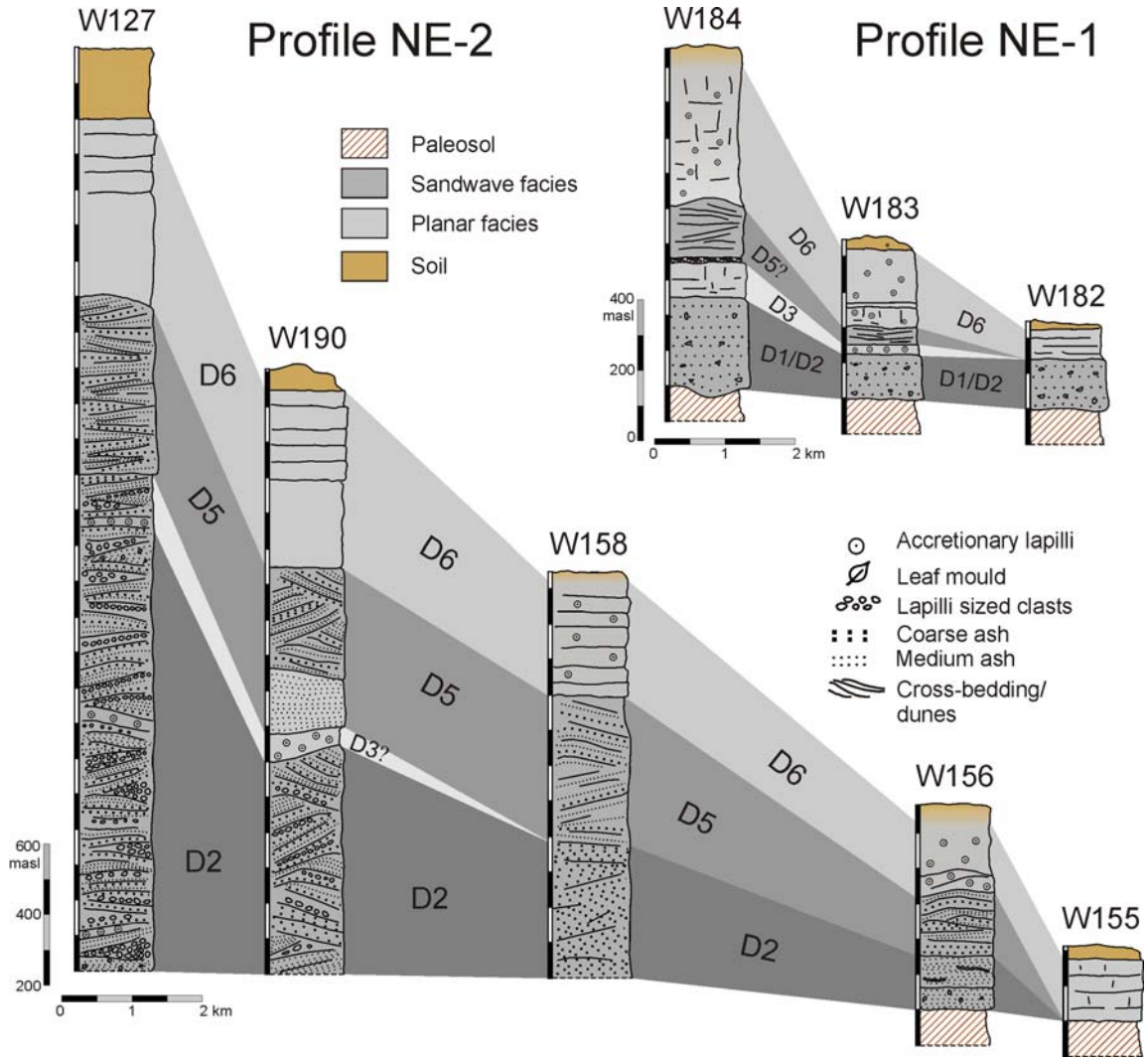

Figure 5.22: Profiles North-east of the Masaya caldera showing the different facies of the MT present towards this direction.

The area north of the caldera is characterized by a thick Masaya Tuff, at the localities near the caldera, where the base is not exposed. The cross-bedded subunit D2 is thick and coarse-grained, but it is not possible to distinguish different dunes or major surge events. At the nearest locality to the caldera (W10), which was used to define the vertical variations of the MT, all the subunits are exposed. However, some of them are missing in the other outcrops (e.g. subunits D5 and D6 at W8, or D5 at W36). At distal exposures (~15 km), the tuff is just 60 cm thick and consists of cross- and planar beds at the bottom and parallel planar beds with accretionary lapilli at the top (Fig. 5.23).

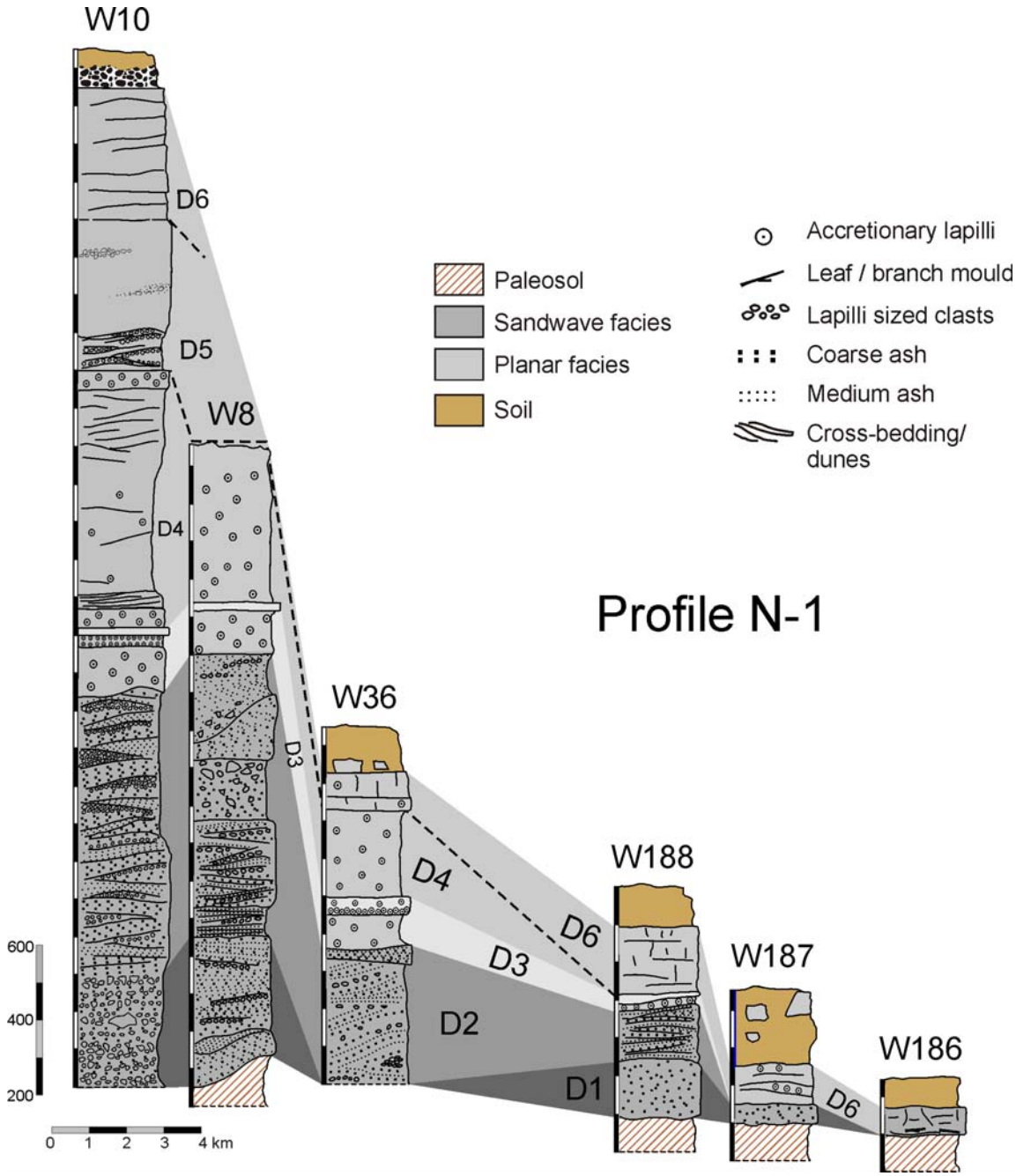

Figure 5.23. Facies variation with distance from the caldera towards the north. In profile N-1 are most of the MT subunits exposed.

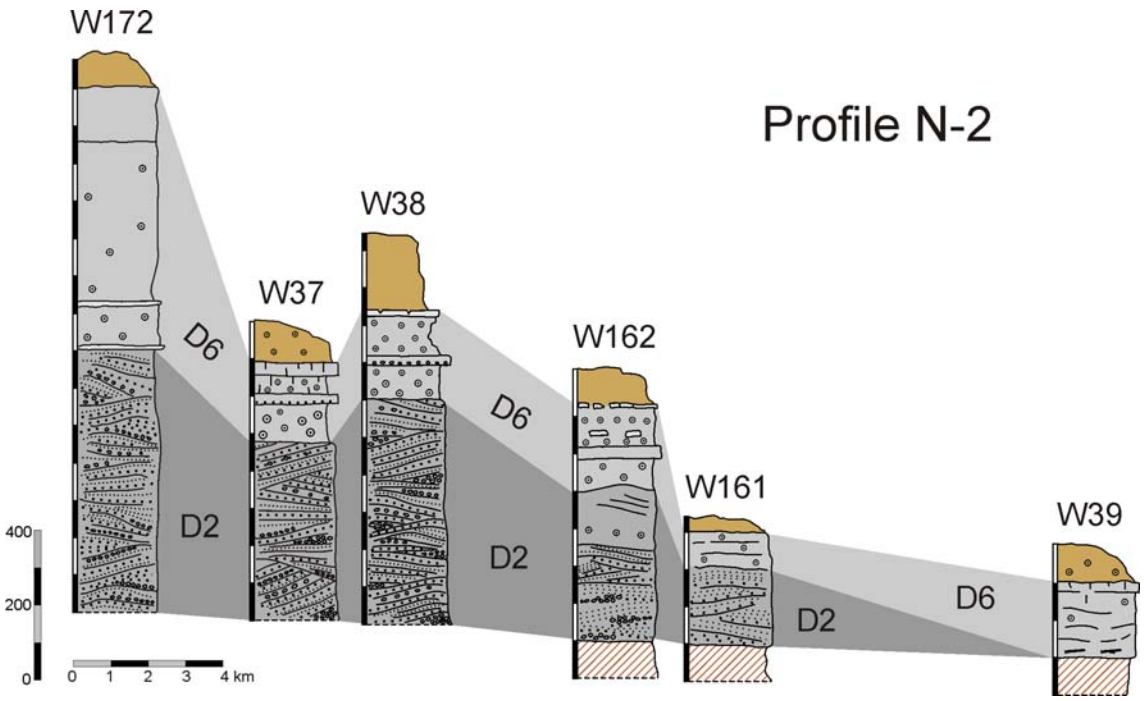

North-west

The NW area of the caldera is where the tuff reaches its maximum lateral extent, probably because the flows were more energetic towards this direction and also were influenced by the winds, especially the finer ash fraction. A detailed assessment of the facies changes at proximal exposures is not possible since there are no complete exposures in an area within 5 km from the caldera rim. The surge deposits likely filled a topographic low in the area of the Ticuantepe city and were blocked by the Sierras Las Cuchillas hills, thickening the deposits and leaving an almost flat area with a few not so deep road cuts like e.g. outcrops W128 and W115 in Profile NW-1 (Fig. 5.24). The deposits exposed along the Inter-American Highway, from the Masaya caldera to Managua city (Profile NW-1, Fig. 5.24), suggest that where the flows developed complex relationships due to nearby ridge, showing several dune beds and a more complex sequence like the one shown in Fig. 5.16, possibly due to overlapping flow tongues. At 10-15 km from the caldera towards Managua, the sequence becomes simpler showing a lower bed with faint cross bedding and fine planar tuffs with accretionary lapilli at the top. The most distal exposures at the Chiltepe peninsula show a thin, massive, altered tuff.

Where the flows interacted with the ridge (Las Cuchillas hills), part of them were able to surmount the hills, leaving the deposits which are now cropping out along the San Antonio road as shown in profile NW-2 (W59-W65 in Fig. 5.24). They consist of a coarser lower portion with abundant leaf molds, a middle cross-bedded dune part and a relatively thin (~40 cm) planar accretionary lapilli bearing beds (see Fig. 5.10). With increasing distance to the caldera they become thinner and consist of a couple planar beds with scarce accretionary lapilli.

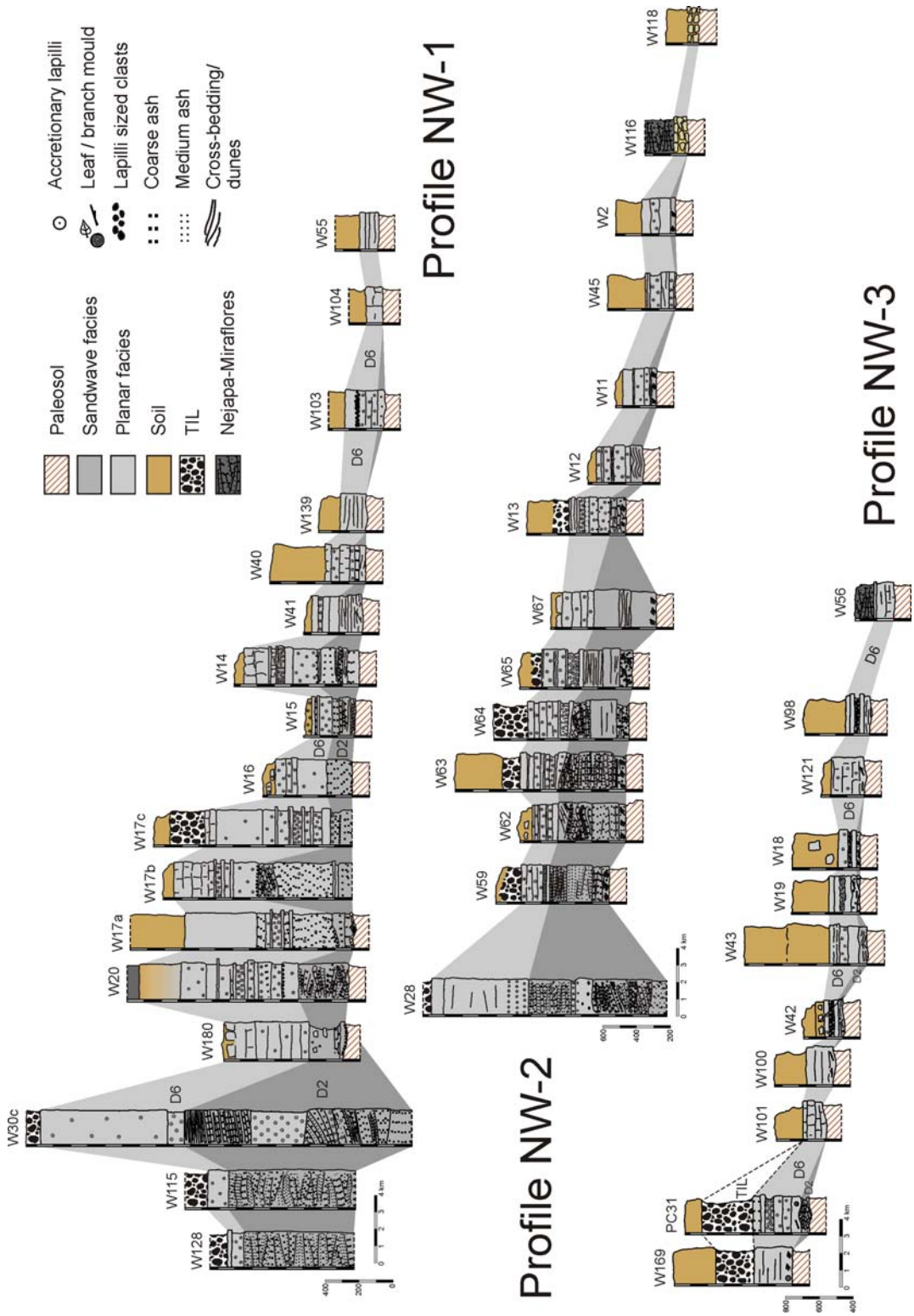

Figure 5.24. Facies variation with distance from the caldera to the NW, in direction to Managua city and the Chiltepe Peninsula.

The north-westernmost profile of the MT (Profile NW-3) is also located in a high topographic area of the older Las Sierras volcano. There the tuff is also thin, very altered and reaches a maximum thickness of ~70 cm. It consists of several planar beds where the lowermost exhibit at most of the outcrops cross bedding and the upper ones are fine-grained with accretionary lapilli (Fig. 5.24).

5.1.3.3 Discussion of facies variations

Previous authors (Wohletz and Sheridan 1979; Sohn and Chough 1989; Druitt 1992) have found proximal to distal facies variations in surges which mostly suggest that they are governed by the decrease in particle concentration and sedimentation rate with increasing distance from vent.

Wohletz and Sheridan (1979) found out a consistent pattern of facies distribution of sandwave facies in proximal areas, massive in medial exposures and planar facies in distal areas in several tuff rings and maars in the SW USA and northern Mexico. They interpreted this variation to a progressive deflation of an initially well-mixed turbulent low particle concentration surge near the vent.

Sohn and Chough (1989) made also facies analyses of pyroclastic surge deposits associated with tuff rings on Cheju Island, Korea. General trends are for the proximal deposits to be relatively unbedded, massive and disorganized, grading laterally into massive beds to sandwave beds and finally to planar or sandwave tuffs in the most distal reaches. They explained these lateral variations as a result of high particle concentrations, turbulent flow and a high deposition rate near the vent. Afterwards the parent surges turned more dilute, the sedimentation rate decreased and the traction bedding processes became increasingly dominant. Druitt (1992) studied the facies variation of the 18 May 1980 Mount St. Helens lateral blast and also concluded that proximal to distal variations are dominated by decrease in particle fallout rate and sedimentation rate with increasing distance from vent.

Summarizing the facies changes at Masaya, it is clear that at the most proximal areas the deposits are coarser-grained and poorly bedded. Farther away, the deposits are dominated by several meters of dunes and cross-beds, suggesting a high turbulence of the flows. At medial areas, the cross bedding is still present at the lower portion of the tuff but fine-grained planar beds with accretionary lapilli are capping the sequence. The distal areas are dominated almost exclusively by planar beds, although locally there could be some minor turbulent flows intercalated with the fine tuffs (e.g. subunit D5 at the northern part of the caldera).

These facies changes suggest a decrease in particle concentration with the distance from the vent, changing gradually from highly concentrated coarser grained deposits at proximal areas to sandwave structures (dunes, cross bedding). The dunes and crossed beds become finer upwards and farther from the vent. The distal tips dominated by planar fine tuff beds with accretionary lapilli mostly represent the finer material deposited by fallout and maybe partly by a weak lateral flow component where particles are carried along the ground in traction carpets, as suggested by Wohletz and Sheridan (1979). Although the MT is overall radially distributed around Masaya caldera, facies variations show that flow and deposition were affected by local topographic conditions, and some flows only expanded sectorially.

5.2 Ticuantepe Lapilli

The Ticuantepe Lapilli is a well-sorted, black scoria lapilli deposit overlying the Masaya Tuff which occurs at the north- and southwest areas of the Masaya Caldera (Fig. 5.25).

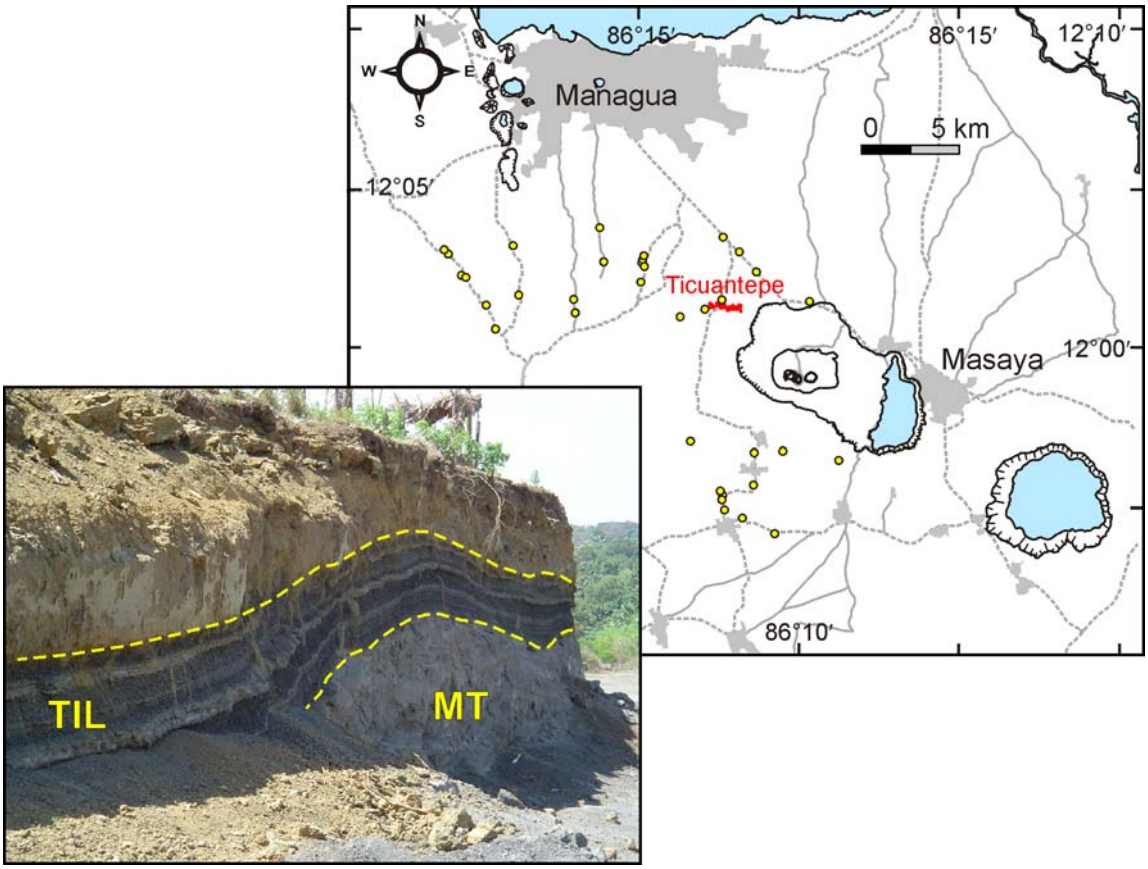

Figure 5.25: Studied outcrops (yellow circles) of the Ticuantepe Lapilli at the north- and south-western areas of the Masaya caldera, with the village of Ticuantepe highlighted in red. The inset is a picture of a proximal outcrop where the TIL (145 cm thick) mantles the topography left by the MT.

5.2.1 Components

The deposit consists of well-sorted vesicular to dense juvenile lapilli with ~5-15 vol.% of mostly light gray basaltic lava fragments (Fig. 5.26).

The vesicular scoria fragments are normally black to brownish, have elongated shapes and contain very small vesicles in hand specimen; the dense ones on the other hand, are light gray and have variable shapes: angular, cauliflower-like and spherical (Fig. 5.26). Both types contain abundant xenoliths of basaltic lavas and plutonic rocks with variable sizes, ranging from a few mm to even 40 mm. They consist of ~5 vol.% of plagioclase, olivine and clinopyroxene phenocrysts in a groundmass of tachylitic glass with <3 vol.% of plagioclase, Fe-oxides and clinopyroxene microlites.

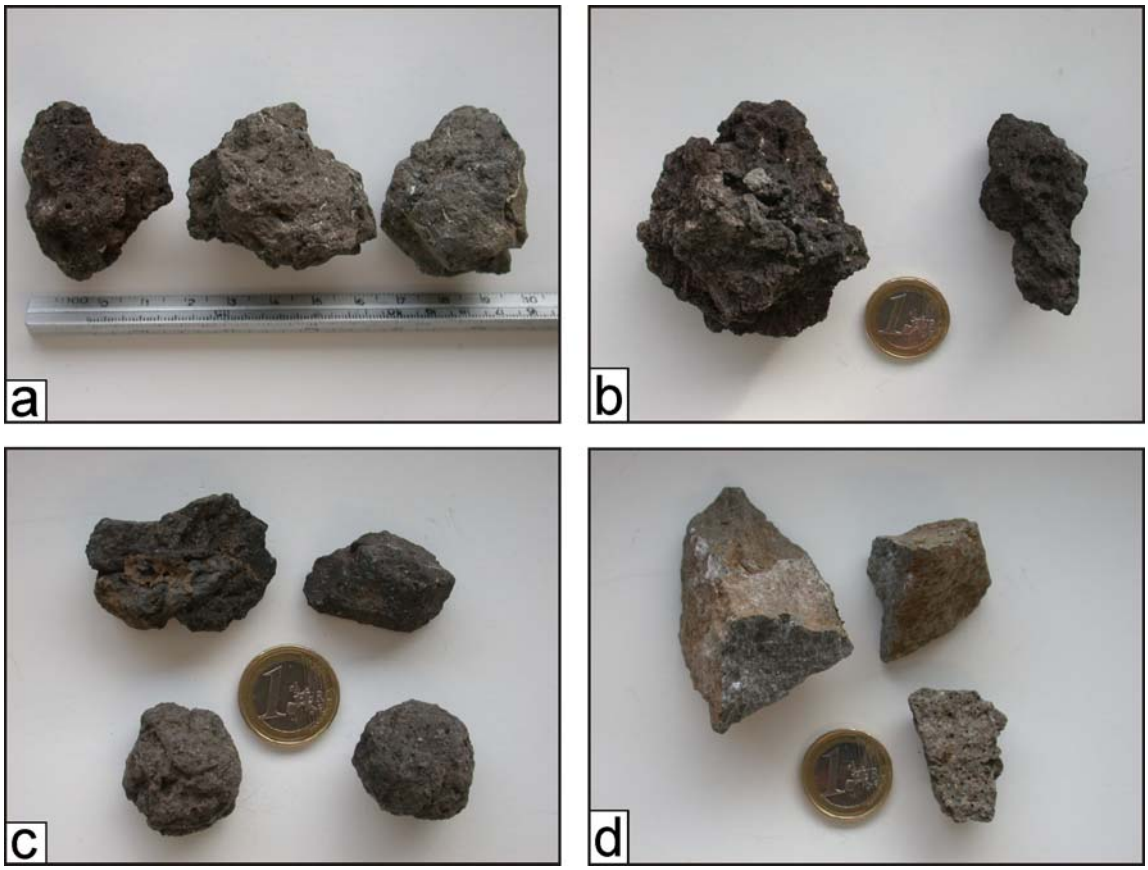

Figure 5.26: Main components of the Ticuantepe Lapilli. [**a**] The three main types of juvenile clasts: vesicular, intermediate and dense, from left to right. [**b**] Highly to moderately vesicular black fragments, some with elongated shapes and reddish colors. [**c**] Typical dense fragments with different shapes like cauliflower, angular and spherical. [**d**] Common angular light gray lithic fragments of TIL.

5.2.2 Internal stratigraphy

The Ticuantepe Lapilli deposit is subdivided by 3 finer-grained (coarse to fine ash) consolidated tuff layers (E2, E4, E6; Fig. 5.27) which separate 4 well-sorted lapilli layers (E1, E3, E5, E7). The juvenile lapilli are black to dark-gray (brownish when altered) vesicular scoria and abundant dense round clasts. The lithic content increases from bottom to top of the lowermost lapilli layer (E1), but no systematic variation could be detected in the upper layers.

5.2.2.1 Subunit E1

This subunit is a well-sorted vesicular and dense lapilli deposit with variations in the grain size and amount of lithic fragments. The maximum observed thickness is 47 cm at ~3 km from the caldera rim.

In the most proximal exposures it can be separated into three layers (Fig. 5.27):

[a] a lowermost well-sorted vesicular and dense lapilli layer with scarce big lithic fragments (~1 vol.% and sizes up to 90 mm). They are mostly fresh angular light gray basaltic lavas but there are also other basalts with different textures but all of them contain olivine.

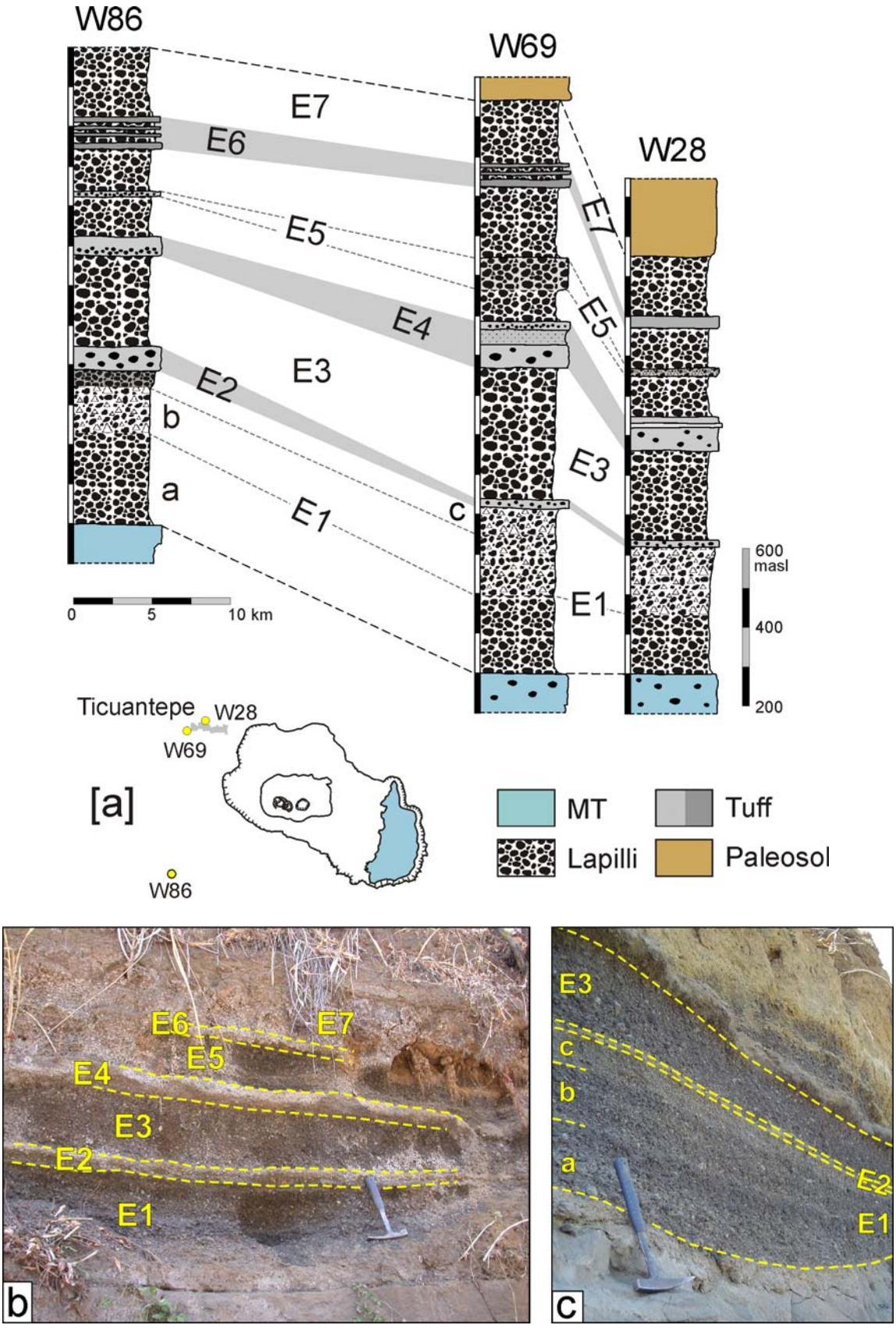

Figure 5.27: The Ticuantepe lapilli at the proximal areas. [**a**] Vertical stratigraphic sequence at outcrops W86, W28 and W69. [**b**] Photograph of the unit at the outcrop W28, located inside the Ticuantepe village. [**c**] Detail of subunits E1-E3 at outcrop W69.

[b] a layer similar to [a] of vesicular and dense lapilli but with smaller grain size and a higher amount lithic fragments (~5 vol.%).
[c] The top of the subunit is a finer and slightly indurated layer, characterized by an increase of the amount of lithic fragments to ~15 vol.%, most of them yellowish and whitish due to hydrothermal alteration.

The juvenile particles are mostly dense lapilli with plagioclase phenocrysts, with a density of ~1.5-2 g/cm^3, and a lesser amount of vesicular lapilli with a density of ~0.6-1 g/cm^3. Microscopically, the vesicular ones consist of tachylite with 40-50 vol.% of vesicles, mostly irregular-shaped and some round, with sizes ranging between 0.06 and 1.2 mm (Fig. 5.28a-c). The dense lapilli have less than 20 vol.% of tiny vesicles with sizes ~0.05-0.1 mm (Fig. 5.28). They also contain small xenoliths (visible at microscopic scale) and ~1 vol.% of phenocrysts, mostly zoned plagioclase but also olivine and cpx, some of them with large sizes (~1.6 mm). The matrix has ~2-3 vol.% of microlites, consisting of plagioclase needles, oxides and clinopyroxene.

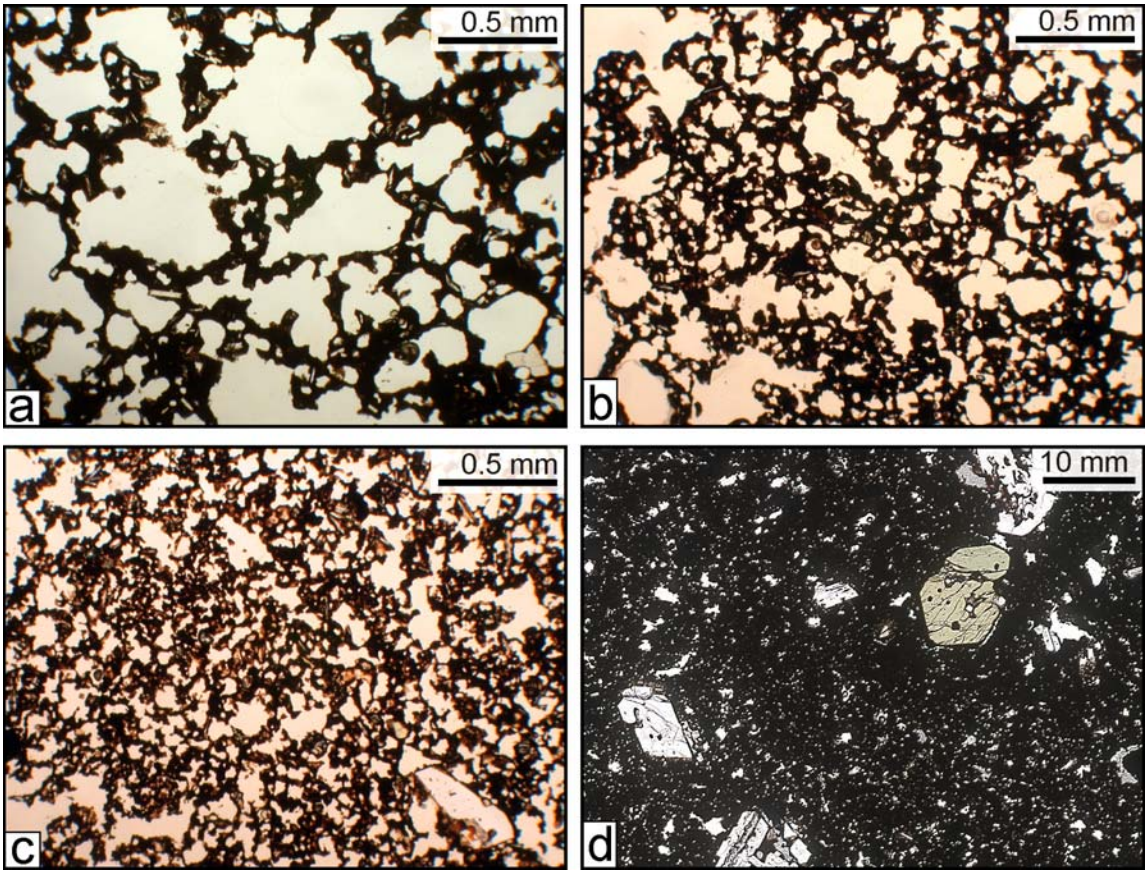

Figure 5.28: Microscopic images of the different types of juvenile fragments of the Ticuantepe Lapilli. [**a-c**] Vesicular fragments with 50-60 vol.% of mostly irregular-shaped vesicles, with decreasing vesicle size from [a] to [c]. [**d**] Scan of a thick section (~100 μm) of a dense clast with 18% of vesicularity and some plag+cpx phenocrysts.

5.2.2.2 Subunit E2
It is an indurated tuff with a maximum observed thickness of 6 cm and made by coarse ash, fine lapilli and whitish lithic fragments in a matrix of fine yellowish to grayish ash.

5.2.2.3 Subunit E3
Well-sorted vesicular and dense lapilli deposit, similar to E1a, but with a maximum observed thickness of 33 cm (Fig. 5.27). It contains ~5 vol.% of country rock, mostly gray fresh angular lavas with maximum grain sizes up to 39 mm but also a high amount of hydrothermal altered ones. In some outcrops even the juvenile fragments are hydrothermally altered.
Microscopically, the moderately vesicular juvenile fragments contain ~50 vol.% of irregular-shaped vesicles with large size variations, ranging from 0.1 to 3.6 mm (Fig. 5.28). The matrix is tachylitic with few microlites, and there is ~1-2 vol.% of phenocrysts, mostly euhedral plagioclase, olivine and clinopyroxene.

5.2.2.4 Subunit E4
Indurated fine ash grayish tuff with sparse lapilli fragments and a very consolidated, thin, yellowish fine layer at the top.

5.2.2.5 Subunit E5
This unit contains well-sorted vesicular and dense lapilli (φ 30-2 mm) and 1-5 vol.% of lithic fragments with a finer grained (φ 10-2 mm) horizon in the middle of the layer, ranging in thickness from 2-8 mm at proximal exposures. The matrix is composed of yellowish fine ash which makes more consolidated than the under and overlying layers.
Microscopically, the vesicular fragments are highly to moderately vesicular tachylite (50-60 % vesicularity, Fig. 5.28a, c) containing small round vesicles (0.06-0.1 mm), irregular large ones (1.7 mm max.) and a few plagioclase and olivine microlites. It also contains 1-2 vol.% of plagioclase and olivine phenocrysts, as well as rare clinopyroxene and Fe-oxides. It includes abundant xenoliths and inclusions of denser tachylite.

5.2.2.6 Subunit E6
It is an indurated ash tuff made up by an intercalation of yellowish fine ash with fine lapilli with a maximum observed thickness of 7 cm at a distance of 3 km from the caldera.

5.2.2.7 Subunit E7
The topmost subunit E7 is a well-sorted vesicular and dense lapilli with ~2% of lithic fragments and an average grain size between 4 and 30 mm. It is similar to E5 containing also a thin hardened fine ash horizon at the middle of the subunit (Fig. 5.27).

5.2.3 Lateral facies changes
The maximum observed thickness in the nearest outcrop to the caldera rim is 145 cm, whereas the minimum is 22 cm at 5 km to the NW (off the dispersion axis). At proximal exposures, the TIL presents all the subunits described above but at distal areas the tuffs thin out, just one or two remain or they disappear completely (Fig. 5.29) leaving a single lapilli layer.

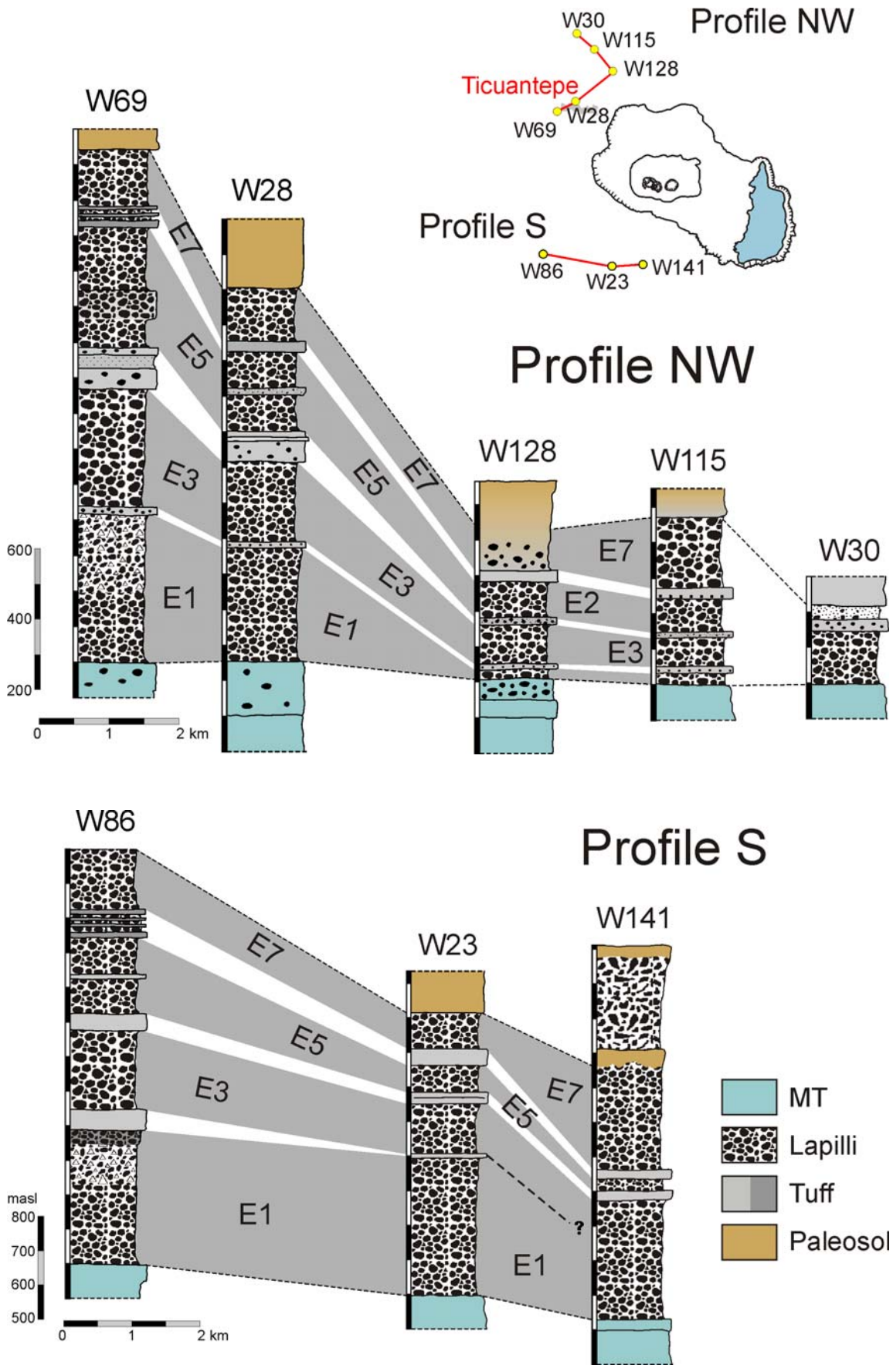

Figure 5.29: Profiles showing the variations of the Ticuantepe Lapilli with distance to the NW and S of the caldera.

5.3 Volume

5.3.1 Thickness distribution and volume

5.3.1.1 Masaya Tuff

The generalized isopachs map shown in Fig. 5.30 was constructed for the Masaya Tuff, based on the thickness data collected from 214 outcrops. Some of these outcrops yielded only a minimum thickness because the base of the unit was not exposed or the unit was partially eroded. The MT isopachs show a radial pattern around the caldera, with a more or less even distribution in all directions out to the 50 cm isopach (Fig. 5.30). Towards the east and south-east no outcrops could be found (just like for the underlying units); if there was any deposition in this area it must have been limited due to the topographic high formed by Las Sierras volcano.

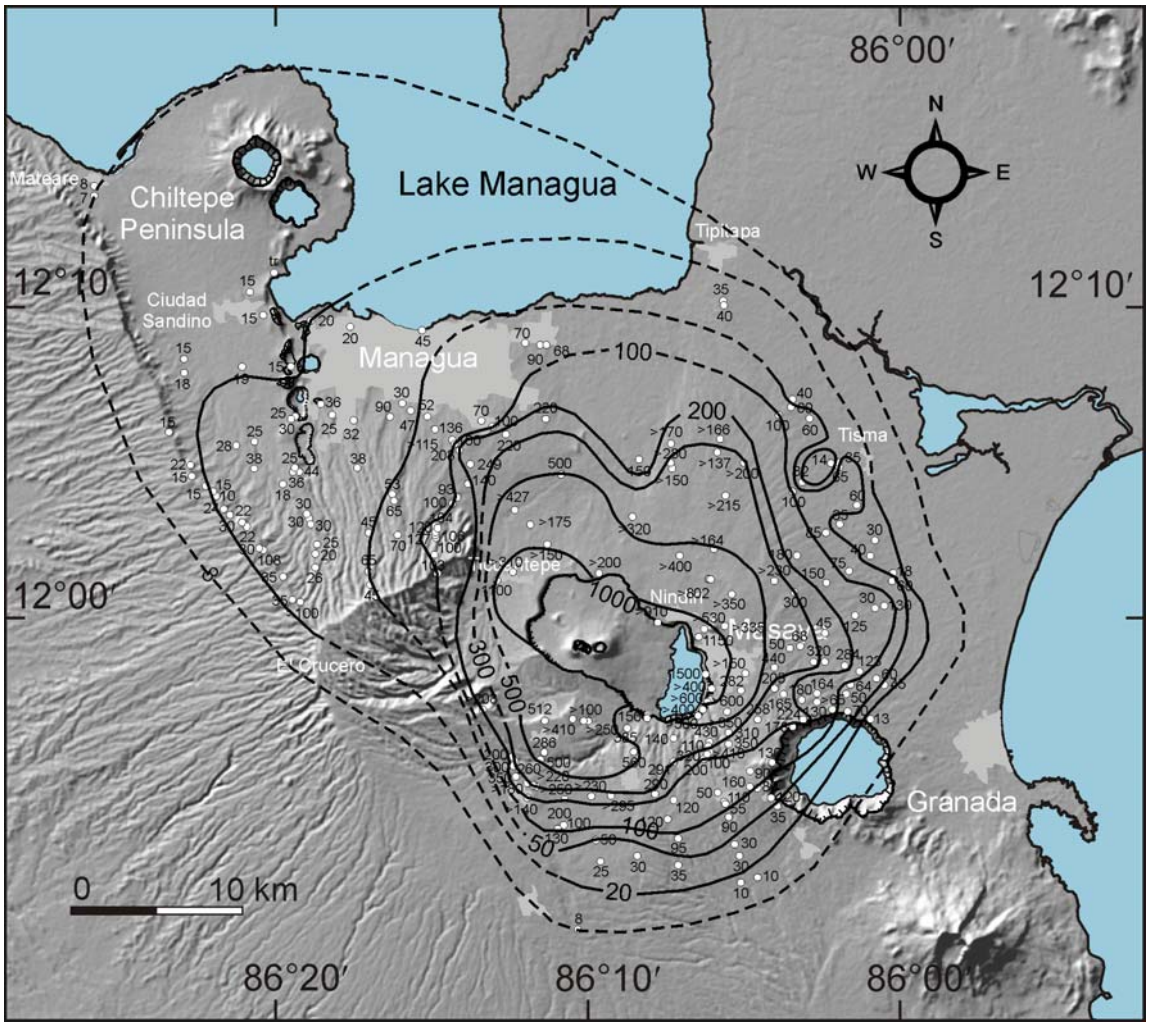

Figure 5.30: Isopach map (thickness in centimetres) for the Masaya Tuff. Note the radial distribution of the tuff and the wider spreading towards NW. At the SW part of the caldera the topographic high of Las Sierras volcano hindered the spreading of the surges.

The more distal isopachs are elongated to the NW, indicating increasing influence of the wind on distal deposition from the surge clouds. The thickness decreases from 15 m at the caldera rim to 1 m at a distance of 10 km, but thicknesses of ~7-8 cm are still observed near Mateare, 35 km from Masaya Caldera or near Jinotepe, ~15 km to the south (Fig. 5.30). The MT deposits buried a paleotopography formed by ridges of older deposits from Apoyo caldera, as can be seen from the curved isopachs in this area. Such areas are south-east of the caldera and towards the western rim of Apoyo caldera as well as north-east in direction to Tisma; there, local thickness variations are so dramatic that they could not be drawn in the map .
Bice (1980) proposed the northeast corner of the Masaya caldera as the source of the Masaya Tuff, but our new isopach maps do not constrain a specific vent site inside the caldera; this is partly due to most of the proximal MT deposits being eroded at the top and therefore giving a minimum thickness only and the lack of good quality exposures all around the caldera rim.
A diagram of the natural logarithm of isopach thickness versus the square root of the area enclosed by each isopach was constructed for the MT. Based on this, a bulk deposit volume of 3.3 km^3 was calculated according to Pyle (1989). The dense rock equivalent (DRE) volume of erupted magma was estimated as ~2 km^3 by subtracting the estimated volumes of lithic fragments and of porosity. Previous volumes for the Masaya Tuff were calculated by Bice (1980) as 4.3 km^3 DRE and Williams (1983a), who used Bice's data beyond the 1 m isopach and estimated a minimum bulk volume of 5.5 km^3.

5.3.1.2 Ticuantepe Lapilli

Bulk deposit isopachs for the Ticuantepe Lapilli were constructed based on 35 exposures, located at the south-west and northwest of the caldera, with the same data gap as for the older tephra units (Fig. 5.31). The limited amount of exposures showing the complete sequence (which are those shown in Fig. 5.29) and erosion evidences present in other outcrops did not allow to draw single isopach maps for the main subunits E1, E3, E5 and E7. The Ticuantepe Lapilli erodes easily because it is a relative loose deposit which lies right below the present soil of the area NW and SW of the Masaya caldera.
The thickness distribution of the TIL suggests a source in the western portion of the caldera and a dispersion axis to the north-west (Fig. 5.31). The bulk volume of the Ticuantepe Lapilli on land was calculated after Pyle (1989) as 0.35 km^3, equivalent to ~0.1 km^3 of dense rock.

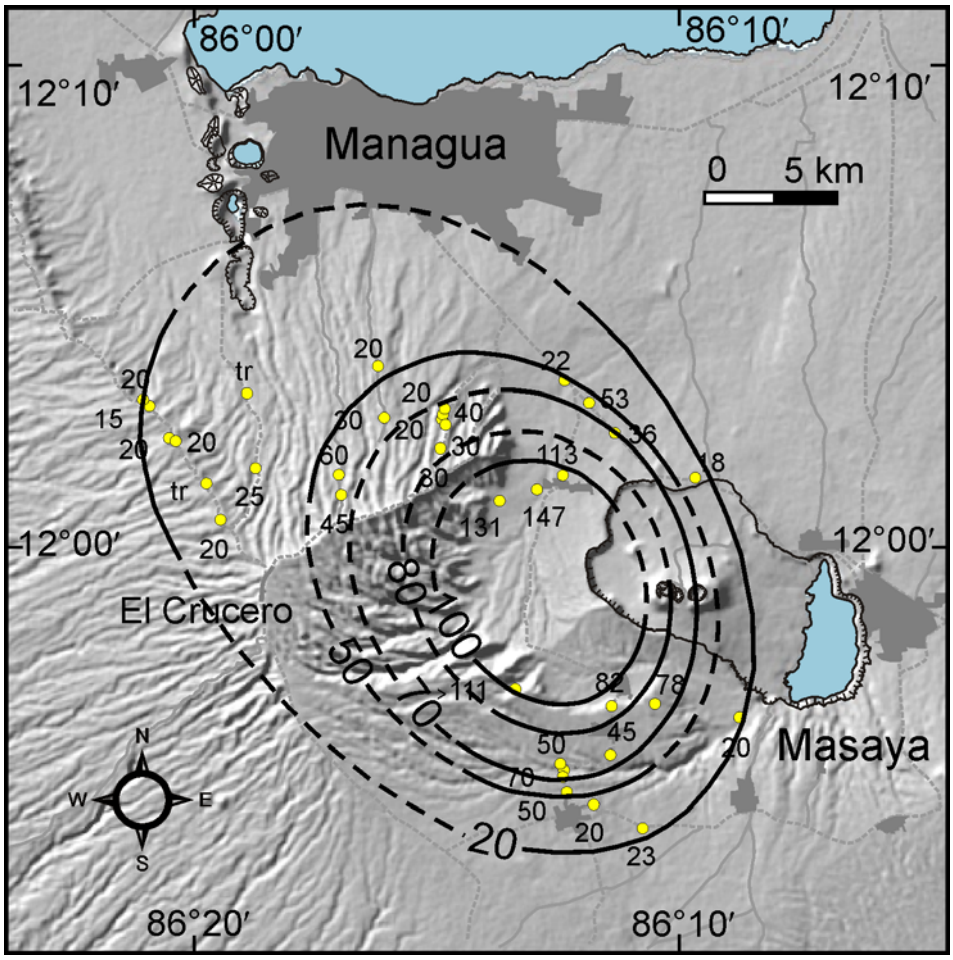

Figure 5.31: Isopachs (in centimeters) for the whole Ticuantepe Lapilli deposit on land. Dashed lines are drawn where the isopachs were extrapolated.

5.4.2 Distal tephra and total volume of the eruption

Marine ash layers chemically similar to the Masaya Tuff glass were found in three cores from the Pacific seafloor offshore Nicaragua. The ash layers were found in gravity cores collected during the cruises SO173 and M54. All three layers are located at the continental slope, two of them were found in the same cores containing the layers correlated with the LCT-MTL. The MT correlated layers locate at shallower depths of less than 50 cm bsf, with the exception of core SO173/3-18 (~1.5 m bsf) and have similar thicknesses ranging from 3 to 5 cm.

The correlation of these ash layers with the Masaya Tuff was made based on chemical similarities of the tephra with the MT glass (Fig. 5.32), and the presence some cm deeper in the sequence of a mafic layer chemically similar to the LCT-MTL and/or a felsic layer correlated with the Chiltepe Tepha.

An isopach map for the total material transported and deposited during the MT eruption, considering the marine distal ashes at the Pacific, is shown in Fig. 5.33.

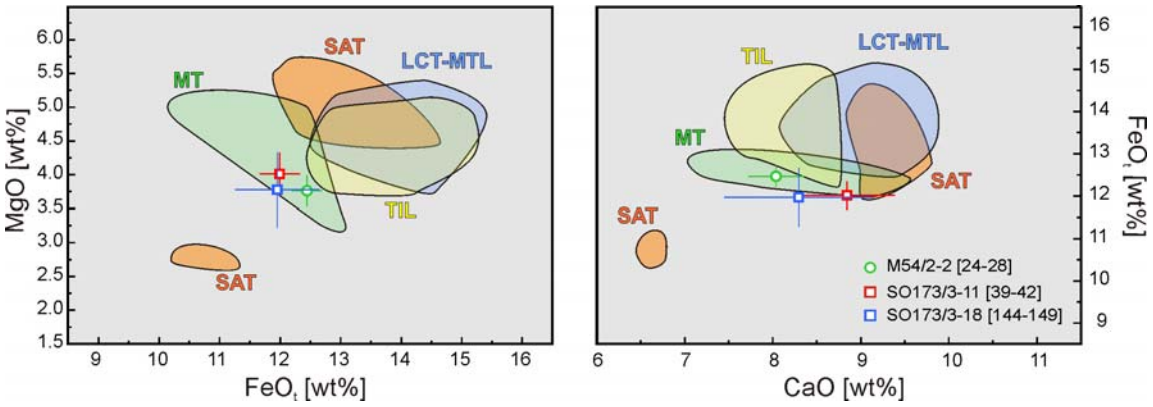

Figure 5.32: Chemical correlation of the glass composition between some of the marine ash layers collected in the cruises M54 and SO173 and the youngest Masaya Tephra (SAT, LCT-MTL, MT-TIL). Symbols represent the mean value from all measurements of a sample, with the corresponding standard deviation.

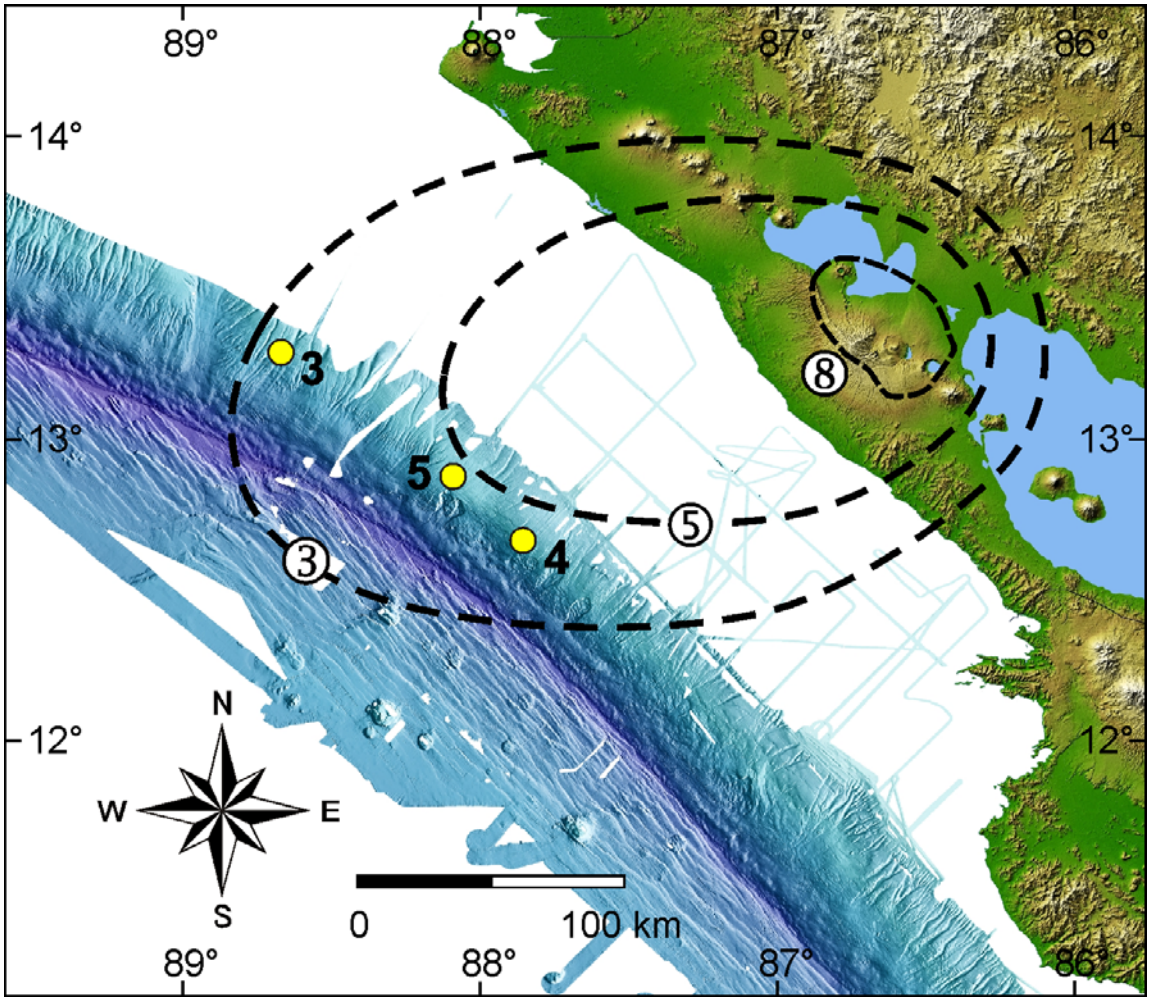

Figure 5.33: Distal isopachs in centimeters for the Masaya Tuff deposit based on correlations made with 3 marine tephra layers found at the Pacific offshore Nicaragua. The dots give the location of the gravity cores containing the layers and indicate the thickness.

The total volume for the MT deposit was calculated in 9.6 km³ (~3.9 km³ DRE), using the method of Fierstein and Nathenson (1992); ~65% of this volume was deposited as distal ash.
The total volume of tephra produced by the MT-TIL eruption, including the distal ashes, was calculated in 10 km³ (~4 km³ DRE).

5.4 Eruption parameters

5.4.1 Eruption column height and wind speed

The eruption column height of the Masaya Tuff cannot be simply calculated by comparison with models, but it can be done for the Ticuantepe Lapilli. The calculations are only for the whole deposit, since the sequence described from E1-E7 is present in only a few outcrops, not enough to construct feasible isopach and isopleth maps of the different subunits.
Whole deposit isopleth maps of juvenile (MP) and lithic fragments (ML) for the Ticuantepe Lapilli are shown in Fig. 5.34, though the small amount of data both show a similar pattern with the axis towards NW.

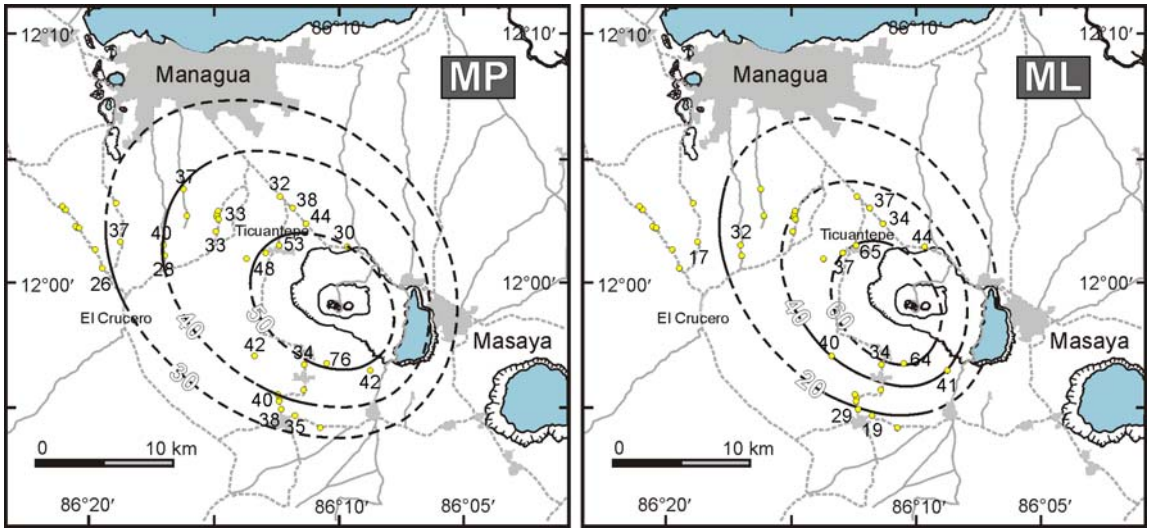

Figure 5.34: MP and ML isopleth maps for the Ticuantepe Lapilli deposit. Contours and size data are given in milimeters.

Comparing the downwind and crosswind ranges of the isopleths of Fig. 5.34 with the models of Carey and Sparks (1986) yields eruption column heights for the TIL eruption between 21-30 km, with the best quality data pointing to a maximum height of 26 km (Fig. 5.35) which was affected by wind speeds of the order of ~20 m/s (Fig. 5.35). Other models like those of Fig. 5.36a-b yielded similar results, just the diagram for lithic fragments (density=2500 kg/m³) shows a nice trend with a much lower height of ~14 km (Fig. 5.36c).

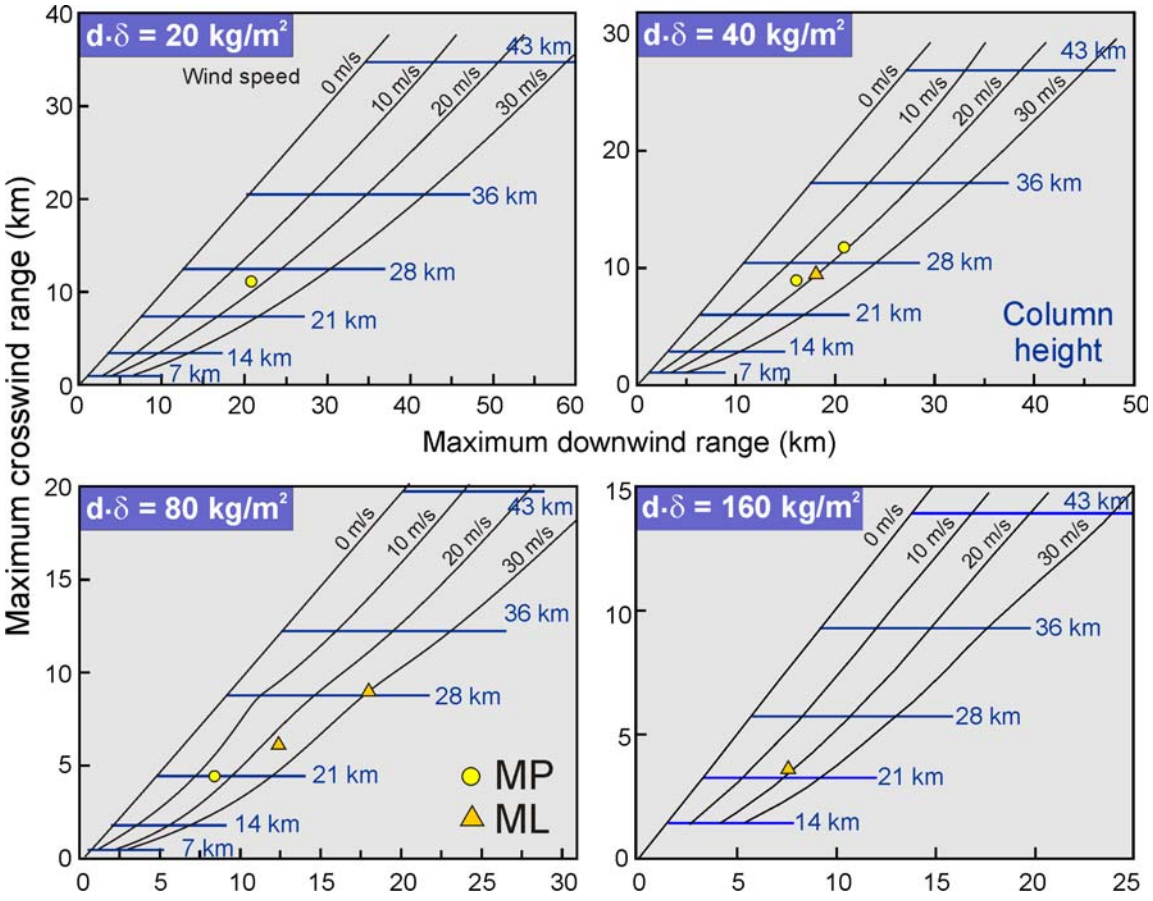

Figure 5.35: Crosswind range versus maximum downwind range for the MP and ML isopleths of the TIL. The fields are those from the Carey and Sparks (1986) models.

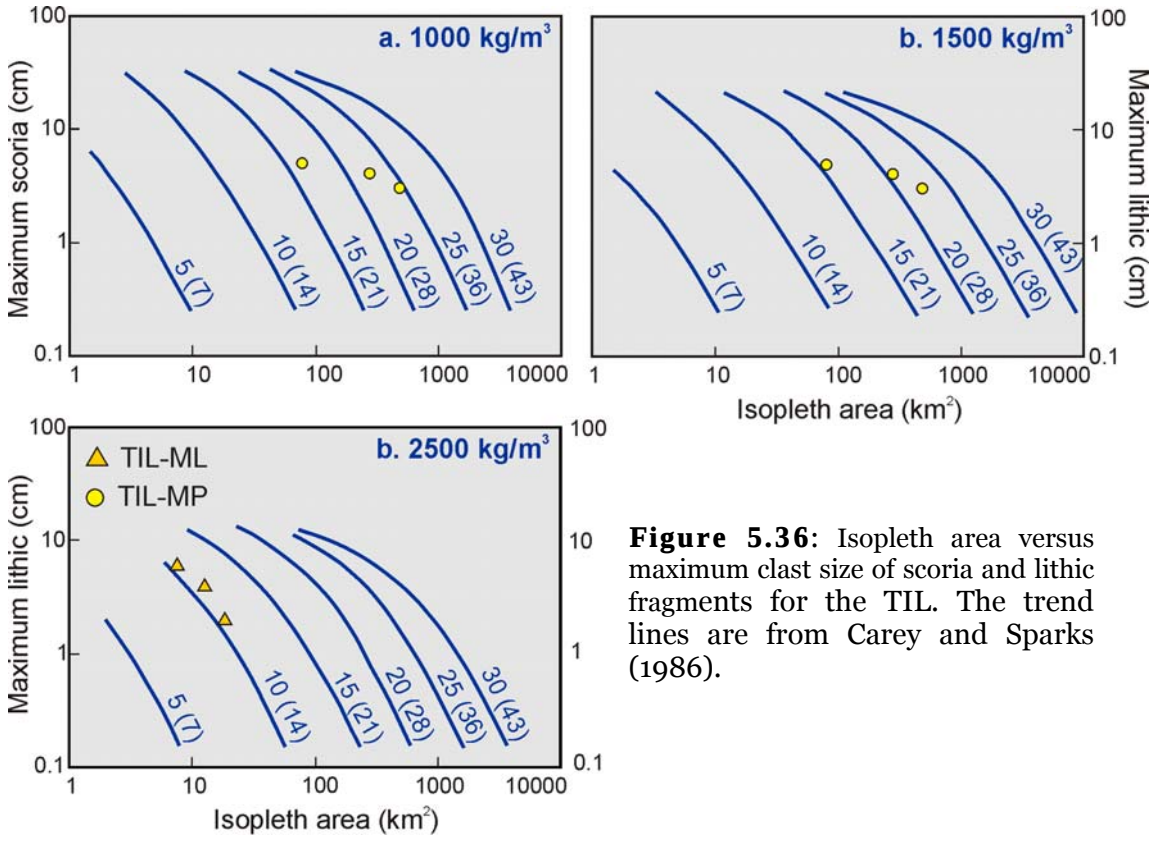

Figure 5.36: Isopleth area versus maximum clast size of scoria and lithic fragments for the TIL. The trend lines are from Carey and Sparks (1986).

5.4.2 Mass eruption rates

To estimate the mass flux of the TIL eruption the diagram of Wilson and Walker (1987) was used (Fig. 5.37). Unfortunately most of the maximum juvenile and lithic fragment size yielded results that are not reliable, since they plot below the dashed line. The only data point that plotted above the line indicates a mass flow rate between 10^7 and $3x10^7$ kg/s.

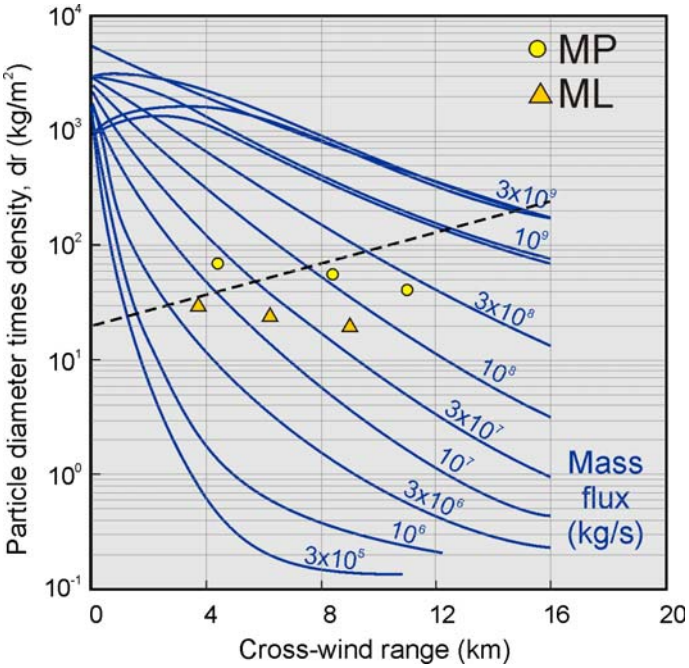

Figure 5.37: Mass flux rates for the Ticuantepe lapilli after Wilson and Walker (1987). Data above the dashed line is considered reliable.

The data of mass flow rate and the eruption column height obtained by the previous methods were subjected to a cross-check using the diagram of Woods (1988), as shown in Fig. 5.38.

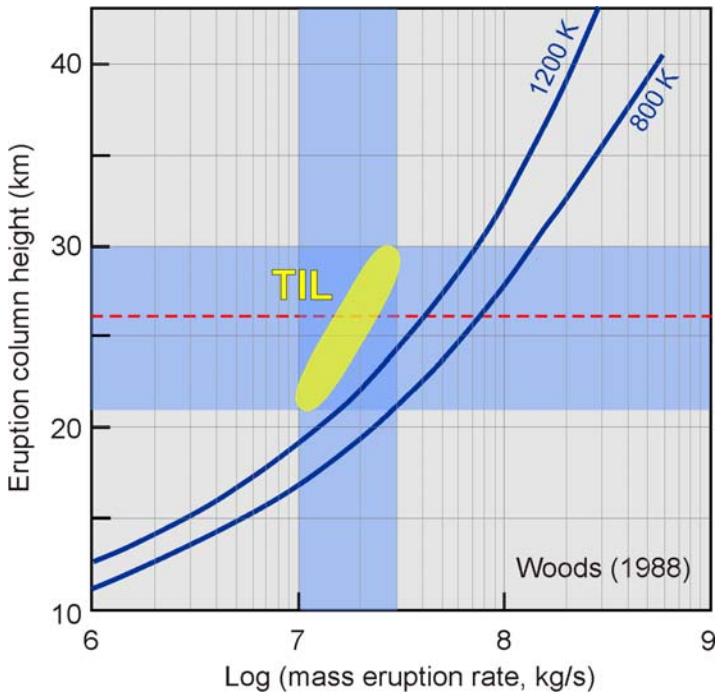

Figure 5.38: Eruption column height versus log of the mass eruption rate for the TIL. The temperature lines are from Woods (1988).

The blue areas on the diagram illustrate the ranges of column height and of mass flux obtained for the TIL with the models of Carey and Sparks (1986) and Walker and Wilson (1986), respectively. The yellow ellipse relates both parameters and show that both data are reasonable, since they plot near the 1200 K curve of Woods (1988).
Based on the calculated DRE volume for the Ticuantepe Lapilli and the density of basaltic magma (2700 kg/m^3), the erupted mass for TIL was estimated in 2.7x10^{11} kg, and with such a mass flow rate indicates that the TIL eruption lasted from 3 to 8 hours.

5.4.3 Dispersal characteristics

The Ticuantepe Lapilli fallout deposit has a wide Plinian dispersal in thickness (Fig. 5.39) as well as in grain size (Fig. 5.40). The Masaya Tuff is also plotted in the diagram of Fig. 5.39 only as a comparison, because the MT was produced by a different eruptive mechanism and its thickness distribution pattern was controlled by a different transport and depositional mechanism. Yet the diagram emphasizes the unusually wide distribution of the MT.
The MT was produced by series of phreatomagmatic eruptions where magma-water interaction played an important role in the magma fragmentation and therefore in the grain size and distribution characteristics of the deposits. In this way the Masaya Tuff eruption could be classified as a very large "Surtseyan" eruption.

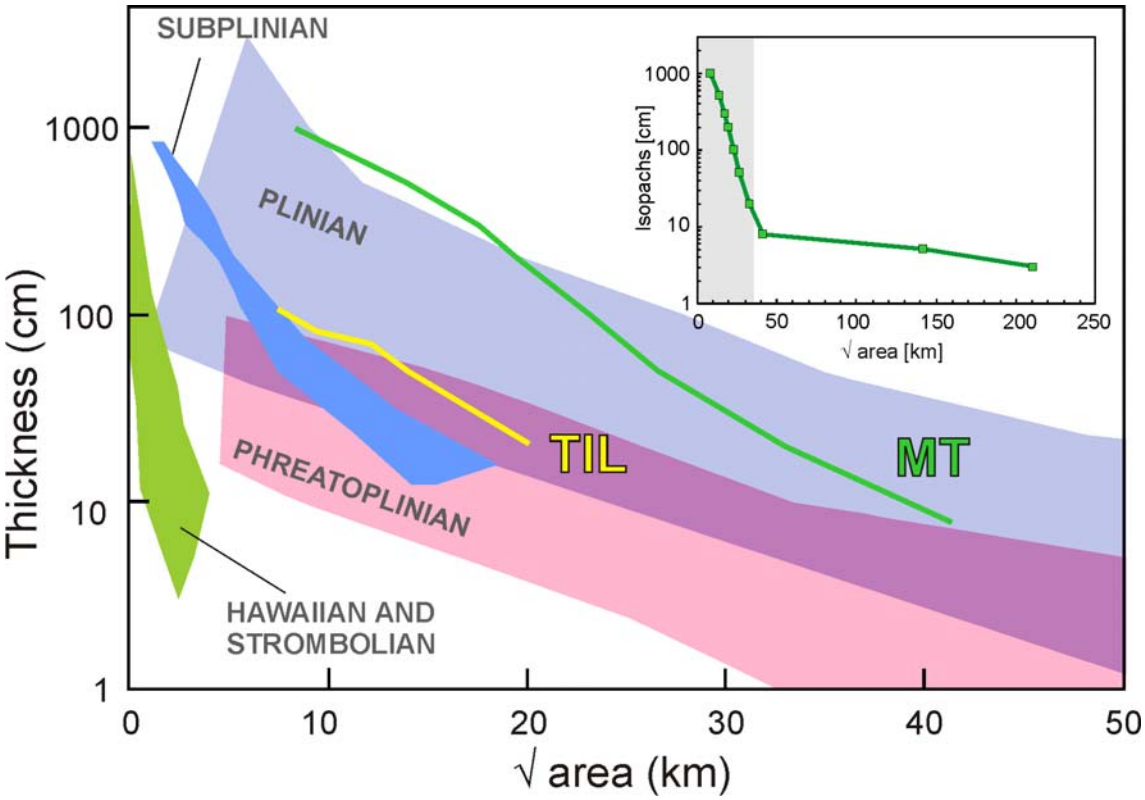

Figure 5.39: Diagram ln isopach versus square root of the area enclosed by the isopachs for the Ticuantepe Lapilli. The MT is also plotted in the diagram, just for comparison. The fields of Plinian, Subplinian and Phreatoplinian eruptions are from Houghton et al. (2000). The inset at the top right corner shows the same diagram but in a larger scale, in order to represent the distal deposits.

The discrimination diagram of Pyle (1989) considers both types of eruptions, magmatic and phreatomagmatic, but it requires the half distance thickness parameter (b_t) and the grain size half distance (bc) which are lacking for the Masaya Tuff. The Ticuantepe Lapilli has a b_t=3 km, a b_c=18.2 km for juvenile fragments, and bc=6.8 km for lithic fragments, which place it in the Fig. 5.40 plot clearly in the Plinian field. The half distance ratio for juvenile fragments is very high and locates outside the diagram.

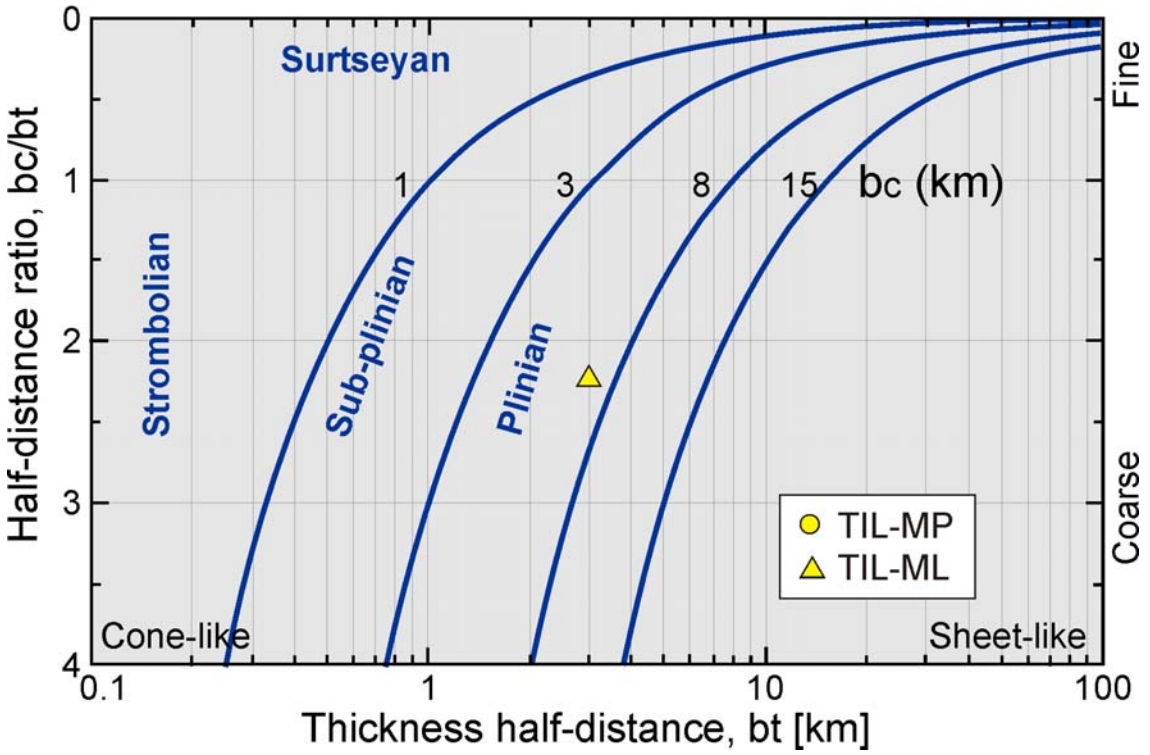

Figure 5.40: Classification scheme of Pyle (1989) based on the thickness half-distance versus half distance ratio for the maximum juvenile (MP; out of the diagram with a bc/bt of ~6) and maximum lithic fragment (ML) of the Ticuantepe Lapilli.

5.5 Interpretation

The lithological characteristics of the Masaya Tuff like poor sorting, high ash content, abundance of dunes and cross-bedding as well as the radial distribution around the caldera, support the interpretation of a pyroclastic surge deposit given by Williams (1983a). The low vesicularity of most of the juvenile clasts, presence of armored lapilli and abundant accretionary lapilli, rims of hardened ash around branch molds and the cementation of the deposit in most of the exposures, suggest that the surges were wet and formed from phreatomagmatic eruptions that involved groundwater and probably lake water in the pre-existing caldera. The presence of abundant leaf molds and a local blast deposit at the base of the tuff suggests the beginning of the Masaya Tuff eruption was a sudden catastrophic lateral blast that destroyed the vegetation all around the caldera. The absence of charcoal despite the abundance of plant molds indicates a low temperature during transport.

The proximal-distal facies distribution in all directions from the Caldera is consistent with what has been observed in other phreatomagmatic surge deposits around the world, changing from massive to crude bedded coarser deposits through sandwave dominated facies with abundant dunes and cross-bedded sequences to planar beds at distal areas. The facies changes can be interpreted as product of particle concentration and sedimentation rate decrease from proximal to distal areas.

In the case of the Masaya Tuff, the distal deposits and the upper part of the sequence in medial ones are dominated by fine grained planar beds containing accretionary lapilli. This characteristics and the elongation of the isopachs beyond the 50 cm towards the NW (the dominant direction of winds), support the idea that they are mostly (but not completely) fallout fine ash produced by the surge, as was already suggested by Bice (1980). In some distal outcrops around Managua city it was possible to find evidences of lateral transport like undulated lamination or low-angle cross-bedding at the bottom of the planar beds.

The Ticuantepe Lapilli fallout deposit shows that the final stage of the eruption was able to generate a Plinian eruption column (reaching maximum heights of 21-30 km) when availability of water for magma-water interaction decreased but not declined completely. The deposit show characteristics of limited magma-water interaction, as indicated by the tuff intervals E2, E4 and E6 and the finer grained layer at the top of the subunit E1, the abundance of hydrothermal lithic fragments, and the presence of poorly vesicular juvenile clasts. The source of this eruption was probably a vent located at the NW side of the caldera. Calculated mass flow rates of ~10^7 kg/s suggest the eruption had a duration of 3-8 hours.

The complete eruptive period evacuated ~ 4 km^3 of magma, and at least the half of this volume was carried out by the wind and deposited as distal ash in the Pacific Ocean.

Chapter 6

Geochemical characteristics of the Masaya Tephras

Masaya volcano is interesting not only for having produced highly explosive basaltic eruptions but also for the chemical characteristics of its products. It is one of the few arc volcanoes in Central America and the Caribbean that possesses a tholeiitic affinity (Walker 1989), with the magmas showing distinctive geochemical features such as high FeO contents, high concentrations of large-ion-lithophile (LIL-) elements and unusual $^{87}Sr/^{86}Sr$, Ba/La and ^{10}Be, which are interpreted as slab signals (Walker et al. 1990; Walker et al. 1993; Morris et al. 1990; Carr et al. 2004). Walker et al. (1993) interpreted the apparent chemical homogeneity of the Masaya volcano lavas and pyroclasts with time to reflect a large "open-system" reservoir.
This chapter shows that there are compositional variations between and within the younger Masaya tephras that can be attributed to fractional crystallization as well as to different mantle sources.

6.1 Magma compositions

The five youngest Masaya tephra units can also be classified as tholeiitic basalts, with SiO_2 contents of 50-52 wt% and MgO of 3.9-4.8 wt%, except for a few samples of the Masaya Tuff which have 52-53 wt% of silica and plot right at the limit of basalt to basaltic andesite (Fig. 6.1). They also have high Fe_2O_3 contents (12-15 wt%) and relatively low alkalies (3.5-4.3 wt%). The c. 60 ka older Plinian Fontana Tephra (FT; Wehrmann, 2005) shown for comparison is more evolved with a basaltic-andesitic composition.
Comparison of these tephras with average compositions of island arc tholeiites and calc-alkaline basalts (Perfit et al. 1980), shows that they contain higher SiO_2, TiO_2, FeO, Na_2O and P_2O_5 and lower CaO than average island arc basalts. The more mafic LCT-MTL, in fact, have similar TiO_2, SiO_2, Al_2O_3 and Na_2O contents to those of the average MORB.
In terms of chemical compositions, the 5 studied Masaya Tephra units form three separate groups in all variation diagrams (Figs. 6.1-6.4): the SAT, LCT-MTL and the MT-TIL. This supports the field-based interpretations that LCT and MTL are different facies of the products of one eruption, and that TIL represents a terminal phase of the MT eruption.

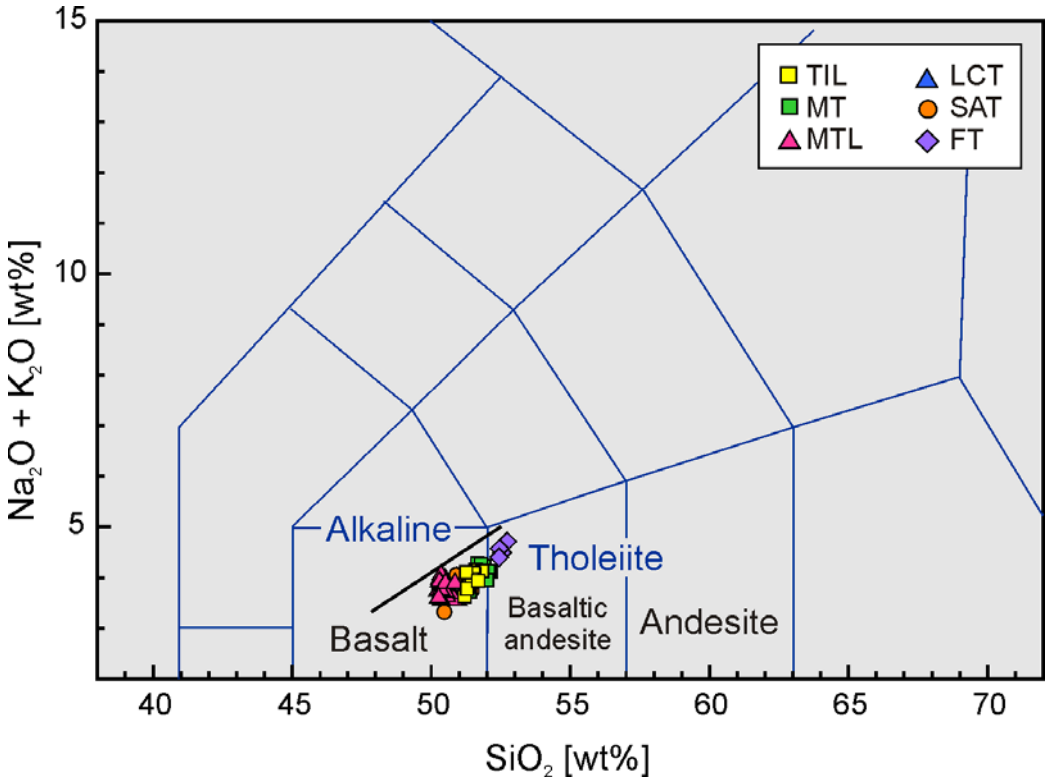

Figure 6.1: Total alkali-silica (TAS) diagram for the youngest Masaya tephras (field boundaries of Le Maitre et al. 1989). The older Fontana Tephra (FT) is included for comparison. Bulk-rock compositions are normalized as anhydrous. The black line is from McDonald and Katsura (1964) divides alkaline series from subalkaline or tholeiite series.

6.1.1 Major element compositions

Analyses of bulk scoria samples with XRF show that the SAT and LCT-MTL are less evolved than the MT-TIL. The older SAT reaches the highest MgO contents (4.6-4.8 wt%) and, at comparable MgO, has higher SiO_2 and K_2O but lower TiO_2, Fe_2O_3 and P_2O_5 contents than the LCT-MTL (Fig. 6.2). The MT-TIL has the lowest MgO, TiO_2 and Fe_2O_3, and the highest SiO_2, Al_2O_3 and Na_2O contents, underlining its most evolved character (Fig. 6.2). The general increase in silica, aluminum and alkalis together with a decrease in iron and titanium with decreasing MgO would be expected from differentiation by fractional crystallization of the common phenocryst phases (pl, cpx, ol, mt). However, the unsteady variations particularly of SiO_2 and K_2O with decreasing MgO between the three groups already shows that they can not all be related to each other by fractional crystallization.

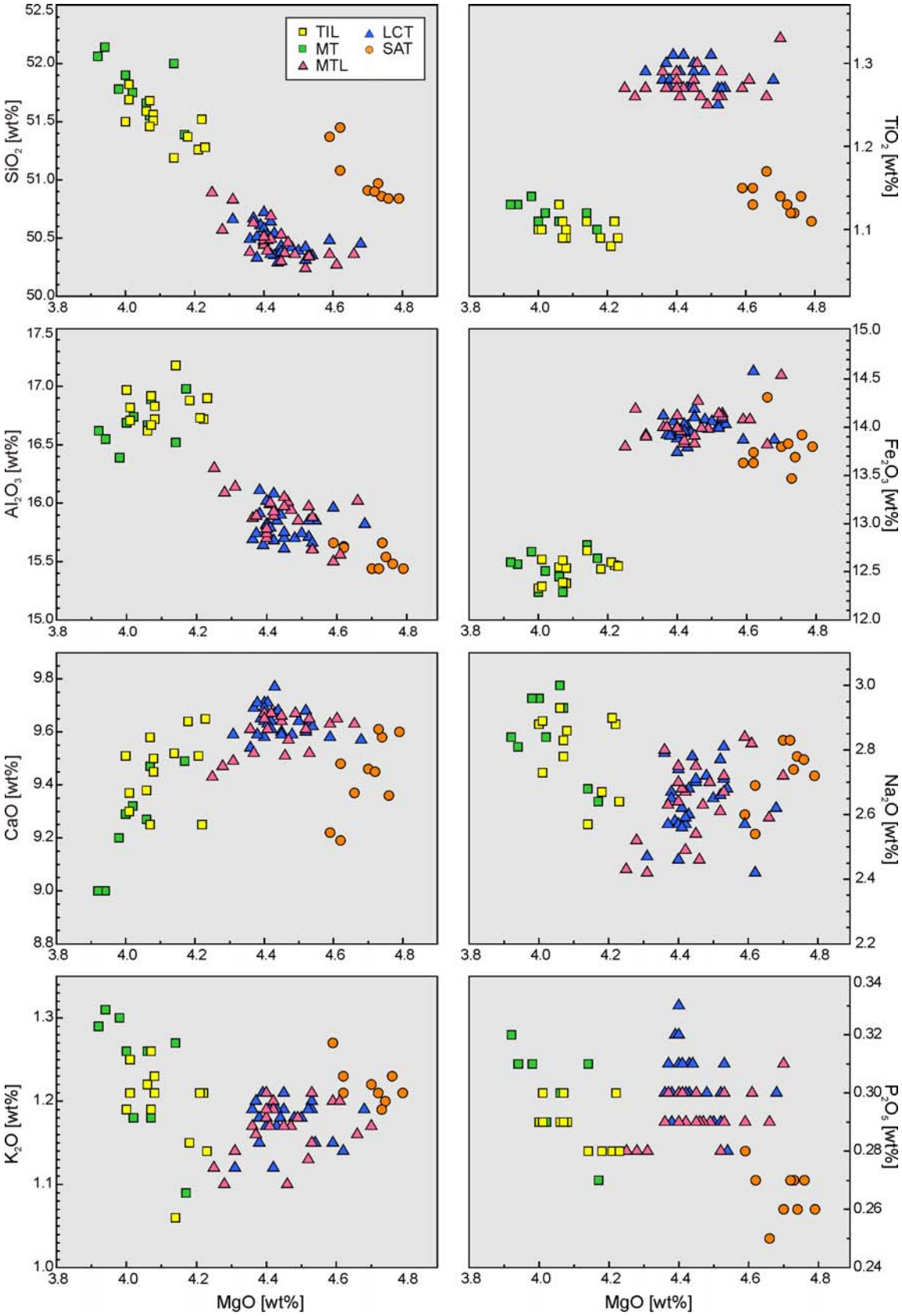

Figure 6.2: Major element variations using MgO as an index of fractionation for the youngest Masaya tephras.

6.1.2 Trace Elements

The low concentrations near XRF detection limits of trace elements compatible with mafic mineral phases, such as Cr, Co and Ni, imply that significant fractionation of olivine and clinopyroxene was involved in forming the present rock compositions. The less evolved SAT and LCT-MTL have retained higher contents of compatible elements like Co and V than the MT-TIL (Fig. 6.3). The decrease in V, together with Fe_2O_3, with decreasing MgO suggests fractionation of Ti-Fe oxides. Sr, which is compatible to plagioclase, increases with decreasing MgO through all three groups suggesting that no or only minor plagioclase fractionation occurred as supported by the Al_2O_3 variation (Fig. 6.3).

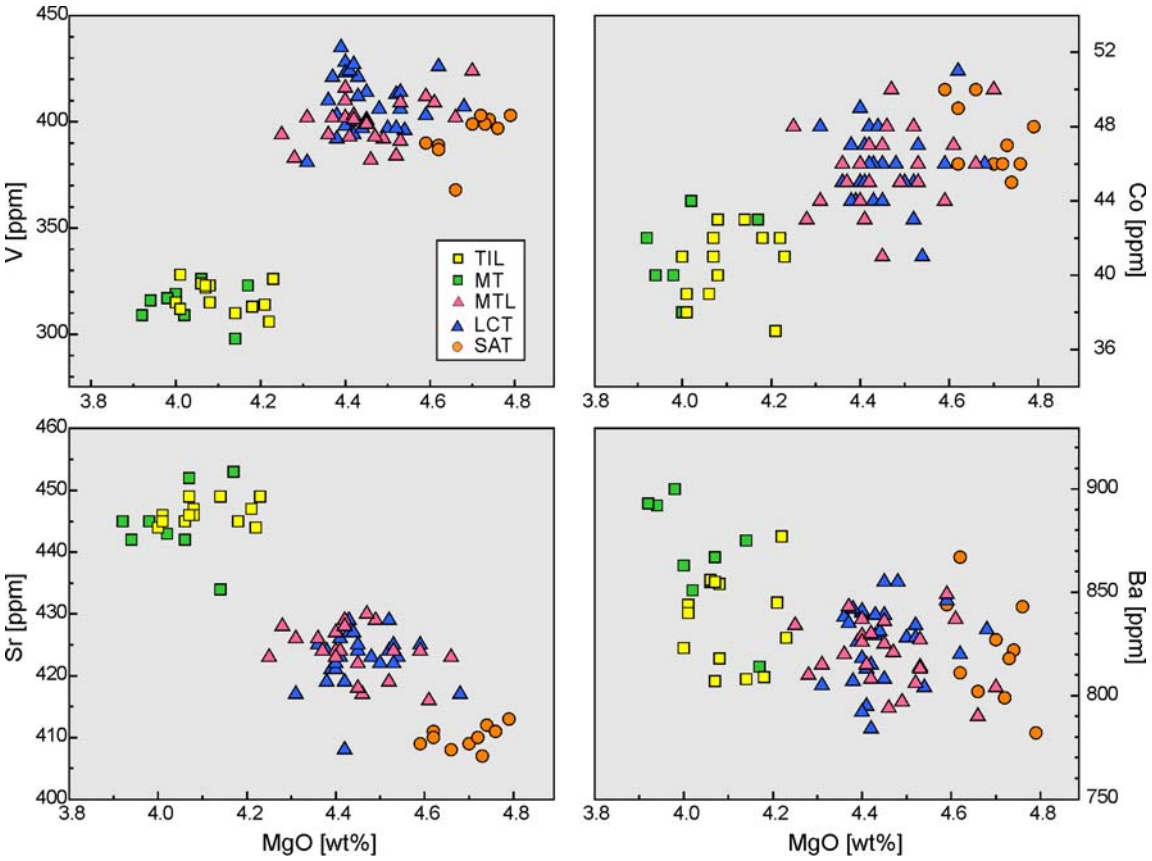

Figure 6.3: Trace element variations of the younger Masaya tephras. V is compatible with Fe-Ti oxides, Co with olivine and clinopyroxene, Sr with plagioclase. LCT-MTL and SAT show similar compatible element contents whereas MT-TIL has lower V and Co and higher Sr and Ba concentrations.

The SAT has higher contents of Sc, Y and Zr but lower contents of other High Field Strength (HFS) elements (e.g. Pb, Th, Hf, U, Nb, Ta) compared to the LCT-MTL and MT-TIL, which overlap in HFSE contents at their different MgO concentrations (Fig. 6.4). The concentrations of Large Ion Lithophile elements (LILE), however, increase from LCT-MTL to MT-TIL with decreasing MgO (Fig. 6.5). The SAT, on the other hand, differs by higher contents of Cs, Rb, Sr and Eu, while Ba is lower, compared to the other Masaya Tephras (Fig. 6.5). The SAT thus is clearly distinct from MT-TIL and LCT-MTL in terms of its higher LILE/HFS ratios.

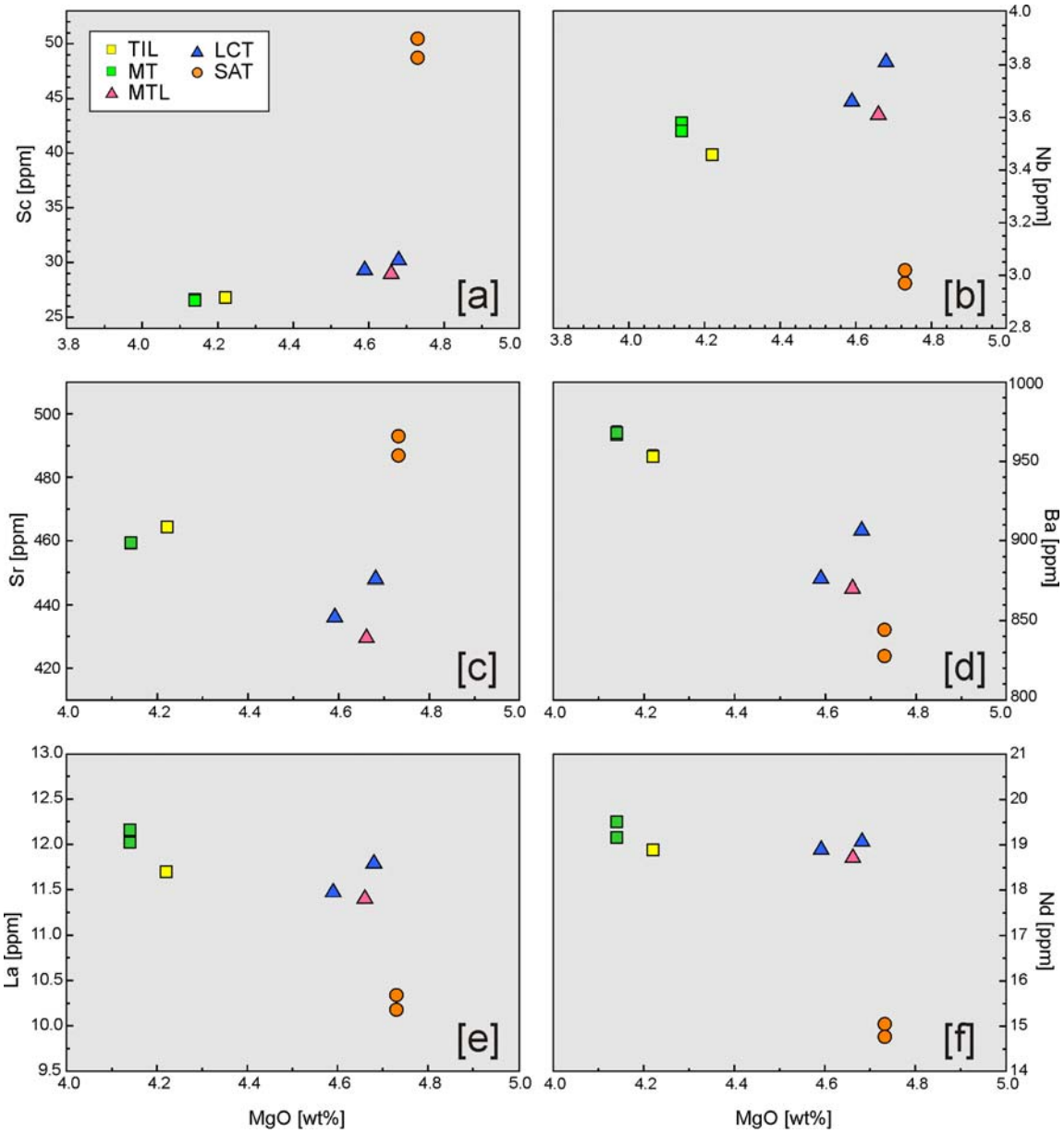

Figure 6.4: Trace element content variations with the MgO content for the Masaya younger tephras. [**a**], [**b**] High Field Strength element (HFSE), [**c**], [**d**] Large Ion Litophiles (LIL) elements and [**e**], [**f**] Rare Earth Elements (REE).

The LCT-MTL and MT-TIL have almost identical Rare Earth Element (REE) contents despite their different MgO contents; only Tb is lower in MT-TIL and Eu is slightly more depleted. The SAT differs by its generally lower REE concentrations (Fig. 6.4) but the REE pattern in Fig. 6.5a is parallel to that of MT-TIL and LCT-MTL except for the absence of a negative Eu anomaly. The presence of negative Eu anomalies in LCT-MTL and MT-TIL reflects some plagioclase fractionation despite the lack of Sr and Al depletion.

Multi-element spider diagrams including other trace elements apart from the REE for the Masaya Tephras in general show a peak-trough pattern typical of subduction-related rocks (Fig. 6.5b). High values of Ba, Rb, K contrast with

depletion in Nb and Ta. The peak in P of the Masaya tephras differs from the average island-arc composition (Fig. 6.5b).

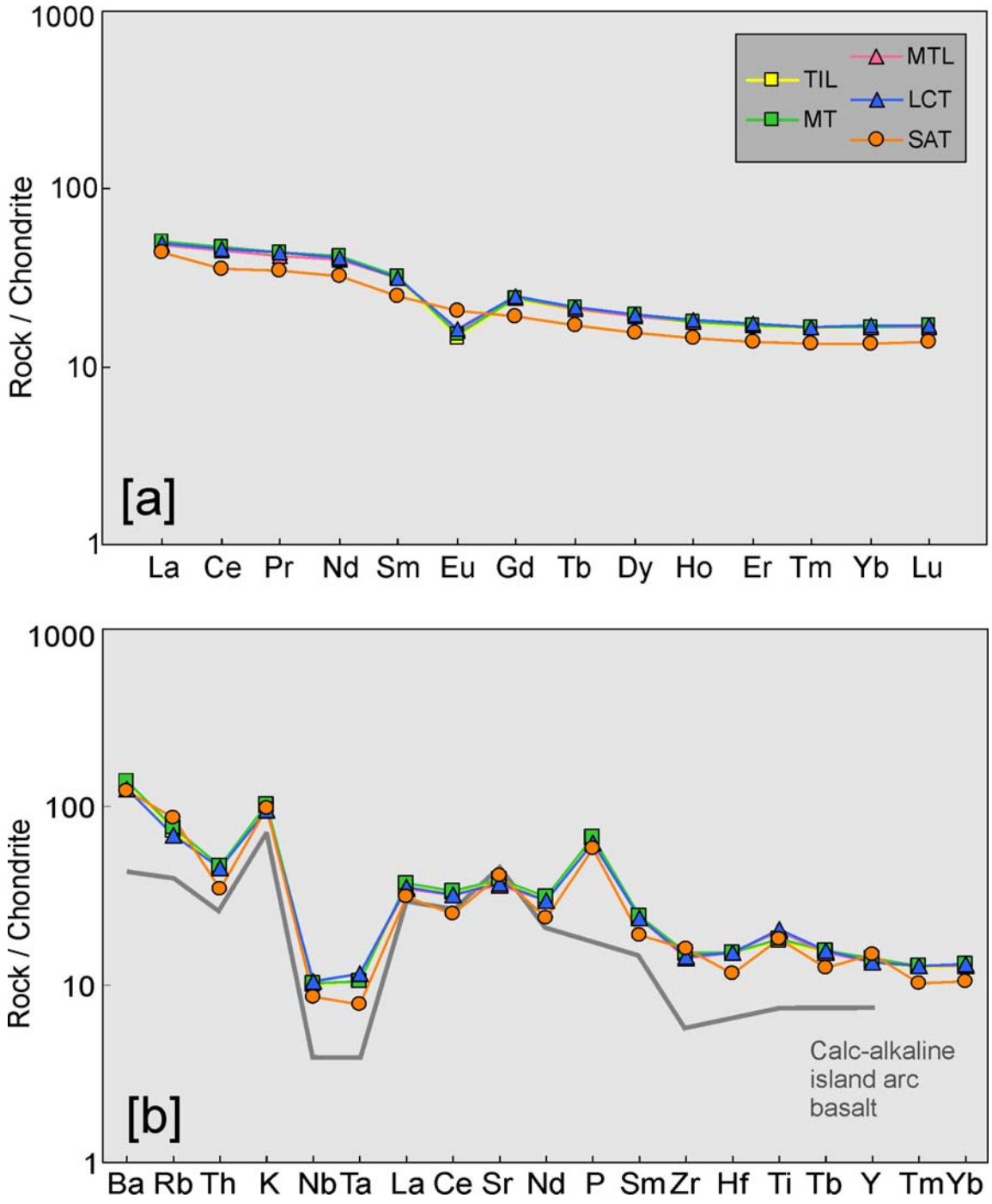

Figure 6.5: Multi-element diagrams for trace elements of the Masaya Tephras. [**a**] REE patterns normalized to the chondrite values of Sun and McDonough (1988). [**b**] Trace elements normalized to chondrite according to Thompson et al. (1984); the gray line is a typical pattern for calc-alkaline island arc basalt.

6.1.3 Comparison with other deposits

6.1.3.1 Comparison with other Masaya-related rocks

Other Masaya rocks, used for comparison with the tephras studied here, include pre-caldera lavas exposed in the caldera walls and post-caldera lavas that crop out mostly inside the caldera and at the flanks of the Masaya cones, among them numerous historical lava flows produced between 1680 to 1772. The analytical data is from Walker et al. (1993), some unpublished data from SFB 574 subproject C2, and two own analyses of lava flows exposed at the caldera rim. Las Sierras Group (LSG) constitutes the basement of the central-western Nicaraguan area but has never been geochemically investigated. One analysis by Walker et al. (1993) is included here. The basaltic-andesitic Fontana Tephra (FT) is the oldest tephra which has been related to the Masaya caldera complex. However, Wehrmann (2005) showed that it was probably erupted from a vent to the west of, and outside, the Masaya caldera and within the older Las Nubes caldera; this would make FT part of the Las Sierras Group.

Pre-and post-caldera lavas show wide compositional ranges, are mostly more mafic than the tephras, and particularly the post-caldera lavas reach relatively high MgO contents of <5.9 wt% (Fig. 6.6). The Fontana Tephra and the single LSG sample have higher silica (52.4-52.8 wt%) and alkali but lower CaO and Al_2O_3 concentrations at MgO contents similar to MT-TIL. The variations of major elements such as SiO_2 and CaO with MgO from the lavas through all the tephras would be compatible with differentiation by fractional crystallization. The same holds for several trace elements such as Ba, Y, Hf which form a continuous trend of enrichment with decreasing MgO from the lavas through LCT-MTL and MT-TIL to FT (Fig. 6.7). The decrease in Sc would be compatible with clinopyroxene fractionation. Other elements, however, vary in a different fashion. At least four compositional clusters are evident in the TiO_2-MgO diagram, MTL-LCT is unusually Nb-rich, and SAT has a deviating composition in all trace elements shown in Fig. 6.7.

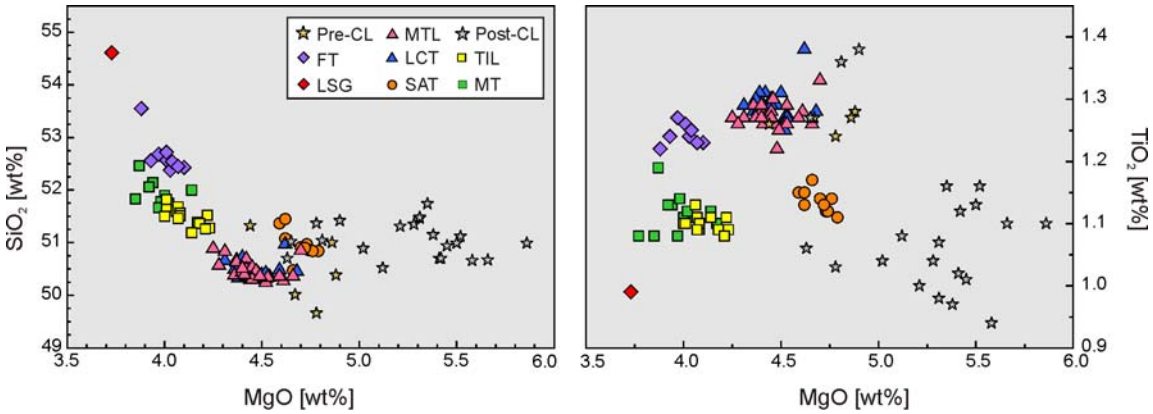

Figure 6.6: Diagrams of major elements versus MgO, comparing the younger Masaya tephras with older tephra units related to the Masaya system and pre- and post-caldera lava flows. LSG=Las Sierras Group, Pre-CL=pre-caldera lavas, Post-CL=post-caldera lavas.

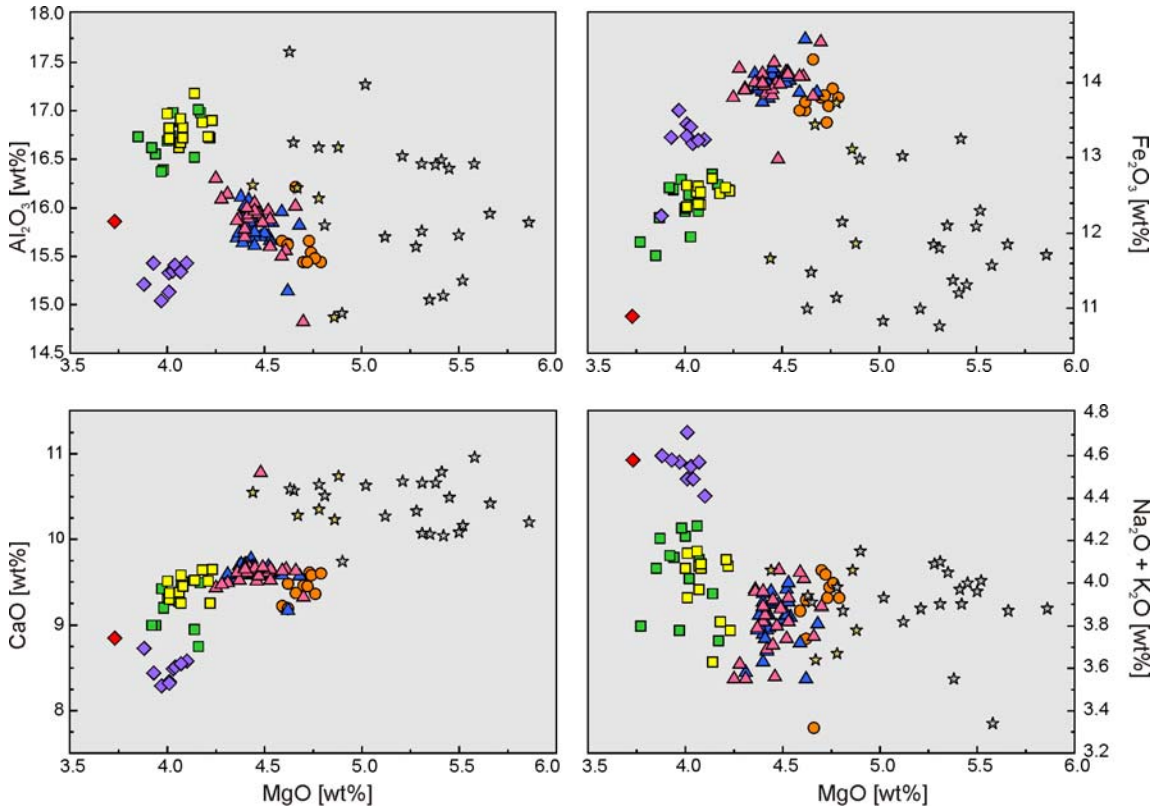

Figure 6.6: Continued...

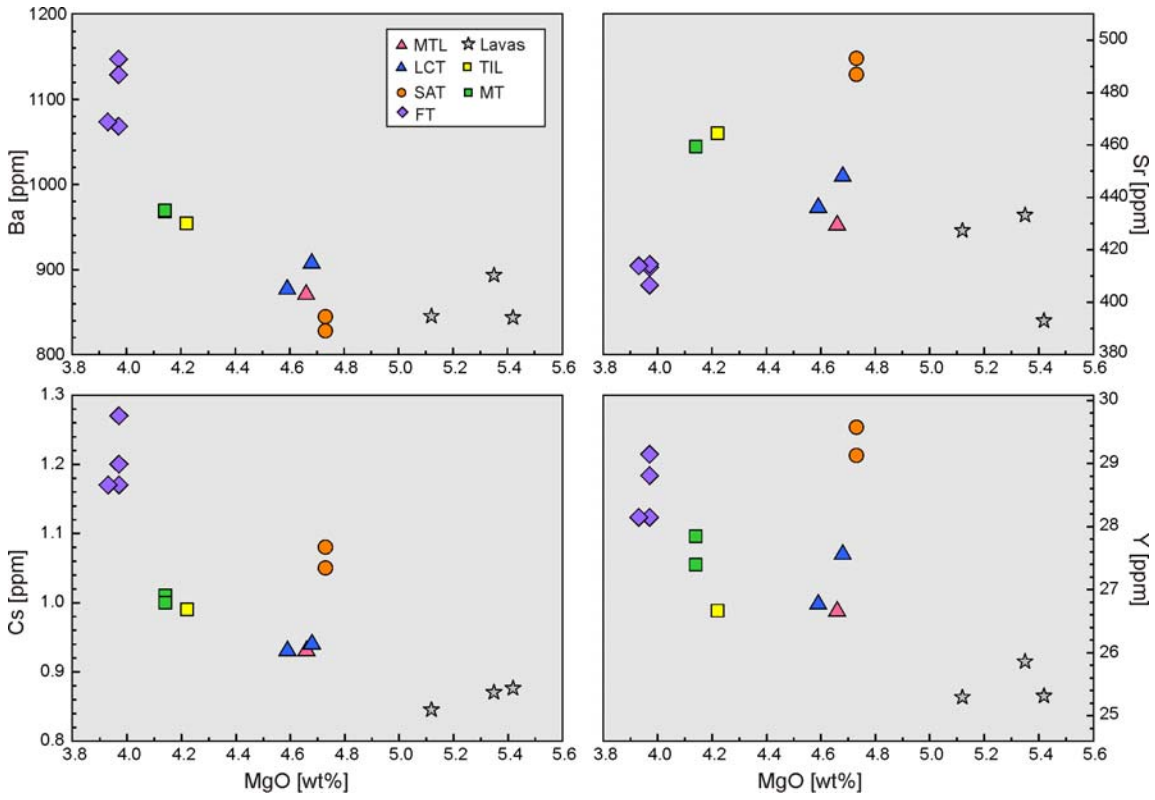

Figure 6.7: Trace element variations with MgO for the younger Masaya Tephras compared to FT and some post-caldera lavas. Note the divergent behaviour of SAT.

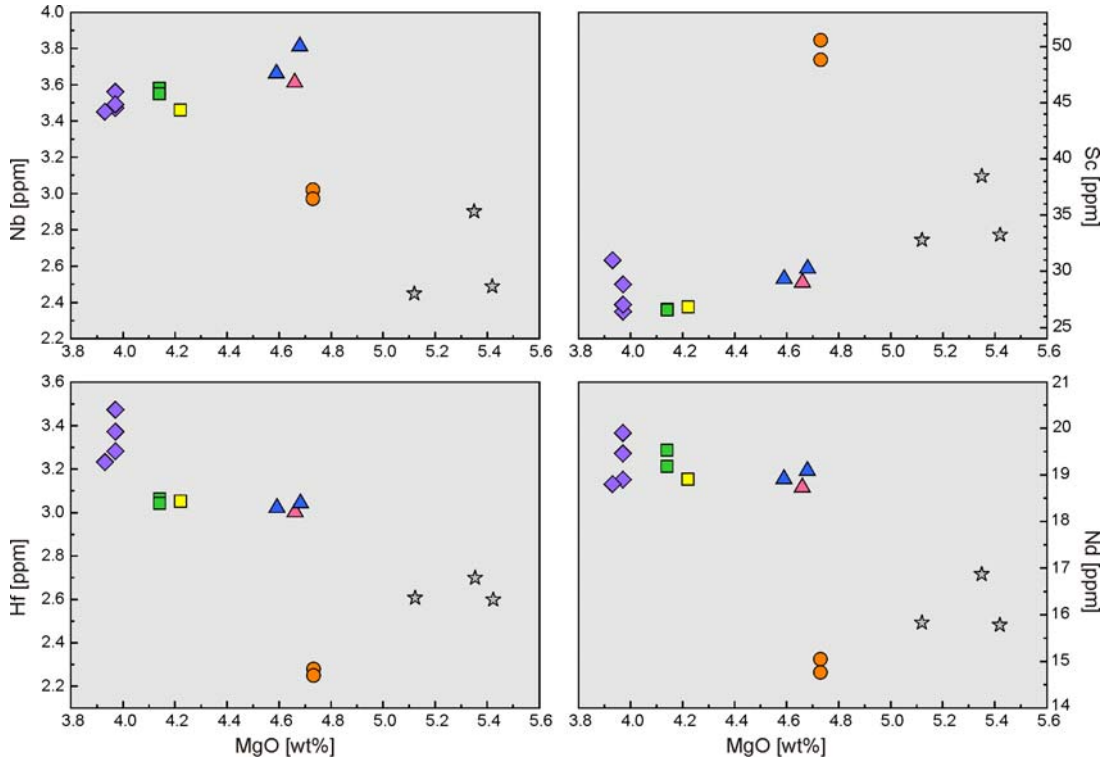

Figure 6.7: Continued...

6.1.3.2 Comparison with the Nejapa-Granada rocks

In western-central Nicaragua there are two main volcanic structure alignments formed by scoria cones and maars, one is the Nejapa-Miraflores lineament, located NW from Masaya caldera and from Managua city to the eastern part of the Chiltepe Peninsula, and the other is the Granada cinder cone field SE of Masaya near Granada city.

The chemical affinities of the Nejapa and Granada (NG) rock series have been studied in detail by Walker (1984) and Walker et al. (1990). They identified low-Ti and high-Ti compositional groups which show distinct trace element characteristics (Fig. 6.8). The low-Ti rocks have higher LILE and LREE concentrations than the high-Ti group. Walker et al. (1990) interpreted that the low-Ti magmas originated in parts of the mantle wedge more strongly modified by influx from the subducted slab whereas high-Ti magmas come from parts of the wedge relatively free of this subduction zone influence. The NG rocks are also one of the few arc tholeiites around the Caribbean plate and the only rocks in the Central American arc with low absolute concentrations of LILE and LREE (Walker et al. 1990).

The younger Masaya rocks studied here overlap with, and extend the evolved end of the low-Ti NG trends (Fig. 6.8), which is consistent with observations made above suggesting the source of these rocks is strongly influenced by subduction materials like sediments. The LCT-MTL group and some lavas, however, would correspond to an intermediate-Ti trend (Fig. 6.8). Notable deviations, however, occur in the Ba/La vs. TiO_2 diagram, where MT-TIL and SAT overlap with intermediate-Ti and LCT-MTL with high-Ti NG compositions (Fig. 6.8).

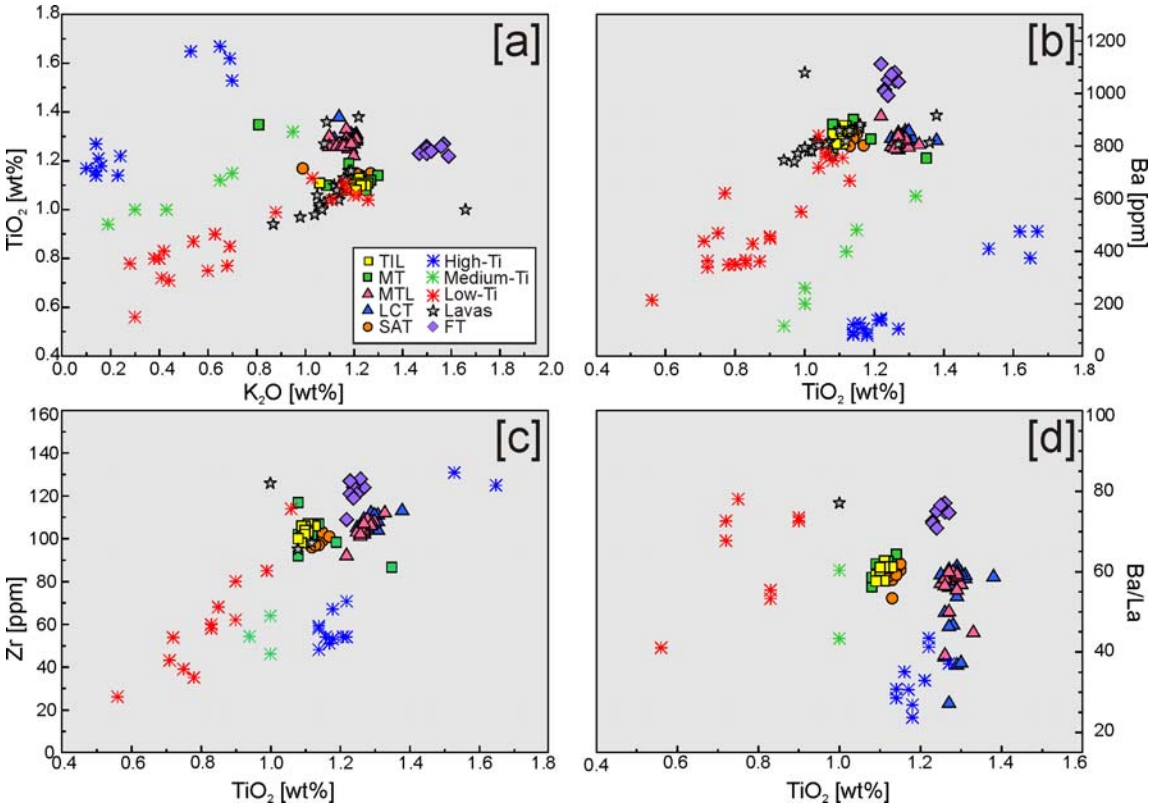

Figure 6.8: Diagrams comparing the Masaya units with the three groups of the Nejapa-Granada rocks differentiated by Walker et al. (1990). [**a**]. Diagram TiO_2-K_2O and [**b**]-[**d**] variations of incompatible elements and ratios with TiO_2.

The multi-element spider diagram of Fig. 6.9 shows that the Masaya tephras have higher concentrations of the incompatible elements, are more strongly enriched in LILE and lower in Nb than the average low-Ti and high-Ti Nejapa-Granada basalts from Walker et al. (1990). Also, Sr is relatively depleted.

6.1.4 Geochemical variations in stratigraphic order

In this section, compositional data are shown in stratigraphic order to better visualize the temporal succession of compositional changes observed in the variation diagrams above. Walker et al. (1993) described longer-term compositional changes thought to coincide with caldera-formation events. However, they used the stratigraphy of Williams (1983) which was incomplete as shown in this thesis. The data shown here is in the correct stratigraphic order.

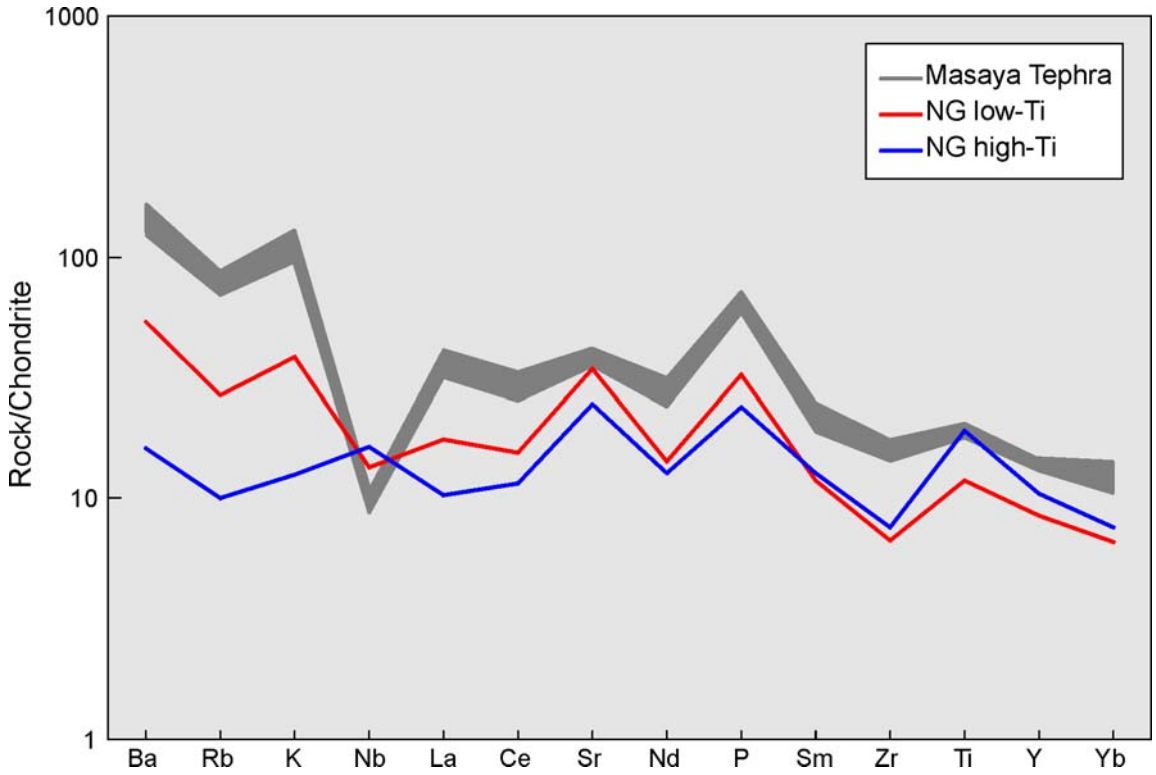

Figure 6.9: Multi-element variation diagram comparing the Masaya tephras (SAT, LCT-MTL, MT-TIL) with average low-Ti and high-Ti Nejapa-Granada rocks from Walker (1989). Note the similarity of the Masaya pattern with the low-Ti group. Chondrite normalization after Thompson et al. (1984)

6.1.4.1 Bulk rock compositions

The MgO contents of the youngest Masaya Tephras (Fig. 6.10) show that these become more evolved with the time from the ca. 6 ka SAT through the ca. 2 ka LCT-MTL to the ca. 1.8 ka MT-TIL. However, the steady decrease in MgO is not accompanied by a similarly steady increase in SiO_2 and alkalis or a steady decrease in CaO, and there is little stratigraphic variation in incompatible elements such as Ba.

The ca. 60 ka Fontana Tephra (FT) is similarly evolved as the MT-TIL in terms of MgO content (Fig. 6.10). Yet CaO and Sr are much more depleted and alkalis and Ba are much more enriched. These differences suggest a different magmatic evolution of the FT with respect to the youngest Masaya tephras, supporting the interpretation of Wehrmann (2005) based on thickness and grain size distribution, that the Fontana Tephra originated from a vent outside the Masaya associated with an older, different magma system.

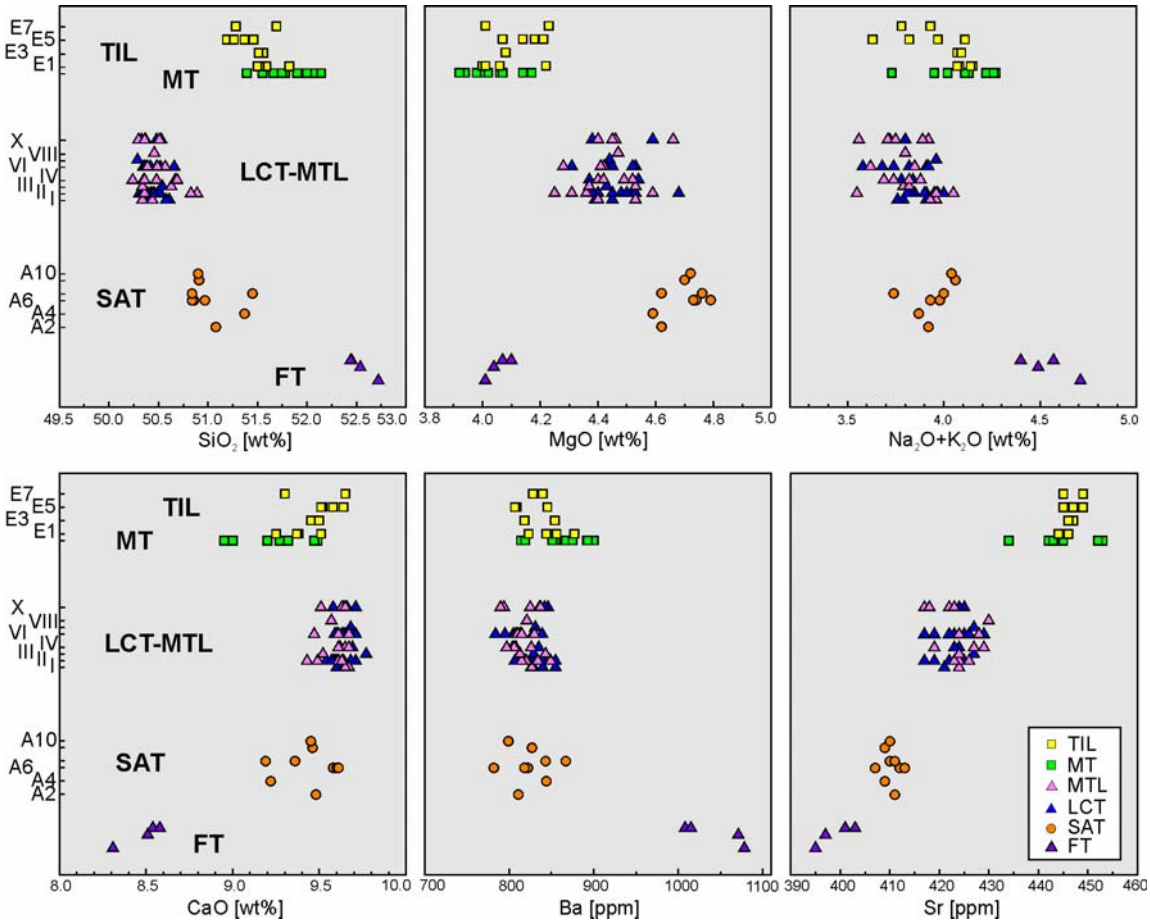

Figure 6.10: Stratigraphic variations of selected bulk rock major and trace elements of the youngest Masaya Tephras: The San Antonio Tephra (SAT), La Concepción Lapilli-Masaya Triple Layer (LCT-MTL) and the Masaya Tuff-Ticuantepe Lapilli (MT-TIL). The older Fontana Tephra (data from Wehrmann 2005) is included for comparison.

6.1.4.2 Glass compositions

Bulk-rock compositions are affected by the abundance of phenocrysts which may be partly accumulated or otherwise modified from the original equilibrium composition (Rose et al. 1978; Carr and Walker 1987). The maximum degree of differentiation reached in a magma system is thus best represented by the matrix glass compositions, which is the composition of the magmatic liquid at the time of eruption.

The matrix of juvenile scoria fragments of the Masaya tephras consists of both sideromelane and tachylite, and both types occur mingled in single scoria clasts. Dense to poorly vesicular juvenile clasts, however, consist entirely of tachylite. The major element concentrations, determined by electron microprobe, scatter widely within each unit (Fig. 6.11). On average, the glass compositions in Fig. 6.11 roughly mimic the bulk-rock variations in Fig. 6.10. However, the differences in MgO contents of the glasses are less well pronounced; in fact, the SAT glass has MgO concentrations almost identical to the LCT-MTL. The minimum MgO contents suggest that locally achieved maximum degrees of differentiation were similar for all three groups but LCT-MTL did not reach the enrichments in SiO_2 and alkalis observed for the other two groups.

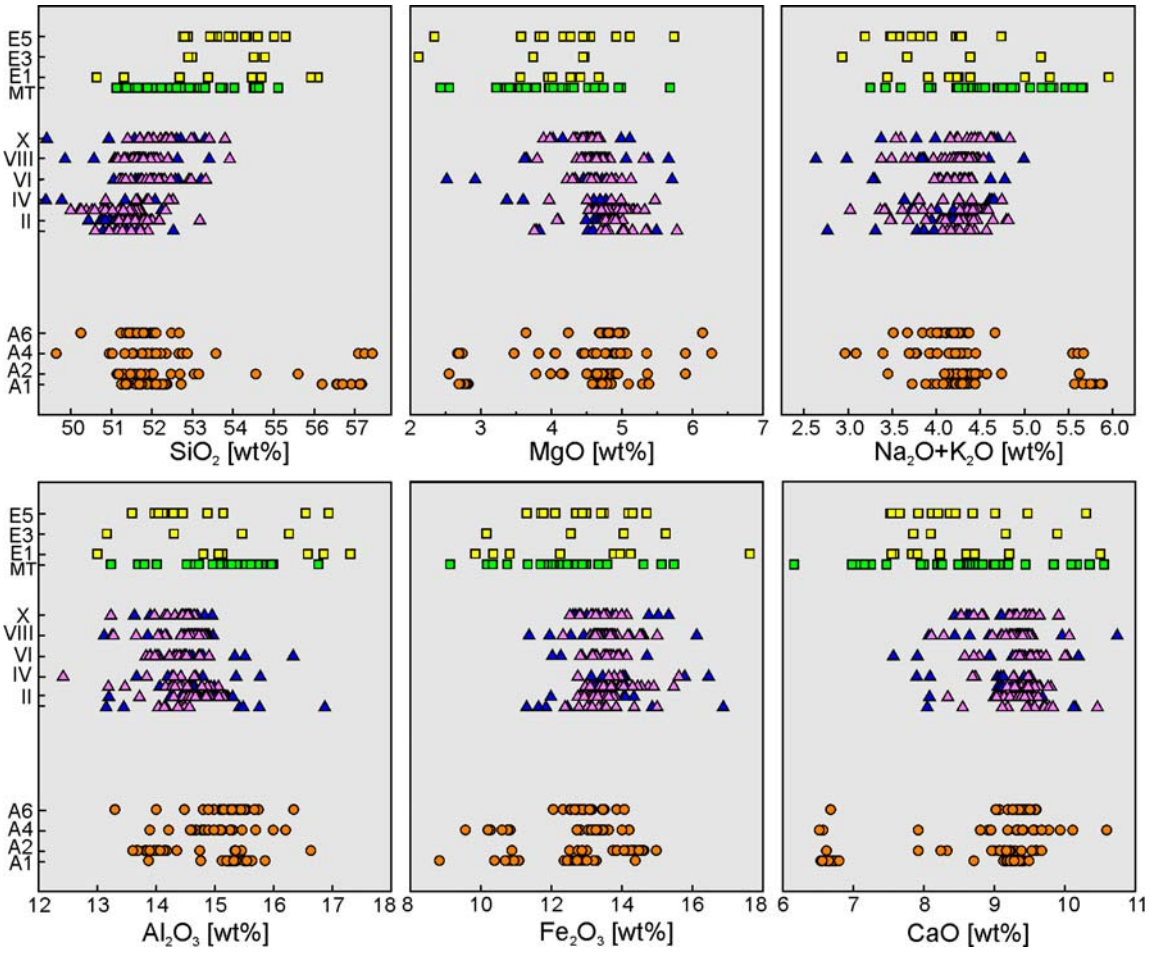

Figure 6.11: Major element stratigraphic variation of the matrix glass compositions of the youngest Masaya Tephras. Symbols are the same as in Fig. 6.10.

Trace element compositions of the tephra glasses were determined by Laser-Ablation-ICPMS. The stratigraphic variations of trace-element ratios are shown in Fig. 6.12. All elements used for these ratios are incompatible elements such that the ratios should not change during fractional crystallization. A possible exception is Y which may be fractionated with apatite; although there is a minor decrease in P_2O_5 from LCT-MTL to MT-TIL (Fig. 6.2) indicating some apatite fractionation, the Y/Nb ratio increases from LCT-MTL to MT-TIL and Y was probably little affected by apatite fractionation.
The different element ratios of the three groups in Fig. 6.12 indicate different mantle source conditions for each group. The vertical variations are not steady, which suggests that there was not a gradual change in sources but rather irregular tapping of different sources.

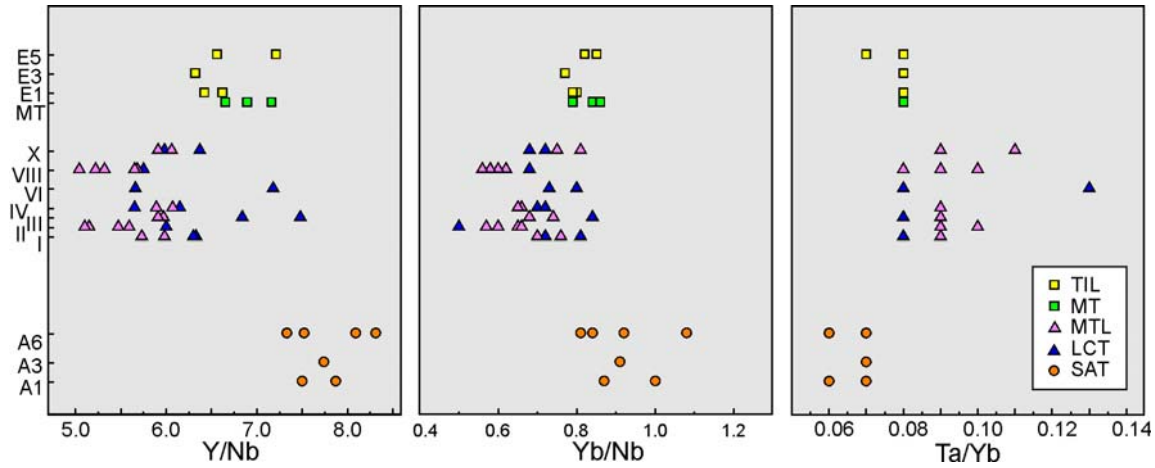

Figure 6.12: Stratigraphic variation of selected trace element ratios of the matrix glasses of the youngest Masaya Tephras.

6.1.4.3 Mineral chemistry

The compositions of the main mineral phases of the Masaya Tephras (plag+ol+cpx) are very similar. On average, the SAT has the most calcic plagioclase and the most magnesian olivine in agreement with its most mafic bulk composition (Fig. 6.13). All three groups contain some low-An plagioclase and high-Fe clinopyroxene that may have formed late in equilibrium with the most evolved glass compositions. The MT-TIL displays a very wide range particularly in plagioclase and olivine compositions. Since this tephra was produced by the most strongly phreatomagmatic eruption, this wide range may be partly due to the inclusion of xenocrysts although no obvious disequilibrium features were observed in thin sections. On the other hand, the fact that MT-TIL contains higher-An plagioclase than LCT-MTL despite its more evolved composition can be related to a higher water content of this magma (or higher P_{H2O} during crystallization). The clinopyroxenes are very similar in composition for the three units and the only difference is that SAT augite has slightly higher MgO contents (Fig. 6.13).

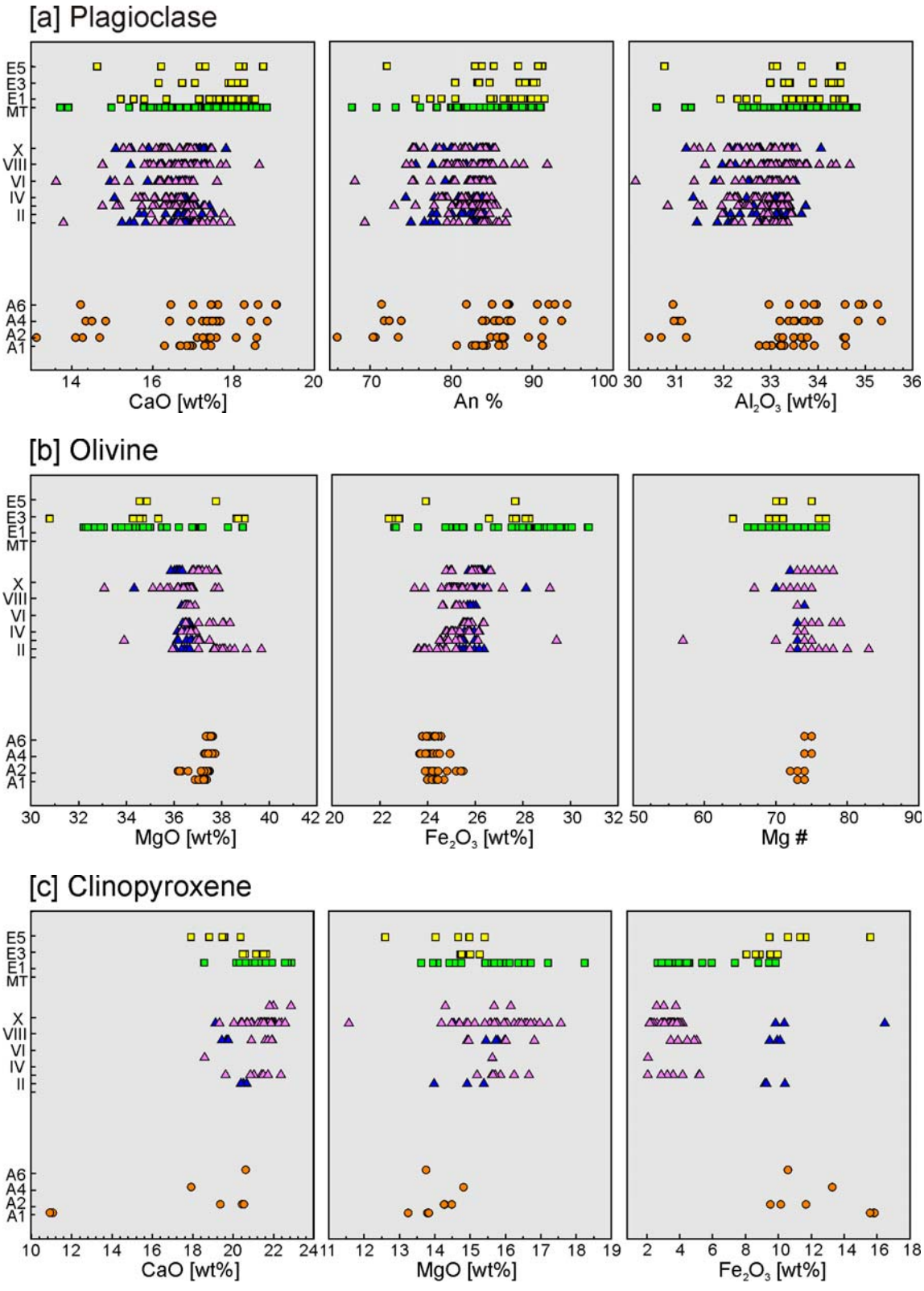

Figure 6.13: Stratigraphic compositional variations of the main mineral phases of the younger Masaya tephras units: [**a**] plagioclase, [**b**] olivine and [**c**] clinopyroxene. Symbols used are the same as in previous figures.

6.2 Vertical variations within the tephras

Many pyroclastic deposits are characterized by vertical compositional changes that represent changes in magma composition during the course of the eruption (Carr and Walker 1987). These changes indicate eruption from a compositionally zoned magma chamber, typically such that the eruption of lower-temperature, degassed, differentiated materials is followed by higher-temperature, more gas-rich, less-differentiated products (Hildreth 1981). The first tephra erupted is usually the top of the magma chamber but progressively later layers come from a wider range of depths because magma extraction typically does not proceed parallel to the surface, but parallel to flow lines whose shape is a function of conduit and chamber geometry, physical properties of magma and rate of extraction (Spera 1984). The changes in composition in a deposit are not only due to petrochemical processes like fractionation, assimilation or contamination, but can also be product of mechanical processes operating during magma rise and eruption. These can redistribute the components like crystal phases (e.g. Carr and Walker 1987) or two magma types with different densities and rheological properties. Examples of vertical chemical variations in tephras from several volcanoes in Central America have been reported by Rose et al. (1978) and Carr and Walker (1987).

6.2.1 SAT

6.2.1.1 Bulk rock composition

The bulk rock compositions of stratigraphic samples of the San Antonio Tephra indicate the lowermost subunits (A2, A4) have the most evolved compositions with higher SiO_2, Al_2O_3, K_2O, and Zr, and lower FeO, MgO, V contents (Fig. 6.14). That Co and Ni concentrations are also slightly elevated may result from minor accumulated olivine although Ni is close to the limit of detection. The most primitive compositions occur in the subunits at the middle of the sequence, the thickest fallout tephra subunits A6 and A7. The overlying surges have an intermediate composition between these two groups (Fig. 6.14).

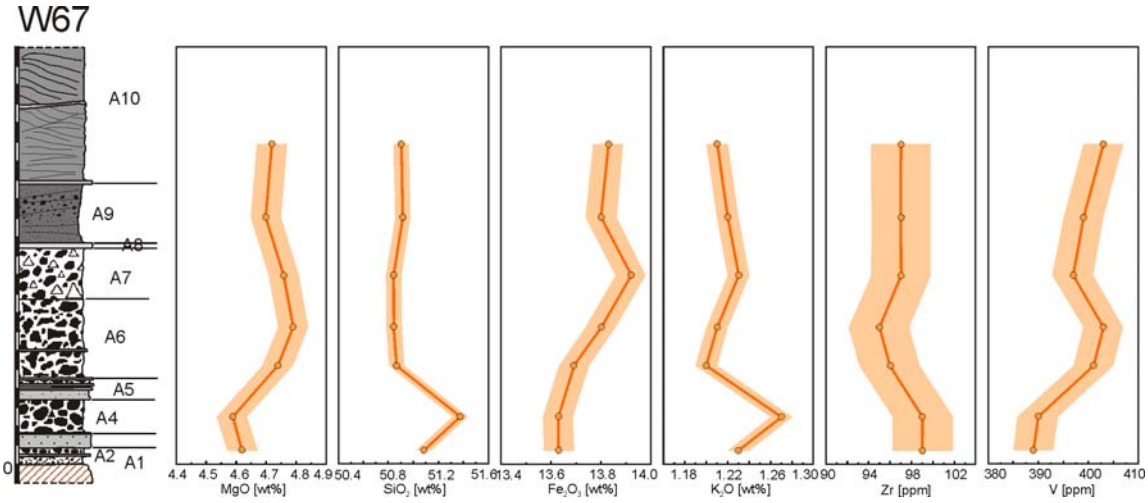

Figure 6.14: Vertical variations of bulk rock major and trace elements of the San Antonio Tephra at outcrop W67 (see chapter 3 for location). The light orange areas represent the analytical error.

High concentrations of CaO and V but low concentrations of K_2O and Ba at the level of A6 may result from some pl+cpx accumulation, diluting the incompatible elements, although this is not evident in the Rb and Nb variations.

6.2.1.2 Glass compositions

To evaluate if these variations are due to crystal concentration, analyses of both matrix glasses and glass inclusions in phenocrysts were made with the electron-microprobe. Glass and bulk-rock compositions are compared in Fig. 6.15.

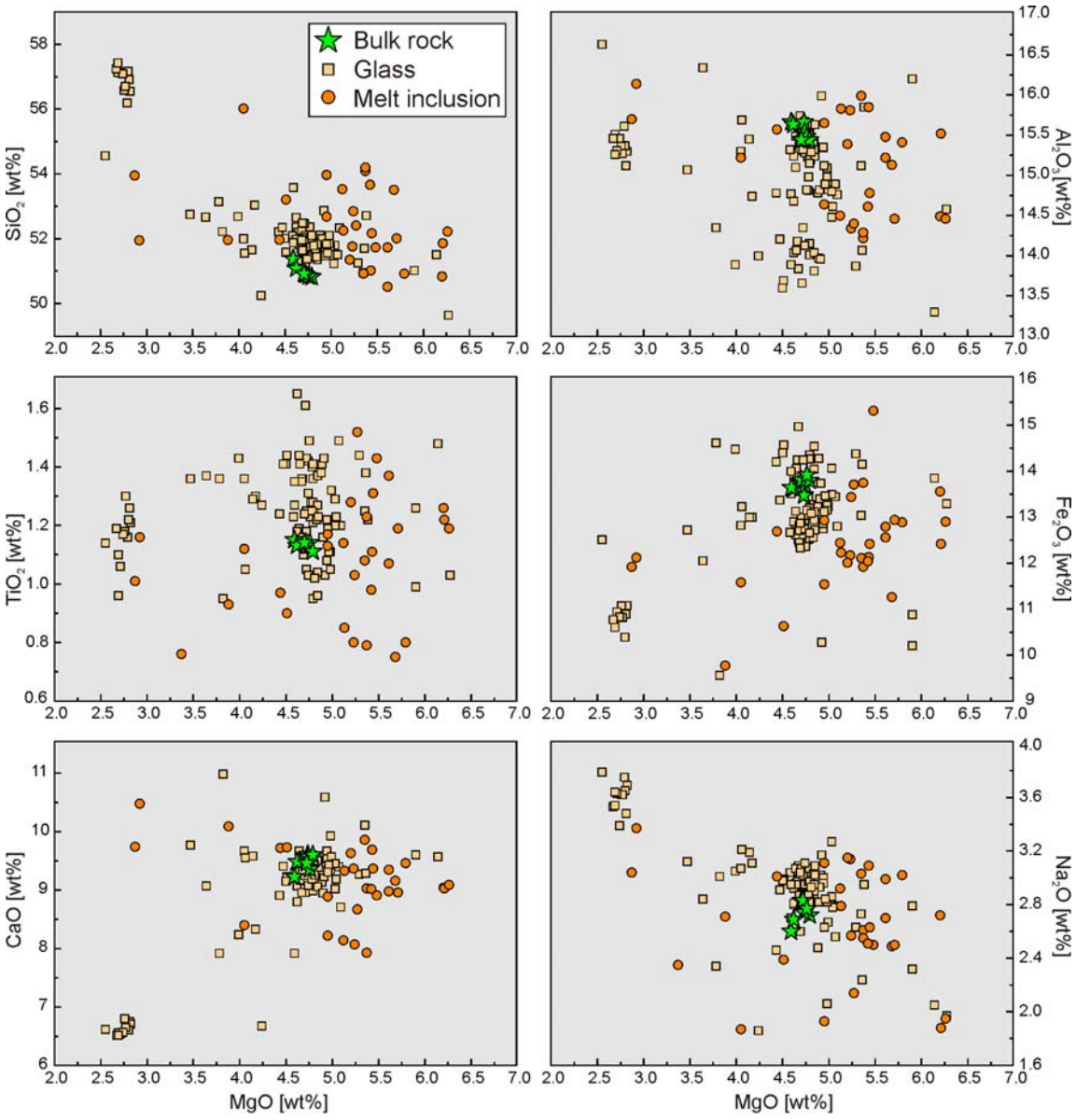

Figure 6.15: Diagrams of major elements versus MgO comparing the XRF bulk rock compositions with the EMP-measured matrix and inclusion glasses.

As expected, melt inclusions have higher MgO contents than the matrix glasses and a wider range of the other major elements, suggesting that they were trapped at different stages of magmatic diferentiation. The majority of matrix glasses have MgO, CaO, Fe_2O_3 and TiO_2 contents similar to bulk rock showing that the few phenocrysts present exert no significant control on the bulk composition. Only the relatively high Al_2O_3 and low Na_2O contents in bulk rocks relative to matrix glass reflect some effect of plagioclase phenocrysts.
An interesting observation is that the SAT has two major glass compositions: a more mafic one with SiO_2 contents between 51-54 wt% and MgO of 3.5-5.5 wt%, and a more evolved one with 56-58 wt% SiO_2 and 2.5-3 wt% MgO (Figs. 6.15, 6.16, Table 6.1). The most evolved glass is a highly vesicular pale brown sideromelane which lacks microlites (Fig. 6.16). Glass compositional data arranged in stratigraphic order shows that such evolved clasts occur only in the subunits A1 and A4 (Fig. 6.17). The variation diagrams in Fig. 6.17 show that the low-Mg glass may be derived from the high-Mg glass by phenocryst (pl+cpx+ol+mt) fractionation decreasing CaO and Fe_2O_3 while enriching SiO_2 and alkalis. Al_2O_3 and TiO_2 are buffered by the opposing effects of the remaining mineral phases versus plagioclase and magnetite, respectively.

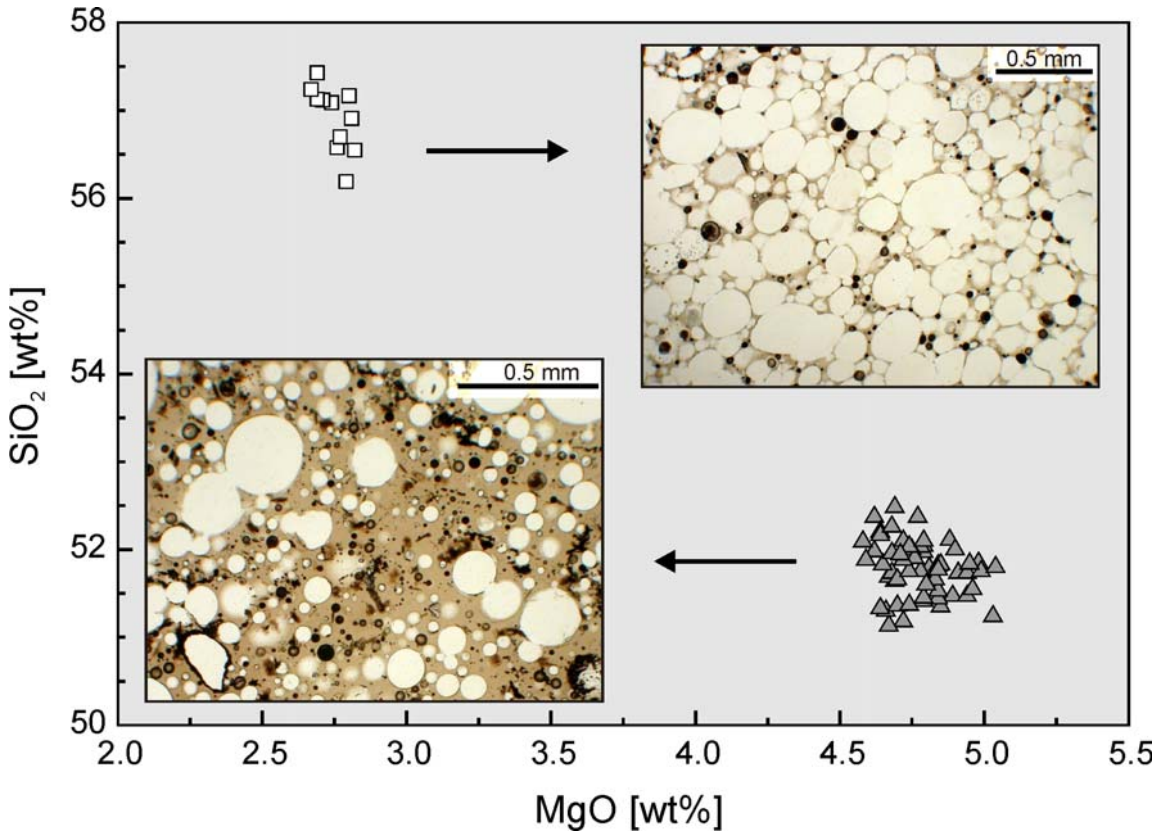

Figure 6.16: Physical and chemical characteristics of the juvenile fragments showing different glass compositions in the SAT scoriae. The evolved glass (higher SiO_2, lower MgO) is highly vesicular, pale-brown, microlite-free; the mafic glass (higher MgO, lower SiO_2) is less vesicular, brown, with some micro-phenocrysts and microlites.

Table 6.1: Average chemical compositions of the SAT glass types

	Mafic glass	Evolved glass
SiO_2	51.79	56.92
TiO_2	1.26	1.16
Al_2O_3	14.95	15.37
Fe_2O_3	13.23	10.82
MnO	0.23	0.26
MgO	4.78	2.75
CaO	9.30	6.63
Na_2O	2.93	3.60
K_2O	1.28	2.11
P_2O_5	0.24	0.38

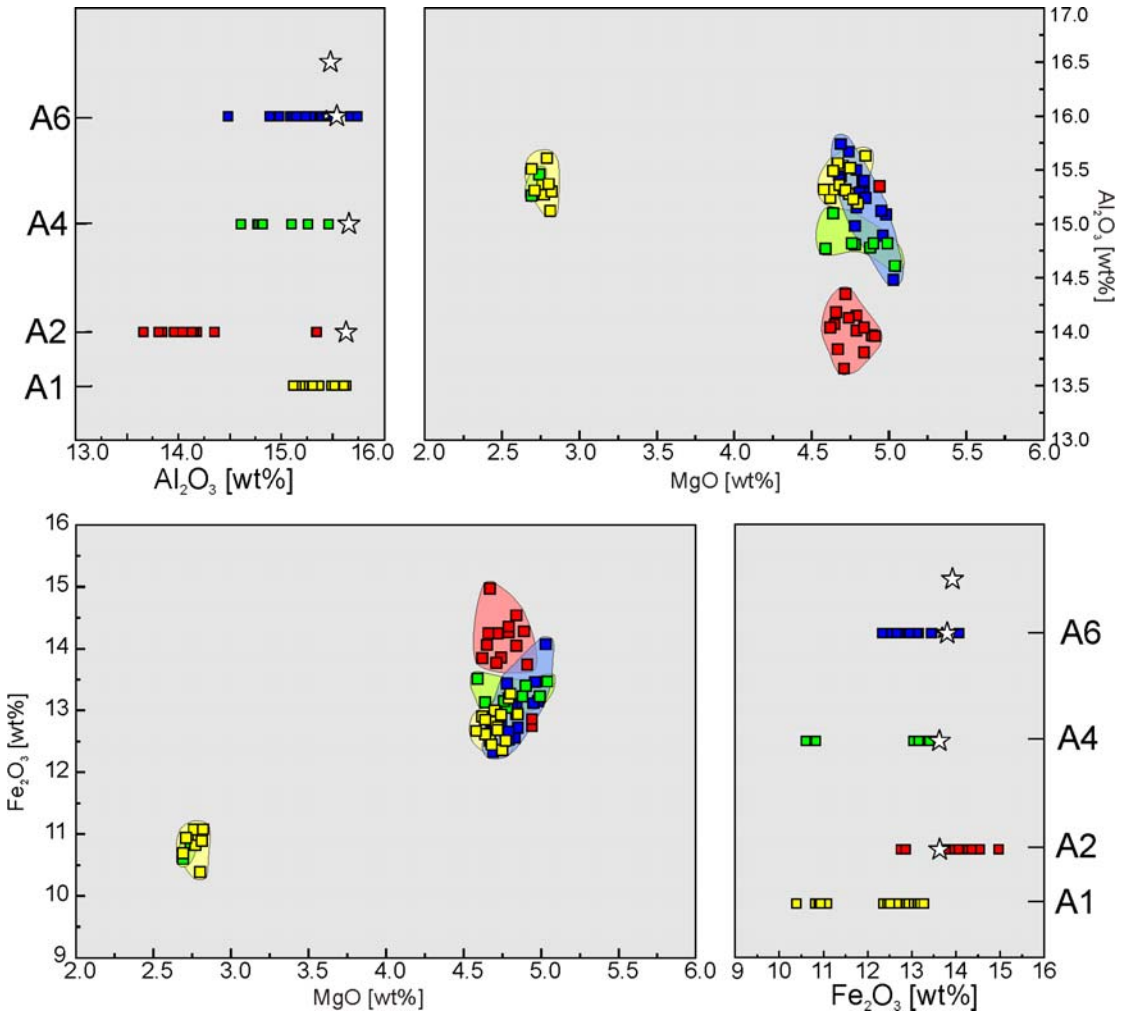

Figure 6.17: Variation diagrams of Al_2O_3 and Fe_2O_3 versus MgO showing the composition of the matrix glass of the SAT fallout layers (subunits A1-A6). Vertical variation of the same elements with the stratigraphy are also included. The bulk rock compositions (white stars) are shown for comparison.

6.2.1.3 Mineral compositions

The dominant mineral phase is calcic plagioclase with a composition ranging from An_{66} to An_{94}, mostly anorthite but extending to bytownite and labradorite (Fig. 6.18a). The microlites in the groundmass are less calcic than the phenocrysts. Stratigraphically, the plagioclase of subunits A2-A4-A6 has two main compositions, most of them are more Ca-rich at 80-95 An% between but a few crystals have lower 65-75 An% (Fig. 6.18b). There is a slight stratigraphic variation in the Ca-rich plagiclase with A1 having the less calcic compositions and A2 the most calcic. The glass inclusions in plagioclase also have the most mafic composition in subunit A2 and are less mafic in A1 and A6.

Olivine is the second most abundant mineral in the SAT, but still is present in a much lesser amount than plagioclase. They have Fo contents between 72 and 75%, which vary slightly stratigraphically with subunits A1 and A2 having the lowest Mg# and a wider range of values and the upper A4 and A6 having Mg# higher than 74% (Fig. 6.18c).

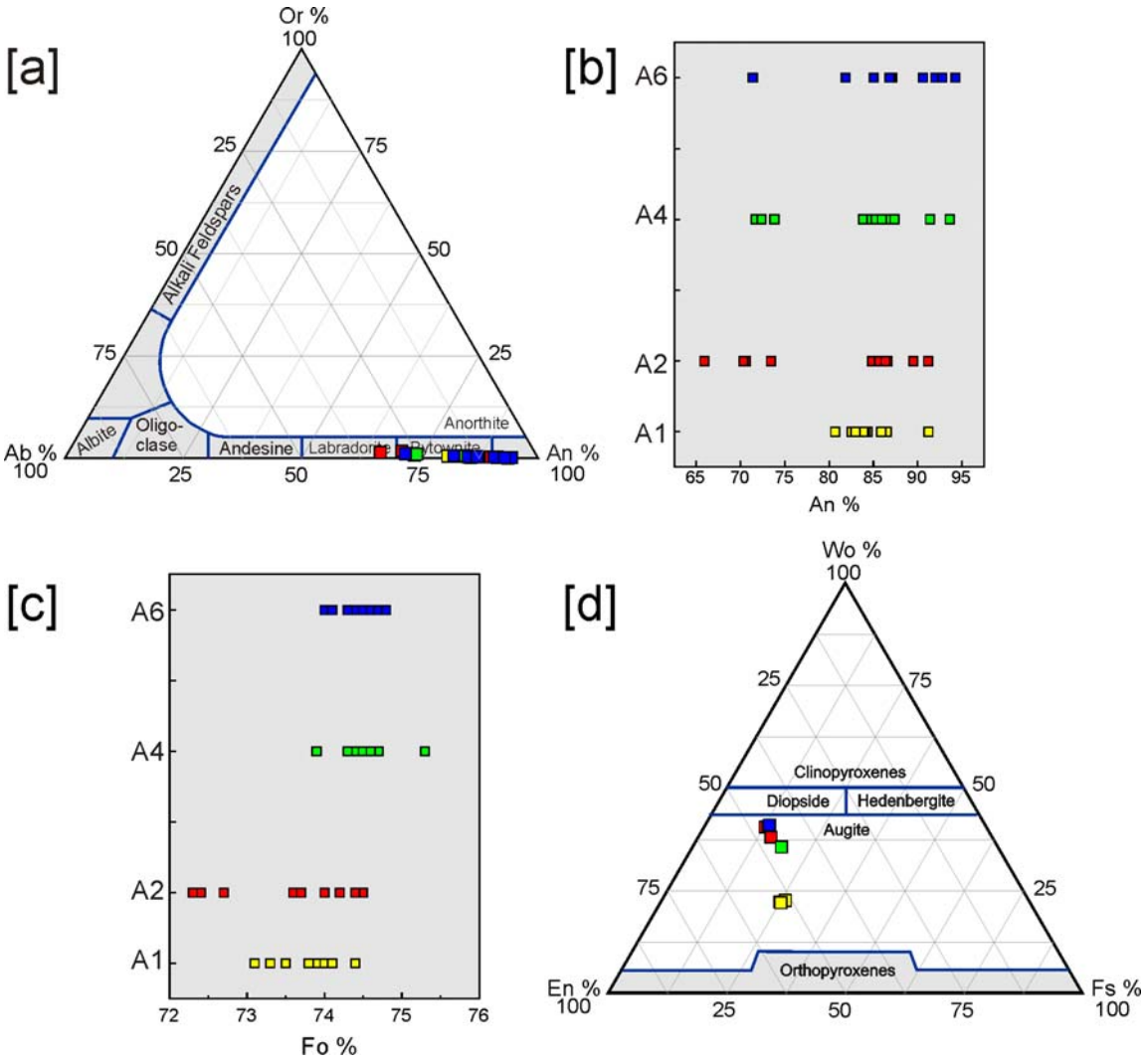

Figure 6.18: Chemical composition of the main SAT mineral phases: [**a**] Ternary diagram for feldspars. [**b**] Stratigraphic variation of the An% of the SAT plagioclase. [**c**] Variation of the Fo% at the SAT olivine. [**c**] Ternary diagram for the classification of pyroxenes, the few SAT pyroxenes are augites.

The few clinopyroxene crystals found in the SAT scoria have an augite composition (Wo_{22-41} En_{46-53} $FsBB_{13-26}$, Fig. 6.18d). Only clinopyroxenes of subunit A1 (yellow squares) are more Fe-rich and Ca-poor.

6.2.2 LCT-MTL

6.2.2.1 Bulk rock compositions

The LCT and MTL show very similar bulk rock, glass and mineral compositions with no systematic difference, indicating a cogenetic origin as is supported by the stratigraphy.

The LCT sequence as sampled in proximal exposures only shows a general decrease in SiO_2, K_2O, V and Zr vertically upward while other element variations are minor or somewhat irregular (Fig. 6.19). Particularly irregular behavior is shown by the thin lowermost layers B0-B3. An excursion to higher SiO_2, Y, Zr and lower MgO occurs at subunit B9.

The overall vertical variation in the MTL is also very narrow; the earliest products are the most mafic and become more evolved upwards with a general increase in SiO_2, Al_2O_3, Nb, Sr and a decrease in MgO, TiO_2, Fe_2O_3, Co, Ni, Y, Zr (Fig. 6.20). Other elements like CaO and alkalis show a very slight decrease. Subunit C3 has anomalously low CaO, K_2O, Nb and Rb. The thick topmost subunit C10 diverges from the general trend for several elements like SiO_2, CaO, Na_2O, Co and Sr (Fig. 6.20).

Some of the minor chemical variations seen in the subunits may be due to some contamination, since the juvenile lapilli contain tiny xenoliths of few mm size.

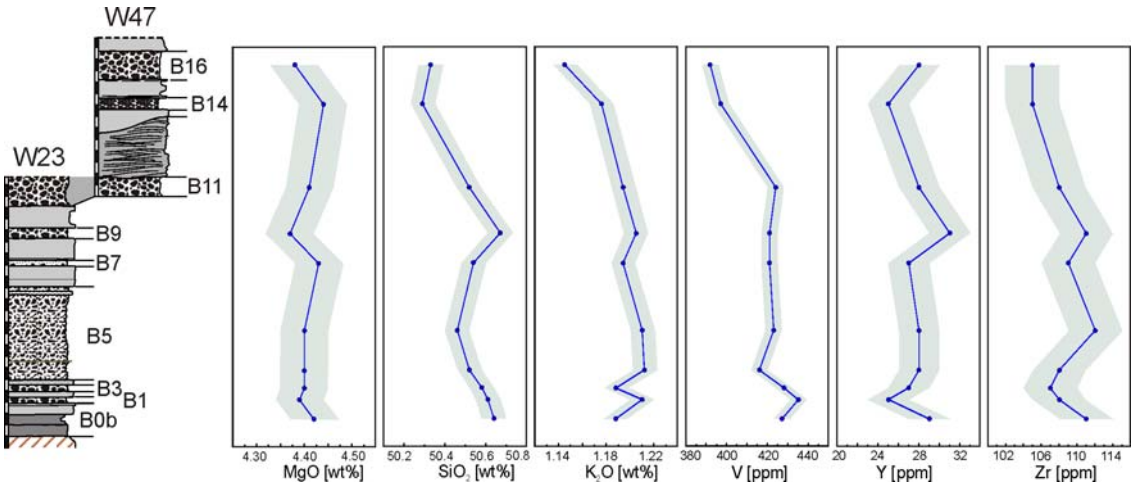

Figure 6.19: Bulk rock chemical stratigraphic variations of selected elements in LCT. Most of the subunits (B0-B11) were sampled at outcrop W23 and the upper ones at outcrop W47 (B14-B16). The light blue area indicates the analytical error.

In Fig. 6.21 the bulk-rock compositional data are arranged according to the combined LCT-MTL stratigraphic succession of subunits I-X proposed in chapter 4. Each of subunits I-X now includes several analyzed samples and hence there is some scatter in each composition but still some subtle stratigraphic changes can be noted (Fig. 6.21). Al_2O_3 increases and Fe_2O_3

decreases upward. Other elements like TiO2, alkalis, V, Ba, show a decrease up to subunit VI, followed by an increase in VIII and decreases again at the topmost subunit X, whereas Sr increases up to VI and then decreases (Fig. 6.21).

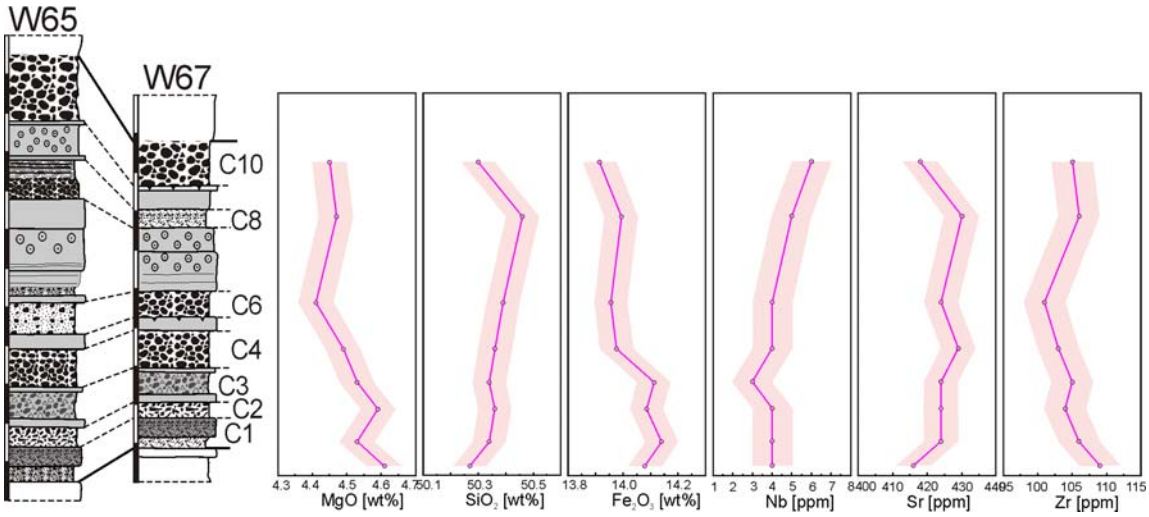

Figure 6.20: Bulk rock chemical stratigraphic variations of selected elements in the MTL at outcrops W65 and W67. The light pink area indicates the analytical error.

6.2.2.2 Glass compositions

The LCT-MTL matrix glass has higher contents of SiO_2, MgO, Na_2O and less Al_2O_3 and CaO as a clear evidence for calcic plagioclase accumulation in the bulk rock (Fig. 6.22). This overprinted possible minor olivine accumulation such that the glass contains more MgO than the bulk rock. The higher Fe_2O_3 contents in the bulk rock can be attributed to magnetite crystals.

The melt inclusion glasses have a basaltic to basaltic-andesitic composition and are mostly hosted in plagioclase (96%). As expected, they are more mafic than the matrix glass; chemical changes from inclusion to matrix glasses (decreasing MgO but increasing CaO) suggest that olivine fractionation was more important during the earlier phase of differentiation (Fig. 6.22).

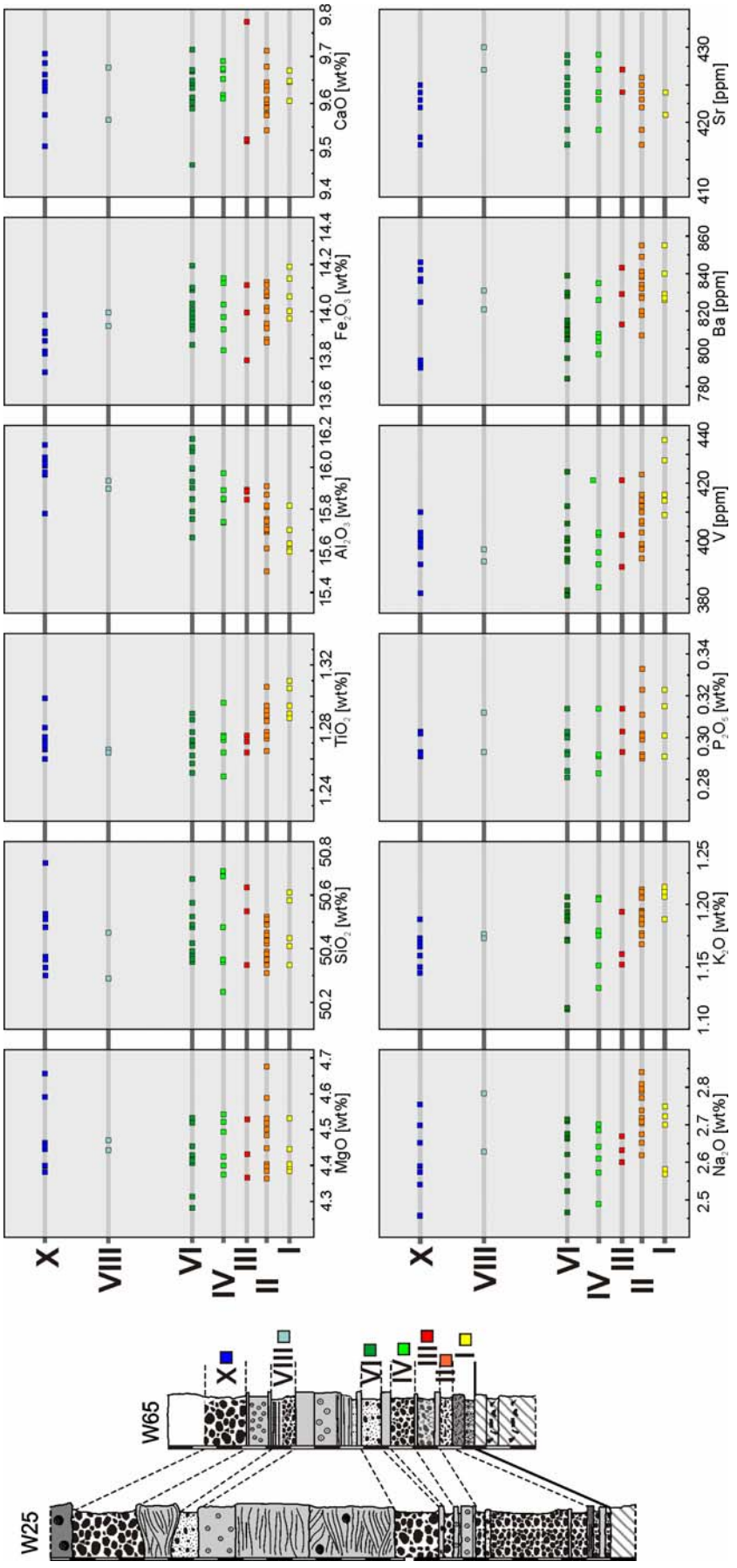

Figure 6.21: Vertical variations of selected bulk rock major and trace element concentrations in the order of subunits I-X of the correlated LCT-MTL stratigraphy. Typical profiles of the LCT (W25) and MTL (W65) sequences are shown for comparison.

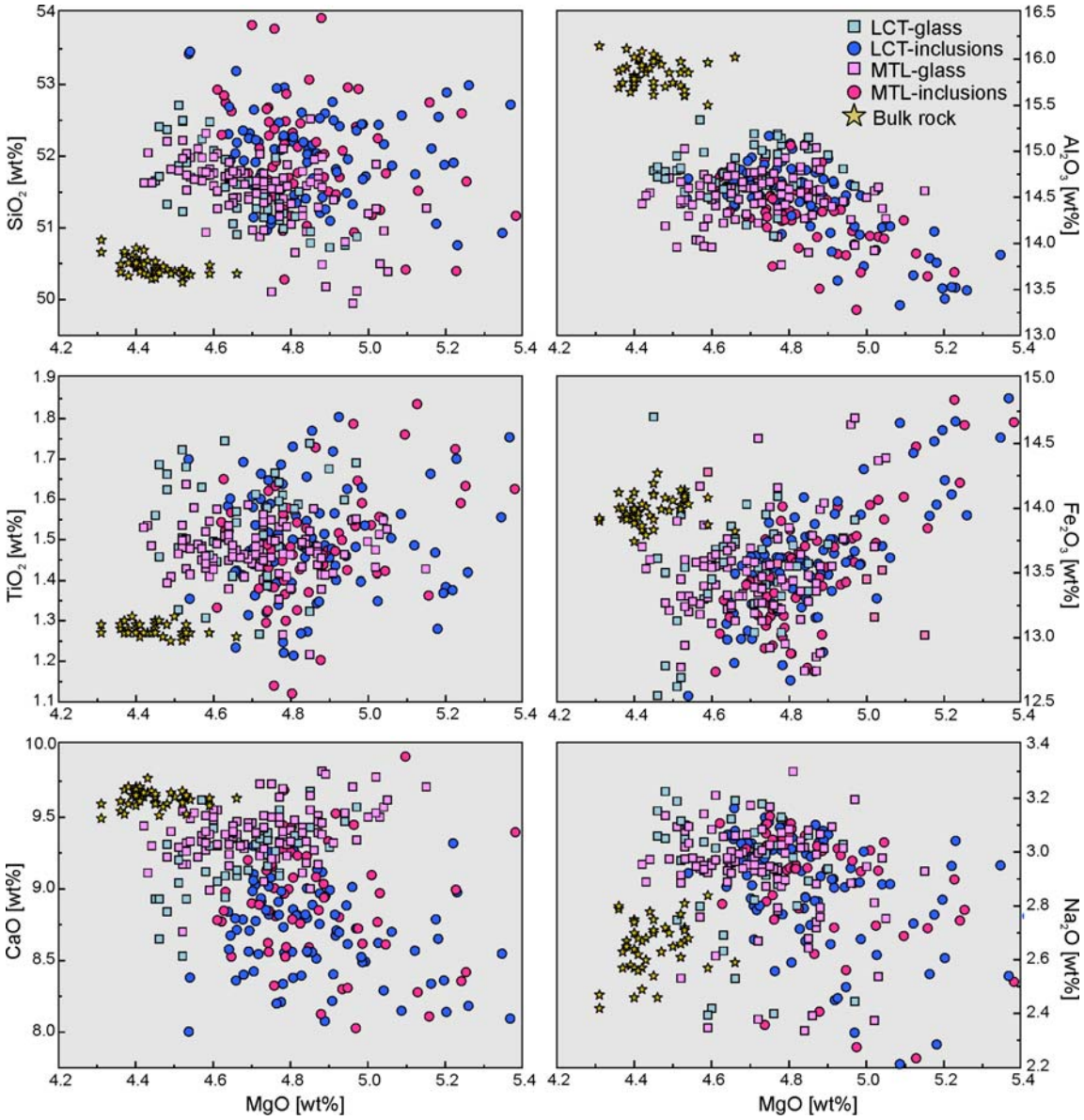

Figure 6.22: Comparison between the matrix and melt inclusions glass compositions and the bulk rock for the LCT-MTL. There is no major differences in composition between LCT and MTL.

The major element composition of the LCT-MTL glasses with the stratigraphy shows little vertical changes, with the glass of the earlier products (I-VI), on average, having a slightly more mafic composition (Fig. 6.23). These stratigraphic changes are contrary to those exhibited by the LCT bulk rock, but similar to those of the MTL sequence at W65 and W67 becoming more evolved upwards in the sequence. The glass compositional variations agree with fractionation of the observed mineral phases (plag+ol+cpx).

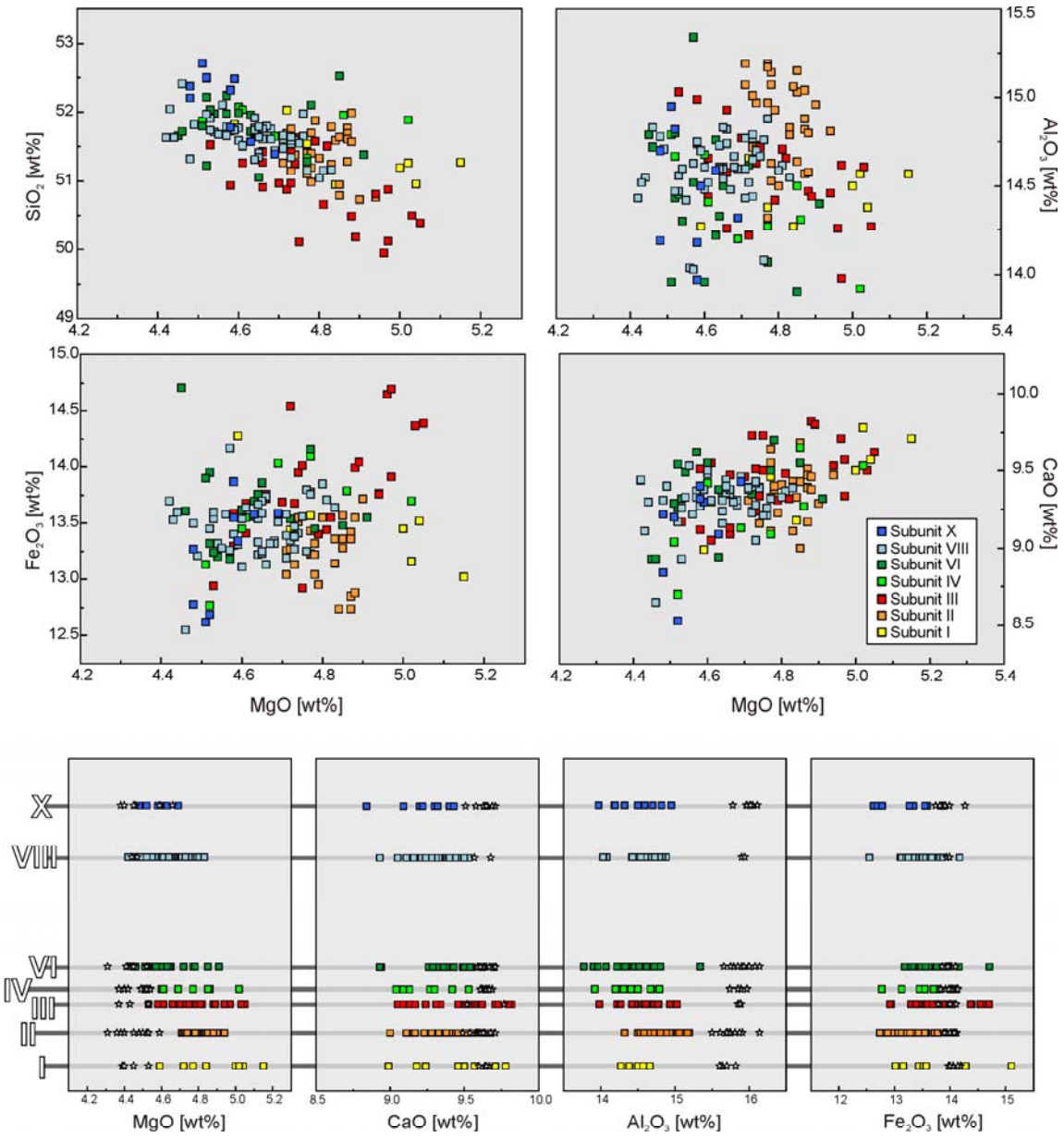

Figure 6.23: Stratigraphic changes in major element composition of the LCT-MTL matrix glasses. The upper diagrams show the variations of selected major elements with MgO. The lower diagrams show the compositional ranges of some elements with the stratigraphy, showing the bulk rock compositions (white stars) for comparison.

6.2.2.3 Mineral chemistry

The minerals of both units are identical in composition, confirming again the relationship between both units already given by bulk-rock and glass compositions, lithologic characteristics and stratigraphic relationships. The dominant mineral phase is calcic plagioclase, mostly bytownite and some anorthite (An_{73} to An_{89}; Fig. 6.24d); the microlites of the groundmass are at the calcic end of this range.

Most of the plagioclase phenocrysts have abundant glass inclusions (Fig. 6.24a) which vary in composition from basalt to basaltic andesite (SiO_2 50-53 wt%, MgO averages 4.5-5.5 wt%). The basaltic inclusions occur in the lower units I-III and the basaltic andesite inclusions in the upper subunits IV-X.
The olivine phenocrysts have Fo 70-80% (Fig. 6.24c) with some variation in each subunit. Subunit-VIII olivines tend to the lowest Fo contents.
The clinopyroxenes are augites (Wo_{32-43} En_{30-51} Fs_{10-31}) with MgO contents increasing from subunit I to VI to then possibly decrease slightly toward the top (Fig. 6.24c). However, these apparent variations could be an artifact of the few data available for some subunits because augites are rare.

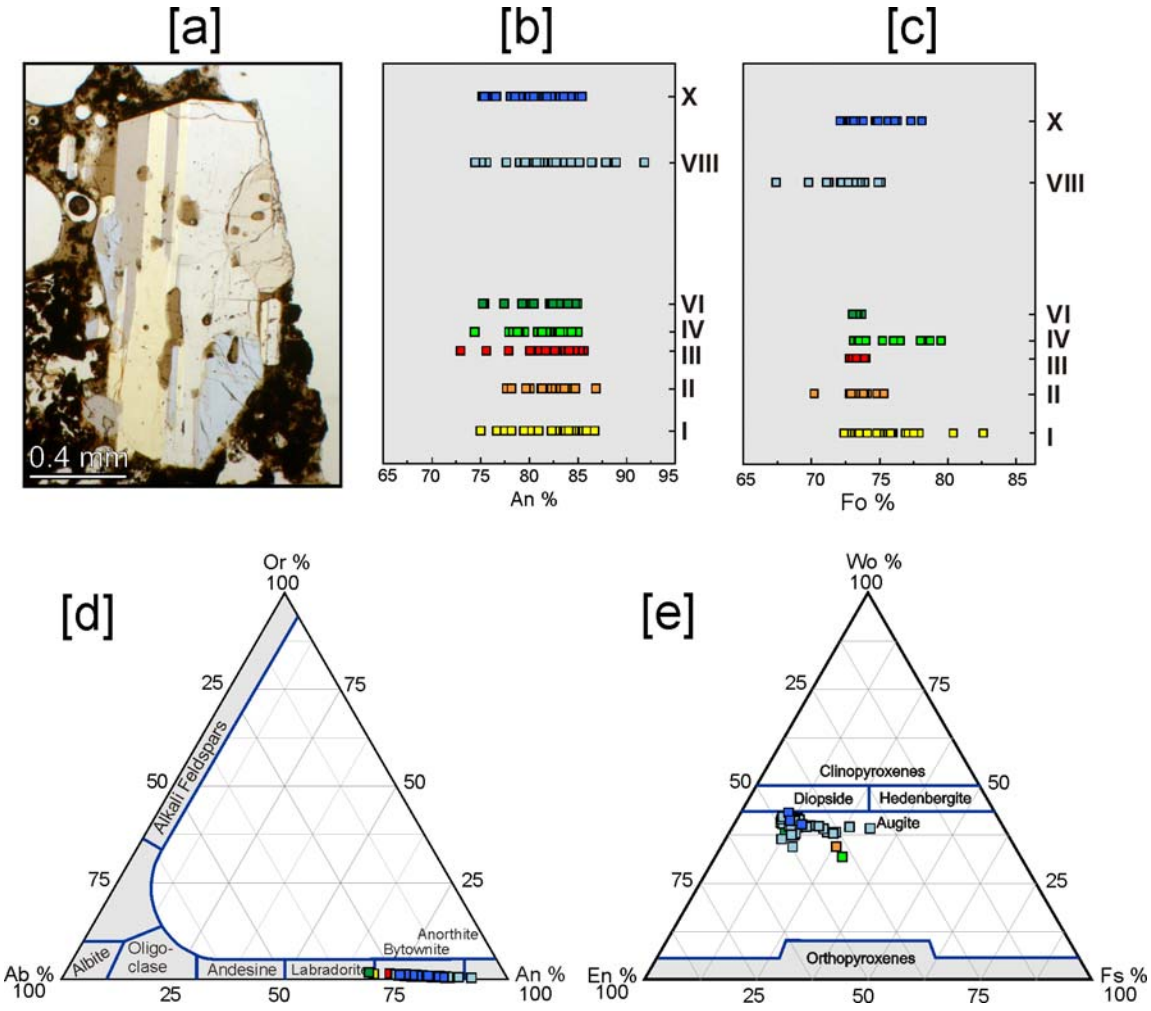

Figure 6.24: Compositions of the major mineral phases of the LCT-MTL. [**a**] Typical plagioclase phenocryst rich in glass inclusions.[**b**] Vertical variations in An content. [**c**] Vertical variations of Fo in olivine. [**d**] An contents of 73-91% cover the bytownite range. [**e**] Ternary plot showing augite compositions.

6.2.3 MT-TIL

6.2.3.1 Bulk rock composition

Bulk rock compositions of the Masaya Tuff and the Ticuantepe Lapilli overlap but MT extends to more evolved, and TIL to more mafic compositions (Fig. 6.2). A consistent internal stratigraphy for the whole ash-rich MT flow deposits could not be established so that samples cannot be arranged in stratigraphic order as for the fallout deposits. Two samples used for glass analysis taken at nearby outcrops at different stratigraphic heights show that some vertical chemical variation exists. The lower sample has higher MgO, Al_2O_3, CaO and lower TiO_2, FeO and K_2O than the upper sample.

Stratigraphically controlled bulk rock analyses of the TIL scoria show a fairly continuous trend of upward increasing MgO, Fe_2O_3, and CaO but decreasing SiO_2 and alkalis (Fig. 6.25). Vertical trace element variations are mostly irregular and lie within analytical uncertainties (Fig. 6.25).

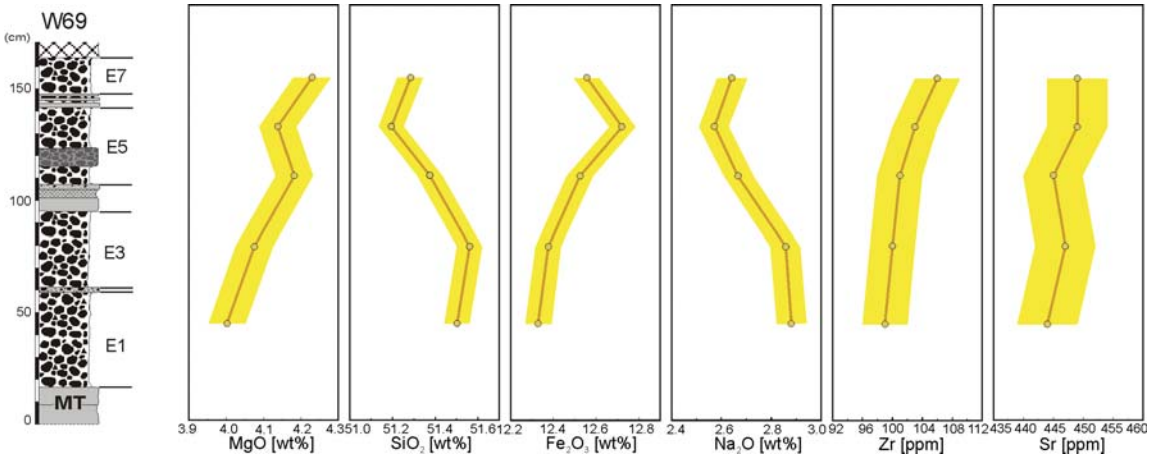

Figure 6.25: Stratigraphic variation of bulk rock compositions of selected elements for the TIL at outcrop W69, near Ticuantepe village.

6.2.3.2 Glass compositions

Glass inclusions in minerals of the MT show a trend of SiO_2, Fe_2O_3, TiO_2 decreasing and Al_2O_3, CaO and Na_2O increasing toward lower MgO contents (Fig. 6.26) that is indicative of olivine-dominated fractionation. The MT matrix glass compositions increase in SiO_2, Fe_2O_3, TiO_2 and Na_2O but decrease in Al_2O_3 and CaO as MgO drops in response to plagioclase-dominated fractionation. The major change in the fractionated mineral assemblage occurred at MgO~5.0 wt% (inflexion point in Fig. 6.26).

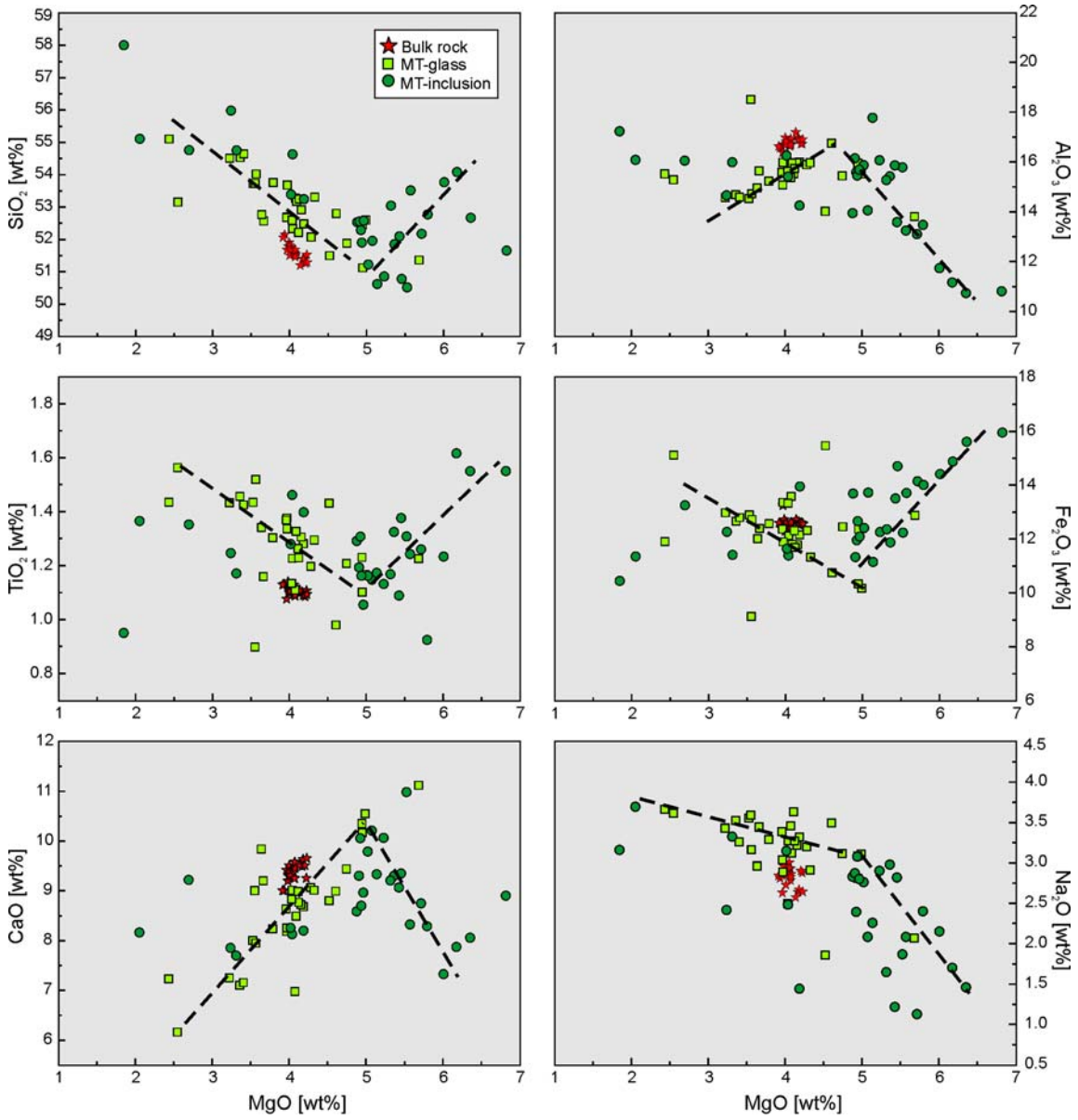

Figure 6.26: Major elements versus MgO for the melt inclusions and matrix glass of the Masaya Tuff compared with the bulk rock compositions. The dashed lines highlight the evolution trends with an inflexion point at MgO~ 5 wt%.

Although the glass compositional ranges of MT (2<MgO<7 wt%) and TIL (2<MgO<6 wt%) are almost identical, the TIL glasses do not show the inflection seen in the MT data but the glass inclusions form a continuous trend with the matrix glasses (Fig. 6.27). With decreasing MgO, SiO_2, Al_2O_3, and Na_2O increase, Fe_2O_3 decreases, and TiO_2 and CaO remain approximately constant. These variations are consistent with fractionation of the phenocryst phases but with a lower ol/pl ratio as for the MT glass-inclusion trend because CaO is buffered.

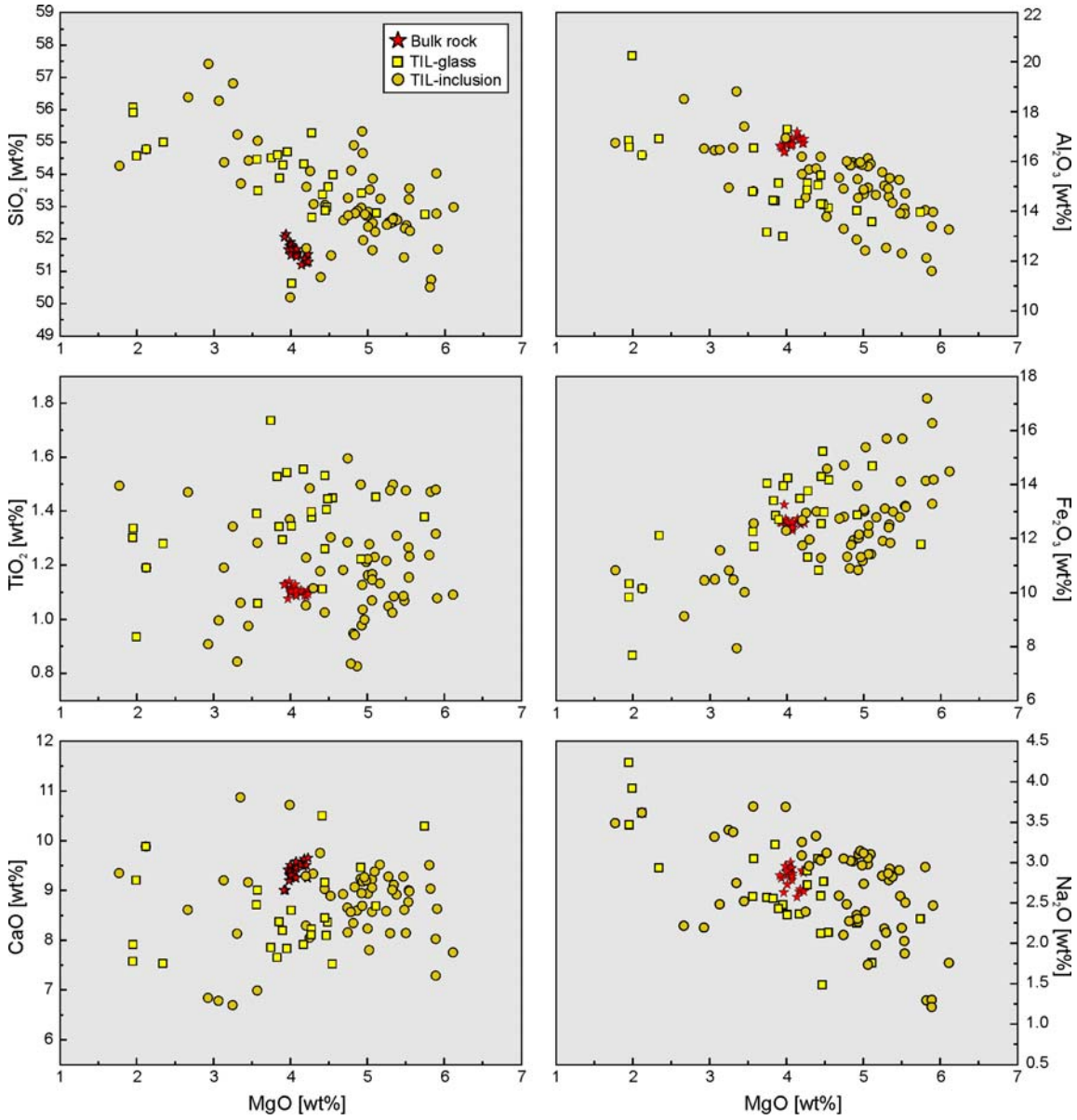

Figure 6.27: Major elements versus MgO for the melt inclusions and matrix glass of the Ticuantepe Lapilli with the MT-TIL bulk rock compositions.

The glasses of both units MT and TIL have higher SiO_2, TiO_2, alkalis and lower Al_2O_3, CaO compositions when compared with the bulk rock compositions (Figs. 6.26, 6.27), consistent with the plagioclase-dominated phenocryst assemblage in the bulk rock.

When distinguishing glass data by stratigraphic origin (Fig. 6.28), different compositional trends for the MT and the upper TIL layer E5 become apparent. With respect to MT glass, TIL-E5 glass forms parallel trends of higher SiO_2, TiO_2 and lower CaO and alkalis, and opposing trends of Al_2O_3 enrichment and Fe_2O_3 depletion. Glass data from the stratigraphically lower TIL layers show some intermediate behavior. The changes in fractionating assemblages derived above from Figs. 6.26 and 6.27 thus occurred gradually from MT to TIL-E5, rather than exactly at the MT-TIL boundary.

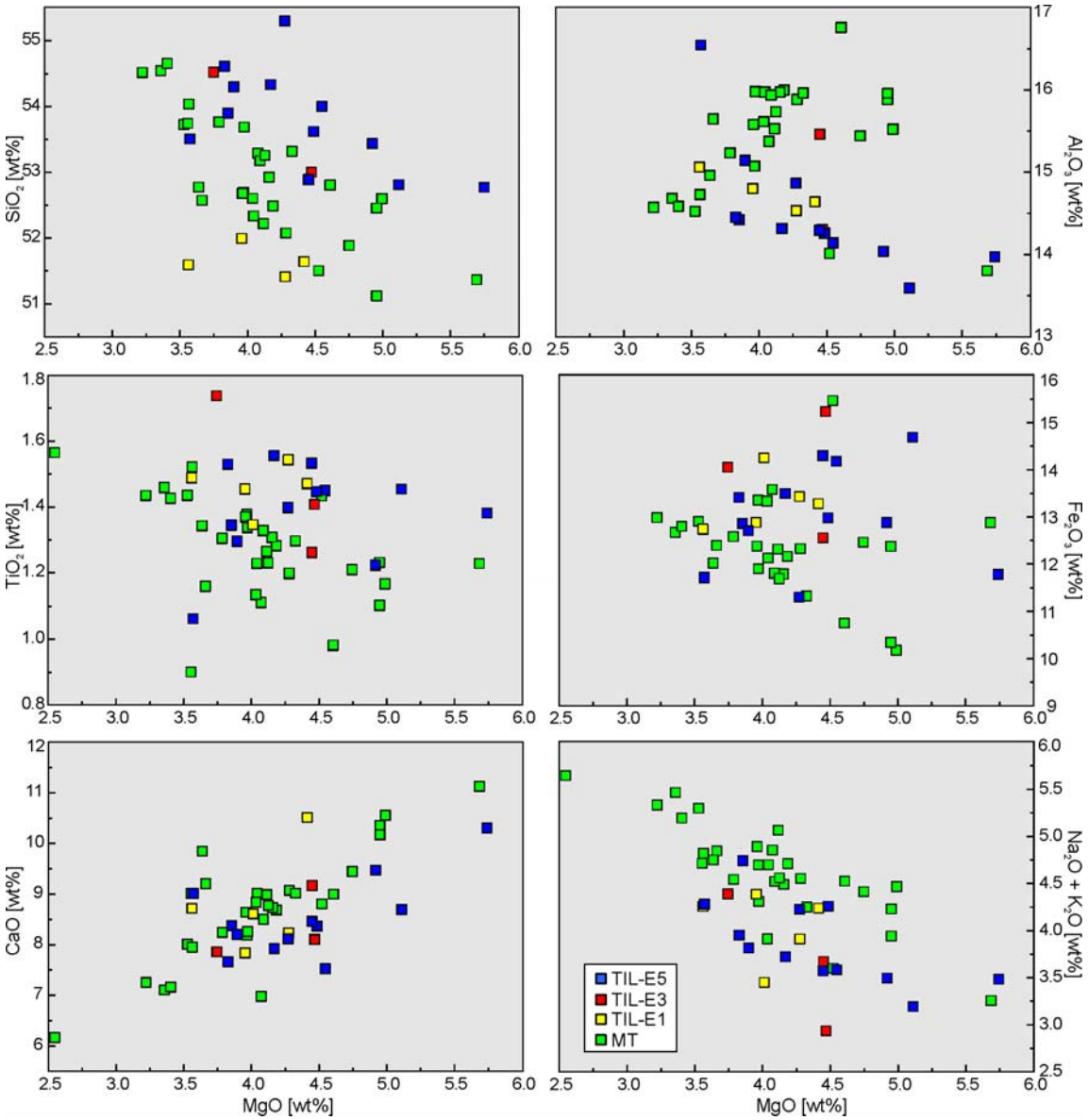

Figure 6.28: Compositional variation of major elements with MgO in MT-TIL glasses identified by stratigraphic position. Note the different trends of MT (green squares) and TIL-E5 (blue squares) glasses.

This gradual change from MT through TIL subunits E1 and E3 to E5 is also illustrated in Fig. 6.29, where the data are plotted in vertical succession. The vertical changes observed in the glass data are not apparent in the bulk-rock compositions, which are partly controlled by the presence of the plagioclase phenocrysts.

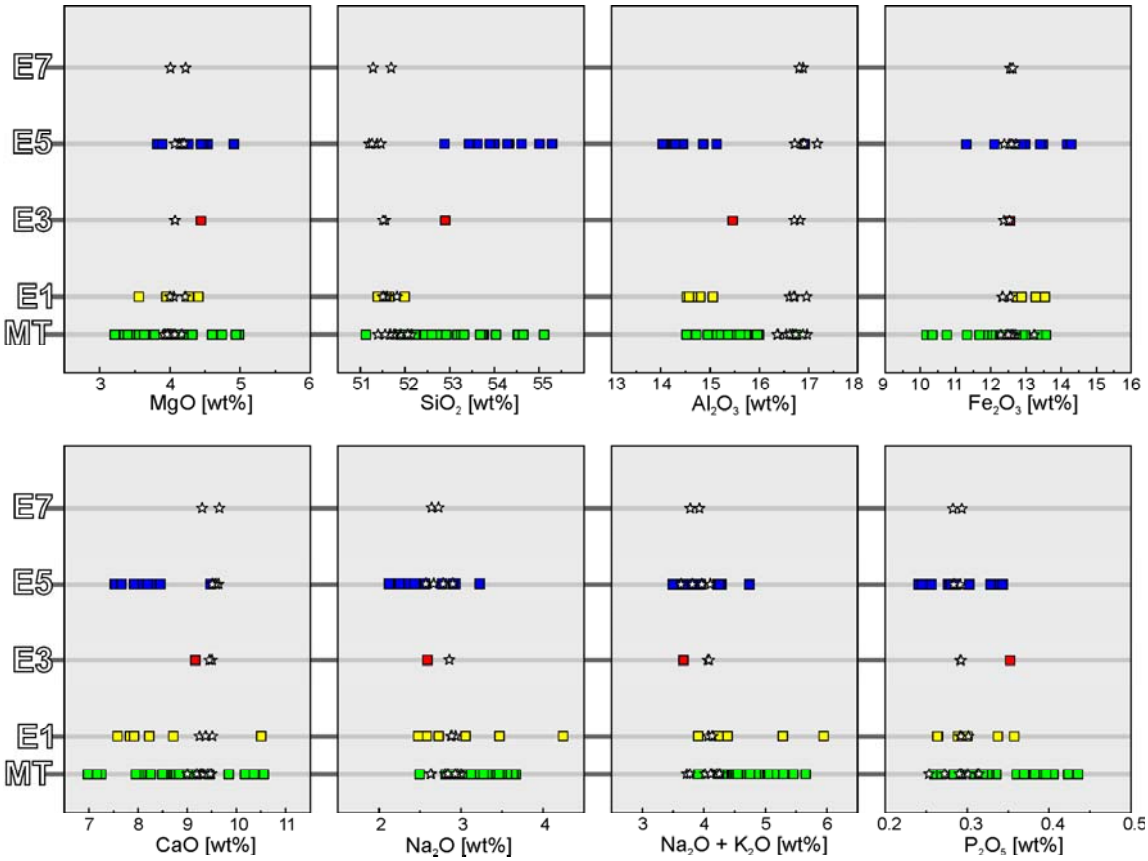

Figure 6.29: Stratigraphic variation of the glass compositions of the MT-TIL compared with the bulk rock compositions (white stars).

6.2.3.3 Mineral compositions

As in the other Masaya tephras, the main mineral phases of the MT-TIL are plagioclase, olivine and clinopyroxene. The plagioclase phenocrysts commonly include glass inclusions; some are brown sideromelane but most are black and devitrified. These inclusions are mostly of basaltic composition for those hosted in MT plagioclase and basaltic andesitic for those in TIL plagioclase.

The plagioclase phenocrysts are mostly bytownites with An of 72-92%, with the MT showing the widest compositional range (Fig. 6.30a, c).

The olivine crystals have Mg# between 0.64 and 0.77 (Fig. 6.30e), and no stratigraphic variation could be found with the available data.

The clinopyroxenes are augites (Wo_{32-44} En_{39-50} Fs_{8-24}, Figure 6.30b, d) with contents of FeO increasing and CaO decreasing upward through the stratigraphy. No pyroxenes were found in the samples of subunit E5.

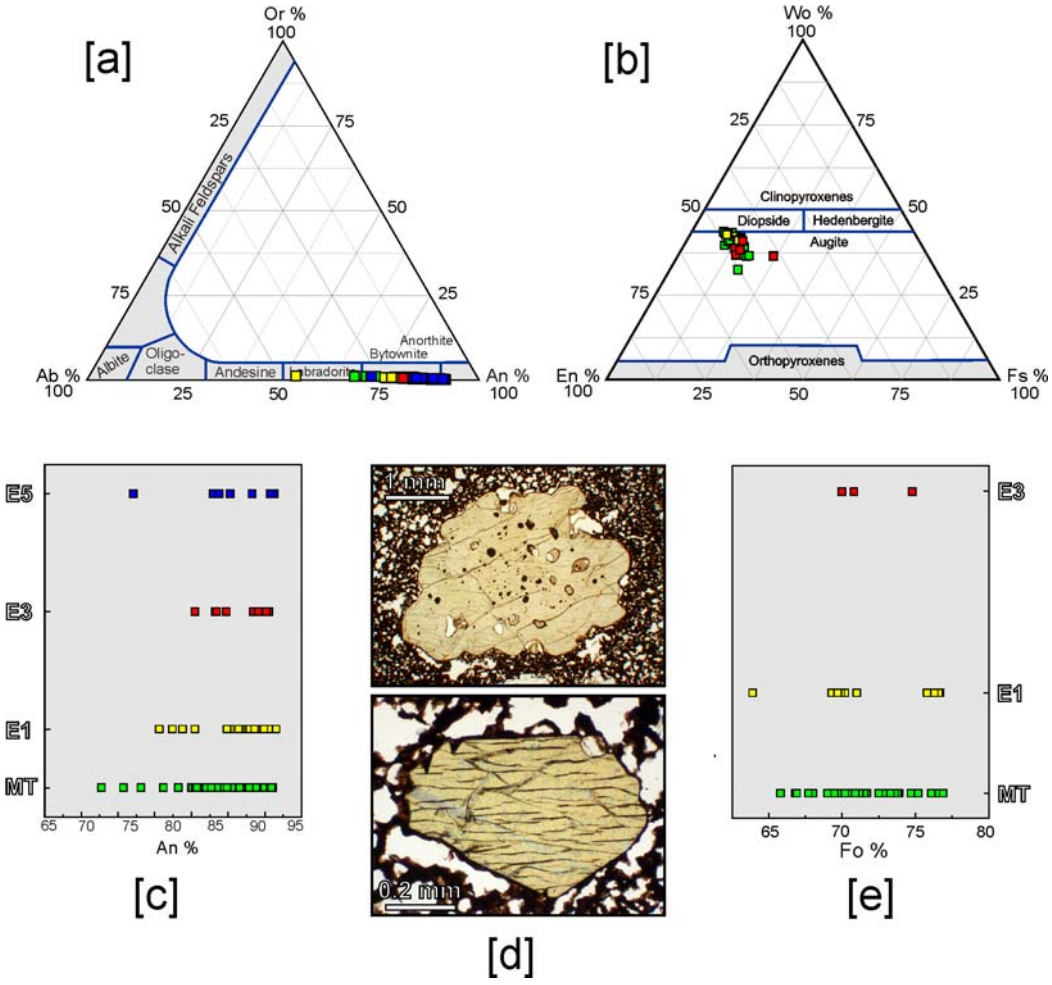

Figure 6.30: Mineral compositions of the MT-TIL. [**a**] Plagioclase ternary compositions. [**b**] Augite compositions in the pyroxene quadrilateral. [**c**] Vertical variation of An content. [**d**] Images of an augite with abundant melt inclusions, and a typical augite phenocryst. [**e**] Vertical changes in Fo content in olivine.

6.3. Origin and evolution of the magmas

Walker et al. (1993) stated that the magmas erupted by the Masaya caldera complex have remained relatively homogeneous in composition over time. Volcanoes similar to Masaya in age, size and tectonic setting commonly generate a wider range of magma compositions from basalt to dacite or even rhyolite. Walker et al. (1993) explained the apparent homogeneity by the presence of a large open-system magma reservoir in which various replenishing inputs become homogenized.

The present study of the three large Masaya tephras, SAT, LCT-MTL and MT-TIL, shows that there are significant compositional differences within the overall narrow range from basalt to basaltic andesite. The origin of such differences is discussed in the following sections.

6.3.1 Mantle sources

As typical subduction related volcanism, the Masaya magma must have been generated in the mantle wedge above the subducting slab. The mantle below western central Nicaragua is not affected by the Galapagos hot spot signature, as it is below Costa Rica and Panama. The possible source composition of the Masaya magmas would thus be primary mantle peridotite variably affected by subducted components creating a modified mantle source (MM of Carr et al. 1990).

Radiogenic isotope ratios are not affected by crystal fractionation and thus potentially allow to distinguish differences in the mantle source of magmas. However, the radiogenic isotope ratios of $^{87}Sr/^{86}Sr$ and $^{143}Nd/^{144}Nd$ of the youngest Masaya Tephras are very similar and do not reveal source variations. They range from 0.704151 to 0.704200 for $^{87}Sr/^{86}Sr$ and from 0.513049 to 0.513060 for $^{143}Nd/^{144}Nd$ (Fig. 6.31); these variations are within the range of analytic error.

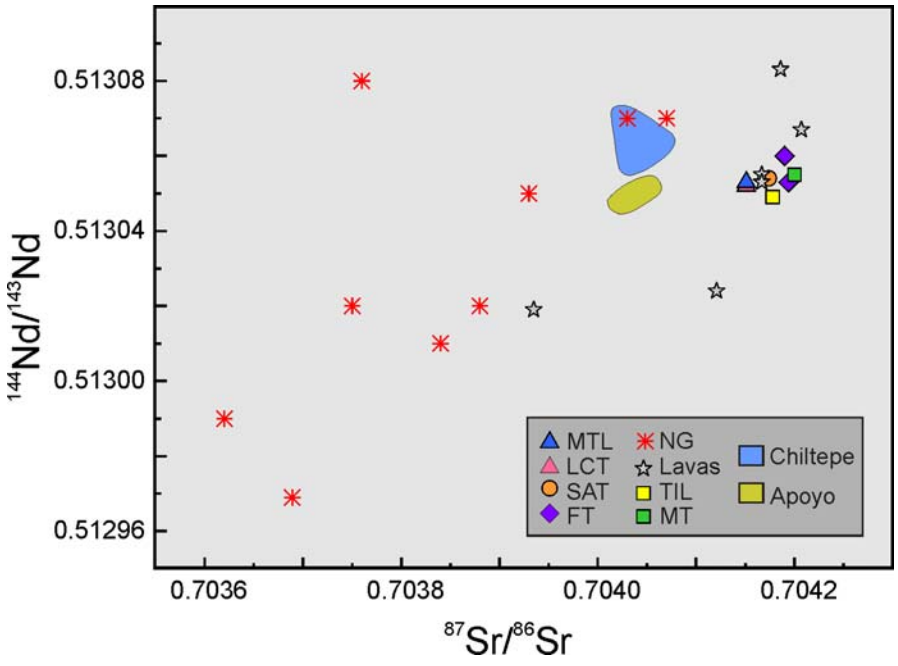

Figure 6.31: $^{144}Nd/^{143}Nd$ vs. $^{87}Sr/^{86}Sr$ diagram comparing the Masaya Tephras to other central Nicaraguan rocks.

In comparison to other rocks from nearby volcanic centres like Apoyo caldera, Chiltepe volcanic complex or the Nejapa-Granada alignments, the Masaya rocks have the highest $^{87}Sr/^{86}Sr$ ratios and high $^{143}Nd/^{144}Nd$ (Fig. 6.31). The high $^{87}Sr/^{86}Sr$ ratios are probably related to fluids derived from subducted sediment; direct mixing with, e.g., sediment melts, should have reduced the $^{143}Nd/^{144}Nd$ ratios simultaneously.
Lead isotopes show a difference between one sample of the FT and the youngest Masaya tephra units (Fig. 6.32), nevertheless this is only shown by one of the two measured samples and it is likely that this divergent behavior is due to analytical problems. The Masaya lavas have lead isotopic ratios different from the tephras, which plot close to the Apoyo data. Since the Apoyo caldera is only ~5 km from Masaya, their sources might be similar.

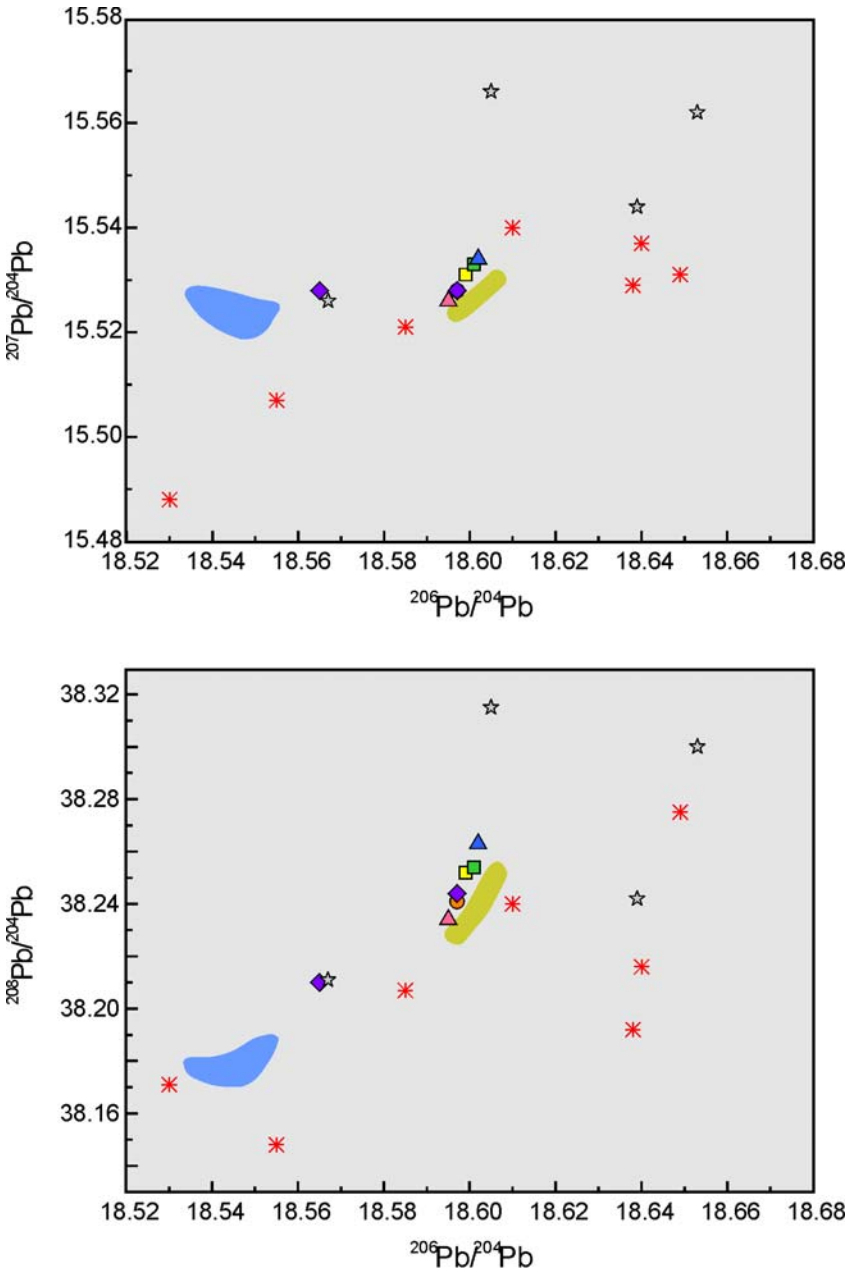

Figure 6.32: Lead isotopic ratios of the Masaya Tephras and nearby volcanic centres, the upper diagram is $^{207}Pb/^{204}Pb$ versus $^{206}Pb/^{204}Pb$ and the lower $^{208}Pb/204Pb$ versus $^{206}Pb/^{204}Pb$. Symbols as in Fig. 6.31.

The absence of significant lead isotopic variations between the tephras, however, does not exclude different slab contributions to their mantle source because Feigenson et al. (2004) noted that the lead isotopic compositions of marine sediments in Central America are exceptionally unradiogenic in Pb, which would allow high sediment contributions to the mantle source without significant changes in Pb isotopes. In fact, the variations in trace-element ratios in Figs. 6.12 and 6.33 show that different source compositions must have existed for the tephras. High LILE but low HFSE contents of the SAT (Figs. 6.4, 6.5, 6.12), and high Ba/La, U/Th, Pb/Ce (Fig. 6.33), imply that its mantle source was more strongly metasomatized than that of the other tephras. There is also a significant difference in trace-element ratios between LCT-MTL and MT-TIL such that the lower LILE contents (low Ba/La in Fig. 6.33) indicate the least metasomatized mantle source for the LCT-MTL, although high U/Th indicates the presence of slab derived fluids.

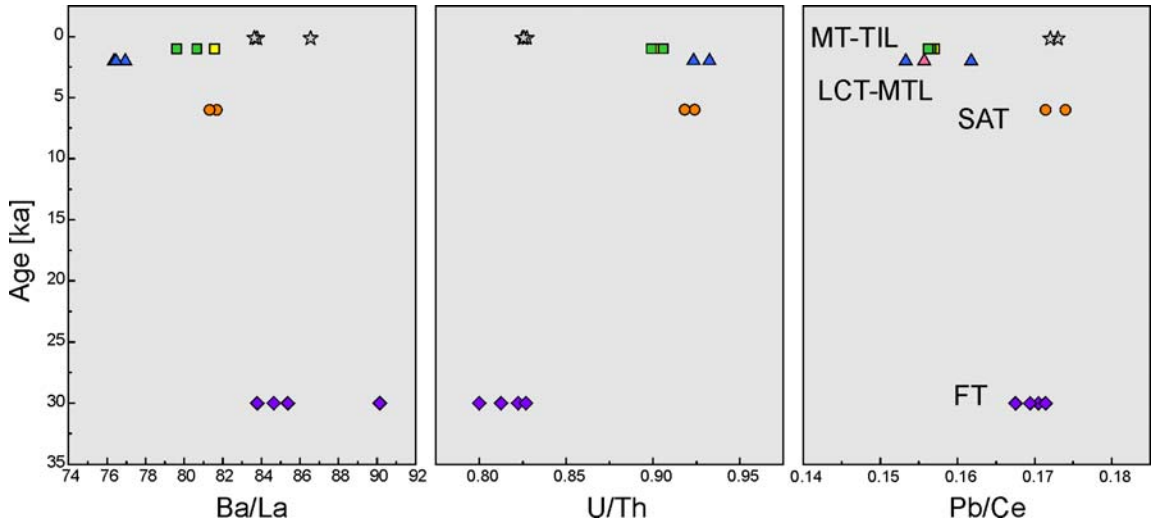

Figure 6.33: Stratigraphic variations of some slab signals, that is trace element ratios which indicate the influence of subduction fluids and sediments. Gray stars are historic Masaya lavas.

The much older Fontana Tephra again has different slab signals from the younger Masaya tephras, but the FT was probably part of Las Nubes rather than the Masaya magma system. The younger Masaya lavas also differ from the tephras high Ba/La and Pb/Ce but low U/Th (Fig. 6.33). In summary, the trace-element variations show that differently composed mantle sources were tapped by the tephras; such changes occurred over about 4000 years between SAT and LCT-MTL, but within only 300 years between LCT-MTL and MT-TIL.

6.3.2 Variations in degree of partial melting

The concentration of incompatible trace elements increases to lower degrees of partial melting; LREE are more incompatible than HREE in garnet-bearing mantle such that high La/Yb indicates low-percent melting (Maaløe, 1994). Elements of similar chemical behavior (e.g., Zr, Hf) may be fractionated at low degrees of melting.

The highest La/Yb, Zr/Hf and Nb/Ta ratios of the SAT (Fig. 6.34) suggest this magma formed by the lowest degree of partial melting. Conversely, such ratios indicate the highest degree of melting for the LCT-MTL magma. This is somewhat surprising because the stronger slab signal of SAT implies water in the mantle wedge would have reduced the peridotite solidus and led to higher degree of melting compared to less modified mantle as the source of the LCT-MTL. Apparently the mantle modification by subduction components and the degree of partial melting are not directly, but possibly inversely, related in the case of Masaya.

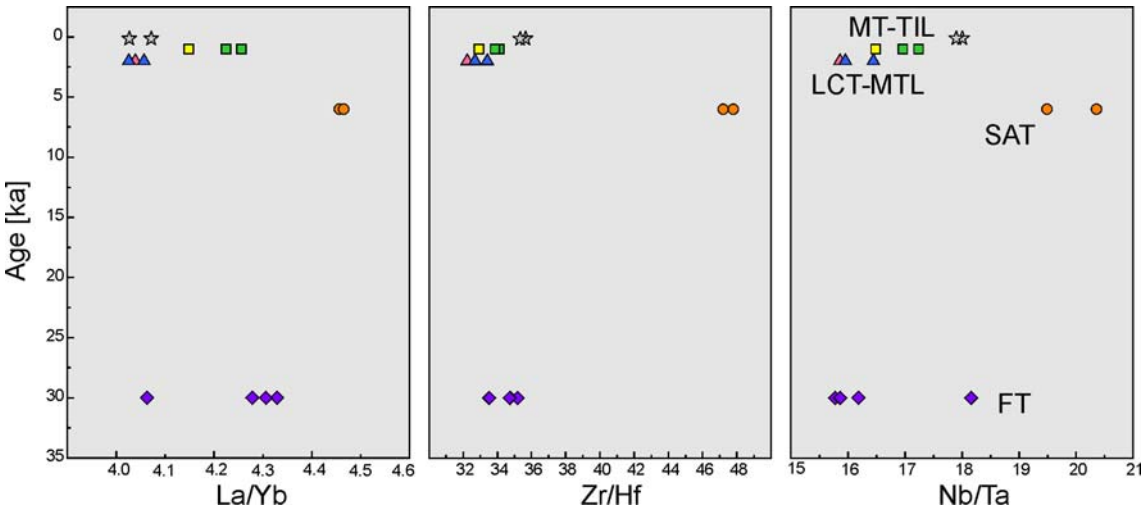

Figure 6.34: Diagrams of La/Yb, Zr/Hf and Nb/Za versus age of the Masaya Tephras including the FT and historic lavas.

6.3.3 Modification during transport and storage

Van Wyk de Vries (1993) argued that Masaya volcano grew at the margin of the Managua Graben, a pull-apart basin (Girard and van Wyk de Vries 2005), such that tectonic structures would act as pathways for rising magma, favouring a rapid ascent and storage at shallow crustal levels. The existence of a large caldera and geophysical studies (Metaxian 1994) support a large shallow reservoir for Masaya. Walker et al. (1993) argued that this would be an open system, periodically replenished reservoir.

The bulk-rock major-element variations of the Masaya Tephras are generally compatible with fractional crystallization of olivine, clinopyroxene and plagioclase, as well as limited fractionation of Fe-Ti oxides (Fig. 6.2). However, it is evident (e.g., in the TiO_2-MgO variation) that the whole rock suite does not follow a single common fractionation trend and that the youngest tephra units cannot be related to each other by fractional crystallization but evolved independantly. This is partly due to their different parental compositions as

discussed above; another factor is that they also had different crystallization histories.

For example, bulk-rock compositional variations in Fig. 6.35 support efficient plagioclase fractionation in the MT-TIL (reducing Al_2O_3, CaO, Sr) together with olivine. TIL glass compositions (Fig. 6.27), however, support ol>pl fractionation (Al_2O_3 increases to lower MgO). More efficient augite than plagioclase fractionation is suggested by the SAT bulk-rock data (reducing CaO, enriching Al_2O_3, Fig. 6.35), whereas plagioclase dominated fractionation when the glass c0mpositions formed (Fig. 6.17). The LCT-MTL bulk-rock data form a cluster with no clear trend although some MTL data support cpx-dominated fractionation (Fig. 6.35). The LCT-MTL glass data, however, shows that olivine dominated fractionation down to 4.8 wt% MgO, when plagioclase became the main fractionated phase (Fig. 6.22). The crystallization and fractionation of plagioclase relative to the ferromagnesian minerals strongly depends on the partial pressure of water. Earlier pl-fractionation as in MT-TIL and SAT suggest higher P_{H2O} with respect to delayed pl-fractionation in LCT-TIL at lower P_{H2O}. This may reflect higher water contents of the MT-TIL and SAT magmas with stronger slab signals. However, P_{H2O} depends on both water content and absolute pressure at crystallization, which will be investigated in the next chapter.

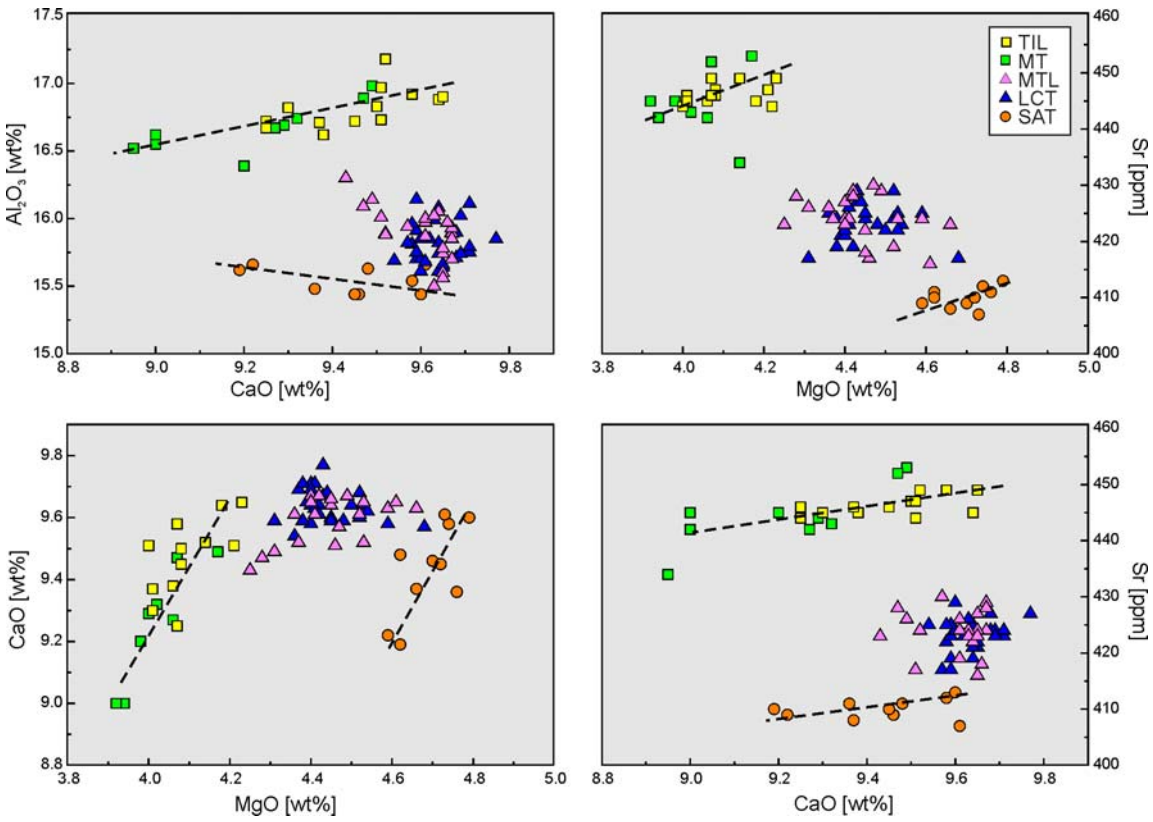

Figure 6.35: Bulk rock compositional variations indicative of pl and cpx fractional crystallization of the Masaya tephra units. The black dashed lines show the fractionation trends.

Chapter 7

Magma chamber conditions

7.1 Pre-eruptive conditions

Compositions of the mineral phases, inclusions and groundmass glass were used to determine the T and P conditions in the magma prior to eruption, based on mineral-melt equilibrium models. Several of these methods were applied and the results compared in order to constrain the most reliable results.

7.1.1 Water content

Measurements of water contents in melt inclusions were carried out with the Fourier-Transform infrared spectroscopy (FT-IR) at the University of Texas at Austin. Since some leakage of the melt inclusions cannot be excluded with certainty, the maximum measured concentrations probably best reflect the initial water contents of the melts. The highest values of water vary between 1.7-2.2 wt% for the SAT, 1.3-1.5 wt% for the LCT-MTL, 3.2-3.4 wt% for the MT and 2.6-2.7 wt% for the TIL.

7.1.2 Temperature of crystallization

Different calculations of temperatures were made for the youngest Masaya tephras using the melt and mineral phases compositions. One of these approaches is the empiric formula of Wallace and Carmichael (1992) using mole fractions of MgO and Al_2O_3 that is independent on the oxygen fugacity. This yielded pre-eruptive temperatures similar for all the units, ranging from 1114-1156°C (± 9°C), except for the evolved glass of the SAT which yielded lower pre-eruptive temperatures of ~1100°C ± 9°C (Table 7.1).

Table 7.1 Temperature results applying different approaches for the youngest Masaya tephra units

Temperature (°C)	SAT		LCT-MTL	MT	TIL
	Mafic glass	Felsic glass			
Wallace and Carmichael (1992)	1125-1156	1099-1104	1119-1146	1117-1148	1114-1143
Kudo and Weill (1970)	1165-1280[1] 1115-1220[2] 1070-1180[3] 745-885[4]	1140-1255[1] 1090-1195[2] 1040-1155[3] 630-810[4]	1120-1230[1] 1075-1175[2] 1030-1135[3] 690-830[4]	1150-1260[1] 1100-1185[2] 1060-1180[3] 730-875[4]	1110-1240[1] 1090-1170[2] 1050-1130[3] 705-810[4]
Housh and Luhr (1991)	1050-1105[5] ~1350[6]	1080-1130[5] 1225-1235[6]	1090-1110[5] ~1380[6]	970-980[5] 1190-1110[6]	1015-1025[5] 1240-1260[6]
Sisson and Grove (1993)	1069-1090	1029-1051	1091-1096	1028-1040	1045-1054
Nielsen and Drake (1979)	1152-1225		1042-1188	1072-1189	1167-1227

[1] P_{H2O}=0 MPa, [2] P_{H2O}=500 MPa, [3] P_{H2O}=1000 MPa, [4] P_{H2O}=5000 MPa [5] using Ab exchange, [6] using An exchange

Other approaches given by plagioclase-melt equilibrium in hydrous systems calculate the temperature of equilibration of coexisting plagioclase and magmatic liquid. The method of Kudo & Weill (1970) and modifications by Mathez (1973) yielded temperatures for the Masaya tephra between 1075-1280°C at pressures lower than 500 MPa, and very low temperatures <1000°C at higher pressures (Figure 7.1, Table 7.1).

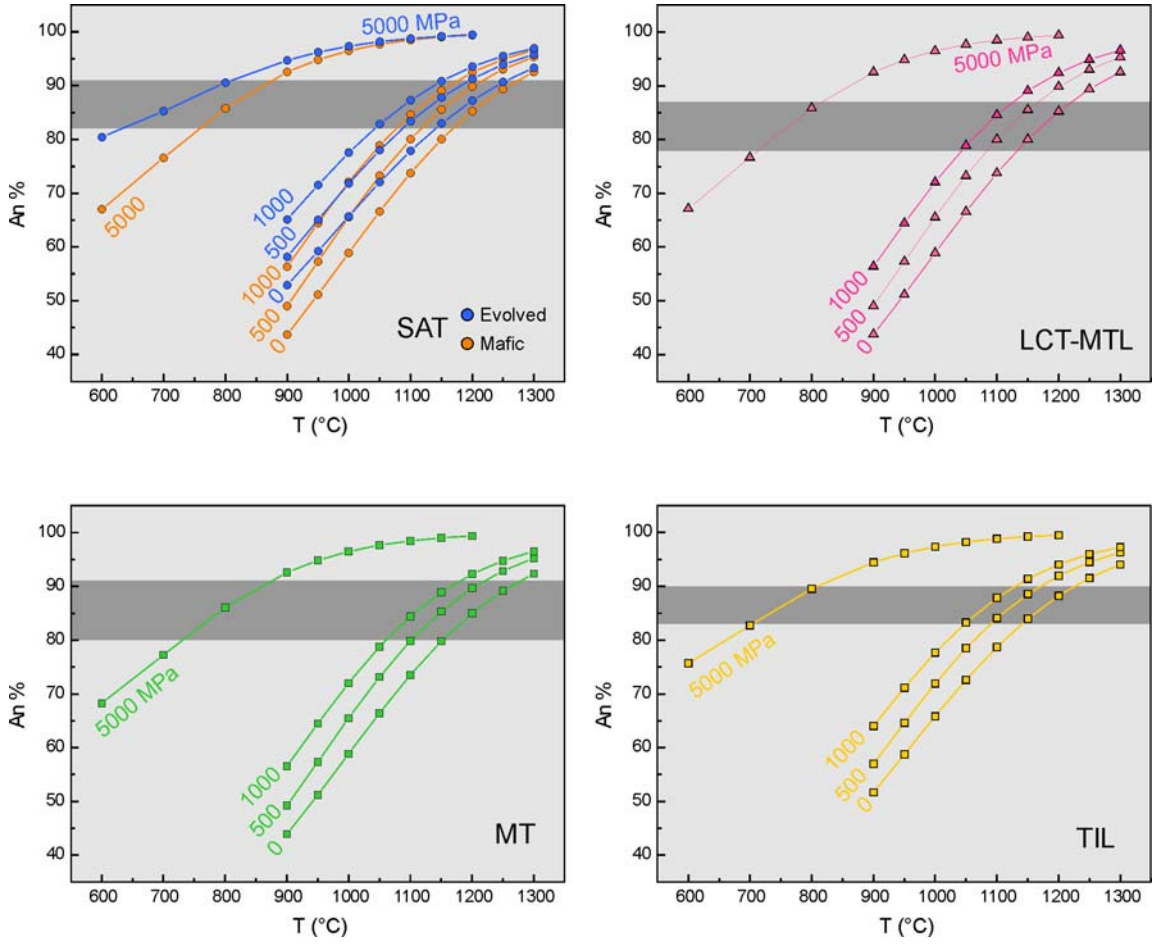

Figure 7.1: Temperature vs anorthite content (An%) of the plagioclase as obtained with the Kudo-Weill plagioclase geothermometer (Kudo and Weill 1982) for the studied units: SAT with its both glass compositions, the mafic member and the evolved one; LCT-MTL, MT and TIL. The darker area show the range of An% measured in the plagioclase phenocrysts.

Using the method of Housh and Luhr (1991), also based on plagioclase-melt equilibrium for hydrous systems, yields the curves shown in Fig. 7.2. They relate the temperature of the system to the H_2O content of the melt in two ways: [1] using the expression for albite (Ab) exchange and [2] for anorthite (An) exchange. An average for the melt composition and the composition of the plagioclase with the highest and the lowest anorthite contents of every unit were used as input data.

By using the temperature ranges at low pressures (0 to <500 MPa), obtained with the Kudo-Weill plagioclase geothermometer, the H_2O content of the melt was calculated as 2.6-3.8 ± 0.54 wt% (An) and 0.3-1.6 ± 0.3 wt% (Ab) for the

SAT mafic, 1.9-3.2 ± 0.54 wt% (An) and 0.7-2.2 ± 0.30 wt% (Ab) for the SAT evolved glass, 3-4.3 ± 0.54 wt% (An) and 0.4-1.6 wt% (Ab) for the LCT-MTL, 2.8-4.8 ± 0.54 (An) and 0.4-2.4 ± 0.30 wt% (Ab) for the MT-TIL. Using the water content obtained by direct melt inclusions measurements with the FT-IR, in return, yield temperatures for SAT mafic between 1050-1105°C (Ab) and ~1320°C (An), 1080-1130°C (Ab) and 1225-1235°C (An) for SAT evolved, 1090-1110°C (Ab) and ~1380°C (An) for LCT-MTL, 970-980°C (Ab) and 1190-1200°C (An) for MT and for TIL 1015-1025°C (Ab) and 1240-1260°C (An; Table 7.1).

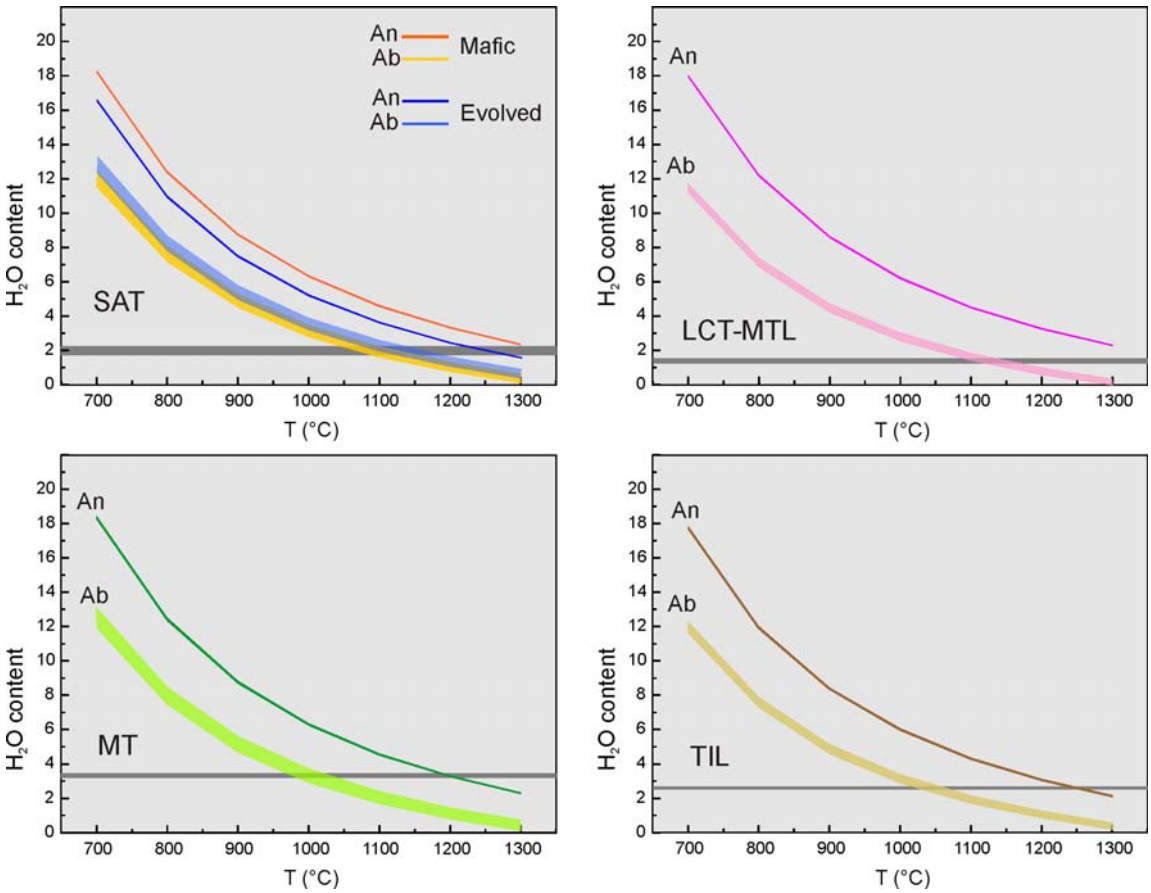

Figure 7.2. Relationship between the water content of the melt and the temperature obtained with the method of Housh and Luhr (1993). The areas shown are the range of variation obtained by using the highest and the lowest An% measured at the plagioclases at the unit. An refers to the curves obtained using the anorthite exchange and Ab those for albite exchange. The dark gray bars are the water contents measured in each unit.

The method of Sisson and Grove (1993) was applied also using the measured water contents. The resulting temperature ranges are: SAT mafic 1070-1090°C, SAT evolved 1030-1050°C, LCT-MTL 1090-1110°C, MT 1028-1040°C and TIL 1045-1055°C.

The method of Nielsen and Drake (1979) using the composition of the melt and of clinopyroxene yielded wide ranges of temperatures: 1152-1225°C for SAT, 1042-1188°C for the LCT-MTL, 1072-1189°C for the MT and 1167-1227°C for the TIL.

Other estimates of crystallization pressures and temperatures for clinopyroxene, plagioclase and olivine were made based on the models of Putirka et al. (1996; 2003) and Putirka (2005). These yielded extremely high temperatures, e.g. plagioclase of the LCT-MTL yielded 1283-1348°C for anhydrous models and 1443-1468°C for hydrous models or for the SAT clinopyroxene yielded temperatures between 1395-1574°C and pressures up to 18 kbar. These results are unrealistic and not consistent with the results of the other applied methods.
A summary of the temperature ranges obtained by the different approaches is presented in Fig. 7.3. Although most results point to temperatures between 1100-1200°C for all of the units, the most confident data are the results of Sisson and Grove (1993) because they are based on direct measurements of the water content. The temperatures obtained with the Housh and Luhr (1991) approach also show that, in most of the cases, the results obtained with the albite exchange equations yielded better results than the anorthite formulation (Fig. 7.3). The results following Putirka (2003) are not represented here because they are out of the range considered in the graphics.

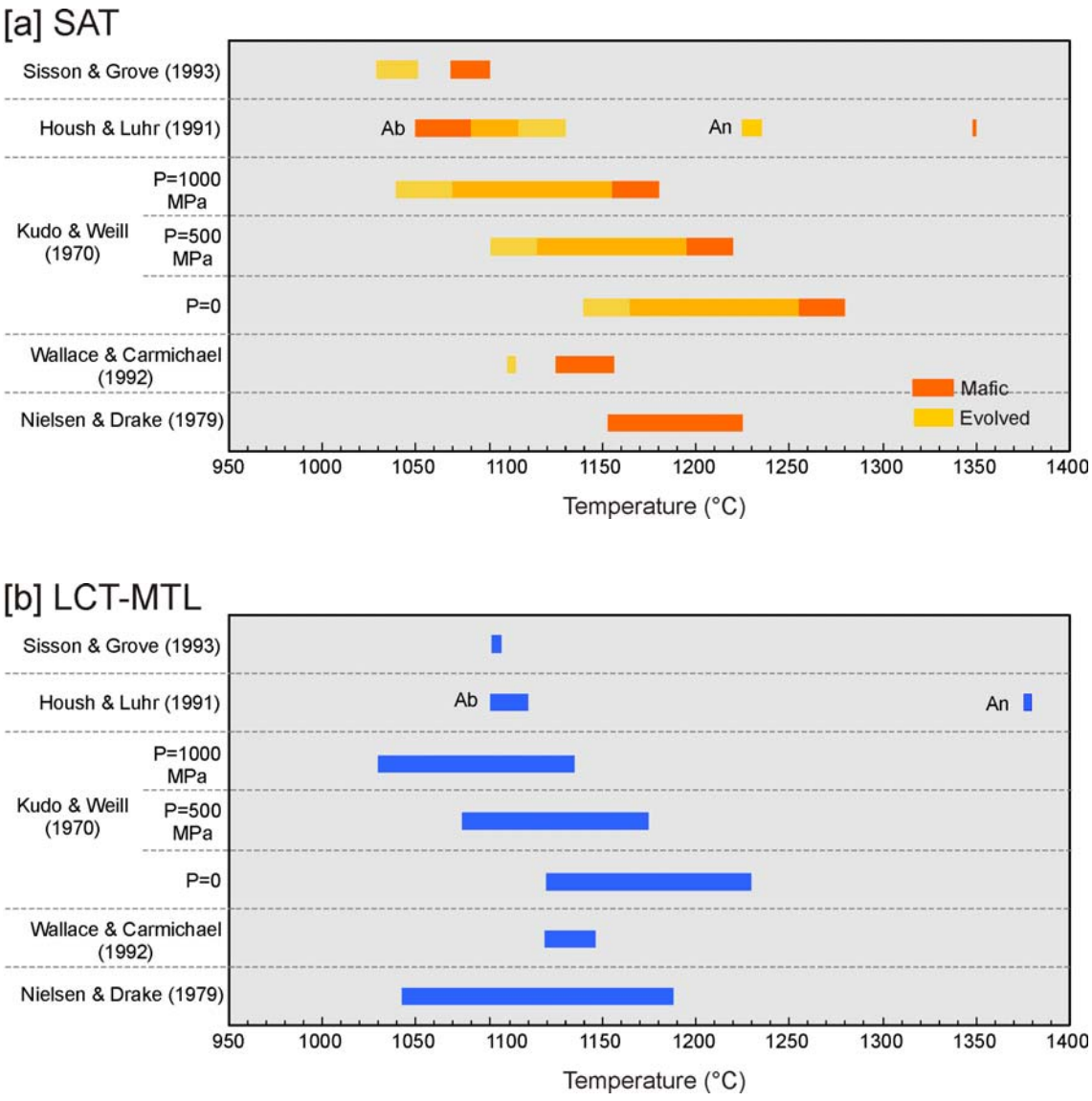

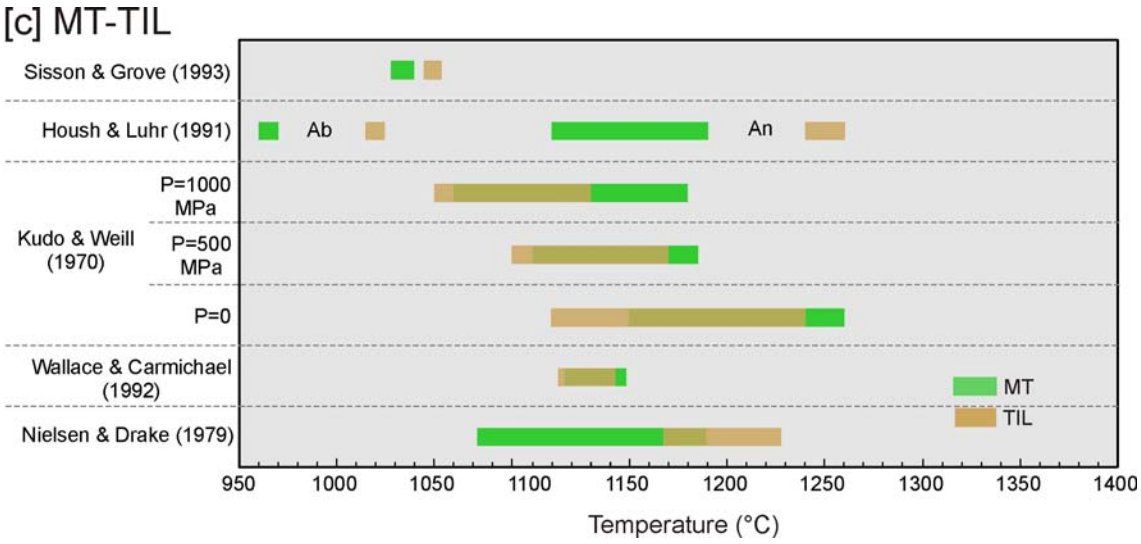

Figure 7.3: Comparison of the temperatures ranges obtained by the different approaches.

7.1.3 Pressure

The CMAS projection of Grove et al. (1982) indicates the crystallization for all units SAT, LCT-MTL and MT-TIL took place at pressures between 100 and 0.1 MPa (Fig. 7.4). Clinopyroxene crystallization pressures calculated after Nimis (1995, 1999) show a range between 0 and 650 MPa (P_{avg} 180 MPa) for SAT, 0-1000 MPa (P_{avg} 300 MPa) for LCT-MTL and 0-950 MPa (P_{avg} 230 MPa).

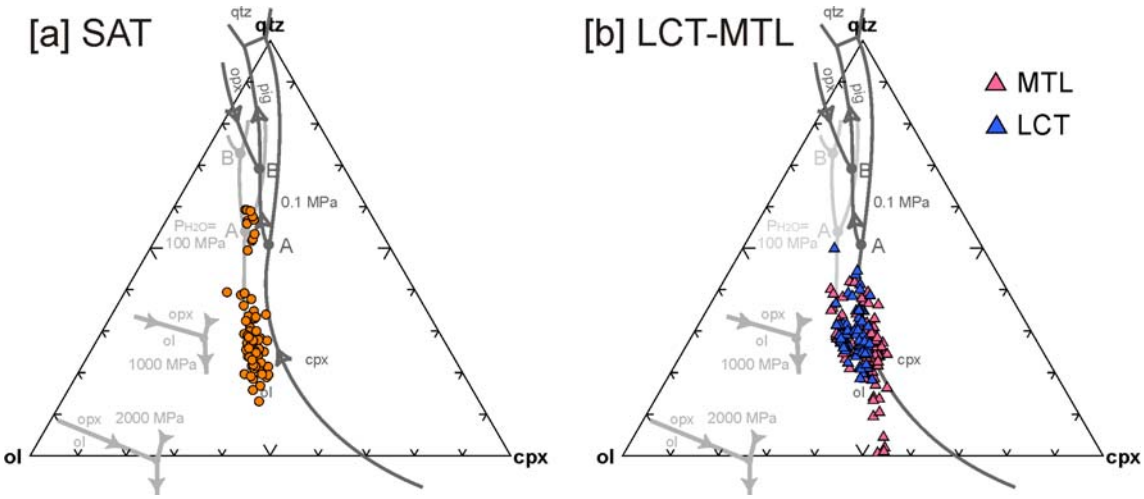

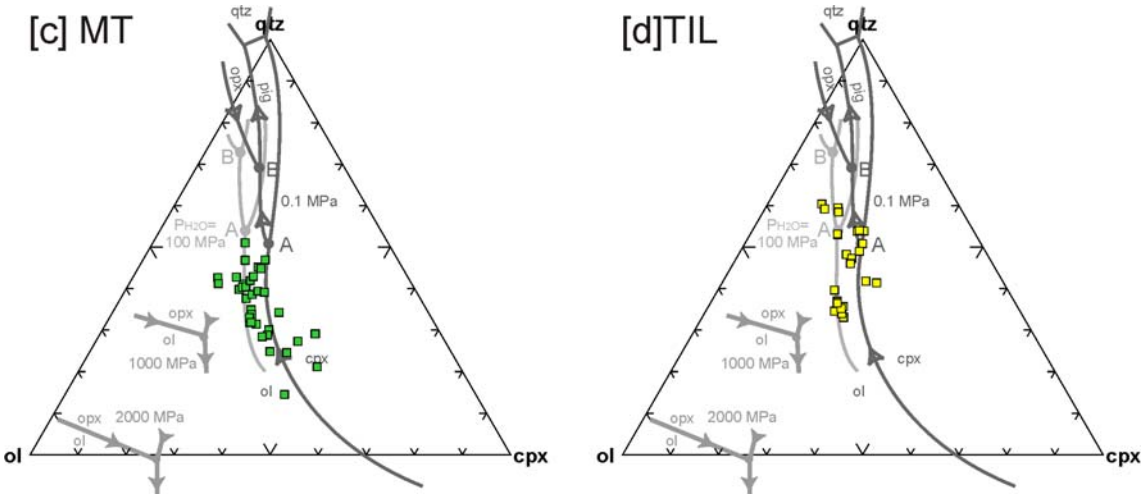

Figure 7.4: CMAS projection for the younger Masaya explosive deposits, the after Grove et al. (1982).

7.1.4 Magma chamber characteristics

The temperatures of crystallization, obtained by means of the crystal-melt equilibrium models, and the pressure estimates give information about the reservoir where the magma was stored and an idea of the timing of crystallization of the main mineral phases.

The pressure calculations suggest that the crystallization took place at relatively low pressures, at ranges between 0.1-300 MPa. These data would be equivalent to a magma chamber at less than 10 km depth where the magma started to crystallize. These results are consistent with the gravimetric studies carried out at Masaya (Metaxian 1994), which found an intrusion at 3–9 km below Masaya.

Chapter 8

Volcanic hazards

The central western region of Nicaragua with the cities of Managua, Masaya and Granada, is the most densely populated area of the country. It also holds a concentration of important socioeconomic infrastructures, such as the International Airport, the Inter-American Highway, government buildings and embassies, factories, and the telephone, water and energy supply companies. This area is surrounded by three volcanic centers that produced highly explosive eruptions in the past: the Chiltepe Peninsula volcanic centers (Apoyeque, Xiloá), Masaya caldera, and Apoyo caldera.

Schmincke (2004) cited examples of cities and megacities with large population densities and high growth rates within the reach of active volcanoes as places of major volcanic risk. Among these cities –which include Tokyo, Naples, México city- he also mentioned Managua as being at risk because it is " built on many young volcanoes, nearby active Masaya volcano, having erupted violently by magma-water interaction in the late Holocene", referring in the last sentence to the Masaya Tuff eruption.

In view of the highly explosive eruptions over the past few thousand years that have been documented here, Masaya caldera (together with the Chiltepe Volcanic Complex) has the highest probability of a similarly large eruption in the future (cf. Freundt et al. 2006). What would be the risk if an eruption like those of the recent past took place at Masaya today?

The concept of risk has been defined as Risk = Hazard x Vulnerability (UNESCO, Blong 1996), where hazard refers to the physical effects produced by an eruption and the vulnerability considers the potential damage for people, buildings, infrastructure and economic activity. In order to make a risk assessment, it is necessary to understand both the hazards and the vulnerabilities (Blong 1996).

In this way, this chapter will first consider the volcanic hazards from Masaya caldera from events similar to the highly explosive eruptions of the last 6,000 years, then the vulnerability of the area around the volcano which might be affected by these events and finally an analysis of the risk in case of future eruptions.

8.1 Volcanic Hazards

The first approach to evaluate the potential volcanic hazards from a volcano is to reconstruct the eruptive history of a volcano. This usually involves detailed study of the deposits from past eruptions determining stratigraphic sequence, distribution, age, volume and characteristics, among others. Numerical modeling is also useful to consider changes in eruptive behavior.

Several volcanic hazard types can be produced by the Masaya caldera complex, including volcanic gases, lava flows, tephra fall and pyroclastic surges. Nevertheless other hazards (e.g. volcanic earthquakes, lahars, etc.) may also occur.

This work will focus in two types of hazards from explosive volcanism: pyroclastic fall and surges. This is because they are among the most dangerous volcanic events and they were responsible for the deposition of the youngest major deposits at Masaya: the San Antonio Tephra, La Concepción Tephra-Masaya Triple Layer, the Masaya Tuff and the Ticuantepe Lapilli.

8.1.1 Hazards from pyroclastic fall

The main hazard of pyroclastic fall is the collapse of buildings under the tephra load accumulating on rooftops. Two important aspects are to consider: the thickness of tephra which accumulates in a defined area, and the quality of the roofs and structures. According to Pyle (2000), it only takes an accumulation of dry tephra that exceeds 1 kPa load stress, equivalent to a dry non-compacted thickness of 10 cm of basaltic tephra, to trigger the collapse of at least of low-quality roof structures. Blong (2003) found out that even residential buildings with steel roofs on timber frame suffered heavy damage with a tephra load of 2 kPa during the 1994 eruption of Rabaul (Papua New Guinea).

Ballistically ejected large fragments can cause severe damage in the areas near the vent. Some ballistic blocks have been reported to reach distances as far as 5.5 km from the vent at Arenal Volcano in Costa Rica (Melson and Sáenz 1973), and 8 km at Fuego Volcano in Guatemala (Rose et al. 1973; 1978). Ballistic blocks were not ejected or did not reach as far as the most proximal outcrops of both fall and surge deposits during the Masaya eruptions studied here. Nevertheless, ballistic block ejection may occur during a future eruption.

8.1.2 Hazards from pyroclastic surges

Pyroclastic surges are turbulent, often highly energetic currents that can travel at speeds exceeding 100 km per hour. They are not restricted to low topographic areas as are lahars and can surmount topographic highs, as is shown by the radial distribution of the Masaya Tuff across the pre-existing topography.

The main hazards from surges include destruction by the force of the current, impact by rock fragments, burial by deposits, incineration, noxious gases and asphyxiation (Valentine 1998; Baxter et al. 2005). At Unzen volcano, the ash cloud surge accompanying the June 3, 1991 pyroclastic density current ($5x10^5$ m^3) killed a group of journalists and volcanologists, shifting the carbonized bodies and nearby cars about 80 m from their original position (Nakada 2000). This surge was small compared to those that deposited the Masaya Tuff.

Pyroclastic surges are considered deadly dangers over proximal areas of high-energy lateral spreading, but turn into relative harmless ash clouds depositing fall ash at greater distance (Wohletz 1998).

8.1.3 Hazards from the Masaya caldera complex

The eruptive past of the Masaya caldera complex indicates that the system has experienced 3 main highly explosive eruptive periods in the last 6,000 years. These periods produced 3 major fallout-dominated events, able to form Plinian eruptions and moderate sized pyroclastic surges (SAT, LCT-MTL, TIL), as well as a large Surtseyan eruption which deposited a thick widespread base surge deposit, the MT.

The eruptions which generated the two older fallouts –SAT and LCT-MTL- had a similar sequence of events, starting with minor phreatomagmatic activity followed by the paroxysmal Plinian eruptions. Intense phreatomagmatic activity

produced the surges that dominated the waning phase of the eruptions. The youngest TIL marked the end of the last big eruption which formed the Masaya Tuff and it consists of fallout deposits with some influence of magma-water interaction.
The phreatomagmatic eruptions forming the Masaya Tuff produced highly energetic, so-called base surges that radiated directly from the vent to great runout distance and were able to surmount topographic barriers several hundred meters high. The geologic record shows no precursory activity that may have announced their appearance, but the eruption itself started with a blast forming a thin basal layer rich in quenched vitric fine-lapilli which destroyed the existing vegetation. Although distal deposition became increasingly affected by wind, it was still controlled by rapid lateral flow as far away as Managua city (~15 km from the caldera), as indicated by the cross-bedding and pinch and swell structures in the lowermost part of the deposit. For comparison, the surge that destroyed the city of St. Pierre on Martinique in 1902 left a deposit only <10 cm thick (Boudon and Lajoie 1989).
The sudden occurrence and rapid spreading of such a surge leaves little chance for countermeasures once the eruption is in progress. Even the Subplinian to Plinian, mainly fallout-producing eruptions of Masaya were repeatedly interrupted by collapse of the eruption column and production of pyroclastic surges, although these were of much lower energy and lateral runout compared to the Masaya Tuff.
Actually known examples of base surges like those of the Masaya Tuff are scarce, most of base surges have maximal long runouts of <10 km from the vent, whereas the MT reached more than 15 km. One example of a widespread surge was the Agnano-Monte Spina eruption (4.1 ka) of the Campi Flegrei which spread base surges to 15 km from the vent (de Vita et al. 1999).

8.2 Vulnerability of the area

The vulnerability refers to the life and economical loss that may affect an area due to a hazard. This includes people's lives, buildings, lifelines (transport, communication, energy sources, etc), agriculture and other economic activities (Blong 1996).

8.2.1 Population

The area around the Masaya caldera located between the two lakes (Lake Nicaragua and Lake Managua) is the most densely populated of the country (Fig. 8.1).

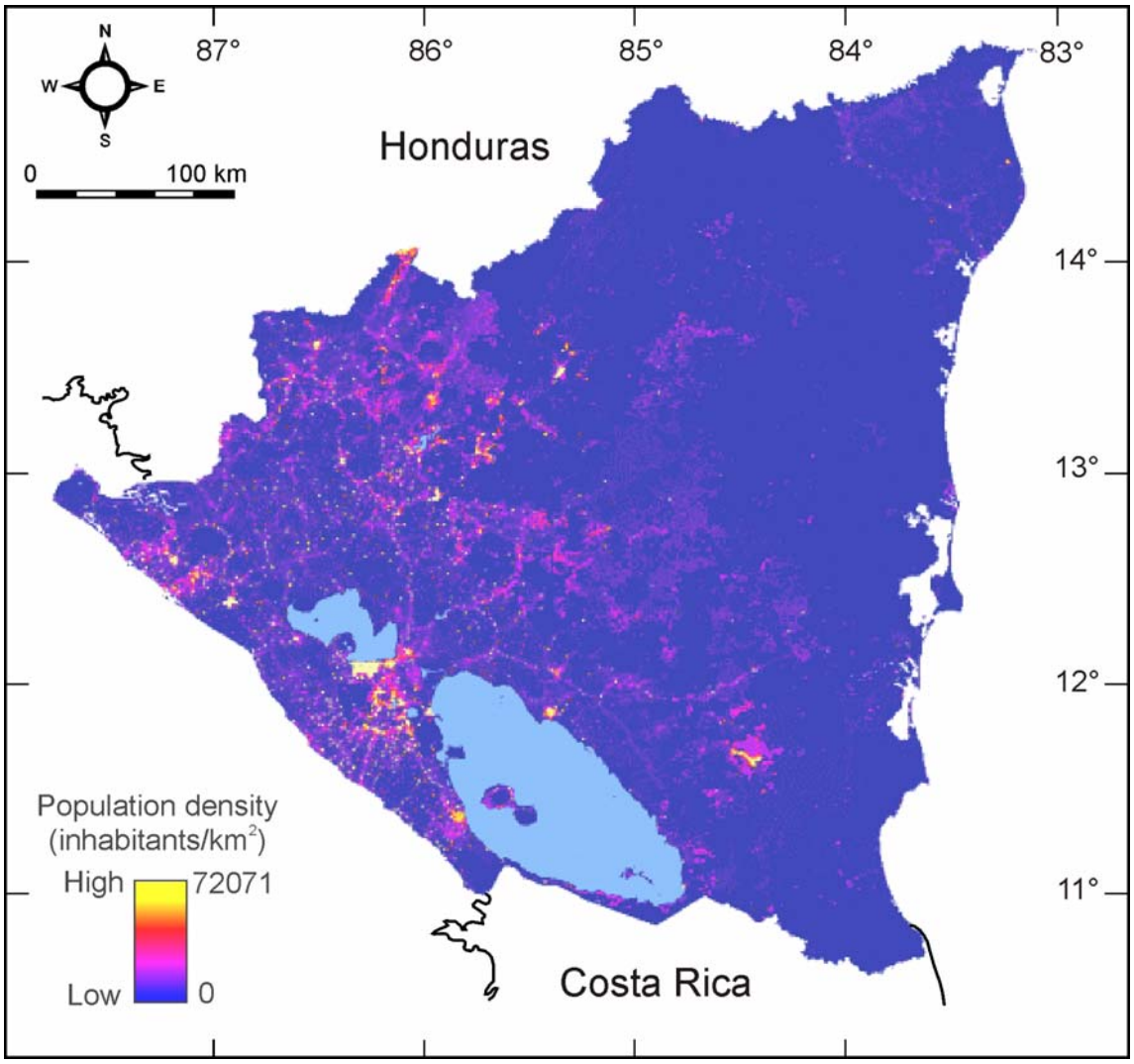

Figure 8.1: Population density map of Nicaragua. Note that the highest density is at the area between the two big lakes where the Masaya caldera complex lies. The big yellow area at the southern edge of the Managua lake is the capital Managua. Source: INETER

Nicaragua is politically divided into 17 Departments and each Department is subdivided into Municipal Units. According to this political division, the area of interest around the Masaya caldera includes parts of 4 Departments -Managua, Masaya, Carazo and Granada- and thereby about 26 Municipal Units, which are shown in Fig. 8.2.

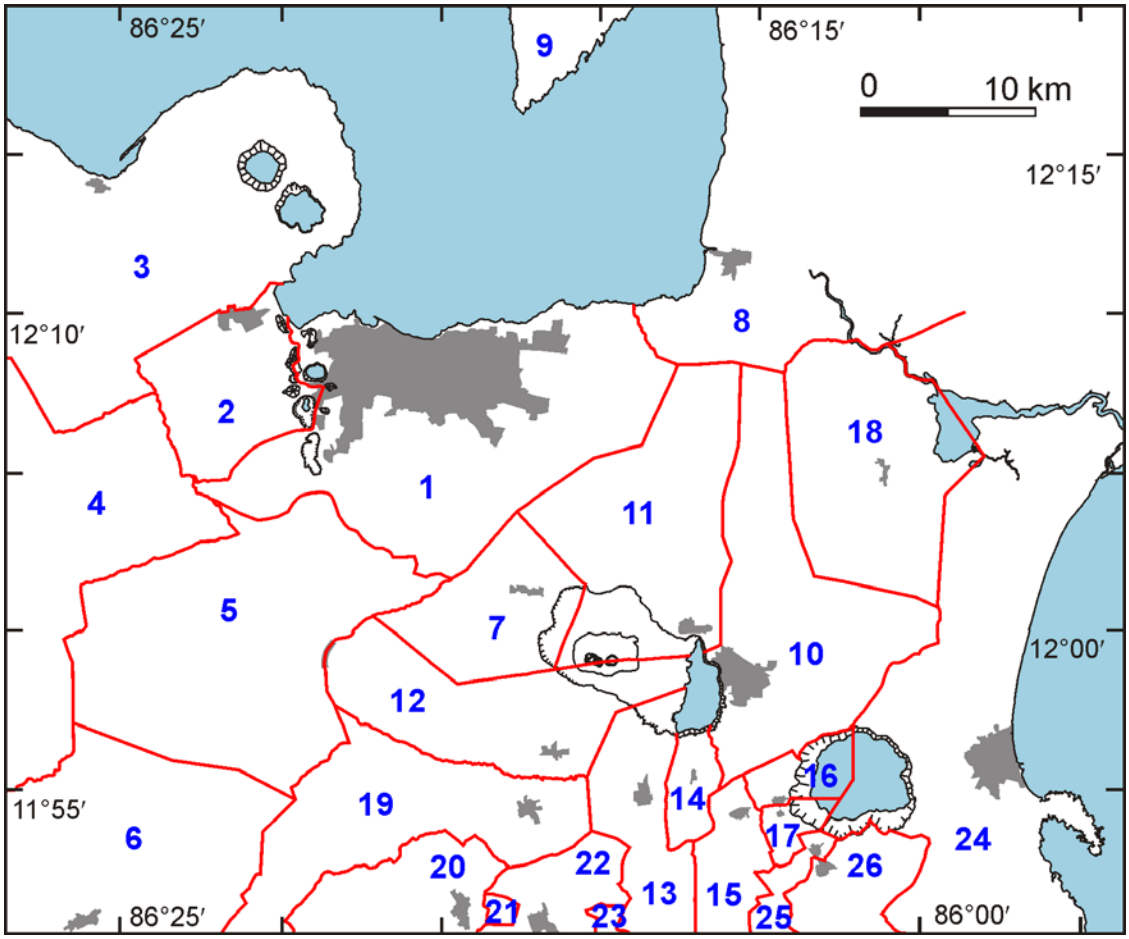

Figure 8.2: Political division and location of main cities of the area around the Masaya caldera. The numbers indicate the Municipal Units: 1. Managua, 2. Ciudad Sandino, 3. Mateare, 4. Villa Carlos Fonseca, 5. El Crucero, 6. San Rafael del Sur, 7. Ticuantepe, 8. Tipitapa, 9. San Francisco Libre, 10. Masaya, 11. Nindirí, 12. La Concepción, 13. Masatepe, 14. Nandasmo, 15. Niquinohomo, 16. Catarina, 17. San Juan de Oriente, 18. Tisma, 19. San Marcos, 20. Diriamba, 21. Dolores, 22. Jinotepe, 23. El Rosario, 24. Granada, 25. Diriá, 26. Diriomo.

Characteristics of the population of each Municipal Unit in the studied area are summarized in Table 8.1, including number of inhabitants, population density and number of houses.

The number of inhabitants and the population density is especially high in this area due to the presence of some of the most important cities of the country: Granada, Masaya and the capital Managua, which has more than one million inhabitants and ca. 5000 inhabitants per km^2. Other municipal units of smaller size which are located less than 2 km from Masaya caldera's rim also have high population densities (>250 inhabitants per km^2), and include Ticuantepe, Nindirí, La Concepción, Masatepe and San Marcos (Table 8.1).

Table 8.1: Geographical aspects of every municipal unit inside the studied area

Municipal Unit	Area (km^2)	Inhabitants (Projection for 2000)	Population Density Inhab/km^2	Number of Houses
Managua	267.17	1316981	4929	178168
Ciudad Sandino	51.11	131316	2569	10557
Mateare	297.40	24680	83	2860
Villa Carlos Fonseca	562.01	32818	58	4894
El Crucero	225.72	22107	98	5314
San Rafael del Sur	357.30	41574	116	7827
Tipitapa	975.30	108457	111	15537
Ticuantepe	60.79	24377	401	3808
Masaya	146.62	139701	953	21719
Nindirí	142.91	36845	258	5778
La Concepción	65.67	32944	502	5036
Masatepe	59.40	28778	484	4920
Nandasmo	17.63	9227	523	1397
Niquinohomo	31.69	15916	502	2669
San Juan de Oriente	9.20	30738	406	625
Catarina	11.49	8299	722	1334
Tisma	126.17	12697	101	1896
San Marcos	118.11	30692	260	5062
Diriamba	348.88	57512	165	10209
Dolores	2.62	6781	2588	1049
Jinotepe	280.52	38939	139	7281
El Rosario	14.08	4494	319	812
Granada	592.07	111886	189	18526
Diriá	25.52	6075	238	1168
Diriomo	50.08	20102	463	3596

Note: The number of inhabitants is given as a projection for the year 2000, based on the 1995 population census (INEC 1997b)

8.2.2 Buildings

According to Blong (1996) building and contents can suffer through a variety of damage types, including burial, ignition/incineration, foundation failure, racking, impacts from ballistic ejecta, collapse, transport, undermining, excessive wall or roof loads and corrosion; which may produce total destruction to negligible damage. Other aspects can influence the risk of a building or house, like the location, design, construction materials, compliance with wind or earthquake codes, maintenance, contents, etc (Blong 1996), but this is variable according to the type of hazard.

For hazards from tephra fallout, the type and quality of the houses and roofs is a very important aspect to consider. The 3rd Housing Census in Nicaragua of the year 1995 (INEC 1997a) revealed that in the study area 51% to 72% of the houses have zinc-sheet roofs, 7% to 21% have fiber reinforced cement, 4% to 36% clay or cement tiles, and 2% to 7% of houses have thatch or waste material roofs. This last category of houses, would not even resist minimal 10 cm of tephra coverage. Although relevant quantitative data on resistance of roof structures to ash loading are lacking, experience from Pinatubo (Spence et al. 1996) shows that all structures listed above would have a high risk of partial to total damage when loaded with fallout ash.

8.2.3 Lifelines

Lifelines are roads, telecommunication networks, gas and water pipelines and electricity distribution systems which seem to be particularly vulnerable to volcanic hazards (Blong 1996). As it was mentioned before, the area considered around the Masaya caldera holds a concentration of lifelines, such as the International Airport, the Interamerican Highway, government buildings and embassies, factories, and the telephone, water and energy supply companies. Actually the Interamerican Highway crosses the rim of the Masaya caldera at its northern portion, at the same place where the "Railroad" lava flow flowed beyond the caldera margin reaching a distance of 8 km from its vent (Williams 1983). Blong (1996) cites some examples of potential damage to the lifelines as would be the destruction of a road by a lava flow, the removal of a high-tension transmission tower by a pyroclastic flow, water supply contamination from airfall tephra and of course the danger that ash poses for aircraft engines.
Important economic losses are caused every year by the acid rain produced by the Masaya volcano degassing, but in the case of a bigger eruption the situation would be much worse with the plantations covered with ash and lapilli.

8.3 Volcanic risk assessment

The distribution of the deposits from the youngest explosive eruptions of the Masaya caldera complex indicating the location of the municipal units which were previously characterized in terms of vulnerability is shown in Fig. 8.3.

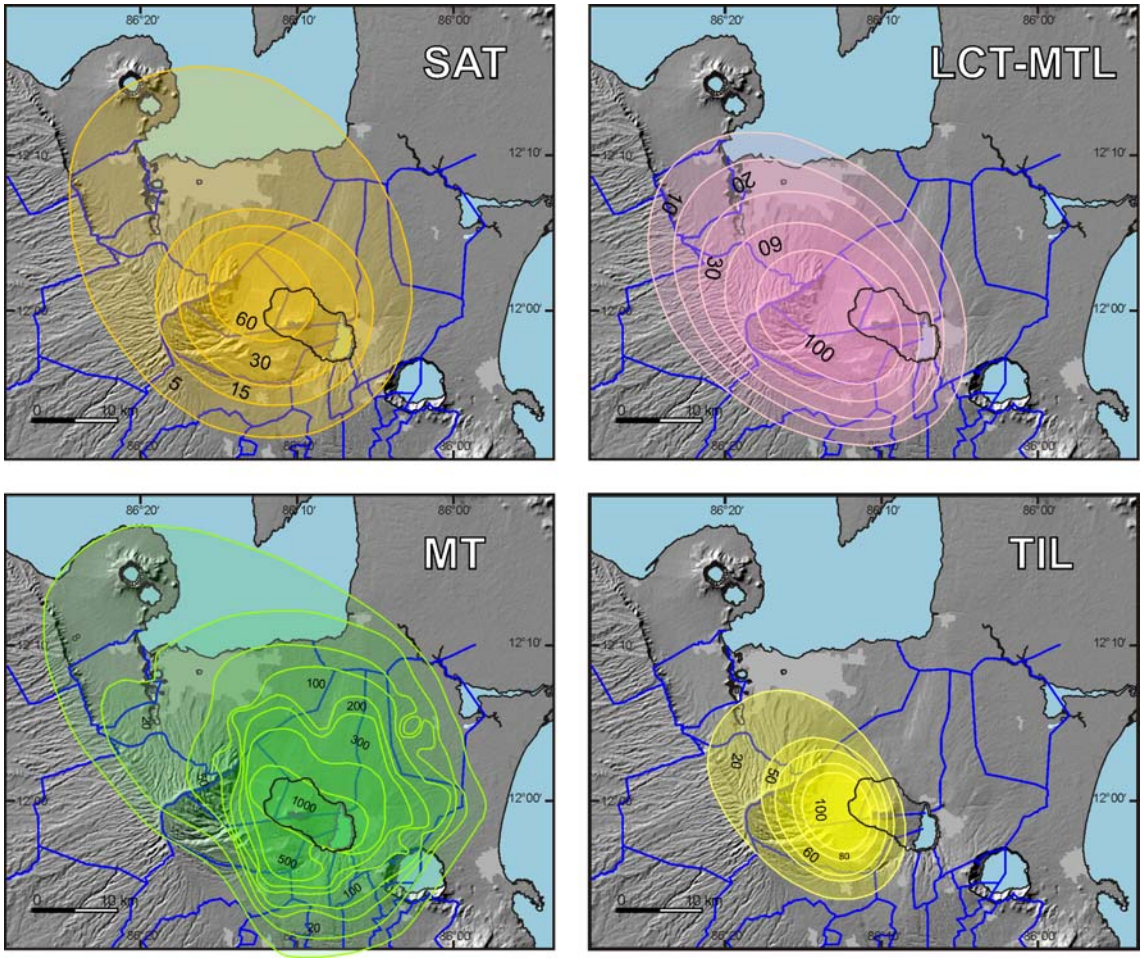

Figure 8.3: Bulk deposit distribution of the SAT, LCT-MTL, MT and TIL showing the political subdivision in Municipal Units of Fig. 8.2.

The isopach maps are, to variable degrees, limited by the lack of more distal exposures or the incomplete preservation of thin distal deposits. This means that some of the political units which show no coverage by these deposits, could actually have been affected by distal tephra fallout of up to 20 cm thickness, still more than enough to cause roof collapse.

The results of which areas were the most affected by the large eruptions at Masaya, according to the type of eruptions and hazard, and the characteristics of each municipal already mentioned, were used to evaluate which would be affected in the case of a similar eruption in the future. Based on criteria including cumulative thickness of the pyroclastic units studied, population density and distance of the main cities from the caldera rim, a risk map considering each Municipal unit was constructed (Fig. 8.4).

Naturally, the Municipal units with higher risk are those located very near the Masaya caldera, especially in the west to northwest, the direction of the prevailing winds when most of these explosive eruptions occurred. These communities happen to be the most populated. The ones with the highest cumulative thickness of tephra, and thus most likely to sustain damage from similar (or even smaller) future eruptions, are Ticuantepe and Nindirí, each with more than 20 m of cumulative tephra. They are followed by Masaya (also located at the caldera rim), for which the main hazard is posed by pyroclastic surges, since it is located in the opposite direction of the prevailing winds and the low southeast part of the caldera is filled by a lake, such that a future eruption there would be strongly phreatomagmatic. Smaller cities and Municipal Units in the south, like San Marcos, Masatepe and Nandasmo, have average cumulative thicknesses from 3 to 6 m of tephra, so they are considered areas of medium risk. The least affected cities would be those near the Pacific coast (Villa Carlos Fonseca, San Rafael del Sur), or at distances of more than 10 km to the east or southeast of the caldera, which might experience distal ash showers.

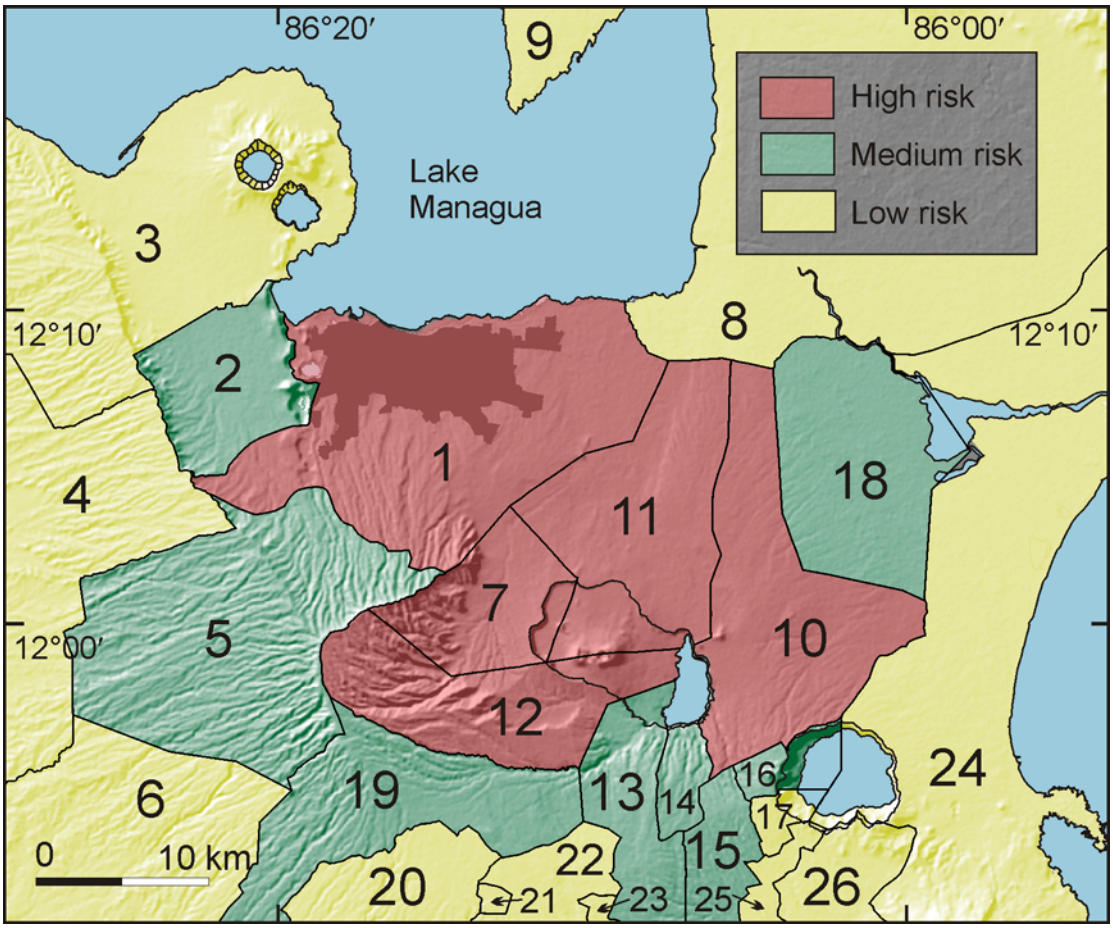

Figure 8.4: Risk map of the Masaya caldera and surrounding areas based on criteria like cumulative thickness of the recent tephra units, population density and distance of the main cities from the caldera rim. The numbers indicate the municipal units shown in Fig. 8.2.

8.4 Discussion

Explosive eruptive activity, like that exhibited by the Masaya caldera complex in the last 6,000 years, is a major threat to western central Nicaragua, where four of the most important departments are located: Managua, Masaya, Granada and Carazo. These departments comprise 26 Municipal Units, some of which also have highly populated cities located on or very near the caldera rim, like it is the case of Masaya city.

The map of estimated volcanic risk for the Municipal Units and cities around the caldera presented here indicates high risk for Ticuantepe, Nindirí, Masaya and La Concepción, all located near the caldera rim, and also for Managua, the most densely populated city of the country and therefore with a high concentration of the lifelines.

Although the more recent activity at Masaya consisted of minor pyroclastic and mainly effusive eruptions inside the caldera (Walker et al. 1993), there is no geologic evidence that large eruptions should not occur again. The types of large eruptions that one can expect from Masaya are Plinian or Surtseyan type. The Plinian eruptions may produce extensive basaltic fall that accumulates to form

heavy loads on building structures and pollutes the air with dust, and the Surtseyan eruptions can give rise to violent pyroclastic surges of great extent and capable of surmounting topographic highs, causing severe damage along their path. In the case that an event of a similar type and magnitude as the one that produced the Masaya Tuff would happen in the future, the surge would reach Managua city in minutes and present a deadly danger to most of 2 million people living in this area.

Because of the grave hazard to large populations, it is important to continue detailed studies of the eruptive past of Nicaragua's volcanic centers, and to maintain continuous monitoring. As Schmincke (2004) stated: "whether a volcanic eruption leads to major loss in human lives or not depends on the population density in the proximity of a volcano and its state of preparedness and organization". What is important is to recognize the potential dangers and to have in place effective and timely contingency plans; this can reduce the loss of lives. A particular problem in this case is that the unusual basaltic Plinian type of eruption has never been witnessed and the geological records provide no clues on their initiation. Hence, where geophysical signals of an impending basaltic eruption are recorded, there is presently no way to determine whether this will be a relatively harmless Strombolian or a potentially desastrous Plinian eruption. There is a great probability, however, that the eruption would involve phreatomagmatic, surge-producing phases, particularly if it occurred in the lake-filled eastern part of the caldera.

Chapter 9

Summary and discussion

9.1 Stratigraphy

Previous work (Williams 1983; Bice 1985) had identified the Fontana Tephra, the Masaya Triple Layer, and the Masaya Tuff as eruptive products of the Masaya caldera. Field work by Wehrmann (2005) and geochemical comparisons presented here favor an eruption of the ca. 60 ka FT from a vent in the older Las Nubes caldera. The present re-investigation of the geological record shows that there were three basaltic eruptions from the Masaya caldera in the last 6000 years producing widespread tephras: the ca. 6 ka SAT, the 2.1 ka LCT-MTL, and the 1.8 ka MT-TIL. The stratigraphic work presented here is based on detailed lithologic logging of more than 200 outcrops but also benefits from the distinct chemical compositions that characterize each tephra and allowed to verify or discard uncertain field-based correlations. As an example, a surge deposit at the intersection of the Masaya-Tipitapa road with the Inter-American Highway looks very similar to the MT but chemical analyzed showed it represents a slightly older, local phreatomagmatic eruption at the caldera rim.

The newly identified San Antonio Tephra (SAT) consists of a lower Plinian scoria fallout and an upper phreatomagmatic pyroclastic-surge package. The fallout package is stratified by intercalated ash beds reflecting temporary access of external water during this mainly magmatic phase of eruption. A fallout bed rich in hydrothermally altered lithics marks the transition to phreatomagmatic activity, which produced the surges, ash fallout, and two more lapilli fallout beds.

The major stratigraphic problem confronted when studying the Masaya deposits was related to La Concepción Tephra and the Masaya Triple Layer. Both have different internal architectures and dispersal directions (LCT to the south, MTL to the northwest) – a fact not recognized by earlier studies - but occur at the same stratigraphic level. However, both have identical compositions of bulk-rock, matrix and inclusion glass, and phenocrysts, and thus are different facies of one eruption product derived from a single magma reservoir. Although there are no connecting outcrops, a correlation between the two facies is proposed here using lithological and geochemical characteristics. The LCT-MTL eruption began with a phreatomagmatic explosion, followed by mainly magmatic Plinian scoria fallout repeatedly interupted by phreatomagmatic phases which gradually dominated the eruptive behavior until a very strong Phreatoplinian eruption occurred as the terminal phase. The duration of this multi-phase eruption was long enough to experience significant changes in wind direction and strength affecting the tephra dispersal.

The Masaya Tuff / Ticuantepe Lapilli (MT-TIL) eruption started with a sudden blast event, which marked the beginning of a series of phreatomagmatic explosions that emplaced unusually widespread base surges (MT). When the availability of external water for magma-water interaction decreased, eruption style changed to high columns emplacing stratified Plinian scoria fallout (TIL).

Geochemical correlations allowed to identify basaltic ash layers on the Pacific seafloor as distal equivalents of all three Masaya tephras. These correlations

were important because they allowed much more realistic estimates of erupted volumes and helped to constrain the tephra ages.

9. 2 Origin of the Masaya caldera

The origin of the Masaya caldera is still a matter of debate. It has been proposed that the caldera formed by subsidence following passive subterranean withdrawal of magma (McBirney 1956; Williams and McBirney 1979) or during a series of collapses, over an extended period of time, resulting from magma withdrawal during large, explosive, basaltic eruptions (Bice 1980; 1985). Williams (1983a) argued that the collapse occurred due to eruption of ~10 km^3 magma in the form of widespread pyroclastic surges (the Masaya Tuff) and a basaltic ignimbrite which he claimed to occur below the Masaya Tuff and exposed along the entire perimeter of the Masaya caldera. In spite of repeated field visits to the cited and other outcrops, no such ignimbrite deposit could be found during the present study. The only possible candidate observed was a loose, poorly-sorted, lithic-rich deposit with black round bombs, which crops out locally in a quarry along the road crossing the southern rim of the caldera in direction to Masatepe. The bulk rock composition of the bombs was analysed by XRF and share the same composition with the Masaya Tuff. The features exhibited by this deposit do suggest a pyroclastic density current origin. Other deposits with basaltic ignimbrite-like characteristics do occur around the caldera but these are clearly older and related to Las Sierras Group volcanism.

The 6x11 km Masaya caldera is elongated parallel to the volcanic front and its scalloped walls suggest that it formed by series of subsidence events rather than a single collapse. Semicircular scars at the rim at least in some cases are vents of minor phreatomagmatic eruptions. The depression has an area of 55 km^2 and the wall is highest (~150 m) at the eastern (near Masaya city) and western parts of the caldera which is filled to unknown depth by younger volcanic deposits and the lake in the southeast. Assuming a minimum subsidence of 150 m, the volume of the caldera basin would be ~8 km^3.

The three Masaya tephras combine to a total tephra volume of at least 5 km^3 demonstrable on land. The offshore stratigraphic work suggests these tephras combine to >25 km^3 (~10 km^3 DRE), with the SAT alone accounting for 14 km^3 and the MT for 10 km^3. These two eruptions are the only ones demonstrated to have a sufficiently large volume to have formed a caldera. Most likely the SAT eruption initiated the subsidence of the Masaya caldera which would thus be about 6000 years old, with possible additional subsidence occurring during the later eruptions. The highly phreatomagmatic nature of the MT surge deposits is probably due to the presence of a lake inside the pre-existing caldera.

The extra-caldera morphology and the rock successions exposed in the caldera walls show that Masaya was a flat shield volcano dominantly build by low-viscosity lava flows prior to caldera subsidence. The ~150 m thick mafic tephra and lava succession of the caldera walls must be younger than 24 ka, because it does not contain the Apoyo tephras. These are abundantly exposed around the caldera but are probably hidden below the floor inside the caldera. Masaya is thus a young volcano that rapidly evolved through a shield-building phase to caldera formation with large-volume, highly explosive eruptions. During the past ~1.5 ka, Masaya has only shown intra-caldera activity of cinder cone formation with frequent but low-intensity eruptions and lava flows (Walker et al. 1993).

9.3 The generation of basaltic Plinian eruptions

Basaltic eruptions are the most common type of volcanism on Earth and typically occur in the form of Strombolian, Hawaiian or Surtseyan eruptions or lava flows (Wilson and Head 1981). The existence of basaltic Plinian eruptions, first documented by Williams (1983) at Masaya and by Walker et al. (1984) in New Zealand, has only recently found more scientific attention (Houghton et al. 2004; Sable et al. 2006; Wehrmann et al. 2006).

It is widely accepted that the mechanism of magmatic eruption of low-viscosity basaltic magmas is determined by the extent to which the melt and gas phases separate during ascent through the conduit. With little separation the thoroughly vesiculated magma erupts in Hawaiian fashion, with efficient separation single bursts of Strombolian eruptions occur (Wilson and Head 1981; Parfitt and Wilson 1999; Parfitt 2004). Magma fragmentation is much more efficient with the former than the latter.

The typical features of Plinian eruptions are high discharge rates and the formation of positively buoyant eruption columns that rise to stratospheric levels where they drift laterally with the wind at the level of neutral buoyancy. Physical models of such eruption columns (e.g., Woods 1988) show that strong buoyancy depends on eruption temperature and on rapid heat transfer from hot pyroclasts to entrained air. Rapid heat transfer requires fine fragmentation of the magma. Plinian eruptions are commonly associated with felsic magmas for which fragmentation models have been developed. These attribute fine fragmentation either to overpressure building up in growing bubbles constrained by high-viscosity melt (Sparks 1978; Barclay et al. 1995) with fragmentation occurring at some threshold vesicularity (Houghton and Wilson 1989) or to strain rates produced during decompression which exceed the viscous relaxation and cause brittle fragmentation of the melt (Cashman et al. 2000; Papale 1999). In both cases, high melt viscosity is a prerequisite of fine fragmentation so that these models are not applicable to low-viscosity basaltic melts.

Basaltic magmas may become highly viscous by crystallization (e.g. Sparks and Pinkerton 1978; Tait et al. 1989). For Strombolian eruptions Taddeucci et al. (2004) found an increase in explosivity related to an increased ratio of microlite-rich tachylitic to microlite-poor sideromelane scoriae at Etna volcano. But the Masaya Tephras are characterized by very low phenocrysts and microlites contents, commonly between 1-3 vol.% and maximum of 10 vol.% Since crystallization is a slow, diffusion-limited process, the paucity of microlites indicates relatively high ascent rates.

Magmatic temperatures of the basaltic magmas producing the Masaya tephras were around 1100°C, about 300°C hotter than typical felsic magmas. Although eruption temperatures probably were somewhat lower due to interaction with external water (see below), the higher eruption temperatures may have compensated less efficient fragmentation with respect to felsic magmas in forming buoyant Plinian eruption columns.

It could be argued that unusually high volatile contents may have caused intense fragmentation in the case of the Masaya tephras. However, water content of the magmas measured in melt inclusions are moderate (1.5-3.4wt%); other basaltic magmas with much higher water contents only produced Strombolian eruptions such as Cerro Negro volcano in Nicaragua with up to 6 wt% H_2O (Roggensack et al. 1997) or Fuego volcano in Guatemala with 4-6 wt% H_2O (Sisson and Layne 1993; Roggensack 2001). CO_2 contents of the Masaya magmas are below the

detection limits of FT-IR, probably because the magma chamber was relatively shallow so that CO_2 escaped from the magma before reaching the storage level.

Magma-water interaction is known to cause fine fragmentation of basaltic magmas. Walker et al. (1984) invoked interaction with a hydrothermal system to explain the basaltic Plinian eruption at Tarawera volcano (but Houghton et al. (2004) show that there is no evidence to support this). McPhie et al. (1990) and Mastin (1997) argue that magma-water interaction caused the anomalous highly explosive basaltic eruption of the Keanakakoi Ash in 1790 at Kilauea, Hawaii. This deposit has surge beds, is fine-grained, contains accretionary lapilli and other evidences of water involvement; however, it does not have Plinian dispersal. Magma-water interaction occurred during all three Masaya eruptions to variable extent. Opening and terminal, but also intervening phases of the eruptions were fully phreatomagmatic as evidenced by low-vesicularity scoria, abundant lithics, surge beds and fine-grained tuffs, and accretionary and armored lapilli. Also some of the Plinian fallout beds show evidence of magma-water interaction by varying lithic contents, appearance of hydrothermal lithics (showing that water access occurred deeper in the conduit), or presence of lower-vesicularity juvenile lapilli together with the highly vesicular scoria. However, such magma-water interaction during Plinian phases must have been minor or else cooling by water and lithics would have consumed the heat required to form a buoyant eruption column. Yet such minor interaction may have been sufficient to cause more efficient fragmentation of the magma compared to purely magmatic conditions.

Textural studies of intermediate to felsic pumice lapilli from Plinian eruptions led to the conclusion that complex processes of mixing and deformation of magma rising in the conduit play a significant role in the eruption dynamics (Gardner et al. 1998; Hammer et al. 1999; Polacci et al. 2001). Lautze and Houghton (2007) observed at Stromboli that the proportion in which freshly rising, degassing and stagnant, degassed basaltic magma batches mixed dynamically in the conduit was a controlling factor of the explosivity of the Strombolian eruptions. Such relationships have also been inferred for the basaltic Plinian eruptions of Tarawera 1886 and Etna 122 BC (Houghton et al. 2004), where partial gas-melt separation occurred despite the apparently high discharge rates. At Masaya, the SAT and LCT-MTL sequences show vertical variations in amount and type of juvenile fragments similar to those observed at Etna. The most voluminous and widespread layers, SAT-A6 and LCT-MTL-II, are dominated by highly vesicular irregular to fluidal-shaped sideromelane fragments. In contrast, smaller fallout layers of these tephras have variable amounts of sideromelane, tachylite and mingled fragments. Such mingled fragments represent magma batches that experienced different degrees of degassing, gas-melt separation, and cooling times and re-mixed during ascent through the conduit (cf. Pallister et al. 1996; Rosi et al. 2004). The highly vesicular sideromelane clasts represent fresh, gas-rich and strongly degassing magma that obviously had a major role in forming Plinian eruptions.

Wehrmann (2005) used the abundance of microlite-free highly vesicular sideromelane in the Fontana Tephra to argue that this basaltic Plinian eruption was caused by catastrophic degassing in response to delayed homogeneous bubble nucleation during high ascent rates. Such sudden and extensive degassing may then have caused intense fragmentation and high exit velocity at the vent. This process may also have operated in the formation of the younger Masaya tephras which also contain abundant sideromelane fragments and

where the magma had an even higher water content than that of the Fontana Tephra. However, measurements of porosity and textural characteristics of the clasts would be needed to test this model.

Another mechanism generating sudden decompression and degassing is (partial) collapse of the volcanic edifice (Coltelli et al. 1998). However, this is not applicable to Masaya which had a big reservoir and a flat shield-volcano edifice. Such a flat edifice favors frequent and rapid ascent of basaltic magmas whereas high volcanic edifices generate compressional stresses that hinder magma ascent (Pinel and Jaupart 2004). Considering that basaltic Plinian eruptions occurred at flat Masaya and at high Etna, this does not appear to be a crucial factor in the generation of such eruptions.

In summary, properties of the magma reservoirs of the Masaya tephras such as chemical composition, crystal content, depth and temperature, and dissolved water content were not different from other reservoirs producing Strombolian or Hawaiian eruptions. There is no evidence of the injection of new magma into the reservoirs that might have triggered the eruptions. Even the large size of the reservoirs probably was not crucial for the mechanism of eruption, because Walker et al. (1993) and Metaxian (1994) argue that there is presently a large reservoir beneath Masaya feeding the small Strombolian historic eruptions.

The critical processes determining the style of eruption most probably operated in the conduit. The following model is consistent with the available data but additional investigations (e.g., vesicle and crystal textures) would be needed for further confirmation.

The eruptions began with phreatomagmatic explosions clearing the vent to facilitate higher discharge during subsequent eruption. The low viscosity of the crystal-poor hot basaltic melt allowed for some gas-melt separation during degassing and ascent. Simultaneously, external water repeatedly gained access into the conduit where it partially quenched the magma. Due to both reasons, there was variably degassed and cooled magma in the conduit that mixed with rising surges of fresh, actively degassing magma. Stronger discharge from the reservoir caused a high proportion of fresh magma in such mixtures, leading to intense fragmentation and higher eruption temperatures. Since it is unlikely that influx of external water was completely turned off and on, vaporization of such water probably assisted the fragmentation process. The multi-phase eruptions occurred over extended periods of time as shown by changing wind directions in the case of LCT-MTL. Cooling by water influx may thus have temporarily blocked the conduit, causing build-up of pressure below the plug. Phreatomagmatic explosions (which separated Plinian events in all three tephras) may have destroyed such plugs and caused sudden decompression of the underlying magma, triggering catastrophic degassing. Whatever the details of these processes, it seems clear from the lithology of the deposits that some extent of magma-water interaction played an important role in generating the basaltic Plinian eruptions at Masaya. The reasons for the high discharge rates necessary to maintain a Plinian eruption remain unknown; it may be speculated that the active tectonics of the Managua graben may have favored rapid reservoir evacuation either directly or by facilitating early roof subsidence.

9.4 Magmatic evolution

The central Nicaraguan section of the Central American Volcanic Arc (CAVA) is where the crust is thinnest and the subduction angle is the steepest (Carr 1984; Carr et al. 2004). Geophysical data indicates deep-reaching serpentinization of the subducting plate (Ranero et al. 2003; Grevemeyer et al. 2005). A strong influence of subducted components on arc-magma compositions is to be expected and slab signals such as Ba/La reach peak values in central Nicaragua (Carr et al. 2004, Walker et al., 1993, Morris et al. 1990). The magmas inherit such slab signals from their source in the mantle wedge which may be modified by invading fluids or partial melts from the subducted slab (Plank and Langmuir 1993; Carr et al. 1990; Leeman et al. 1994).

The Masaya tephras have Ba/La ratios of 76-82 which lie well within the regional range of the central Nicaraguan rocks (Carr 1984; Carr et al. 2004). However, the present study shows that there were variations with time at Masaya in element ratios such as Ba/La, U/Th and Pb/Ce. The strongest slab component is seen in the ca. 6 ka old SAT, the least subduction influence in the 2.1 ka LCT-MTL, and an intermediate influence in the 1.8 ka MT-TIL. Over such a short time span, the composition of a given mantle region would not change significantly. The Masaya magma system rather switched between different source regions over time periods of a few thousand to only several hundred years. Similar changes have been observed between the low-Ti and high-Ti rocks of the Nejapa-Granada volcanic zones (Walker et al. 1990) but no time constraints were provided there.

Element ratios indicative of the degree of partial melting in the mantle (e.g., La/Yb) suggest the lowest melting degree for the SAT, the highest for the LCT-MTL, and an intermediate degree for the MT-TIL. Since chemical slab signals are commonly believed to be associated with slab-derived fluids invading the mantle wedge and reducing its solidus temperature, stronger slab signals would be expected to correlate with higher degree of melting. However, the Masaya tephras show the opposite behavior: an inverse relation between strength of slab signals and degree of partial melting. This suggests that either there is a significant contribution of decompression melting unrelated to mantle hydration, or the hydrating water and the enrichment of slab-derived elements are somehow decoupled. Melt-inclusion water contents are lowest (<1.5 wt%) in the LCT-MTL with the lowest slab signal but highest melting degree, intermediate (<2.2 wt%) in the SAT with maximum slab signal but minimal melting, and highest (<3.4 wt%) in the MT-TIL that is intermediate with respect to melting and slab influence. Although the differences in water contents are small and there are some uncertainties in their determination, they certainly do not show an easy correlation with either slab components or melting degree.

The primary melts at Masaya experienced extensive olivine fractionation such that the erupted products have MgO contents of 4.8-3.9 wt%. Bulk-rock and particularly matrix and inclusion glass compositional variations indicate upper-crustal fractionation of the pl, ol, cpx, mt phenocryst phases that operated somewhat differently for the three tephras.

The SAT magma fractionated ol+pl+cpx in proportions that largely buffered the CaO and Al_2O_3 contents with decreasing MgO. However, some of the melt reached a higher degree of differentiation (2.5-2.8 wt% MgO) and was re-mixed with the less evolved melt during eruption. A change from ol-dominated to stronger pl-controlled fractionation occurred at 4.8 wt% MgO in the LCT-MTL. An even sharper change from ol- to pl-dominated fractionation occurred at 5

wt% MgO in the MT-TIL magma. The late dominance of pl-fractionation suggests lower P_{H2O} for LCT-MTL and MT-TIL relative to SAT, in which pl extends to higher An-contents.

9.5 Volcanic hazards

Although the recent activity at the northwestern part of Masaya consisted of minor pyroclastic and mainly effusive eruptions inside the caldera, there is no geologic evidence that larger-magnitude explosive eruptions should not occur again. The worst-case scenarios one can expect from Masaya would be the generation of Plinian and violent Surtseyan eruptions.

The presence of the lake inside the caldera gives a high probability that a future eruption at the SE end would be Surtseyan again. If it were similar to the eruption of the Masaya Tuff, it would generate pyroclastic surges of great extent and capable of surmounting topographic highs, causing severe damage along their path. Such surges could reach Managua city in minutes and present a deadly danger to most of 2 million people living in this area.

Geophysical monitoring at Masaya would probably register signals of an imminent eruption of basaltic magma. However, neither this nor other studies were able to identify presursory characteristics that would help to determine if such an eruption will be Strombolian or Plinian in nature. If a Plinian eruption occurred, it would produce extended basaltic lapilli and ash fall that accumulates to heavy loads on building structures and pollutes the air with dust. The experience from the three past Plinian events at Masaya has been used in this study to quantify the hazard from Plinian fallout for each of the municipal units in the Masaya-Managua area separately. This is a first attempt to provide a data basis for emergency plans and crisis management. Certainly more research is needed to better understand the dynamics of basaltic Plinian eruptions in order to develop physical models that can then be applied to better assess the hazards at Masaya and elsewhere.

Bibliography

Barckhausen U, Ranero CR, von Huene R, Cande SC, Roeser HA (2001) Revised tectonic boundaries in the Cocos plate off Costa Rica: Implications for the segmentation of the convergent margin and for plate tectonic models. J Geophys Res 106:19207-19220

Barclay J, Riley DS, Sparks RSJ (1995) Analytical models for bubble growth during decompression of high viscosity magmas. Bull Volcanol 57: 422-431

Baxter PJ, Boyle R, Cole P, Neri A, Spence R, Zuccaro G (2005) The impacts of pyroclastic surges on buildings at the eruption of the Soufrière Hills volcano, Monserrat. Bull Volcanol 67: 292-313

Bice DC (1980) Tephra stratigraphy and physical aspects of recent volcanism near Managua, Nicaragua. PhD thesis, University of California, Berkeley, pp 1-422

Bice DC (1985) Quaternary volcanic stratigraphy of Managua, Nicaragua: Correlation and source assignment for multiple overlapping plinian deposits. Geol Soc Amer Bull 96:553-566

Blong RJ (1996) Volcanic hazards risk assessment. In: Scarpa, Tilling (eds) Monitoring and mitigation of volcano hazards, Springer, pp 675-698

Boudon G, Lajoie J (1989) The 1902 Peléean deposits in the Fort Cemetery of St. Pierre, Martinique: a mode for the accumulation of turbulent nuées ardentes. J Volcanol Geotherm Res 38: 113-130

Bulletin of the Global Volcanism Network (1993) Smithsonian Institution 18(6):4

Carey S, Sparks RSJ (1986) Quantitative models of fallout and dispersal of tephra from volcanic eruption columns. Bull Volcanol 48:109-125

Carr MJ (1984) Symmetrical and segmented variation of physical and geochemical characteristics of the Central American volcanic front. J Volcanol Geotherm Res 20:231-252

Carr MJ, Walker JA (1987) Intra-eruption changes in composition of some mafic to intermediate tephras in Central America. J Volcanol Geotherm Res 33: 147-159

Carr MJ, Feigenson MD, Bennett EA (1990) Incompatible element and isotopic evidence for tectonic control of source mixing and melt extraction along the Central American arc. Contrib Mineral Petrol 105:369-380

Carr MJ, Feigenson MD, Patino LC, Walker JA (2004) Volcanism and geochemistry in Central America: Progress and problems. In: Eiler J (ed) Inside the subduction factory. Geophys Monogr Ser 138:153-174

Cashman KV, Sturtevant B, Papale P, Navon O (2000) Magmatic fragmentation. In: Sigurdsson H, Houghton B, McNutt S, Rymer H, Stix J (eds) Encyclopedia of volcanoes, Academic Press, San Diego, pp: 421-430

Coltelli M, Del Carlo P, Vezzoli L (1998) Discovery of a Plinian basaltic eruption of Roman age at Etna volcano, Italy. Geology 26:1095-1098

Collins DE, Niccum MR, Bice DC (1976) Preliminary summary of late Pleistocene and Holocene volcanic and sedimentary stratigraphy of the Managua area, Nicaragua. Publicaciones Geológicas del Instituto Centroamericano de Investigación y Tecnología Industrial V:105-112

Connor C, Williams SN (1990) Interpretation of gravity anomalies, Masaya caldera complex, Nicaragua. In: Larue DK, Draper G (eds) Transactions of the 12th Caribbean Geological Conference, St. Croix:495-502

Cruden AR (1988) The structure of South-West Nicaragua: A preliminary assessment. Rep URAP 89001, Swed Agency for Res Coop with Dev Countries, Inst Nicaraguense de Mineria, Swedish Geological AB, Lule3, Sweden

Dames and Moore Inc - LAMSA (1978) Estudio Geológico de las ciudades del sistema metropolitano. ViceMinistero de Planificación Urbana, pp 1-143

DeMets C (2001) A new estimate for present-day Cocos-Caribbean plate motion: Implications for slip along the Central American volcanic arc. Geophys Res Lett 28:4043-4046

De Vita S, Orsi G, Civetta L, Carandente A, D'Antonio M, Deino A, di Cesare T, Di Vito MA, Fisher RV, Isaia R, Marotta E, Necco A, Ort M, Pappalardo L, Piochi M, Southon J (1999) The Agnano-Monte Spina eruption (4100 years BP) in the restless Campi Flegrei caldera (Italy). J Volcanol Geotherm Res 91:269-301

Druitt TH (1992) Emplacement of the 18 May 1980 lateral blast deposit ENE of Mount St. Helens, Washington. Bull Volcanol 54:554-572

Dzurisin D, Lockwood JP, Casadevall TJ, Meyer R (1995) The Uwekahuna Ash Member of the Puna Basalt: product of a violent phreatomagmatic eruptions at Kilauea volcano, Hawaii, between 2800 and 2100 14C years ago. J Volcanol Geotherm Res 66:163-184

Ehrenborg J (1996) A new stratigraphy for the Tertiary volcanic rocks of the Nicaraguan highland. Geol Soc Am Bull 108:830-842

Feigenson MD, Carr MJ, Maharaj S, Juliano S, Bolge L (2004) Lead isotope composition of Central American volcanoes: Influence of the Galápagos plume. Geochem Geophys Geosys (5)6, doi:10.1029/2005GC000915

Fierstein J, Nathenson M (1992) Another look at the calculation of fallout tephra volumes. Bull Volcanol 54:156-167

Freundt A, Kutterolf S, Schmincke H-U, Hansteen T, Wehrmann H, Pérez W, Strauch W, Navarro M (2006) Volcanic hazards in Nicaragua: Past, present and future. In: Rose WI , Bluth GJS, Carr MJ, Ewert JW, Patino LC, Wallance JW (eds) Volcanic hazards in Central America. Geol Soc Am Spec Pap 412:141-165

Gardner JE, Carey S, Sigurdsson H (1998) Plinian eruptions at Glacier Peak and Newberry volcanoes, USA: Implications for hazards in the Cascades volcano range. Geol Soc Am Bull 110: 173-187

Girard G, van Wyk de Vries B (2005) The Managua Graben and Las Sierras-Masaya volcanic complex (Nicaragua); pull-apart localization by an intrusive complex: results from analogue modeling. J Volcanol Geotherm Res 144:37-57

Grevemeyer I, Kaul N, Diaz-Naveas JL, Villinger HW, Ranero CR, Reichert C (2005) Heat flow and bending-related faulting at subduction trenches: Case studies offshore of Nicaragua and Central Chile. Earth Planet Sci Lett 236: 238-248

Grove TL, Gerlach DC, Sando TW (1982) Origin of calc-alkaline series lavas at Medicine Lake volcano by fractionation, assimilation and mixing. Contrib Mineral Petrol 80:160-182

Hammer JE, Cashman KV, Hoblitt RP, Newman S (1999) Degassing and microlite crystallization during pre-climactic events of the 1991 eruption of Mt. Pinatubo, Phillipines. Bull Volcanol 60:355-380

Hildreth EW (1981) Gradients in silicic magma chambers: implications for lithospheric magmatism. J Geophys Res 86:10153-10193

Houghton BF, Wilson CJN (1989) A vesicularity index for pyroclastic deposits. Bull Volcanol 51:451-462

Houghton BF, Wilson CJN, Pyle DM (2000) Pyroclastic fall deposits. In: Sigurdsson H, Houghton B, McNutt S, Rymer H, Stix J (eds.) Encyclopedia of volcanoes, Academic Press, San Diego, pp 555–570

Houghton BF, Wilson CJN, Del Carlo P, Coltelli M, Sable JE, Carey R (2004) The influence of conduit processes on changes in style of basaltic plinian eruptions: Tarawera 1886 and Etna 122 BC. J Volcanol Geotherm Res 137:1-14

Housh TB, Luhr JF (1991) Plagioclase-melt equilibria in hydrous systems. Am Mineral 76:477-492

INEC-Instituto Nacional de Estadísticas y Censos (1997a) VII Censo Nacional de Población y III de Vivienda 1995: Vivienda-Municipios II

INEC-Instituto Nacional de Estadísticas y Censos (1997b) VII Censo Nacional de Población y III de Vivienda 1995: Población-Municipios IV

Krusi A, Schultz J (1979) Base surge deposits of the Nicaragua volcano Masaya. Geol Soc Amer Abstract with Programs 11(3):87-88

Kuang JS (1971) Estudio Geológico del Pacífico de Nicaragua: Nicaragua. Catastro Invent Rec Nat Inf Geol 3, pp 1-101

Kudo AM, Weill DF(1970) An igneous plagioclase thermometer. Contr Mineral Petrol 25:52-65

Kutterolf S, Freundt A, Pérez W, Wehrmann H, Schmincke H-U Temporal succession and magnitudes of highly-explosive volcanic eruptions in west-central Nicaragua. J Volcanol Geotherm Res (in press)

Kutterolf S, Freundt A, Schacht U, Mörz T, Peréz W, Wehrmann H, Bürk D, Schmidt M, Schmincke H-U Marine Tephras from explosive volcanism in Nicaragua - Implications for volcanology and marine science at the Pacific slope (submitted to G3)

Lautze NC, Houghton BF (2007) Linking variable explosion style and magma textures during 2002 at Stromboli volcano, Italy. Bull Volcanol 69:445-460

Leeman WP, Carr MJ, Morris JD (1994) Boron geochemistry of the Central American volcanic arc –Constraints on the genesis of subduction-related magmas. Geochim Cosmochim Acta 55:1799-1806

Le Maitre RW, Bateman P, Dudek A, Keller J, Lameyre Le Bas MJ, Sabine PA, Schmid R, Sorensen H, Streckeisen A, Woolley AR, Zanettin B (1989) A classification of igneous rocks and glossary of terms. Blackwell, Oxford

Maaløe S (1994) Estimation of the degree of partial melting using concentration ratios. Geochim Cosmochim Acta 58 (11) 2519-2525

MacDonald GA, Katsura T (1964) Chemical composition of Hawaiian lavas. J Petrol 5:83-133

Mastin LG (1997) Evidence for water influx from a caldera lake during the explosive hydromagmatic eruption of 1790, Kilauea volcano, Hawaii. J Geophys Res 102:20093-20109

Mathez EA (1973) Refinement of the Kudo-Weill plagioclase thermometer and its application to basaltic rocks. Contrib Mineral Petrol 41:61-72

McBirney AR, Williams H (1965) Volcanic history of Nicaragua.Univ Calif Publ Geol Sci, Berkley and Los Angeles, pp 1-65

McBirney AR (1956) The Nicaraguan volcano Masaya and its caldera. Amer Geophys Union Transactions 37:83-96

McPhie J, Walker GPL, Christiansen RL (1990) Phreatomagmatic and phreatic fall and surge deposits from explosions at Kilauea volcano, Hawaii, 1790 A.D.: Keanakakoi Ash Member. Bull Volcanol 52:334-354

Melson WG, Sáenz R (1973) Volume, energy and cyclicity of eruptions at Arenal Volcano, Costa Rica. Bull Volcanol 37:416-437

Métaxian JP (1994) Étude Sismologique et Gravimetrique d'un volcan actif: dynamisme interne et structure de la Caldera Masaya, Nicaragua. Université de Savoie, France, pp 1-319

Morris JD, Leeman WP, Tera F (1990) The subducted component in island arc lavas : constraints from Be isotopes and B-Be systematics. Nature 344: 31-36

Nakada S (2000), Hazards from pyroclastic flows and surges. In: Sigurdsson H, Houghton B, McNutt S, Rymer H, Stix J (eds) Encyclopedia of Volcanoes, Academic Press, pp 945-955

Niccum M (1976) Regional tectonic, geologic and seismic data with hazard classifications: Appendix A, unpublished report for use with Woodward-Clyde Consultants, Inc. reports in Managua, Nicaragua: San Francisco, California, Woodward-Clyde Consultants Inc

Nielsen RL, Drake MJ (1979) Pyroxene-melt equilibria. Geochim Cosmochim Acta 43:1259-1272

Pallister JS, Hoblitt RP, Meeker GP, Knight RJ, Siems DF (1996) Magma mixing at Mount Pinatubo: petrographic and chemical evidence from the 1991 deposits. In: Newhall CG, Punongbayan RS (eds) Fire and mud: eruptions and lahars of Mount Pinatubo, Phillipines. University of Washington Press, Seatle, pp 687-732

Papale P (1999) Strain-induced magma fragmentation in explosive eruptions. Nature 397: 425-428

Parfitt EA (2004) A discussion of the mechanisms of explosive basaltic eruptions. J Volcanol Geotherm Res 134:77-107

Parfitt EA and Wilson L (1999) A Plinian treatment of fallout from Hawaiian lava fountains J Volcanol Geotherm Res 88:67-75

Pérez W, Freundt A (2006) The youngest highly explosive basaltic eruptions from Masaya Caldera (Nicaragua). In: Rose WI , Bluth GJS, Carr MJ, Ewert JW, Patino LC, Wallance JW (eds) Volcanic hazards in Central America. Geol Soc Am Spec Pap 412:189-207

Perfit MR, Gust Da, Bence AE, Arculus RJ, Taylor SR (1980) Chemical characteristics on island arc basalts: implications for mantle sources. Chem Geol 30: 227-256

Pinel V, Jaupart C (2004) Likelihood of basaltic eruptions as a function of volatile content and volcanic edifice size. J Volcanol Geotherm Res 137: 201-217

Plank T, Langmuir CH (1993) Tracing trace elements from sediment input to volcanic output at subduction zones. Nature 362:739-743

Polacci M, Papale P, Rosi M (2001) Textural heterogeneities in pumices from the climactic eruption of Mount Pinatubo, 15 June 1991, and implications for magma ascent dynamics. Bull Volcanol 63:83-97

Putirka KD (2005) Mantle potential temperatures at Hawaii, Iceland, and the mid-ocean ridge system, as inferred from olivine phenocrysts: evidence for thermally driven mantle plumes. Geochem Geophys Geosys 6, doi:10.1029/2005GC000915

Putirka K, Johnson M, Kinzler R, Longhi J and Walker D (1996) Thermobarometry of mafic igneous rocks based on clinopyroxene-liquid equilibria, 0-30 kb. Contrib Mineral Petrol 123:92-108

Putirka KD, Mikaelian H, Ryerson F, Shaw H (2003) New clinopyroxene-liquid thermobarometers for mafic, evolved, and volatile-bearing lava compositions, with applications to lavas from Tibet and the Snake River Plain, Idaho. Am Mineral 88:1542-1554

Pyle DM (1989) The thickness, volume and grain-size of tephra fall deposits. Bull Volcanol 51: 1-15

Pyle DM (2000) Sizes of volcanic eruptions. In: Sigurdsson H, Houghton B, McNutt S, Rymer H, Stix J (eds) Encyclopedia of Volcanoes, Academic Press, pp 263-269

Ranero CR, Phipps Morgan J, McIntosh K and Reichert C (2003) Bending-related faulting and mantle serpentinization at the Middle America trench. Nature 425: 367-373

Rymer H, van Wyk de Vries B, Stix J, Williams-Jones G (1998) Pit crater structure and processes governing persistent activity at Masaya volcano, Nicaragua. Bull Volcanol 59:345-355

Roggensack K (2001) Unraveling the 1974 eruption of Fuego volcano (Guatemala) with small crystals and their young melt inclusions. Geology 29:911-914

Roggensack K, Hervig Steven, McKnight, Williams SN (1997) Explosive Basaltic Volcanism from Cerro Negro Volcano: Influence of volatiles on Eruptive Style. Science 277: 1639-1642

Rose WI, Bonis SB, Stoiber RE, Keller M, Bickford T (1973) Studies of volcanic ash from two recent Central American eruptions Bull Volcanol 37:338-364

Rose WI, Anderson AT, Woodruff LG, Bonis SB (1978) The October 1974 basaltic tephra from Fuego volcano: description and history of the magma body. J Volcanol Geotherm Res 4:3-53

Rosi M, Landi P, Polacci M, Di Muro A, Zandomeneghi D (2004) Role of conduit shear on ascent of the crystal-rich magma feeding the 800-year-BP Plinian eruption of Quilotoa volcano (Ecuador). Bull Volcanol 66:307-321

Sable JE, Houghton BF, CJN Wilson and RJ Carey (2006) Complex proximal sedimentation from Plinian plumes: the example of Tarawera 1886. Bull Vol 69:89-103

Sandberg S, Connor C (2002) Geophysical investigation of the hydrogeologic structure and magma at Masaya volcano, Nicaragua. Eos, Transactions AGU 81

Sebesta J (1997) Dynamic development of the relief in the Managua area, Nicaragua. Acta Univ Carol Geogr 2:93-109

Schmincke H-U (2004) Volcanism. Berlin and Heidelberg, Springer Verlag, pp 1-334

Schumacher R, Schmincke H-U (1991) Internal structure of occurrence of accretionary lapilli-a case study at Laacher See Volcano. Bull Volcanol 53:612-634

Sisson TW, Grove TL (1993) Experimental investigations of the role of H2O in calc-alkaline differentiation and subduction zone magmatism. Contrib Mineral Petrol 113: 143-166

Sisson TW, Layne GD (1993) H2O in basalt and andesitic glass inclusions from four subduction-related volcanoes. Earth Planet Sci Lett 117, 619-635

Sohn YK, Chough SK (1989) Depositional processes of the Suwolbong tuff ring, Cheju Island (Korea). Sedimentology 36: 837-855

Sparks RSJ (1978) The dynamics of bubble formation and growth in magmas: a review and analysis. J Volcanol Geotherm Res 3:1-37

Sparks RSJ, Pinkerton H (1978) Field measurements of the rheology of lava. Nature 276:383-385

Spence RJS, Pomonis A, Baxter PJ, Coburn AW, White M, Dayrit M (1996) Building damage caused by the Mount Pinatubo eruption of June 15, 1991. In: Newhall CG, Punongbayan RS (eds) Fire and Mud: Eruptions and lahars of Mount Pinatubo, Phillipines. Seattle, University of Washington Press, pp. 1055-1062

Spera FJ (1984) Some numerical experiments on the withdrawal of magma from crustal reservoirs. J Geophys Res 89:8222-8236

Sun SS, McDonough WF (1989) Chemical and isotopic systems of oceanic basalts: implications for mantle composition and processes. In: Saunders AD, Norry MJ (eds) Magmatism in the ocean basins. Geol Soc London Spec Pub 42: 313-345

Tait S, Jaupart C, Vergniolle S (1989) Pressure, gas content and eruption periodicity of a shallow, crystallising magma chamber. Earth Planet Sci Lett 92:107-123

Thompson RN, Morrison MA, Dickin AP, Hendry GL (1984) An assessment of the relative roles of crust and mantle in magma genesis: an elemental approach. Phil Trans R Soc A310: 549-590

Valentine GA (1998) Damage to structures by pyroclastic flows and surges, inferred from nuclear weapons effects. J Volcanol Geotherm Res 81:117-140

van Wyk de Vries (1993) Tectonics and magma evolution of Nicaraguan volcanic systems. PhD thesis, Milton Keynes UK, the Open University, pp 1-328

Walker GPL, Self S, Wilson L (1984) Tarawera 1886, New Zealand - A basaltic Plinian fissure eruption. J Volcanol Geotherm Res 21:61-78

Walker JA (1984) Volcanic rocks from the Nejapa and Granada cinder cone alignments, Nicaragua, Central America. J Petrol 25:299-342

Walker JA (1989) Caribbean arc tholeiites. J Geophys Res 94:10539-10548

Walker JA, Carr MJ, Feigenson MD, Kalamarides RI (1990) The petrogenetic significance of interstratified high-and low-Ti basalts in Central Nicaragua. J Petrol 31:1141-1164

Walker JA, Williams SN, Kalamarides RI, Feigenson MD (1993) Shallow open-system evolution of basaltic magma beneath a subduction zone volcano: the Masaya Caldera Complex, Nicaragua. J Volcanol Geotherm Res 56:379-400

Wallace P, Carmichael ISE (1992) Sulfur in basaltic magmas. Geochim Cosmochim Acta 56:1863-1874

Wehrmann H (2005) Volatile degassing and plinian eruption dynamics of the mafic Fontana Tephra, Nicaragua. PhD Thesis, University of Kiel, pp 1–90

Wehrmann H, Bonadonna CB, Freundt A, Houghton BF, Kutterolf S (2006) A basaltic-andesitic plinian eruption revisited: case study of Fontana Tephra, Nicaragua. In: Rose WI , Bluth GJS, Carr MJ, Ewert JW, Patino LC, Wallance JW (eds) Volcanic hazards in Central America. Geol Soc Am Spec Pap 412:209-223

Weinbeg RF (1992) Neotectonic development of western Nicaragua. Tectonics 11:1010-1017

Weyl R (1980) Geology of Central America. In: Bender F (ed) Beiträge zur regionalen Geologie der Erdepp, Gebr. Borntraeger, Berlin - Stuttgart, pp1-371

Williams H, McBirney AR (1979) Volcanology. San Francisco, Freeman Cooper, pp 1-379

Williams SN (1983a) Geology and eruptive mechanisms of Masaya Caldera Complex, Nicaragua. PhD thesis, Dartmouth College, Hanover New Hampshire, pp 1-169

Williams SN (1983b) Plinian airfall deposits of basaltic composition. Geology 11: 211-214

Williams-Jones G, Rymer H, Rothery DA (2003) Gravity changes and passive SO2 degassing at the Masaya caldera complex, Nicaragua. J Volcanol Geotherm Res 123:137-160

Williams-Jones G (2001) Integrated Geophysical Studies at Masaya volcano, Nicaragua. PhD thesis, The Open University

Wilson L, Head (1981) Ascent and eruption of basaltic magma on the Earth and Moon. J Geophys Res 86:2971-3001

Wilson L, Walker GPL (1987) Explosive volcanic eruptions-VI. Ejecta dispersal in Plinian eruptions: the control of eruption conditions and atmospheric properties. Geophys J R astr Soc 89:657-679

Wohletz KH (1998) Pyroclastic surges and compressible two-phase flow. In: Freundt A, Rosi, M (eds) From magma to tephra: Modelling physical processes of explosive volcanic eruptions. Developments in Volcanology 4, Amsterdam, Elsevier, pp. 247-312

Wohletz KH, Sheridan MF (1979) A model of pyroclastic surge. In: Chapin CE, Elston WE (eds) Ash-Flow Tufs. Geol Soc Amer Spec Pap 180:177-194

Woods AW (1988) The fluid dynamics and thermodynamics of eruption columns. Bull Volcanol 50:169-193

Woodward-Clyde Consultants (1975) Summary report of investigation of active faulting in Managua, Nicaragua and vicinity. Viceministerio de Planificación Urbana

Acknowledgments

This work would not have been possible without the guidance and patience of my advisor Armin Freundt, who especially during the “final sprint” had to invest lots of time checking the chapters of my thesis and the presentation. Steffen Kutterolf was like my second advisor, always offering unconditional help in the field, in the office, in the lab and making pressure on me to work on the chemistry.

SFB-C4 members Heidi Wehrman and Hans-Ulrich Schmincke also collaborated a lot in the field and also in the work after. Thanks also to other SFB members, especially Kaj Hoernle, Thor Hansteen, Kristin Garofalo, Seth Sadofsky and Ken Heydolph.

The fieldwork, in which this thesis is based on, was possible thanks to the logistic support from the staff of the Instituto Nicaragüense de Estudios Territoriales (INETER), especially Wilfried Strauch, Guillermo Rocha, Antonio López and Eduardo Mayorga. Jeisson Chávez also helped with the fieldwork.

Sample preparation was mostly made by Cosima Burkhart and the analytical work was only possible the collaboration of Mario Thoner, Dagmar Rau, Folkmar Hauff and Dieter Garbe-Schönberg. Magma water content analysis were carried out at the University of Texas at Austin thanks to the support of Jim Gardner.

James A. Walker kindly sent me the chemical data of the Masaya lavas and Bruce Houghton some papers about the work on basaltic Plinian eruptions at Etna and Tarawera.

The old and new generation of people in the SFB floor made the time of my PhD nicer: Deniz, Dietmar, Thomas, Monika, Rieka, Ken, Marten, Ulrike, Olli and Silke. Ernst Flüh and Emanuel Söding helped me in the first steps of my life in Kiel. Although in the last months I quit going to the Mensa, during the first years I enjoyed the lunches and summer days together with Anne, Cord, Jorchi and Anke.

Guillermo Alvarado first introduced me to the fascinating world of volcanic deposits, he was my model to follow and also responsible for me coming to Kiel.

My 0ne year younger soul-twin Ivonne shared with me all of the moments from the beginning, starting from taking the plane to Germany, through learning German in the Goethe Institut and our first days in Kiel to the long working nights. It was simply great to have someone here who I rely on and to who I could talk in Costa Rican mixed with German words when it was needed.

To my mother I have to thank everything I am, her infinite love and also because she was the person that suffered the most during my stay here.

And finally to Lars, the person who had a lot to do with the fact that the last four years in Kiel became one of the best times of my life.